SYNTHESIS AND CHARACTERIZATION OF SPINEL TYPE MAGNETIC AND NON-MAGNETIC OXIDE NANOMATERIALS

thesis

submitted to the

UNIVERSITY OF PUNE

for the degree of

DOCTOR OF PHILOSOPHY

in Chemistry

By

S. Vijayanand

Research Guide

Dr. P. A. JOY

Research Co-Guide

Dr. H. S. POTDAR

Physical and Materials Chemistry Division

National Chemical Laboratory

Pune 411008

India

September 2010

CERTIFICATE

Certified that the work incorporated in the thesis

Synthesis and Characterization of Spinel Type Magnetic and Non-Magnetic Oxide Nanomaterials

submitted by **Mr.** S. VIJAYANAND for the Degree of *Doctor of Philosophy* in Chemistry was carried out by the candidate under our supervision at the Physical & Materials Chemistry Division of National Chemical Laboratory, Pune. Such material as has been obtained from other sources has been duly acknowledged in the thesis.

Dr. H. S. Potdar
(Research Co-Guide)

Dr. P. A. Joy
(Research Guide)

DECLARATION

I, hereby declare that the thesis entitled "Synthesis and Characterization of Spinel Type Magnetic and Non-Magnetic Oxide Nanomaterials ", submitted for the Degree of Doctor of Philosophy in Chemistry to the University of Pune, has been carried out by me at the Physical & Materials Chemistry Division, National Chemical Laboratory, Pune, India, Under the joint supervision of Dr. P. A. Joy (Research Guide) and Dr. H. S. Potdar (Research Co-Guide). The work is original and has not been submitted in part or full by me for any other degree or diploma to this or any other university.

Date: S. Vijayanand

...Dedicated to my Parents and to my brother...

Acknowledgements

It is a great pleasure to express my gratitude and sincere thanks to all those who helped me directly and indirectly to complete this work. This thesis would not have been possible without all these people and their constant encouragement.

First of all I would like to express my immense and sincere gratitude to my research supervisor ***Dr. P.A. Joy*** *for his constant support and guidance throughout my research work. I really admired the way he handle the scientific and nonscientific things with utmost perfection and sincerity. There is no doubt that I learnt so many things from him especially how to analyze and get valuable information even from small things, and how to solve a problem. My heartfelt thanks for his valuable time in bringing this output and shaping this thesis in the perfect manner.*

I could not find enough words to thank the efforts and input rendered by my research co-supervisor, ***Dr. H.S. Potdar****, to bring this thesis to this stage. The enthusiasm and interest he paid to resolve any technical problems is an inspiration for me. He is one of the genuine, humble and down-to-earth people I have seen. Many many thanks to him for his effort to teach so many scientific things which can be seen as an output in this thesis.*

I owe my deepest gratitude to ***Dr. Veda Ramaswamy,*** *who introduced me to the research world by giving an opportunity in this prestigious laboratory. Also I would like to express my whole hearted thanks for her personal support and care during my difficult situations.*

I am very much grateful to ***Dr. K. Vijayamohanan, Dr. C.V. Rode, Dr. P.P. Patil*** *for their valuable discussions and facilities that they afford to me to make this work more meaningful.*

I am grateful to Dr. S. Sivaram, Director, NCL who gave me an opportunity to work

in this esteemed research laboratory and also to CSIR for financial support. I wish to thank Dr. S. Pal, Head of Physical Chemistry Division for allowing me to use all the facilities in the division.

My sincere thanks to Dr. B. L. V. Prasad, Dr. C. S. Gopinath, Dr. K. Sreedhar, Dr. S. B. Deshpande, Dr. Ravi, and Dr. Ajith Kumar for their valuable advice and help. I am highly indebted to Mr. A.B. Gaikwad, Dr. K. R. Patil, Mr. Gholap, Mr. Naren, Mr. Kethan, and Dr. S. Kulkarni, who were helpful for characterizing various samples. Also I acknowledge Dr. Dewyani Patil for the sensor measurements. I extend my gratitude to Mr. Deepak Jori, Mr. Punekar and other office staffs for their timely help.

I forever indebted to my former teacher Dr. R. Saraswathi from Materials Science Department, Madurai Kamaraj University, Madurai.

My deepest and heartiest thanks goes to all my seniors, Dr. Raj, Dr. Joly, Dr. Deka, Dr. Sanjay, Dr. Seema and Dr. Shekar, fellow lab mates Sreeja, Khaja, Mangesh, Pankaj, Govind, Jaya, Lenin, Ramsundar and Bindhu without their help and support it is unimaginable to complete this work. Also I would like to mention about late Harwade kaka for his care and memories.

I take time to convey my gratitude to the project students who worked with me Venkatesh, Mani, Hemjoti, Selvaraj, Mathi, Souda, Yogita, Ramya for their help.

I would like to thank Geethy, Deepthi, Soya, Lilly, Pavan, Ranjith, Aneesh, Sister Mary, Anju, Hanna, Rojisha, Maneesh for their nice and friendly atmosphere.

I also acknowledge the homely environment provided by the Tamil group friends Edwin, Palani, Senthil Kumar, Nagarajan, Nellai Nagaraj, Sridhar, Pandiyarajan, Mohan, Dharma, Kannan & Sangeetha, Suresh, Padmaprasad, Viswanathan, Sabarinathan, Selva, Dhana, Kashmir, Senthil, Venkat, Sivaranjani, Rajambal.

I owe my deepest appreciation to Dr. Chidambaram, Dr. Bala, Dr. Pradeep (poori), Dr. Mallikarjuna, Mr. Ramanujam, Mr. Marimuthu, Mr. Senthil Kumar, for their guidance and advice. Poori deserves a special mention for the carring and love. Also I would like to give my appreciation to Balaji anna and his family for their concern.

I am very grateful to the GJ Hostel friends Dhanraj (room partner), Alson, Joyashish, Ajay, Venu(matchi), Manoj (matchi), Swaroop anna, Eldho, Venu, Rajesh, Suresh, Sandeep, Prasanna anna who made my stay very memorable.

It is a pleasure for me to thank my NCL friends Deepaknand (thadiyan), Vinod (thadi), Sumesh, Kuttan, Beena, Any, Thusara, Vinisha, Vinayak, Bhaskar, Nagesh, Manasi, Deepthi, Ravi, Ajay, Sheetal, Jijil, Soumya, Leena, Hari, Vivek and Jayprakash Nadgeri.

In this occasion I would like mention my friends ***Thirumoorthy, Saravanakumar, Kannan, Saravanaprabhu*** *and* ***Caroline*** *for their constant support and help especially during my toughest time.*

My deepest acknowledgement goes to ***Amma, Appa, Anna, Anni, Ammu and Sappu*** *for their love, support and encouragement which made me to come upto this level.*

S. Vijayanand

Contents

List of Tables

List of Figures

Abstract

Synthesis and studies of nanosized materials have been intensively pursued in the recent past not only because of their fundamental scientific interest but also for their interesting size and shape dependent properties such as electrical, optical, catalytic, thermal and magnetic properties as well as applications. Oxides play a very important role in many areas of chemistry, physics, and materials science. Different metallic elements are able to form a large diversity of oxide compounds. These can adopt a vast number of structural geometries with interesting properties.

In technological applications, oxides are used in the fabrication of microelectronic circuits, sensors, piezoelectric devices, fuel cells, coatings for the passivation of surfaces against corrosion, as catalysts, etc. In the emerging field of nanotechnology, the goal is to make nanostructures having special properties with respect to those of bulk. Oxide nanoparticles can exhibit unique chemical properties due to their limited size and a high density of corner or edge surface sites. In the recent years, various methods have been developed for the preparation of novel nanostructures of oxides. The nanostructures can be generated by a number of preparation methods that typically are described under physical and chemical methods.

Nanosized spinel type magnetic oxides are of great interest from the view point of a wide range of applications, including information storage, magnetic fluids, catalysis, batteries, sensors, supercapacitors, biomedical applications, etc. In most of the envisaged applications, the nanoparticles perform best when the size of the particles is below a critical value, which is dependent on the material and applications. However, synthesis of morphology controlled nanosized oxides without using any templates or surfactants is challenging one from the view point of avoiding organic pollutants.

The present thesis deals with the synthesis, characterization and studies on the properties of some spinel type magnetic and non-magnetic oxides as well as nanoparticles of the multiferroic oxide, bismuth ferrite. The first chapter is a brief introduction to oxide nanomaterials and the applications of oxides and nanosize oxides in the areas of sensors, catalysis, Li-ion batteries, supercapacitors, magnetism and multiferroism.

Chapter Two presents the experimental details of a modified co-precipitation/digestion method and an auto-combustion method adopted for the synthesis of the spinel based oxides and bismuth ferrite, with brief introduction to the different characterization methods employed in the present work. All the experimental methods and characterization techniques used are briefly discussed in the specific sections.

Third chapter describes the synthesis of molecular precursor cobalt hydroxy carbonate in the form of nanorods through a simple coprecipitation/digestion route. Further the chapter discusses about the formation of cobalt oxide Co_3O_4 with same morphological feature of its precursor cobalt hydroxy carbonate. The as prepared Co_3O_4 has been characterized using different techniques and tested for gas sensing property on CO gas and its catalytic oxidation of veratryl alcohol to veratryl aldehyde. The material is found to exhibit superior gas sensing and catalytic properties. Also it deals with the synthesis of the spinel type $ZnCo_2O_4$, its characterization and its gas sensing property of LPG gas.

Chapter four describes the results from the studies on the application of the Co_3O_4 nanostructures in Li batteries and supercapacitors. Co_3O_4 is utilized as the anode material for Li-ion batteries. The results showed a three fold increase over the capacity of the commercially used carbonaceous anode material. Similarly, better performance is obtained when the Co_3O_4 nanorods is used as a supercapacitor.

Chapter five deals with the synthesis and magnetic properties of nanosized Fe based spinel oxides such as $Fe_3O_4/\gamma Fe_2O_3$, $CoFe_2O_4$, and $ZnFe_2O_4$. The effect of digestion time on synthesis has been shown in case of $Fe_3O_4/\gamma Fe_2O_3$ system. In the case of $CoFe_2O_4$ and $ZnFe_2O_4$, the effects of method of synthesis on the magnetic properties are discussed.

The synthesis of nanoparticles of the multiferroic system $BiFeO_3$ and detailed studies on the magnetic properties are discussed in Chapter six. Different methods of synthesis show variations in the magnetic characteristics and these studies are described in detail in this chapter. Single phase material is found to exhibit interesting magnetic properties.

Chapter seven is an over all summary of the thesis based on the studies on the different nanosized oxide systems described in the previous chapters and a discussion on the future perspectives.

Chapter 1

Introduction

1.1 Materials Science

Materials science is an interdisciplinary subject with a combination of chemistry, physics and engineering [1]. Materials science and technology plays a vital role in the development of human civilization. Starting from the stone age we experienced bronze age, iron age and at present synthetic materials age which gives plastics and fibrous composites to build light weight technology. As a phase of development, material science has extended to a new era which is nothing but smart materials age. The smart materials will be able to select and execute specific functions in response to a change in an external stimuli.

In general, materials can be classified into polymers, ceramics, metals, semiconductors and composites. Due to the tremendous growth in science and technology, materials with different functions have been developed, such as superconductors, optical, electrical and magnetic materials. The multidisciplinary area of material science led to the development of intelligent materials such as sensors, actuators, optoelectronics, magnetoelectric and biomimetic materials. Another important phase in the development of materials science is hybrid materials. There are many interesting advanced developments in theory, design and synthesis are taking place in the central area of hybrid materials shown in Figure 1.1. Table 1.1 summarizes some uses of the advanced materials.

To generalize, materials science is defined as the one which is related to the combination of understanding the chemistry and physics with structure and physical properties and correlating this to engineering for device applications.

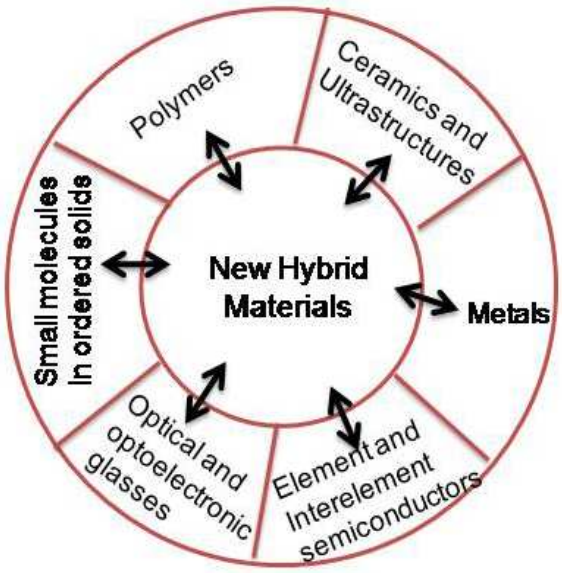

Figure 1.1: Schematic representation of new hybrid materials.

Table 1.1: Example uses of advanced materials in devices and machines [2].

Electrical	Photonics	Mechanical
Energy storage (batteries and supercapacitors)	Flat-panel displays	Very strong materials (aerospace, gas turbines)
Energy generation (fuel cells, photovoltaics)	Optical information processing	High temperature materials (jet, rocket and auto engines)
Superconducting magnets and train levitation	Information storage (CDs and DVDs)	Light weight materials (auto, aerospace)
Information processing (semiconductors)	Energy conservations (“smart windows”)	Abrasion resistance (bearings, machinery)
Sensors	Sensors	Vibration damping
		Fuel and oil applications seals (in rockets and hydraulic systems)
		Surface coatings

1.2 Metal Oxides

In this technologically rich world of materials, metal oxides play a very important role in many areas of science and technology [3]. Metal oxides are one of the most abundant ones in the earth's crust. Almost all the metals can form their oxides through oxidation by oxygen from air at the appropriate temperature and pressure. Although there exists different metal oxides such as alkali and alkaline earth metal oxides, rare-earth oxides, etc., transition metal oxides are of special interest because of the interesting electrical and magnetic properties that they exhibit. The transition metals of interest can be easily accommodated in the interstices of the close packed layers of O^{2-} ions. Depending on the electronic configuration of the metal ions and the structural geometries, oxides can be insulators, semiconductors or metallic. Oxides are chemically stable and therefore, attracts attention towards various applications. Potentially important properties exhibited by metal oxides are the high-T_c superconductivity such as in layered cuprates, colossal magnetoresistance (CMR) observed in perovskite manganites, ferroelectricity, ferro- and ferrimagnetism, multiferroicity where magnetism and ferroelectricity coexists together, etc. Also, metal oxides are both technologically and industrially important because of their interesting properties and overall characteristics such as hardness, thermal stability, thermal conductivity, and chemical resistance. For example, SiO_2 is well known for its optical properties, ferrimagnetic iron oxides such as the spinel ferrite, γ-Fe_2O_3 and as hexagonal ferrite $BaFe_{12}O_{19}$, are familiar for their application in data storage and hard magnets. Metal oxides with variable electron mobility are used as semiconductors (ZnO, V_2O_5) or superconductors ($YBa_2Cu_3O_7$). Ferroelectric or dielectric perovskite type oxides such as $BaTiO_3$, $PbZrTiO_3$, etc are extensively used in electronic devices. In addition to this, oxides find applications in many fields such as in refractories to withstand very high temperatures, in catalysis as an active material, promoter and support, in the field of gas sensors, Li-ion batteries, fluorescent lights, cellular phones, fuel cells, etc. It is worth noting here and highlight the application of oxides to reduce environmental pollution by their use as a catalyst or sorbent to remove CO, NO_x and SO_x during combustion of fossil derived fuels.

Spinels and perovskites are two important structural classes of oxides with interesting properties and wide applications.

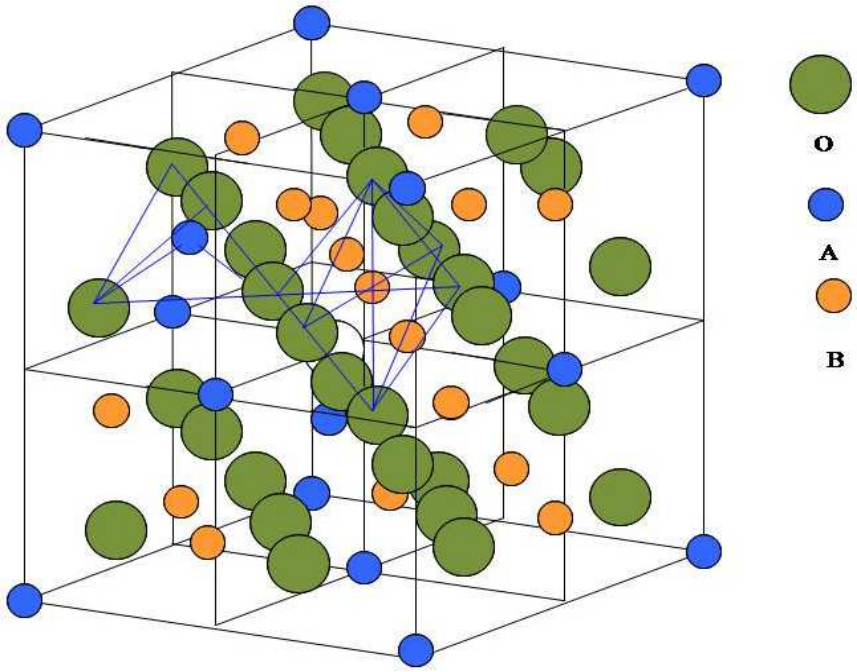

Figure 1.2: The Spinel structure.

1.3 Spinel type oxides

Spinel type oxide is a class of material which crystalizes in a face centered cubic structure with the general formula AB_2O_4 [4]. In the spinel structure, A and B can be divalent, trivalent, or quadrivalent cations including magnesium, zinc, manganese, aluminium, chromium, titanium, etc. The structure is also known for the chalcogenides also, instead of the oxide anion. If the spinel structure consist of Fe as one of the major component, the oxides are called as ferrites. Ferrites can also crystalize as hard ferrites in other structures like garnet and magnetoblumbite structures which are derived from the spinel structure.

Spinel type oxides are derived from the mineral spinel, $MgAl_2O_4$, and can be represented by the general formula AB_2O_4. The crystal structure was determined independently by Bragg [5] and Nishikawa [6]. The unit cell of a spinel consists of eight formula units and therefore, may be represented as $8[AB_2O_4]$ so it may be represented as $A_8B_{16}O_{32}$. Within the face-centered cubic lattice formed by 32 oxygen ions there exist two types of interstitial positions which can be occupied by the metallic cations. There are 64 tetrahedral interstitial sites surrounded by 4 oxygens (called as A site) and 32 octahedral sites surrounded by 6 oxygens (called as B site). In the spinel structure, 8 out of 64

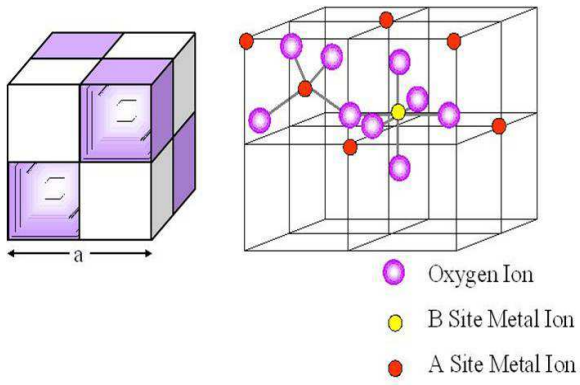

Figure 1.3: Tetrahedral and octahedral sites in the spinel structure.

Table 1.2: Different types of spinels.

S.No	Type	General formula
1	Normal	$(A^{2+})[B_2^{3+}]O_4$
2	Inverse	$(B^{3+})[A^{2+}B^{3+}]O_4$
3	Mixed	$(A_{1-x}^{2+}B_x^{3+})[A_x^{2+}B_{2-x}^{3+}]O_4$

() represents Tetrahedral site, [] represents Octahedral site.

tetrahedral sites and 16 out of 32 octahedral sites are occupied by the cations. For better understanding and visualization, the unit cell can be subdivided into eight octants, with edge $a/2$, where a is edge length of the unit cell. The space group for the spinel ferrite has been identified as Fd3m with the space group number *227* [7, 8]. Depending on the occupation and distribution of the cations in the tetrahedral and octahedral sites, spinels can be further classified as normal, inverse and mixed spinels which can be represented in general as $(A_xB_{1-x})[A_{1-x}B_{1+x}]O_4$ where ( ) representing the tetrahedral sites and [ ] representing the octahedral sites. If each sublattice is occupied by only one type of cation i.e. when $x = 0$, the spinel is said to be normal where as if $x = 1$, it is called as inverse spinel. When $0 < x < 1$ the spinel is defined as the mixed one. The structure of the spinel is represented in Figure 1.2. The tetrahedral and octahedral sites are shown in Figure 1.3. Table 1.2 depict the types of spinels with the general formula of representation. By changing the distribution of cations one can tune some of the interesting properties such as magnetic, electric, etc [9–11].

Table 1.3: Some applications of spinel oxides

Spinel Oxide	Applications
Co_3O_4, $ZnCo_2O_4$	Sensor, batteries, catalysts, etc.
$MgAl_2O_4$	Refractory
$CoAl_2O_4$	Pigments, catalyst, H_2 production
$Li_{1-x}Mn_2O_4$	Batteries
Fe_3O_4	MRI, Magnetic hyperthermia, Drug delivery
$Ni_{1-x}Zn_xFe_2O_4$	Pulsed current monitor, transformer cores antenna rods, microwave devices, telecommunication.

Ideal cubic close packed structure of oxygen anions can accommodate metal ions in tetrahedral site with ionic radius ≤ 0.35 Å and in octahedral sites with a radius ≤ 0.55 Å. Hence in order to accommodate cations with ionic radius larger than the above mentioned values, at the respective sites, the lattice has to be expanded. The factor that governs and characterize the expansion of tetrahedral and octahedral sites is the oxygen parameter represented by u. For the ideal spinel structure u has a value of 3/8 [12].

Spinel type oxides possess wide range of applications in the field of catalysis, sensors, batteries, pigments, fuel cells, solar cells, memory devices, transformers, etc. It is out of scope of this thesis to represent all the applications of spinel type oxides. Some of the applications of spinel type oxides are shown in Table 1.3

1.4 Perovskite type oxides

Another important and interesting family of oxide is the perovskites with the general formula ABO_3 [13]. The perovskite type family was discovered by the geologist Gustav Rose in 1839 and given the name perovskite in honor of the eminent Russian mineralogist, Count Lev Alexevich von Perovski. In the perovskite structure, A ions can be rare earth, alkaline earth, alkali and other larger ions such as Pb^{2+} and La^{3+}, where as smaller B ions can be 3d, 4d, and 5d transition metal ions. It is also a technologically important material known for their applications such as capacitor, piezoelectric transducer, electrostrictive actuator, superconductor, etc. The compounds with the general formula ABO_3 where the B ion is surrounded by the octahedron formed by the O ion, represents the perovskite type oxides. The structure of a perovskite is shown in Figure 1.4, where

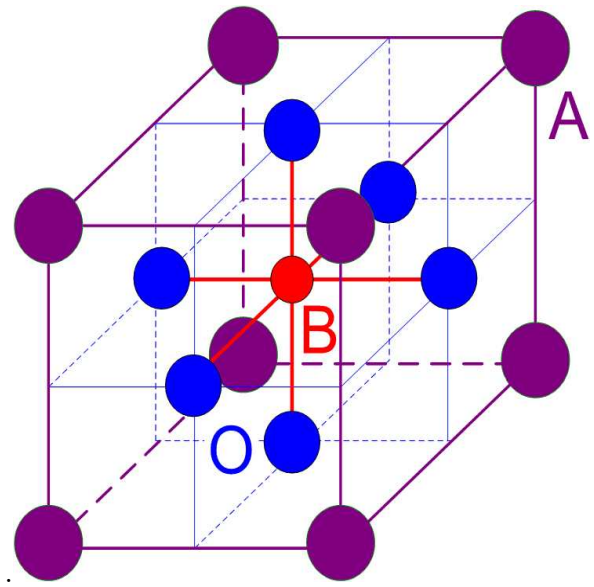

Figure 1.4: Structure of a Perovskite, ABO_3.

Table 1.4: Some perovskites and related oxides [14].

Insulating	Metallic	Magnetic	Superconducting
WO_3	ReO_3	$PbCrO_3$	Na_xWO_3
$NaTaO_3$	$NaWO_3$	$LaCrO_3$	K_xWO_3
$SrTiO_3$	$KMoO_3$	$CaMnO_3$	K_xWO_3
$BaTiO_3$	$SrNbO_3$	$LaMnO_3$	Rb_xWO_3
$KTaO_3$	$LaTiO_3$	$LaCoO_3$	Cs_xWO_3
$LiNbO_3$	$LaWO_3$	$LaFeO_3$	Li_xWO_3

O = oxygen and B = transition metal ion. Table 1.4 shows the overview of some of the perovskite type compounds with the properties such as insulating , metallic, magnetic and superconducting [14].

The ideal crystal structure of perovskites is cubic lattice, with the space group Pm3m. However, many perovskite oxides have slightly distorted variants with lower symmetry such as tetragonal, orthorhombic, and rhombohedral. In addition to this large extent of cation or oxygen deficiency has been observed in many compounds. In the general formula ABO_3, the A cation is coordinated with twelve oxygen ions and the B cation with six. In a ideal cubic structure the contact between A, B and O ions are perfect. The relationship between the radii of the A, B and O ions for ideal cubic structure is given in equation 1.1

Table 1.5: Applications of perovskite oxides. [16].

Multilayer capacitor	$BaTiO_3$
Piezoelectric Transducers	$Pb(Zr,Ti)O_3$
P. T. C. Thermistor	$BaTiO_3$, doped
Electrooptical Modulator	(Pb,La) (Zr,Ti) O_3
Switch	$LiNbO_3$
Dielectric Resonator	$BaZrO_3$
Thickfilm Resistor	$BaRuO_3$
Electrostrictive Actuator	$Pb(Mg,Nb)O_3$
Superconductor	$Ba(Pb,Bi)O_3$ layered cuprates
Magnetic Bubble Memory	$GdFeO_3$
Laser Host	$YAlO_3$
Ferromagnet	$(Ca,La)MnO_3$
Refractory Electrode	$LaCoO_3$
Second Harmonic Generator	$KNbO_3$

$$r_A + r_O = \sqrt{2}(r_B + r_O) \tag{1.1}$$

Goldschmidt explained the deviation from the ideal cubic structure of the perovskite oxides through the factor called tolerance factor t [15], defined as in equation 1.2

$$t = (r_A + r_O)/\sqrt{2}(r_B + r_O) \tag{1.2}$$

For the cubic structure t is close to 1 whereas the value is $0.8 < t < 0.9$ for the distorted perovskite structures. Further, the perovskite type oxides can be classified as ternary and complex perovskite type compounds. The ternary perovskite compounds can be of the from $A^{1+}B^{5+}O_3$, $A^{2+}B^{4+}O_3$, and $A^{3+}B^{3+}O_3$. In the case of complex perovskite type compounds, the general formula is $A(B'B'')O_3$. Partial substitution of A site ions is also possible such as $(A'A'')BO_3$. Hence, in general, the perovskites are termed as inorganic chameleon, because of the tunability in structure and composition for tuning the properties as well. Hence the perovskites are used for a variety of applications as mentioned in Table 1.5

1.5 Nanoscience and Nanotechnology

In the emerging field of science and technology, the term *Nano* as a 'prefix' has become mandatory. Nanometer size i.e. 10^{-9} m, can be achieved by the assembly of the constituents of atoms or molecules of few angstroms or 10^{-10} m in size. Studies on the science of this nanometer scale objects is termed as nanoscience where as technology related to the devices with the minimum feature size in this range is termed as nanotechnology, which is nothing but manipulating and designing matter atom by atom [17–21].

The history of *nano* dates back to many centuries. For example, colloidal gold, a suspension of fine particles of gold, was prepared by Faraday in 1856, which he called as divided gold. The suspension was stable for almost a century. In addition to this, usage of fine powders of gold was also well known for many centuries in the field of ayurveda to increase the memory and to retain the youth. Another best example is the fourth century AD Lycurgus cup made by Roman, which exhibit red color in the transmitted light and green color in the reflected light.

What is then new in the present day nanotechnology is nothing but observation and manipulation, which is key to development. This is made possible today with the invention of microscopes such as scanning tunneling microscope (STM) and scanning probe microscope (SPM). The scanning microscopes help in the manipulation and arrangement of atoms in a representative manner. This fact was predicted in 1959 itself by Richard Feyman who stated that "There is plenty of room at the bottom". The term nano was introduced by Taniguchi in 1974, which in Greek means 'dwarf' to describe such fascinating materials. There are different types of materials that can exist in the nano-form, as mentioned in Table 1.6. These nanosized materials are technologically important due to their unique properties [22–24].

1.6 Oxide Nanomaterials

Among the different classes of nanomaterials, ceramic oxides are important ones. The properties exhibited by the oxides in the nanoregime (1-100 nm) are different from that of their bulk counter parts due to the high density of corners or edge surface sites, defects and electronic structure, which are key factors in determining the properties. For

Table 1.6: Different types of nanomaterials [25].

	Size (approx.)	Materials
Nanocrystals and clusters (quantum dots)	diam 1-10 nm	Metals, semiconductors, magentic materials
Other nanoparticles	diam.1-100 nm	Ceramic oxides
Nanowires	diam. 1-100 nm	Metals, semiconductors sulfides, nitrides
Nanotubes	diam. 1-100 nm	Carbon, layered metal chalcogenides
Nanoporous solids	pore diam. 0.5 -10 nm	Zeolites, phospates etc.
2- dimensional arrays (of nanoparticles)	several nm-μm	Metals, semiconductors, magnetic materials
Surfaces and thin films	thickness 1-1000 nm	A variety of materials
3- dimensional structures (superlattices)	several nm in the three dimensions	Metals, semiconductors, magnetic materials

example room temperature magnetism can be observed in non magnetic metal oxides in nanoparticles [26, 27] The possible changes that can be expected in the oxides in the nanoregime of interest are (i) changes in the structural parameters due to the thermodynamics [28–33], (ii) due to the quantum confinement, changes in the electronic properties through energy shift in exciton levels and optical band gap [34–37], and (iii) high surface area to volume ratio, which makes most of the active atoms available at the surface. For example, nanocrystalline MgO with surface area of 500 m^2/g adsorbs six molecules of SO_2/nm^2 where as bulk MgO having surface area 30 m^2/g adsorbs only 0.7 molecules of SO_2/nm^2 [38]. The surface area enhances the activity, through reactivity of more molecules available at the surface. In addition to this, the possible reasons predicted for this is the high index crystal faces present in the nanooxides which ensures availability of lower coordination ions such as Mg^{2+}_{3c}, Mg^{2+}_{4c}, O^{2-}_{3c} and O^{2-}_{4c}. Also, smaller particle size makes diffusion process easy to reach the core of particles because the surface of nanostructured oxides are different from that of the bulk [39–41].

In most of the technologically related processes, heat transfer plays an important role such as in power generation, microelectronics, and airconditioning. In general, liquids such

as water, ethylene glycol and engine oil are commonly used as thermal conducting fluids. When compared to this, the solid oxides possess better thermal conductivity. But the usage of solid oxides in bulk form along with liquids for enhancing thermal conductivity has problems such as sedimentation which can take place due to the unstability of the mixture which may erode the channel walls [42, 43]. And most importantly this will enhance the operating cost since it requires more pumping power to equalize the pressure drop. One of the efficient way to improve the thermal conductivity of liquids is by using nanosized solid oxides by making the liquid as a nonofluid a new class of the fluid having a dispersion of very fine particles of size 1-100 nm [44, 45]. Some of the highly thermal conducting metal oxides such as Al_2O_3, CuO, SiO_2 and TiO_2 have been made as nanofluids and studied for their thermal conductivity [46–49].

In the case of ferrites related to transformer cores and microwave applications, processing is a crucial step. The final sintered material should be free of voids. In the case of bulk material, due to chemical inhomogeneity and difficulty in composition control, it is very difficult to get a compact void free material. On the other hand, if the particle size of the starting powders are in the nanometer range, due to high reactivity and homogeneity, sintered ferrites of specific size and shape can be achieved for better performance. Similarly, when bulk oxide is used as an anode or cathode material in a battery, there will be a structural change due to the stress and strain developed during the transportation of ions. Where as, the oxide nanomaterials not only shortens the path length for transport of ions but also minimize the stress and strain. Likewise, in almost all fields of applications, oxide nanomaterials can show better performance compared to the bulk counterparts.

Above all, it is important to form a well defined, hierarchically arranged, porous nanomaterials for most of the applications such as in catalysis [50–52], sensors [53, 54], Li-ion batteries [55, 56], fuel cells [57, 58], photovoltaics [59, 60], etc. In most of the cases employed for the synthesis of nanomaterials with well defined morphological features such as nanorods, nanotubes, nanowires, etc., templates are used which limit the growth of the nanomaterials in some dimensions, and the templates need to be removed after formation of the materials of interest. It is preferable to get control on the morphology and to form porous nanomaterials with well defined morphology without any templates [61, 62].

The present work comprised of synthesis of spinel based oxides like Co_3O_4, Fe_3O_4/γ-

Fe_2O_3, $CoFe_2O_4$ and $ZnFe_2O_4$. Co_3O_4 nanorods prepared have been studied for applications such as sensors, catalysis, Li-ion batteries and supercapacitors. The magnetic properties of Fe based spinels have been studied and discussed. In addition to this, detailed studies has been made on the magnetic properties of multiferroic $BiFeO_3$. Therefore, the following sections give brief introduction to the properties and applications studied in this work.

1.7 Some Properties and Applications of Metal Oxides

1.7.1 Magnetic properties

Magnetism is a universal phenomenon associated with all materials that are composed of charged particles. Commonly, the origin of magnetic moment in the atoms of a material is the motion of electrons. A material may respond to an applied magnetic field in two ways, it may get attracted or repelled. Accordingly, the magnetic materials are said to be either paramagnetic or diamagnetic, respectively. The classification is made according to a material's response to an externally applied magnetic field [63]. Paramagnetism is observed in materials that contain atoms with unpaired electrons whereas paired electronic systems behave as diamagnetic. Diamagnetism can be regarded as originating from the shielding currents induced by an applied magnetic field in the filled electron shells. These currents are equivalent to an induced moment present on each of the atoms. This could be better described by stating the Lenz's law for orbital motion of electrons. Lenz's law states that if the magnetic flux enclosed by a current loop is changed by the application of a magnetic field, a current is induced in such a direction that the corresponding magnetic field opposes the applied field. The magnitude of the diamagnetic response is very small in most of the materials except for superconductors which are perfect diamagnets.

A paramagnetic substance consists of atoms or molecules each of which has a net magnetic moment. In the absence of an applied field, these atomic moments point at random directions and cancel one another, so that the net magnetization of the specimen is zero. When a magnetic field is applied, there is a tendency for each atomic moment to turn towards the direction of the field. But the thermal agitation of the moments

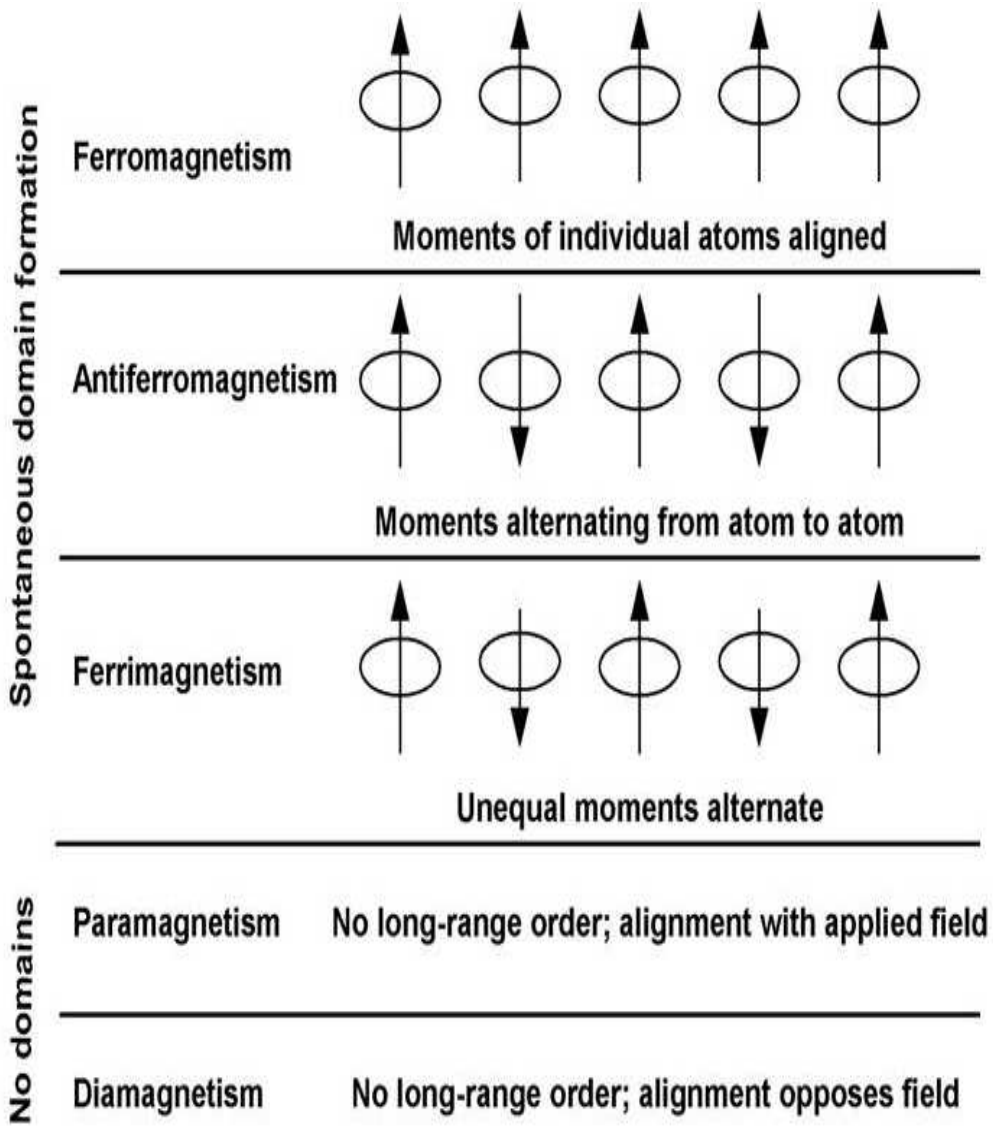

Figure 1.5: Different types of magnetism.

opposes this tendency and tends to keep the atomic moments at random orientations. The result is only a partial alignment of the moments in the field direction. The atoms with incomplete inner electronic shells (transition metal ions and rare earth ions) can have a large net moment and compounds of these elements are strongly paramagnetic.

Ordering of magnetic moments in most magnetic systems is controlled by the magnetic exchange interactions. However, magnetic ordering due to dipole-dipole interactions have also been found in some materials such as in organometallic magnets. Magnetic ordering in materials is observed only below a critical temperature; above this, the materials show paramagnetic behavior. Based on the type of ordering or exchange, magnetic materials are mainly classified in to ferromagnetic, antiferromagnetic, and ferrimagnetic. Various types of magnetism is best understood pictorially by considering the orientations of magnetic moments in a material as shown in Figure 1.5.

Materials that possess ferromagnetism have aligned atomic magnetic moments of equal magnitude. Also, this type of behavior is supported by the crystalline structure of the material that allows for direct coupling interactions between the moments. Thus, there will be strong enhancement in the flux density. Further, the aligned magnetic moments in a ferromagnetic material can give a spontaneous magnetization in the absence of an applied magnetic field. Hence, there will be a permanent magnetic moment in this material. Below a transition temperature called Curie temperature, T_C, the magnetic moments are ordered where as above T_C, ferromagnetic materials are like paramagnets.

Atomic magnetic moments of equal magnitude that are arranged in an antiparallel fashion displays antiferromagnetism. The exchange interaction that couples the magnetic moments are antiparallel to each other and leaves the net magnetization as zero. There will be a long range order below a critical temperature called the Néel temperature (T_N). Above this characteristic temperature thermal energy is sufficient to overcome the magnetic energy to randomize the magnetic moments. Above T_N the material will behave like a paramagnet.

In the case of ferrimagnetic materials, the sublattices possess unequal magnetic moments in an antiparallel manner like in the case of an antiferromagnetic material. But here it shows a net magnetic moment due to the uncompensated spins. It is similar to ferromagnetic material since it contains a permanent magnetic moment even though the net

moment is smaller than that of a ferromagnetic material. Ferrimagnetism is commonly observed in ferrites and garnets.

The temperature dependence of various types of magnetic materials can be explained on the basis of the molecular field theory proposed by Weiss in 1907 [64]. According to him, in paramagnetic substances, the elementary moments will interact with each other. This interaction can be expressed in terms of a fictitious internal field, called as the molecular field, H_m, that acts in addition to the applied field, H. The strength of this field depends on the extent of alignment already attained. Since the molecular field is proportional to the magnetization M,

$$H_m = \gamma M \tag{1.3}$$

where γ is called the molecular field constant and it is proportional to Weiss constant Θ. The paramagnetic susceptibility above the ordering temperature is given by

$$\chi = \frac{C}{T - \Theta} \tag{1.4}$$

where C is the Curie constant. The inverse paramagnetic susceptibility varies linearly with temperature and intercepts the temperature axis at the origin (Curie behavior) or at $T = \Theta$ (Curie-Weiss behavior). The positive and negative values of Θ indicate that the molecular field is either aiding or opposing the applied field, respectively. For a ferromagnet, the value of Θ is approximately equal to T_c, which is large and positive. On the other hand, for the antiferromagnetic and ferrimagnetic materials, Θ is negative.

The Heisenberg exchange interaction,

$$H = -2J_{ij} \sum S_i.S_j \tag{1.5}$$

is used to describe the tendency of the adjacent, localized spin moments (S_i and S_j) to align parallel (J_{ij} is positive, ferromagnetic) or antiparallel (J_{ij} is negative, antiferromagnetic) to each other in a material consisting of magnetic atoms/ions. The strength of the exchange interaction depends on the overlap of the wave functions. The Heisenberg type of exchange (direct exchange) applies only to some localized systems, and for oxides, one needs to consider indirect forms of magnetic exchange. In oxides, the magnetic interaction between two ions should be in such a way that their spin moments have either parallel or

antiparallel alignment. In oxides, the distance between two magnetic ions are, sometimes, two lattice constants apart and no direct exchange or orbital overlap becomes possible. In such cases, there may be an indirect exchange mechanism operating between the two magnetic ions. A possible mechanism in oxides is the superexchange which explains the magnetic interaction between two neighboring transition metal ions separated by an oxide ion, based on the symmetry of p and d states and their occupancy [65].

Superparamagnetism is a phenomenon observed in very fine magnetic particles, where the energy required to change the direction of the magnetic moment of a particle is comparable to the ambient thermal energy. Nanosized magnetic materials exhibit a behavior similar to paramagnetism at temperatures below the Curie or the Néel temperature. It is half-way between ferro and paramagnetism. In this case, below the Curie or Néel temperature, the thermal energy is not sufficient to overcome the coupling forces between neighboring atoms, where as the energy is sufficient to change the direction of the magnetization of the entire crystallite. The resulting fluctuations in the direction of magnetization cause the magnetic moments average to zero [66]. Thus, the material behaves in a manner similar to paramagnetism, except that instead of each individual atom being independently influenced by an external magnetic field, the magnetic moment of the entire particle tends to align with the magnetic field. Thus, these particles are called superparamagnetic particles. Superparamagnetism occurs when the material is composed of very small crystallites (1-10 nm).

Magnetocrystalline anisotropy (K) is an intrinsic property of a magnetic material, which is caused by the spin-orbit interaction of the electrons. K is expressed as

$$K = 25kT/V_{sp} \tag{1.6}$$

where k is the Boltzmann constant and V_{sp} is the volume of a superparamagnetic particle. Above a particular temperature, kT dominates and this temperature is called blocking temperature (T_B). Below a particular size (called critical particle diameter, D_c), the particles become single domains, and in this particle size range the coercivity reaches a maximum. Below a critical diameter the coercivity become zero, because of thermal effect, which are strong enough to spontaneously demagnetize the previously saturated assembly of particles.

Another important property of magnetic materials is magnetostriction [67]. Magne-

tostriction is the change in dimensions of a magnetic material when it is subjected to a magnetic field. The phenomenon is reversible in the sense that an applied stress can led to a change in the magnetic state of the magnetostrictive material. This reversible effect gives magnetostrictive materials a special place among the existing smart materials. It is important to develop different alternatives to the existing materials with reduced cost, easy manufacturing and enhanced properties. Oxide based magnetic materials are being developed as suitable alternatives to the existing alloy based materials.

1.7.2 Magnetism in Ferrites

Ferrites are nothing but the metal oxides having Fe as one of their major components [68,69]. Ferrites can crystallize in spinel, garnet and magnetoplumbite structures. Ferrites are not new since its history dates centuries back with the mineral Fe_3O_4 having the spinel structure with general formula AB_2O_4. Prof. Takeshi Takei of early 1930's, through his remarkable work, is regarded as the father of modern ferrites.

Spinel ferrites possess interesting electrical and magnetic properties and these properties are mainly governed by the cation distribution i.e. the distribution of Fe^{3+} and the divalent metal ion in the tetrahedral and octahedral sites in the spinel structure. In general term it can be best understood with the representation $M^{2+}_{1-x}Fe^{3+}_{x}[M^{2+}_{x}Fe^{3+}_{2-x}]O_4$ where the ions inside and outside the square brackets represent the location of the ions in the octahedral and the tetrahedral sites. Depending on the value of x i.e. when $x = 0$, the spinel is said to be a normal spinel, e.g. $ZnFe_2O_4$ and $CuFe_2O_4$. When $x = 1$, the spinel is called an inverse spinel, e.g. Fe_3O_4, $CoFe_2O_4$, etc. Another class of the spinel is called mixed spinel when $0 \leq x \geq 1$, e.g. $Ni_{1-x}Zn_xFe_2O_4$, $Mn_{1-x}Zn_xFe_2O_4$, etc. The distribution of cations over the sites strongly depends on the synthesis method and processing temperature.

There are three kinds of magnetic exchange interactions possible between the metal ions which occupy the tetrahedral (A) site and the octahedral (B) site. The superexchange interactions taking place through the intermediate O^{2-} ions are A-O-A, B-O-B and A-O-B interactions. The negative interactions between metal ions at different sites depend on the factors such as (i) distance between these ions and oxygen ions, (ii) angle between the three ions, say for example when the angle is 180°, interaction will be

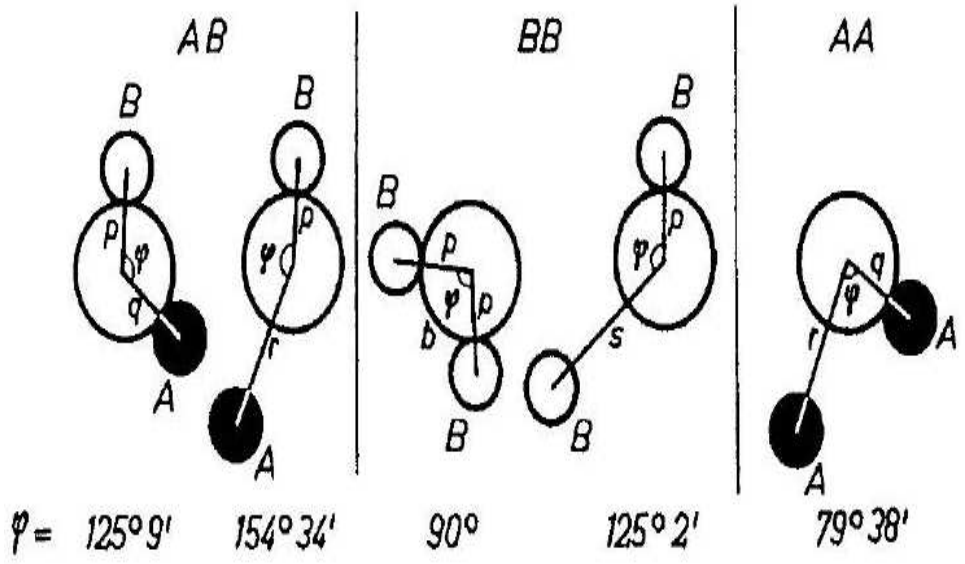

Figure 1.6: Different types of magnetic exchange interactions in a ferrite.

higher. The interatomic distances and the angles between ions for the different types of interactions are shown in Figure 1.6 [69]. Among this A-O-B interaction is the major one followed by next acceptable interaction B-O-B, where as A-O-A interaction is very weak. The molecular field theory gives a better understanding since the magnetic moment corresponding to magnetism is completely localized on a particular ion. Though the exchange mechanism is similar to that of antiferromagnetic case, in the case of ferrimagnetic exchange complication arises because **A** and **B** sites are crystallographically different.

1.7.3 Magnetism in Perovskites

The existence of magnetism in perovskites is mainly due to the presence of localized d electrons which possess localized spins [70]. The important things to be taken into consideration are the local electronic configuration and multiplet structure. Due to the inter-atomic exchange and correlation, there will be formation of a multiplet configuration, with a net spin. Hund's rule is qualitatively applicable to the perovskites with localized d electrons. The d electron configuration is specified by $t_{2g}^n e_g^m$ where n and m are the occupations of the t_{2g} and e_g levels. The different valance states and different electronic configurations of the cations are closer in energy to each other than for the free ion. This is a result of the polarization and electron screening of the Coulomb interactions. In a

perovskite, ligand-field splitting should be taken into account while applying Hund's rule. However Hund's rule is violated if the ligand-field splitting is greater than the intra-atomic exchange energy.

The presence of localized spins favors long range magnetic ordering through superexchange. Superexchange involves the antiferromagnetic coupling between nearest-neighbour cations by exchange of electrons with the intervening oxygen ion. Few examples of magnetically ordered perovskites are $LaMnO_3$, $LaCrO_3$, $PbCrO_3$, $CaMnO_3$, $LaFeO_3$, etc. Jahn-Teller effect plays an important role in the case of perovskites with the localized d electrons. Due to the Jahn-Teller distortion of MnO_6 octahedra in $LaMnO_3$, e_g orbitals loose their degeneracy. The Mn^{+3}-O-Mn^{+3} exchange interactions become anisotropic and results in A-type antiferromagnetic spin ordering, but with a positive Θ. In the A-type AFM ordering, the ferromagnetically ordered adjacent Mn-planes are coupled antiferromagnetically resulting in no net magnetic moment. However, in the substituted perovskite manganites such as (LaCa)MnO_3, Mn^{4+} ions are present apart from Mn^{3+} and this gives rise to ferromagnetic ordering and that leads to interesting properties [71]. The ferromagnetic ordering could not be explained by the simple superexchange scenario. Hence, the concept of double exchange was suggested for explaining this behavior in certain hole-doped manganites [72]. The double exchange between the Mn^{3+} and Mn^{4+} ions is maximum when Mn-O-Mn bond angle is 180°. Thus, any deviation of the bond angle towards 180° results in stronger magnetic exchange and hence an increase of T_c.

1.7.4 Dielectric properties

A dielectric material is usually an insulating material and exhibits an electric dipole structure. In a dipole structure, there is a separation of positive and negative electrically charged entities on a molecular or atomic level. Dielectricity, piezoelectricity and ferroelectricity are important electrical properties [73]. Materials having high dielectric properties or dielectric constant are used as capacitors in electronic applications. The basic property is the dielectric polarization, which can be defined as the finite displacement of bound charges of a dielectric in response to an applied electric field, and the orientation of their molecular dipoles if the latter exists. The dielectric properties vary widely with the nature of the material and are a function of the applied field, humidity, crystal

structure, etc. In a dielectric material electric dipole will get orient with the applied field. The process of dipole alignment is called polarization.

There are three types of polarization i) electronic, ii) ionic, and iii) orientation. Depending on the material and also on the manner of the external applied electric field, dielectric materials exhibit at least one of these polarizations. Electronic Polarization results from a displacement of the center of the negatively charged electron cloud relative to the positive nucleus of an atom by the electric field. This polarization will be in all materials provided if there is the presence of an electric field. Ionic polarization occurs only in materials that are ionic. Here the net dipole moment is due to the result of displacement of cations and anions in opposite directions when a field is applied. Orientation polarization is found only in materials having permanent dipole moments. Polarization results from a rotation of the permanent moments into the direction of the applied field.

The total polarization 'p' of a substance is equal to the sum of the electronic, ionic and orientation polarizations. It is also possible for either absence or negligibility of one or more contributions of these polarizations. For example there will not be any ionic polarization in the case of covalently bonded materials.

Ferroelectric materials exhibit spontaneous polarization, that is, polarization in the absence of an electric field. We can consider this as a dielectric analogue of a ferromagnetic material which shows a permanent magnetic behavior. The criteria for ferroelectricity is that the material should not possess centrosymmetry. In a ferroelectric material, the dipole moment results from the relative displacements of the ions. For example, displacement of O^{2-} and Ti^{4+} ions in $BaTiO_3$, from their symmetrical positions. However, ferroelectricity will be lost if we heat the material above a certain temperature called ferroelectric Curie temperature. Spontaneous polarization in this material is a result of interactions between adjacent permanent electric dipole moments aligned in the same direction.

Piezoelectricity or pressure electricity is nothing but a phenomenon where polarization is induced which results in an electric field by the application of an external force. The direction of the field can be reversed by reversing the sign of the external force. These properties arise in materials with complicated structure and low degree of crystal symmetry.

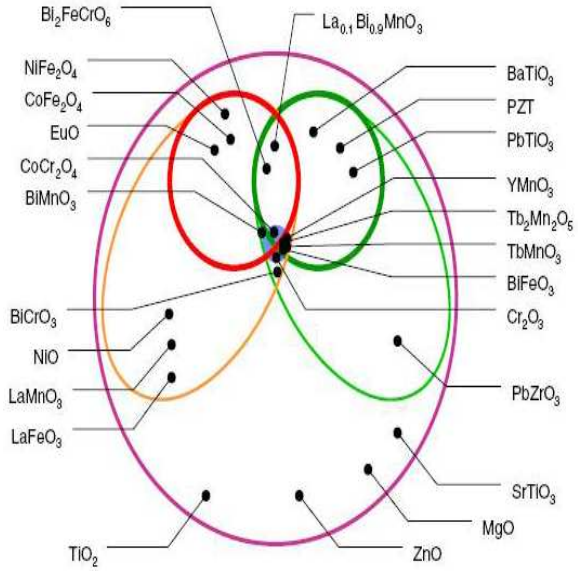

Figure 1.7: Illustration of a magnetoelectric coupling. Green and orange ellipse - electrically and magnetically polarizable materials. Circle inside green and orange ellipse - Ferroelectric and ferro- or ferrimagnetic polarization. The small circles in the middle denote systems exhibiting magnetoelectric coupling [74].

1.7.5 Multiferroism

The term multiferroism has been coined to describe materials in which two or all three of ferroelectricity, ferromagnetism and ferroelasticity occur in the same phase [75]. This means that the materials have a spontaneous magnetization which can be reoriented by an applied magnetic field, a spontaneous polarization which can be reoriented by an applied electric field and a spontaneous deformation which can be reoriented by an applied stress. The simultaneous existence of these three or even two in the same phase are rare in nature.

Even though magnetism and ferroelectricity tend to exclude one another, there are some systems in which these properties co-exist and such systems are known as magnetoelectric [76–78]. A magnetoelectric materials has a spontaneous magnetization that can be switched by an applied magnetic field, a spontaneous polarization that can be switched by an applied electric field and often coupling between the two. This has open a new gate way in technology where we have additional degree of freedom for manipulating the function [79, 80]. Especially in memory elements ferroelectric polarization and magnetization are used to encode binary information of FeRAMs (ferroelectric random access memories) and MRAMs (magnetic random access memories). Hence this combination of FeRAMs

and MRAMs offers a non-volatile magnetic storage system because it uses a low-power electrical write operation and non-destructive magnetic read operation. Illustration of a magnetoelectric coupling in oxides is shown in Figure 1.7.

The first magnetoelectric (ferromagnetic + ferroelectric) material reported was nickel iodine boracite ($Ni_3B_7O_{13}I$) [81]. Later on, many multiferroic boracite compounds have been synthesized [82,83] . But all of them have complex structures with many atoms and more than one formula unit per unit cell. The major break through happened with the replacement of some of the d^0 B cations in ferroelectric perovskite oxides by magnetic d^n cations [84]. For example in the compound $(1-x)Pb(Fe_{2/3}W_{1/3})O_3 - xPb(Mg_{1/2}W_{1/2})O_3$, Mg and W are diamagnetic and cause the ferroelectricity and d^5 Fe^{3+} ion is responsible for magnetic ordering [85]. The B site disordered perovskite $Pb_2(FeTa)O_6$ behaves both as ferroelectric and antiferromagnetic with weak ferromagnetism below around 10 K [86]. Like wise, some other perovskite materials which show multiferroic properties (ferroelectric and mostly ferromagnetic) are manganites of small rare earth elements (e.g. $TbMnO_3$, $HoMnO_3$) and yttrium ($YMnO_3$) [87–89].

In addition to this, several compounds have been reported with rare earth ferrites and substitution of rare earth elements in the A site of the perovskite structure with the general formula $A_{1-x}RE_xFeO_3$, where RE = Y, Eu, Yb, Gd, Dy etc [90–96]. By this way of substituting a rare earth ion of size slightly smaller than the A site ion, distortion may be induced which may result in enhanced multiferroic properties. Also, multiferroism can be introduced by coupling the ferroelectric and ferro- or ferrimagnetic magnetic materials by making their composites [97–99]. For example, $BaTiO_3$-$CoFe_2O_4$ is a composite multiferroic material where $BaTiO_3$ and $CoFe_2O_4$ are well known for their ferroelectric and ferrimagnetic properties, respectively.

1.7.6 Chemical Sensors

Metal oxides have been widely used as gas sensors to detect one or more species in a gas mixture [100–102]. When the metal oxide is exposed to the external stimuli, there will be an interaction in the chemical species at the surface. The interaction can be adsorption, chemical reaction or charge transfer. This may result in a change in the properties of metal oxide by changing its mass, temperature or electrical resistance. Further, this acquired

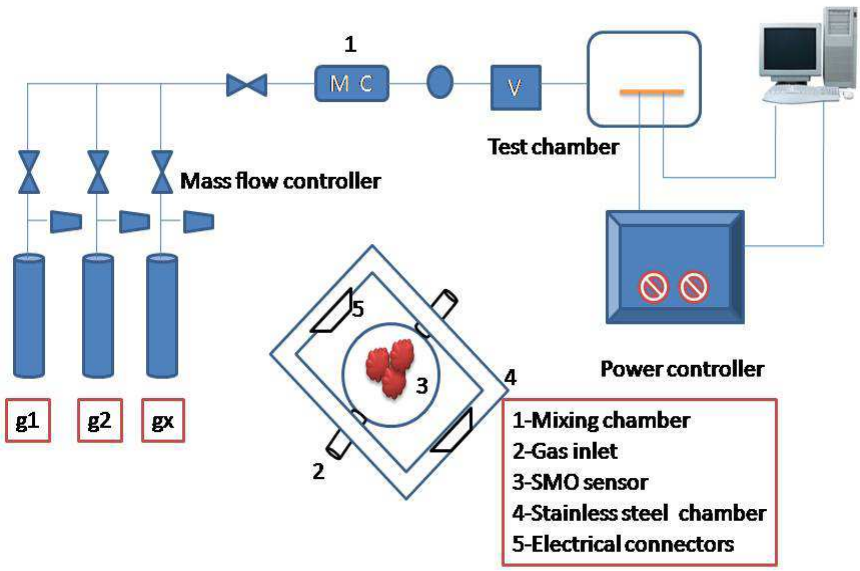

Figure 1.8: Schematic representation of a gas senor.

Table 1.7: Types of metal oxides based gas sensors.

Type	Response
Electrochemical	Potential or resistance change through charge transfer
Chemomechanical	mass change due to adsorbtion
Thermal	temperature change through chemical interaction

change is detected as signals like frequency, current, voltage or conductance. Therefore, basically a sensor contains a receptor which is nothing but a sensitive layer where the physicochemical change will occur. A gas sensor works based on the recognition of a target gas through a gas-solid interface which induces an electronic change on the oxide surface. A transducer transforms the mechanical or electrical response that taking place through the interaction and finally a detector is used to detect the signals as an output. In general, there are three types of common metal oxide based sensors as mentioned in the Table 1.7. Among this, electrochemical sensors are widely used and further it can be classified depending upon their mode of operation as potentiometric (measurement of voltage), amperometric (measurement of current), and conductometric (measurement of conductivity) [103–105]. The semiconductor oxides fall into the category of conductivity, and their gas sensitivity effect was reported in 1953 by Brattain and Bardeen in Ge [106]. The use of semiconducting metal oxides was later reported by Heiland, Bielanski *et al* [107] and Seiyama *et al* [108]. As an industrial product, it was brought out by Taguchi [109]. Depending on their change in the conductance while getting exposed to the reducing gases such as CO, EtOH and H_2O vapors, they can be classified as 'n' type if there is an increase in the conductivity and 'p' type if the conductivity decreases. The schematic representation of a semiconductor based sensor is shown in Figure 1.8.

Gas sensors play a vital role in the applications related to environmental monitoring [101]. For example, detection of nitrogen oxide (NO_x) which has greater impact on the green house effect, detection of sulfur dioxide and H_2S due to their toxicity which may cause death to human beings if the limit exceeds above 250 ppm, are some of the applications. In the area of fuel cells, hydrogen sensors have been developed to detect the leakage of H_2 gas which may form explosive mixture upon leaking in the air [110]. Similarly, there are gas sensors to detect other gases such as NH_3 and amines, ozone, volatile organic compounds, methane, etc. Table 1.8 shows some of the metal oxides used as sensors in the above mentioned field.

Recently, there are some developments using morphology, size and shape controlled nanomaterials which opens up another degree of freedom to explore the gas sensing properties of some transition metal oxides like Co_3O_4 [132], $ZnCo_2O_4$ [133], $ZnFe_2O_4$ [134], etc.

Table 1.8: Some examples of metal oxides for the environmental monitoring.

Metal oxides	Source to be detected	Ref
WO_3	Nitrogen oxide gases	[111]
WO_3-Ti		[112]
In_2O_3		[113]
SnO_2		[114]
SnO_2	sulfur di-oxide	[115]
SnO_2 doped Pd		[116]
Vanadium oxide modifed with TiO_2		[117]
WO_3	H_2S	[118]
SnO_2		[119]
ZnO		[120]
Copper oxide		[121]
WO_3	NH_3 and ammine	[122]
SnO_2		[123]
ZnO		[124]
iorn oxide		[125]
SnO_2	H_2	[126]
WO_3	ozone	[127]
SnO_2		[128]
SnO_2	volatile organic compounds	[129]
WO_3		[130]
cobalt based oxide		[131]

Table 1.9: Application of transition metal oxide as catalysts [135].

Process	Example
Oxidation	Production of SO_3 from SO_2 CO oxidation in emission control
Dehydrogenation (nonoxidative)	Production of styrene from ethylbenzene
Dehydrogenation (oxidative)	Production of formaldehyde from methanol and butadiene from butenes
Selective oxidation	Production of acrolein from propene, and maleic anhydride from benzene or butane
Selective ammoxidation	Production of acrylonitrile from propene
Selective reduction	Reduction of NO, selective hydrogenation of unsaturated ketones
Metathesis	Production of long chain alkenes
Water-gas shift	Production of hydrogen

1.7.7 Catalysis

The term 'catalyst' was coined by Berzelius in 1835 [136]. It is a substance that increases the rate of a chemical reaction with out being consumed. Broadly, catalysts can be classified into homogeneous and heterogeneous. In homogeneous catalysis, the catalyst being used will be single phase, either gas or liquid. Whereas, in heterogenous catalysis, it will exist as a multiphase mixture such as gas-solid mixture. It has an inherent advantage over homogeneous catalysis in terms of stability, low cost, low toxicity, recovery and reusability.

Most of the solid catalysts used in heterogenous catalysis are porous materials with very high internal surface area. In a typical porous catalyst, following steps will be occurring during the reaction

- transport of reactants from the bulk of the fluid to the exterior surface of the catalyst (external mass transfer resistance).
- transport of reactants from the surface to the interior of the catalyst through pores (internal mass transfer resistance).
- adsorption of reactants onto the active sites on the internal surface of the catalyst.

- reaction of adsorbed reactants to form adsorbed products.
- desorption of products.
- transport of products out of the pores to the particle external surface.
- transport of products from the external surface of the catalyst to the main body of the fluid.

Metal oxides have been studied extensively in the field of heterogeneous catalysis [137]. They find their usage at least in any one of the forms like an activator, promotor, or support. Their utility as sorbents to remove CO, NO_x and SO_x are environmentally important to control the pollution. Mainly, in chemical industries, they have been used to convert hydrocarbons to other chemicals. An overview of transition metal oxides used in catalysis is given in Table 1.9. The presence of different oxidation states in transition metal oxides helps to tune and control the selectivity and conversion during a catalytic process.

Developments in nanotechnology and the new synthesis protocols available for controlled synthesis have proven to be more efficient to synthesize tailor made catalysts [138, 139]. In nanostructured materials, both the surface and the defect nature are quite different when compared to the bulk counterparts which plays an important role for enhancement in the catalytic properties [140]. More over, nanomaterials possess most of the active atoms at the surface. There are several literature reports on the influence of size and shape on catalytic reaction of the nanostructured materials over their bulk counter parts [139, 141, 142].

1.7.8 Li-ion batteries

The increase in the worlds population has a great impact over the decrease in fossil fuel reserves. Though fossil fuel is the major energy source that meets the world's current energy requirements, its usage has to be controlled or else eliminated to preserve the nature and to control global warming. One such possibility is the use of renewable energy sources such as solar, wind, geothermal, wave and hydraulic. In this respect hydrogen and oxygen based fuel cells offer an attractive solution for the future energy needs. But it is still

Table 1.10: History of developments in batteries [146]

.

1600	Gilbert (England)	Establishment electrochemistry study
1791	Galvani (Italy)	Discovery of animal electricity
1800	Volta (Italy)	Invention of the voltaic cell
1802	Cruickshank (England)	First electric battery capable of mass production
1820	Ampre (France)	Electricity through magnetism
1833	Faraday (England)	Announcement of Faradays Law
1836	Daniell (England)	Invention of the Daniell cell
1859	Plant (France)	Invention of the lead acid battery
1868	Leclanch (France)	Invention of the Leclanch cell
1888	Gassner (USA)	Completion of the dry cell
1899	Jungner (Sweden)	Invention of the nickel-cadmium battery
1901	Edison (USA)	Invention of the nickel-iron battery
1932	Shlecht & Ackermann (Germany)	Invention of the sintered pole plate
1947	Neumann (France)	Successfully sealing the nickel-cadmium battery
Mid 1960	Union Carbide (USA)	Development of primary alkaline battery
Mid 1970		Development of valve regulated lead acid battery
1990		Commercialization nickel-metal hydride battery
1992	Kordesch (Canada)	Commercialization reusable alkaline battery
1999		Commercialization lithium-ion polymer
2001		Anticipated volume production of proton exchange membrane fuel cell

in the development stage and highly expensive. Under such circumstances, rechargeable Li ion batteries and supercapacitors appear to be the best alternative technologies for energy storage. In practice, there are lot of development in batteries which has already found market value for various applications [143–146].

The battery technology has been developing ever so from its first discovery 200 years ago by Alessandro Volta. Table 1.10 shows development in the history of batteries. Battery is nothing but a device which can store chemical energy and it can be converted into electrical energy. Batteries can be mainly classified into two types namely primary and secondary, where primary batteries are discarded once after complete discharge and on the other hand secondary batteries can be reused by charging it back. The schematic representation of a battery is shown in Figure 1.9.

Among the different kinds of batteries, rechargeable Li-ion batteries is an attractive choice due to its light weight, high power and energy density which powers most of the current portable electronic devices with considerably high potential ($\geq$3V) [145]. Figure 1.10 shows a comparison of energy density of Li-ion battery with other systems.

Due to the high reactivity towards moisture, a lithium cell has be handled in moisture free environment with nonaqueous solvent as electrolyte. Another important issue related to the usage of lithium is the chemical reactivity with non-aqueous electrolyte. There will be a passivating film formation at the metallic lithium anode which leads to the nonuniform plating of lithium during charging. This results in not only short-circuiting but also in local over-heating.

Intensive research work towards lithium insertion compounds as anodes instead of metallic lithium is currently in progress [145, 147, 148]. Initially, the rechargeable Li ion batteries were made using metallic lithium as anode and transition metal sulfide TiS_2 with layered structure as cathode [149]. The insertion of lithium ions inside the Van der Walls gap between the layers during discharge will take place with the reduction of transition metal ions while charging leads to extraction of lithium ion and oxidation of transition metals without damaging the layered structure. But sulfides and other cholcogenides developed later suffer from poor cell voltage ($\leq$2.5V) [150]. This induced immense research on transition metal oxides as an alternative choice, first developed by Goodenough's group during 1980's [151,152]. A maximum cell voltage value up to 5V can

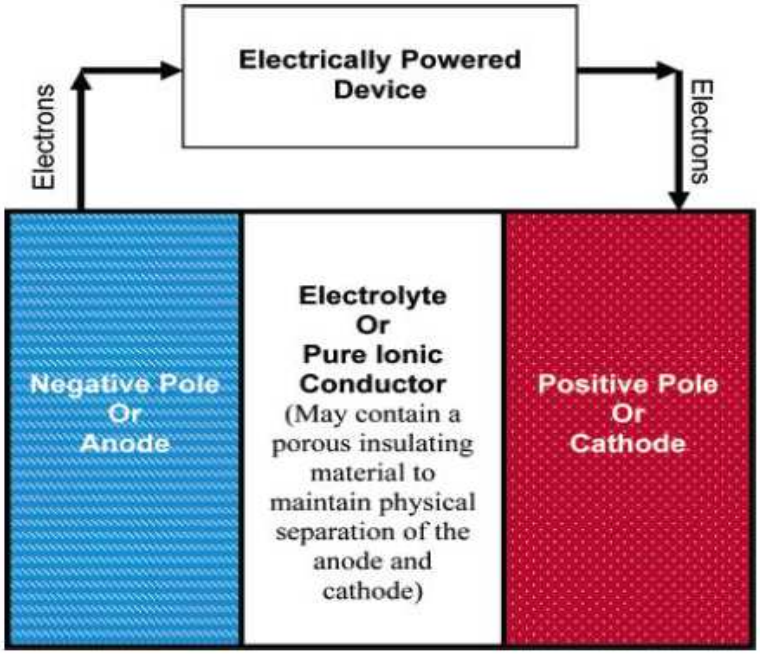

Figure 1.9: Illustration of a battery.

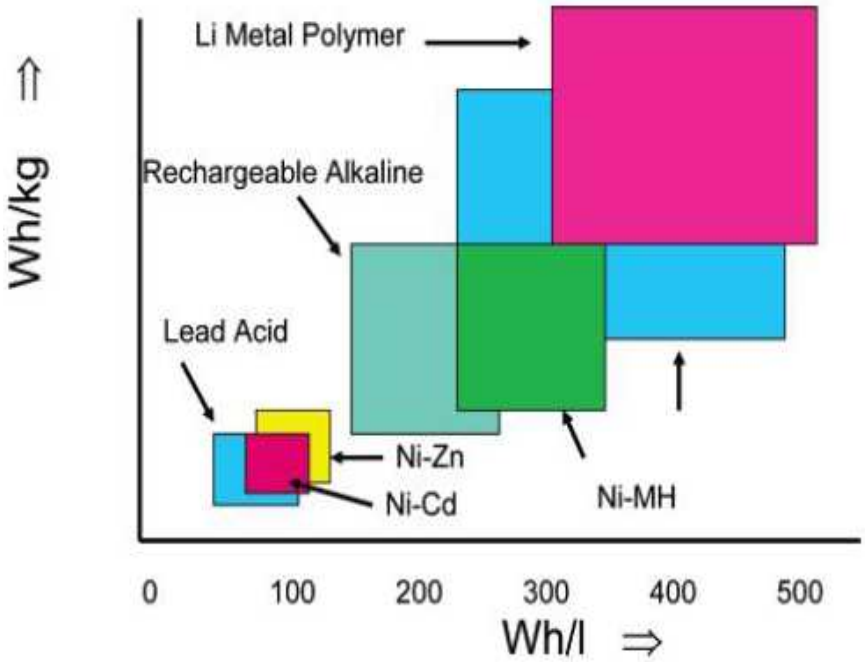

Figure 1.10: Comparison of energy density of Li-ion battery.

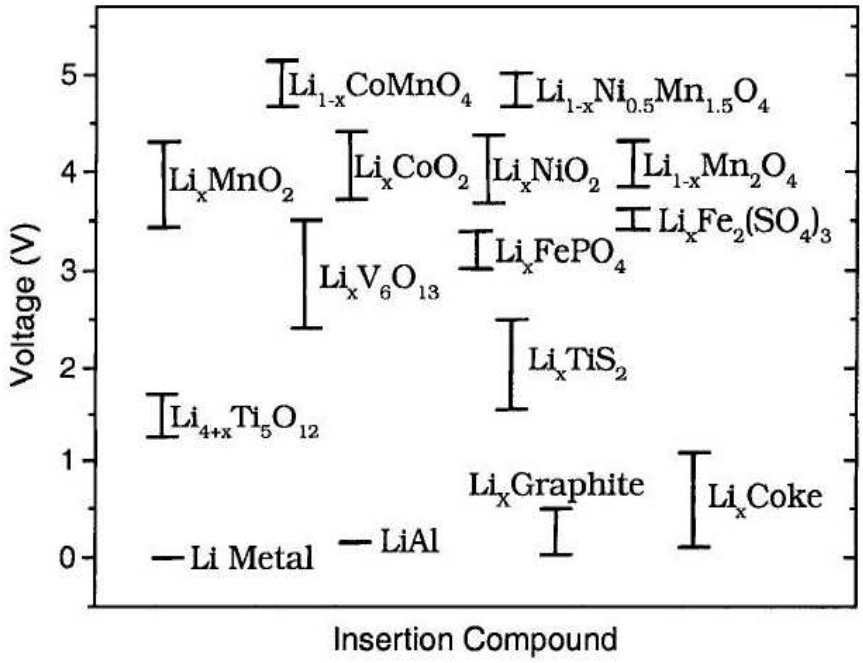

Figure 1.11: Electrochemical potential ranges of some Li insertion compounds with reference to Li [145].

be achieved as shown in Figure 1.11 with different transition metal oxides. The usage of lithium insertion compounds as both cathodes and anodes brings the term 'Li-ion' cells where Li ion shuttles between the cathode and the anode. Figure 1.12 represents the shuttling of Li-ion between the cathode and anode during charge/discharge process. For a suitable Li insertion compound, the following conditions need to be satisfied,

- To maximize the cell capacity, insertion compound should allow large amount of insertion/extraction of Li
- To achieve better cycle life, there should not be any drastic change in the insertion compound during insertion/extraction process
- For high current and power density, it should possess high electronic as well Li ion conductivity
- It should be chemically stable, inexpensive and light weight for commercialization.

In principle, the anode should have faster Li ion insertion/desertion kinetics and less redox potential against Li than cathode to get maximum cell voltage. First commercial-

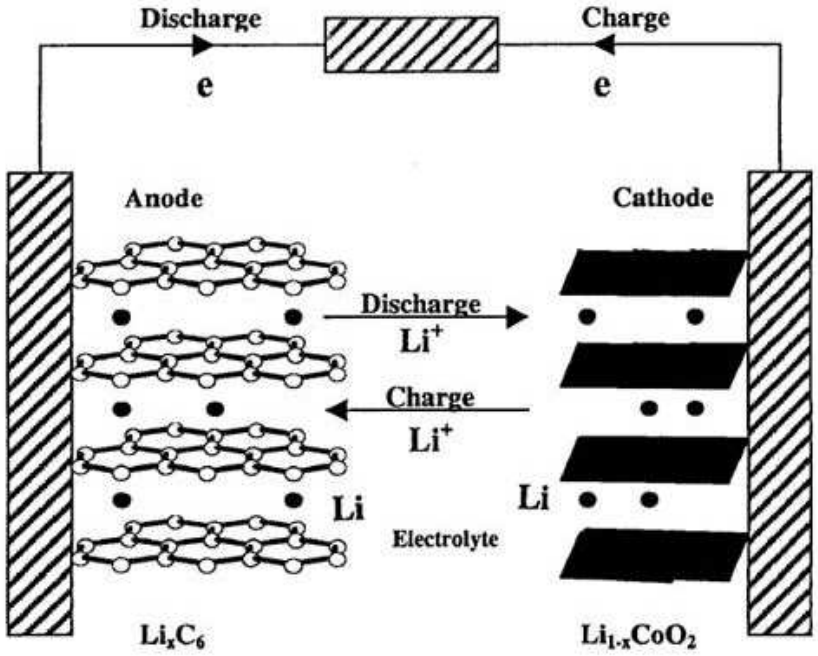

Figure 1.12: Schematic illustration of shuttling of Li during charge/discharge process.

izations of Li ion batteries were made with the combination of low density carbonaceous material combination with the cathode $LiCoO_2$. Carbonaceous material is used because of its abundance, low cost and excellent reversibility for Li insertion. However, the problems associated with carbonaceous anode can be addressed as the inter-layer expansion and degradation of structure due to solvent co-intercalation, as well as limitations in gravimetric and volumetric capacity. Due to the above mentioned reasons, there is an urge for the development of alternate anode materials [153–155] so that it can match with the developed cathode materials like $LiCoO_2$, $LiMnO_2$, $LiMn_2O_4$, etc, having high electrode potential of 4V against Li.

1.7.9 Supercapacitors

Supercapacitors, which are nothing but electrochemical capacitors (ECC), have attracted much attention because of higher charge storage capacity compared to the conventional capacitors [156, 157]. Conventional or electrostatic capacitors consist of two plates separated by an insulator. The process of energy storage is non-faradic. The energy storage is carried out by the separation of positive and negative electrostatic charges. In electro-

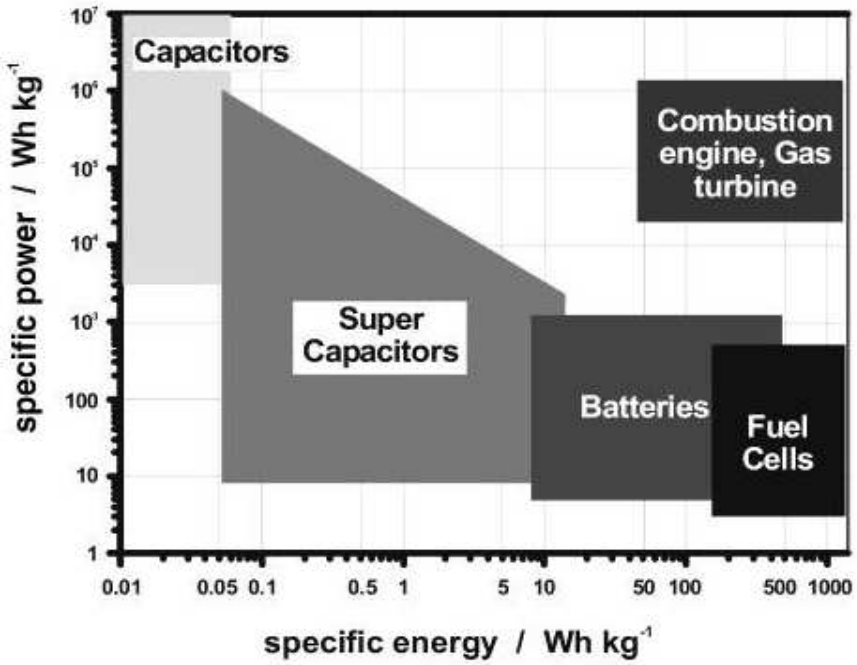

Figure 1.13: Ragone plot: Comparison of power and energy capabilities [157].

chemical capacitors, orientation of electrolyte ions at the electrode/electrolyte interface, referred to as electrical double layer (EDL), are formed and released. EDLs enable the storage of electrostatic charge in the form of ions. In general, porous carbon is used as electrode to adsorb the ions. The resultant parallel movement of electrons is responsible for energy delivering process. It differs from battery in terms of its superiority in specific power. Figure 1.13 shows the Ragone plot which shows the comparison of power and energy capabilities. In the future, the supercapacitor may replace many of the battery applications. Apart from memory applications in electronic devices, it finds a vital role in hybrid vehicles as it has high power density.

Other than carbon, the materials used for supercapacitors are conducting polymers and transition metal oxides. In the case of transition metal oxides, the behavior of energy storage is pseudocapacitive which consists of fast and reversible faradaic redox reactions that can occur within materials having several oxidation states. So far, the best achieved value is attained for hydrous RuO_2 (720 Fg^{-1}) [158]. Due to the high cost and toxicity of ruthenium, much attention is currently focused towards the development of alternate oxides for the supercapacitor applications.

1.8 Scope of the present work

Synthesis of nanomaterials in 1D has attracted much interest in view of its specific properties and applications. However, in most of the synthesis, usage of templates, mainly organic compounds, plays a vital role in synthesizing materials having growth in uniaxial direction. One of the main disadvantage in using templates is that the length being limited by the length of the templates. Also, the usage of a template requires removal of it which further ends as an organic pollutant. Even though we have the choice of different existing methods of synthesis, still it is a challenge to optimize the synthesis and processing conditions to get morphologically defined porous nanostructured oxides. By ensuring molecular level mixing in a precursor, with improved crystallinity of the product, desired shapes like nanorods, nanowires, nanosheets, etc., can be achieved.

Oriental attachment is one of the way to synthesize nanostructured materials with defined morphological features using simple synthetic protocols. The specific morphological feature of the precursor can be transformed topotactically to the corresponding oxide upon pyrolysis in air through oriental attachment. By considering the above issue, the simple and facile coprecipition method has been modified in such a way to get a molecular precursor with rod shaped morphology in the case of the cobalt spinels Co_3O_4 and $ZnCo_2O_4$. The topotactical growth was confirmed by the formation of cobalt oxide with same morphology as that of the precursor after pyrolysis in air. The optimized synthesis conditions not only improved the crystallinity of the molecular precursor (cobalt hydroxy carbonate) but also helped in the formation of porous nanorods of cobalt oxide. Since the porous material has an important role in applications, it has been tested for its utility in the field of catalysis, sensors, batteries and supercapacacitors.

Further as an extension, the same synthetic protocol has been tried in the case of Fe based spinels of the general formula AFe_2O_4, where A = Fe, Zn, and Co. In the case of cobalt ferrite, a homogeneously mixed active precursor has been formed by optimizing the synthesis conditions which on calcination gave the spinel oxide. In the case of zinc ferrite, a very fine nanosized material has been directly obtained at room temperature itself. In all cases, the crystallinity was improved by digesting the precipitate at a mild condition of 70 °C. Further, as the spinel type ferrites are magnetic, the magnetic properties have been studied and used as a tool to get detailed information on the characteristics of the

nanostructures. To get insight and information on the dependence of synthesis conditions on the magnetic properties, these mixed ferrites have also been synthesized through an auto-combustion method. The corresponding magnetic properties are correlated with the effect of synthesis methodologies.

This thesis also comprises of an imperative work on the nanosized, single phase, multiferroic bismuth ferrite. Its detailed magnetic properties on the basis of the impact of the synthesis conditions have been studied.

References

[1] J.F. Shackelford, *Introduction to Materials Science for Engineers,* Prentice Hall, 2009.

[2] H.R. Allcock, *Introduction to Materials Chemistry;* Wiley Hoboken, 2008.

[3] J.L.G. Fierro, *Metal Oxides: Chemistry and Applications,* CRC Press, 2006.

[4] O. Muller, R. Roy, *Major Ternary Structural Families,* Springer-Verlag, 1974.

[5] W.H. Bragg, *Philos. Mag.* 30 (1915) 305.

[6] S. Nishikawa, *Proc. Tokyo Math. Phys.* (1915) 199.

[7] F.S. Galasso, *Structure and Properties of Inorganic Solids,* Pergamon, 1970.

[8] R.W.G. Wyckoff, *Crystal Structures. Vol. 4, Miscellaneous inorganic compounds, silicates, and basic structural information,* Wiley and Sons, New York, 1969.

[9] J.G. Na, T.D. Lee, S.J. Park, *IEEE T. Magn.* 28 (1992) 2433.

[10] Z.J. Zhang, Z.L. Wang, B.C. Chakoumakos, J.S. Yin, *J. Am. Chem. Soc.* 120 (1998) 1800.

[11] R. Arulmurugan, B. Jeyadevan, G. Vaidyanathan, S. Sendhilnathan, *J. Magn. Magn. Mater.* 288 (2005) 470.

[12] K.J. Standley, *Oxide Magnetic Materials,* Oxford University Press, 1972.

[13] R.H. Mitchell, *Perovskites: Modern and Ancient,* Almaz Press Inc., Canada, 2002.

[14] T. Wolfram, S. Ellialioğlu *Electronic and Optical Properties of d-band Perovskites,* Cambridge Universsity Press, 2006.

[15] V. M. Goldschmidt, *Nature* 7 (1926) 2.

[16] L.G. Tejuca, J. L. G. Fierro, *Properties and Applications of Perovskite-type Oxides;* CRC, 1993.

[17] K.J. Klabunde, *Nanoscale Materials in Chemistry,* Wiley-Interscience New York, 2001.

[18] J.A. Rodrguez, M.F. Garcia, *Synthesis, Properties, and Applications of Oxide Nanomaterials,* John Wiley & Sons, 2007.

[19] A.S. Edelstein, R.C. Cammarata, *Nanomaterials: Synthesis, Properties, and Applications*, Taylor & Francis, 1998.

[20] C.A. Mirkin, C.M. Niemeyer, *Nanobiotechnology II: More Concepts and Applications*, Vch Verlag GmbH & Co.KGaA, 2007.

[21] O. Shoseyov, I. Levy, *Nano BioTechnology: Bioinspired Devices and Materials of the Future*, Springer Verlag, 2007.

[22] V.M. Rotello, *Nanoparticles: Building Blocks for Nanotechnology,* Kluwer Academic/Plenum Publishers, 2004.

[23] H. Gleiter, *Adv. Mater.* 4 (1992) 474.

[24] G.A. Ozin, *Adv. Mater.* 4 (1992) 612.

[25] C.N.R. Rao, A. Müller, A.K. Cheetham, *The chemistry of Nanomaterials: Synthesis, Properties and Applications,* John Wiley & Sons GmbH, 2004.

[26] L.S. Panchakarla, Y. Sundarayya, S. Manjunatha, A. Sundaresan, C.N.R. Rao, *Chem. Phys. Chem.* 11 1673.

[27] A. Sundaresan, R. Bhargavi, N. Rangarajan, U. Siddesh, C.N.R. Rao, *Phys. Rev. B.* 74 (2006) 161306(R).

[28] T. Belin, N. Millot, F. Villieras, O. Bertrand, J.P. Bellat, *J. Phys. Chem. B.* 108 (2004) 5333

[29] P. Ayyub, V.R. Palkar, S. Chattopadhyay, M. Multani, *Phys. Rev. B.* 51 (1995) 6135.

[30] J. Schoiswohl, G. Kresse, S. Surnev, M. Sock, M.G. Ramsey, F.P. Netzer, *Phys. Rev. Lett.* 92 (2004) 206103.

[31] S. Tsunekawa, R. Sivamohan, S. Ito, A. Kasuya, T. Fukuda, *Nanostruct. Mater.* 11 (1999) 141.

[32] K.N. Yu, Y. Xiong, Y. Liu, C. Xiong, *Phys. Rev. B* 55 (1997) 2666.

[33] E. Mamontov, T. Egami, *J. Phys. Chem. Solids.* 61 (2000) 1345.

[34] H.Z. Zhang, J.F. Banfield, *J. Mater. Chem.* 8 (1998) 2073.

[35] W.I. Park, G.C. Yi, M.Y. Kim, S.J. Pennycook, *Adv. Mater.* 15 (2003) 526.

[36] M. Yin, Y. Gu, I.L. Kuskovsky, T. Andelman, Y. Zhu, G.F. Neumark, S. O'Brien, *J. Am. Chem. Soc.* 126 (2004) 6206.

[37] K.K. Kim, N. Koguchi, Y.W. Ok, T.Y. Seong, S.J. Park, *Appl. Phys. Lett.* 84 (2004) 3810.

[38] J.V. Stark, D.G. Park, I. Lagadic, K.J. Klabunde, *Chem. Mater.* 8 (1996) 1904.

[39] K.J. Klabunde, J. Stark, O. Koper, C. Mohs, D.G. Park, S. Decker, Y. Jiang, I. Lagadic, D.J. Zhang, *J. Phys. Chem.* 100 (1996) 12142.

[40] K.T. Ranjit, G. Medine, P. Jeevanandam, I.N. Martyanov, K.J. Klabunde, *In Environmental Catalysis,* V.H. Grassion (Editor), CRC Press, Boca Raton, FL, (2005) 391.

[41] E. Lucas, S. Decker, A. Khaleel, A. Seitz, S. Fultz, A. Ponce, W.F. Li, C. Carnes, K.J. Klabunde, *Chem. Eur. J.* 7 (2001) 2505.

[42] B.-X. Wang, L.-P. Zhou, X.-F. Peng, *Int. J. Heat Mass Trans.* 46 (2003) 2665.

[43] P. Keblinski, S.R. Phillpot, S.U.S. Choi, J.A. Eastman, *Int. J. Heat Mass Trans.* 45 (2002) 855.

[44] S.K. Das, S.U.S. Choi, W. Yu, T. Pradeep, *Nanofluids: Science and Technology,* John Wiley & Sons, 2007.

[45] S.P. Jang, S.U.S. Choi, *Appl. Phys. Lett.* 84 (2004) 4316.

[46] D.S. Zhu, X.F. Li, N. Wang, X.J. Wang, J.W. Gao, H. Li, *Curr. Appl. Phys.* 9 (2009) 131.

[47] M.S. Liu, M.C.C. Lin, I.T. Huang, C.C. Wang, *Chem. Eng. Tech.* 29 (2006) 72.

[48] Z.L. Wang, D.W. Tang, S. Liu, X.H. Zheng, N. Araki, *Int. J. Thermophys.* 28 (2007) 1255.

[49] S.M.S. Murshed, K.C. Leong, C. Yang, *Int. J. Therm. Sci.* 44 (2005) 367.

[50] S. Park, R.J. Gorte, J.M. Vohs, *Appl. Catal. A* 200 (2000) 55.

[51] J.C. Ganley, K.L. Riechmann, E.G. Seebauer, R.I. Masel, *J. Catal.* 227 (2004) 26.

[52] T. Rajkumar, G. Ranga Rao, *J. Mol. Catal. A: Chem.* 295 (2008) 1

[53] Z. Jin, H.J. Zhou, Z.L. Jin, *Sensor. Actuat. B* 52 (1998) 188.

[54] S.H. Wang, T.C. Chou, C.C. Liu, *Sensor. Actuat. B* 94 (2003) 343.

[55] J. Liu, H. Xia, L. Lu, D. Xue, *J. Mater. Chem.* 20 (2010) 1506.

[56] Y. Wang, H.C. Zeng, J.Y. Lee, *Adv. Mater.* 18 (2006) 645.

[57] G.S. Chai, S.B. Yoon, J.S. Yu, J.H. Choi, Y.E. Sung, *J. Phys. Chem. B* 108 (2004) 7074.

[58] M. Mamak, N. Coombs, G. Ozin, *J. Am. Chem. Soc.* 122 (2000) 8932.

[59] J. Liu, T. Luo, S.M. T, F. Meng, B. Sun, M. Li, *Chem. Comm.* 46 (2010) 472

[60] M. Zukalov, J. Prochzka, A. Zukal, J.H. Yum, L. Kavan, M. Graetzel, *J. Electrochem. Soc.* 157 (2010) H99.

[61] E.S. Toberer, A. Joshi, R. Seshadri, *Chem. Mater.* 17 (2005) 2142.

[62] P. Jeevanandam, R.S. Mulukutla, Z. Yang, H. Kwen, K.J. Klabunde, Chem. Mater. 19 (2007) 5395

[63] B.D. Cullity, C.D. Graham, *Introduction to Magnetic Materials,* Wiley-IEEE Press, 2008.

[64] J.S. Smart, *Effective Field Theories of Magnetism,* W.B. Saunders Company, Piladelphia& London, 1966.

[65] J.B. Goodenough, *Magnetism and the Chemical Bond,* Interscience Publishers, New York, 1963.

[66] J.L. Dormann, D. Fiorani, E. Tronc, *Adv. Chem. Phys.* 98 (1997) 283.

[67] M.R.J. Gibbs, *Modern Trends in Magnetostriction Study and Application,* Springer Netherlands, 2001.

[68] J. Smit, H.P.J. Wijn, *Ferrites,* Philips Technical Library, Eindhoven, 1959.

[69] A. Goldman, *Modern Ferrite Technology,* Springer Verlag, 2006.

[70] J.B. Goodenough, J.M. Longo, *"Crystallographic and magnetic properties of perovskite and perovskite-related compounds",* Landbolt-Börnstein, New Series, vol. III.4(a), Springer, Berlin, 1970, p. 126.

[71] C.N.R. Rao, B. Raveau, *Colossal Magnetoresistance, Charge Ordering and Related Properties of Manganese Oxides,* World Scientific Pub Co Inc, 1998.

[72] C. Zener, *Phys. Rev.* 82 (1951) 403.

[73] W.D. Callister, D.G. Rethwisch, *Fundamentals of Materials Science and Engineering*, John Wiley & Sons, 2003.

[74] H. Bea, M. Gajek, M. Bibes, A.Barthélémy, *J. Phys.: Condens. Mattter* 20 (2008) 434221.

[75] H. Schmid, *Ferroelectrics* 162 (1994) 317.

[76] C. Ederer, N.A. Spaldin, *Nat. Mater.* 3 (2004) 849.

[77] D.I. Khomskii, *J. Magn. Magn. Mater.* 306 (2006) 1.

[78] S.W. Cheong, M. Mostovoy, *Nat. Mater.* 6 (2007) 13.

[79] J.F. Scott, *Nat. Mater.* 6 (2007) 256.

[80] M. Bibes, A. Barthélémy, *Nat. Mater.* 7 (2008) 425.

[81] E. Ascher, H. Rieder, H. Schmid, H. Stssel, *J. Appl. Phys.* 37 (1966) 1404.

[82] R. Moctezuma, M.E. Mendoza, J.L. Carrillo, *J. Magn. Magn. Mater.* 320 (2008) e186.

[83] D. Andreica, J.P. Rivera, S. Gentil, Z.G. Ye, M. Senthil Kumar, H. Schmid, *Ferroelectrics* 204 (1997) 73.

[84] G.A. Smolensky, A.I. Agranovskaya, V.A. Isupov, *Sov. Phys. Solid State* 1 (1959) 149.

[85] G.A. Smolensky, V.A. Isupov, A.I. Agronovskaya, *Sov. Phys. Solid State* 1 (1959) 150.

[86] W. Brixel, J.P. Rivera, A. Steiner, H. Schmid, *Ferroelectrics* 79 (1988) 201.

[87] S. Kharrazi, D.C. Kundaliya, S.W. Gosavi, S.K. Kulkarni, T. Venkatesan, S.B. Ogale, J. Urban, S. Park, S.W. Cheong, *Solid State Communi.* 138 (2006) 395.

[88] E. Galstyan, B. Lorenz, K.S. Martirosyan, F. Yen, Y.Y. Sun, M.M. Gospodinov, C.W. Chu, *J. Phys.: Condens. Matter* 20 (2008) 325241.

[89] N. Fujimura, T. Ishida, T. Yoshimura, T. Ito, *Appl. Phys. Lett.* 69 (1996) 1011.

[90] C.R. Serrao, J.R. Sahu, K. Ramesha, C.N.R. Rao, *J. Appl. Phys.* 104 (2008) 016102.

[91] P. Uniyal, K.L. Yadav, *Mater. Lett.* 62 (2008) 2858.

[92] P. Uniyal, K.L. Yadav, *J. Phys.: Condens. Matter* 21 (2009) 012205.

[93] R.K. Mishra, D.K. Pradhan, R.N.P. Choudhary, A. Banerjee, *J. Phys.: Condens. Matter* 20 (2008) 045218.

[94] I.O. Troyanchuk, M.V. Bushinsky, D.V. Karpinsky, O.S. Mantytskaya, V.V. Fedotova, O.I. Prochnenko, *Phys. Status solidi B* 246 (2009) 1901.

[95] V.A. Khomchenko, V.V. Shvartsman, P. Borisov, W. Kleemann, D.A. Kiselev, I.K. Bdikin, J.M. Vieira, A.L. Kholkin, *Acta Mater.* 57 (2009) 5137.

[96] Z. Yan, K.F. Wang, J.F. Qu, Y. Wang, Z.T. Song, S.L. Feng, *Appl. Phys. Lett.* 91 (2007) 082906.

[97] C.G. Duan, S.S. Jaswal, E.Y. Tsymbal, *Phys. Rev. Lett.* 97 (2006) 47201.

[98] N. Ortega, P. Bhattacharya, R.S. Katiyar, P. Dutta, A. Manivannan, M.S. Seehra, I. Takeuchi, S.B. Majumder, *J. Appl. Phys.* 100 (2006) 126105

[99] H. Zheng, J. Wang, S.E. Lofland, Z. Ma, L. Mohaddes-Ardabili, T. Zhao, L. Salamanca-Riba, S.R. Shinde, S.B. Ogale, F. Bai, *Science* 303 (2004) 661.

[100] T. Asefa, C.T. Duncan, K.K. Sharma, *The Analyst* 134 (2009) 1980.

[101] S.M. Kanan, O.M. El-Kadri, I.A. Abu-Yousef, M.C. Kanan, *Sensors* 9 (2009) 8158.

[102] T. Anderson, F. Ren, S. Peal-ton, *Sensors* 9 (2009) 4669.

[103] J. Janata, M. Josowicz, P. Vansek, D.M. DeVaney, *Anal. Chem.* 70 (1998) 179.

[104] E. Bakker, M. Telting-Diaz, *Anal. Chem.* 74 (2002) 2781

[105] D. Kohl, *J. phys. D: Appl. phys.* 34 (2001) R125.

[106] W.H. Brattain, J. Bardeen, *Bell Syst. Tech. J.* 32 (1953) 1.

[107] A. Bielanski, J. Deren, J. Haber, *Nature* 179 (1957) 668.

[108] T. Seiyama, A. Kato, K. Fujiishi, M. Nagatani, *Anal. Chem.* 34 (1962) 1502f.

[109] N. Taguchi, U. S. Patent 3631436, 1971.

[110] J. Gong, Q. Chen, M.R. Lian, N.C. Liu, R.G. Stevenson, F. Adami, *Sensor. Actuat. B* 114 (2006) 32.

[111] S. Vallejos, V. Khatko, J. Calderer, I. Gracia, C. Cane, E. Llobet, X. Correig, *Sensor. Actuat. B* 132 (2008) 209.

[112] V. Guidi, D. Boscarino, E. Comini, G. Faglia, M. Ferroni, C. Malagu, G. Martinelli, V. Rigato, G. Sberveglieri, *Sensor. Actuat. B* 65 (2000) 264.

[113] P.C. Xu, Z.X. Cheng, Q.Y. Pan, J.Q. Xu, Q. Xiang, W.J. Yu, Y.L. Chu, *Sensor. Actuat. B* 130 (2008) 802.

[114] J. Kaur, S.C. Roy, M.C. Bhatnagar, *Sensor. Actuat. B* 123 (2007) 1090.

[115] F. Berger, M. Fromm, A. Chambaudet, R. Planade, *Sensor. Actuat. B* 45 (1997) 175.

[116] H. Torvela, J. Huusko, V. Lantto, *Sensor. Actuat. B* 4 (1991) 479.

[117] M. Penza, G. Cassano, F. Tortorella, *Sensor. Actuat. B* 81 (2001) 115.

[118] C.S. Rout, M. Hegde, C.N.R. Rao, *Sensor. Actuat. B* 128 (2008) 488.

[119] D.D. Vuong, G. Sakai, K. Shimanoe, N. Yamazoe, *Sensor. Actuat. B* 105 (2005) 437.

[120] Z. Liu, T. Fan, D. Zhang, X. Gong, J. Xu, *Sensor. Actuat. B* 136 (2009) 499.

[121] K.J. Wallace, S.R. Cordero, C.P. Tan, V.M. Lynch, E.V. Anslyn, *Sensor. Actuat. B* 120 (2007) 362.

[122] M. Tong, G. Dai, D. Gao, *Mater. Chem. Phys.* 69 (2001) 176.

[123] Y.D. Wang, X.H. Wu, Q. Su, Y.F. Li, Z.L. Zhou, *Solid State Electron.* 45 (2001) 347.

[124] M.S. Wagh, G.H. Jain, D.R. Patil, S.A. Patil, L.A. Patil, *Sensor. Actuat. B* 115 (2006) 128.

[125] D.N. Suryawanshi, D.R. Patil, L.A. Patil, *Sensor. Actuat. B* 134 (2008) 579.

[126] G.J. Li, S. Kawi, *Talanta* 45 (1998) 759.

[127] S. Vallejos, V. Khatko, K. Aguir, K.A. Ngo, J. Calderer, I. Gr cia, C. Cane, E. Llobet, X. Correig, *Sensor. Actuat. B* 126 (2007) 573.

[128] G. Korotcenkov, I. Blinov, M. Ivanov, J.R. Stetter, *Sensor. Actuat. B* 120 (2007) 679.

[129] T. Jinkawa, G. Sakai, J. Tamaki, N. Miura, N. Yamazoe, *J. Mol. Cat. A* 155 (2000) 193.

[130] R.S. Khadayate, J.V. Sali, P.P. Patil, *Talanta* 72 (2007) 1077.

[131] S. Ajami, Y. Mortazavi, A. Khodadadi, F. Pourfayaz, S. Mohajerzadeh, *Sensor. Actuat. B* 117 (2006) 420.

[132] D. Patil, P. Patil, V. Subramanian, P.A. Joy, H.S. Potdar, *Talanta* 81 (2010) 37.

[133] X. Niu, W. Du, *Sensor. Actuat. B-Chem.* 99 (2004) 405.

[134] C. Xiangfeng, L. Xingqin, M. Guangyao, *Sensor. Actuat. B* 55 (1999) 19.

[135] H.H. Kung, *Transition Metal Oxides: Surface Chemistry and Catalysis,* Elsevier, 1989.

[136] K. J. Laidler, *Chemical Kinetics,* Harper and Row, New York, (1987) P29.

[137] S.D. Jackson, J.S.J. Hargreaves, *Metal Oxide Catalysis,* Wiley-VCH, 2009.

[138] H.C. Zeng, *Inorg. Chem.* 37 (1998) 1967.

[139] M.S. Chen, D.W. Goodman, *Science* 306 (2004) 252.

[140] Z. Zhang, C.C. Wang, R. Zakaria, J.Y. Ying, *J. Phys. Chem. B* 102 (1998) 10871.

[141] N.R. Shiju, V.V. Guliants, *Appl. Catal. A* 356 (2009) 1.

[142] X. Xie, Y. Li, Z.Q. Liu, M. Haruta, W. Shen, *Nature* 458 (2009) 746.

[143] S. Dhameja, *Electric Vehicle Battery Systems,* Newnes, 2002.

[144] R. Dell, D.A.J. Rand, *Understanding Batteries,* Royal Society of Chemistry, 2001.

[145] G. Nazri, G. Pistoia, *Lithium Batteries: Science and Technology,* Springer Netherlands, 2004.

[146] I. Buchmann, *Batteries in a Portable World,* Cadex Electronics, 2001.

[147] P. Poizot, S. Laruelle, S. Grugeon, L. Dupont, J.M. Tarascon, *Nature* 407 (2000) 496.

[148] B. Scrosati, *Electrochim. Acta* 45 (2000) 2461

[149] M.S. Whittingham, *Science* 192 (1976) 1126

[150] M.S. Whittingham, A.J. Jacobson, *Intercalation Chemistry,* Academic Press, New York, 1982.

[151] K. Mizushima, P.C. Jones, P.J. Wiseman, J.B. Goodenough, *Mater. Res. Bull.* 15 (1980) 783.

[152] M.M. Thackeray, W.I.F. David, P.G. Bruce, J.B. Goodenough, *Mater. Res. Bull.* 18 (1983) 461

[153] Y. Idota, T. Kubota, A. Matsufuji, Y. Maekawa, T. Miyasaka, *Science* 276 (1997) 1395.

[154] C.K. Chan, H.L. Peng, G. Liu, K. McIlwrath, X.F. Zhang, R.A. Huggins, Y. Cui, *Nat. Nanotechnol.* 3 (2008) 31.

[155] D.W. Kim, I.S. Hwang, S.J. Kwon, H.Y. Kang, K.S. Park, Y.J. Choi, K.J. Choi, J.G. Park, *Nano Lett.* 7 (2007) 3041.

[156] B.E. Conway, *Electrochemical Supercapacitors: Scientific Fundamentals and Technological Applications,* Springer, 1999.

[157] M. Winter, R.J. Brodd, *Chem. Rev.* 104 (2004) 4245.

[158] J.P. Zheng, P.J. Cygan, T.R. Jow, *J. Electrochem. Soc.* 142 (1995) 2699.

Chapter 2

Experimental Methods

Introduction

There are various soft chemical methods used for the synthesis of nanosized oxide materials, such as coprecipitation, sol-gel, citrate-gel, hydrothermal, auto-combustion method, etc. In depth details and mechanisms of the various methods are well documented in the literature [1–10]. This chapter briefly describes the methods used for the synthesis of the nanosized oxides studied in the present work and the various techniques used for the characterization of the materials. In the present work, a modified coprecipitation/digestion method, followed by calcination was employed for the synthesis of different oxide nanoparticles. In addition to this, an auto-combustion method was also tried for the synthesis of some of the oxides. Further, different types of instrumental techniques have been employed for characterizing both the precursors and nanosized oxides.

2.1 Synthesis methods

2.1.1 Coprecipitation

Coprecipitation is a convenient and facile route employed for the synthesis of nanomaterials by forming a sparingly soluble product from aqueous solutions. In a precipitation reaction, corresponding metal salts in the form of nitrates, chlorides, sulphates, etc, are used. After precipitation with a precipitating agent, either the oxides are obtained directly or a precursor is formed in the form of hydroxide, oxalate, carbonate, etc, depending on the precipitating agent. These precursors, after calcination at a suitable temperature, will give rise to the required simple metal oxide or a mixed metal oxide. The major steps

governing a precipitation reaction are nucleation, growth and agglomeration. The theory and mechanism behind each individual step is well described in the literature [11–16]. In a precipitation reaction, the primary process taking place is nucleation which can be considered as the key step. During nucleation, there will be formation of numerous small particles. The formation of products result in a sparingly soluble species formed under the condition of higher supersaturation. Supersaturation can be induced by various parameters such as temperature, pressure and chemical reaction. The particles formed will tend to grow/aggregate together either through the process of Ostwald ripening or through oriental attachment to minimize their energy and to become thermodynamically stable. If the crystallinity of the precursor is improved during precipitation, the high energy facets will attach together orientally to give morphologically controlled precursors. Those precursors upon calcination in air will form their corresponding oxides retaining their morphology as such. Such a growth process is called topotatical growth.

In the present work, most of the precipitation reactions have been carried out by using metal nitrates with potassium carbonate as the precipitating agent. Only in the case of Fe_3O_4, corresponding metal chlorides have been precipitated by using ammonium carbonate. Since the purity is very important for a material, all the starting chemicals have been carefully chosen with purity greater than 99%. The schematic representation of the synthesis is shown in Figure 2.1

As represented in Figure 2.1, corresponding metal nitrates and the precipitating agent are added simultaneously from separate burettes to deionized water kept at 70 °C in a round bottom flask, under vigourous stirring conditions. Deionized water is used as a medium for the reaction. Several initial experiments have been performed to control the pH required for the reaction (pH $\approx$ 7–8). With optimized pH conditions, the precipitation reaction is carried out with out any drastic change in pH. The controlled addition and stirring, with digestion at 70 °C helped to increase the crystallinity of the precursor. The same procedure was adapted for the synthesis of all oxides reported in this work, except that the starting chemicals are different, ferrous and ferric chlorides with ammonium carbonate as precipitant in the case of Fe_3O_4 .

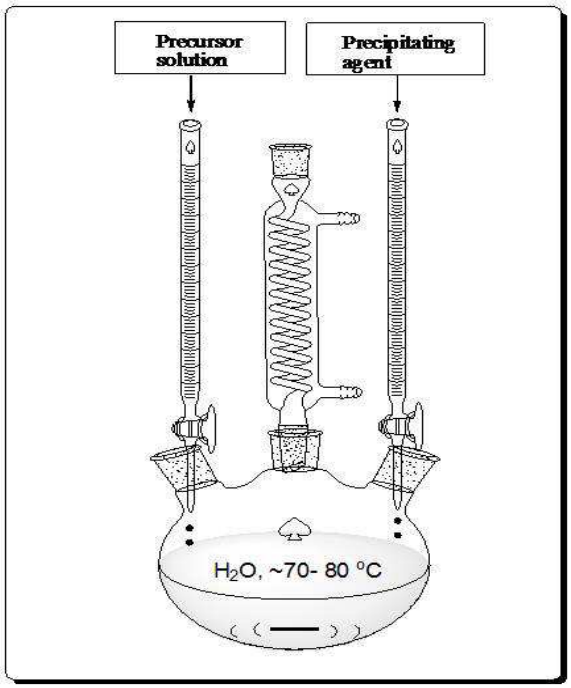

Figure 2.1: Schematic representation of coprecipitation/digestion method employed in the present work.

2.1.2 Auto-combustion method

Auto-combustion method is one of the simplest, time and cost effective method for the synthesis of metal oxides in a single step. It is known as self propagating high temperature synthesis (SHS) and is an alternative method for the production of advanced ceramics. SHS relies on the ability of highly exothermic reactions to be self-sustaining and is an energy efficient process [17, 18]. Simple SHS reactions are those in which a material is synthesized from a homogeneous reactant mixture. In a typical combustion reaction, the mixed reactant powders are pressed into pellets and subsequently ignited, either locally at one point (propagating mode) or by heating the whole pellet to the ignition temperature of the exothermic reaction (simultaneous combustion mode).

An alternative method in the combustion synthesis is the combustion of redox mixtures containing an oxidizer and a fuel [19, 20]. The solution combustion (SC) method of preparation is a relatively new development, being used to prepare a wide variety of oxide materials. This method involves rapid heating of aqueous solutions containing stoichiometric amounts of respective metal nitrate (oxidizer) and fuels like urea, hydrazides,

citric acid, etc [21–28]. A wide range of technologically important oxides with interesting magnetic, dielectric, electrical, mechanical, catalytic, luminescent and optical properties have been prepared by this method. In the solution combustion method, the fuel used are the source of C and H, which on combustion form CO and H_2O and liberate heat. Also, they form complexes with the metal ions facilitating homogeneous mixing of the cations in solution. The process can yield nanosized metal oxides some times having very high surface area.

In the present study, the glycine-nitrate process (GNP) has been used to synthesize some of the nanosized ferrites. Glycine has a carboxylic acid group at one end and amino acid group at other end [29]. Through this zwiterionic character, it can effectively complex metal ions of various ionic sizes. During the combustion reaction, it will act as a fuel also through oxidation by nitrate ion. The fuel/oxidizer ratio mainly governs the powder characteristics such as crystallite size, surface area, agglomeration etc. Theoretically calculated ratios of metal nitrate to fuel for a divalent and a trivalent metal ions is given in equation 2.1 and equation 2.2.

$$M(NO_3)_2 + \frac{10}{9}C_2H_5O_2N = MO + \frac{20}{9}CO_2 + \frac{25}{9}H_2O + \frac{14}{9}N_2 \tag{2.1}$$

$$2M(NO_3)_3 + \frac{30}{9}C_2H_5O_2N = M_2O_3 + \frac{60}{9}CO_2 + \frac{75}{9}H_2O + \frac{42}{9}N_2 \tag{2.2}$$

In the present work, corresponding metal nitrates of AR grade have been used to synthesize the corresponding oxides in a single step. Required moles of metal nitrate and fuel (glycine) were dissolved separately in minimum amount of distilled water and then mixed together. This homogeneous mixture solution was taken in a crystalizing dish of size 150 mm x 75 mm and kept on a hot plate with controlled heating. After evaporation of water, there will be gelation followed by a self ignition to yield the corresponding oxides in a single step. To get control over the particle size and phase purity different ratios of nitrate to fuel has been tried.

2.2 Characterization methods

2.2.1 Powder X-Ray Diffraction

Powder X-Ray diffraction (XRD) is a basic tool for characterization of materials for its phase identification [30, 31]. Each crystalline solid has its unique characteristic X-ray powder pattern, which may be used as a "fingerprint" for its identification. X-ray diffraction is a versatile, non-destructive analytical technique for identification and quantitative determination of the various crystalline compounds, known as 'phases', present in solid materials and powders. Identification is achieved by comparing the x-ray diffraction pattern - or 'diffractogram' - obtained from an unknown sample with an internationally recognized database containing reference patterns of almost all known phases. Modern computer-controlled diffractometer systems use automatic routines to measure, record and interpret the unique diffractograms produced by individual constituents in even highly complex mixtures.

The characteristics of X-Ray diffraction were discovered by W. H. Bragg. When a monochromatic X-ray beam with wavelength λ is projected onto a crystalline material at an angle θ, diffraction occurs only when the distance traveled by the rays reflected from successive planes differs by a complete number 'n' of wavelengths. The incident X-radiation strikes the planes (hkl) at an angle θ. The spacing between these planes is 'd'. Relationship between the wavelength of X-Ray beam, the angle of diffraction θ, and the distance between each set of planes separated with spacing 'd' is given by the Bragg condition

$$n\lambda = 2dsin\theta \tag{2.3}$$

where 'n' is the order of the diffraction. The diffraction of X-Rays on a set of crystals can be represented schematically as shown in Figure 2.2. Bragg's law is the necessary condition for diffraction.

The angular spread of the reflection from a crystal plane is affected not only by the perfection of the crystal but also by the size of the crystal. As the average size of the crystallites decreases, the angular spread of the reflection from a powder will increase. After suitable calibration, the half height width of a reflection in a powder diffractogram

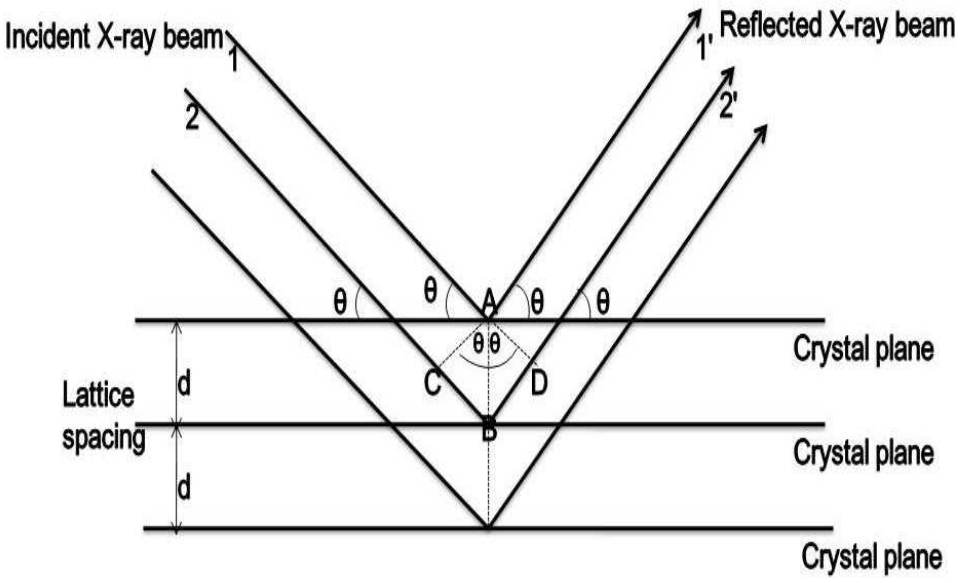

Figure 2.2: Diffraction of X-Rays.

can be used as quantitative measure of the mean crystallite size of the sample. The formula used for calculating crystallite size is the Scherrer formula as given in equation 2.4

$$K = \frac{0.9\lambda}{Bcos\theta} \tag{2.4}$$

where λ, the wavelength of X-Ray, B is full width at half maximum of the pattern, and θ is the Bragg angle. B is corrected for contribution from instrument line broadening by recording the pattern of a standard sample having very large particle size in the micrometer range.

In the present work, all the X-Ray diffraction patterns were recorded on a PANalytical X'PERT PRO model X-ray diffractometer, at the scan rate of 2°/min in the 2θ range of 10 to 80 degrees. In cases where a very small percentage of additional phases is expected, XRD patterns were recorded at a slow scan rate of 0.1°/min.

Powder XRD patterns can be simulated from a knowledge of the crystallographic parameters of the specific material. The minimum required parameters for simulating a pattern are the space group, unit cell lattice parameters, atomic positions and the occupancy parameters of different atoms in the unit cell. In the present work, the XRD patterns of various compounds were simulated using a computer program 'Powder Cell for

Windows', PCW version 2.4, developed by W. Krauz and G. Nolze [32]. Along with the simulated pattern, the corresponding XRD patterns were compared with the standard available data from the Joint Committee on Powder Diffraction Standards (JCPDS), International Center for Diffraction Data, with the card number.

2.2.2 High Resolution Transmission Electron Microscopy (HRTEM)

In nanoscience and nanotechnology observation is one of the key step for manipulation and arrangement of atoms for understanding and development. Human eye can resolve smallest distance between two points of about 0.1–0.2 mm. This distance is the resolving power of the eye. So, to visualize tiny objects, we need a technique or instrument which is the *microscope* to get enlarged images. The word *microscope* is derived from greek -"micros" meaning 'small' and "skopos" meaning 'to look at'. A microscope consists of an illumination source, condenser lens for coverage of beam, an objective lens for magnification and a projector lens for projecting the image which can be photographed or it can be seen in CCD cameras. Here, electrons are being used because electrons are smaller than atoms and therefore, it is possible to "see" details at the atomic level. Through this technique, one can get insight information about size, shape and arrangement of particles in a sample [33]. Through the scattering phenomenon, which occurs during the interaction of electrons with matter, we can get diffraction patterns. For example, there will be a coherent scattering as a result of elastic scattering occurring from well ordered arrangements of atoms in a crystal. The resultant coherent scattering will give spot patterns in case of single crystals and ring patterns for polycrystalline materials. The d-spacing between lattice planes of crystalline materials can be calculated from selected area electron diffraction pattern (SAED) through the relationship

$$dr = \lambda L \tag{2.5}$$

where L is the distance between the specimen and the photographic plate, and the term λL can be taken as a camera constant and r is the radius of the diffracted ring. By calibrating the instrument with a standard sample (Au), we can calculate the camera constant. Hence, through λL and r one can calculate d values which will give information

about the specific crystal structure. As the name implies 'High resolution' one can resolve in depth to get informations like lattice fringes which once again gives information about the d values to know details of the crystal structure [34].

All the nanosized oxides synthesized in this present work were analyzed using a model SEI, PECNAI G^2TF30 transmission electron microscope. The powder sample was dispersed in a solvent with low boiling point like isopropanol and dropped on the carbon and polymeric film coated copper grids for analysis. The coated samples were allowed to dry for overnight to evaporate the solvents before the analysis.

2.2.3 Infrared (IR) spectroscopy

IR spectroscopy analysis is based on the interaction of electromagnetic radiation with matter [35, 36]. It has been widely used for structural analysis, chemical compound identification and monitoring of changes occurring during the course of a chemical reaction. Normally all the atoms in a molecules are in motion to some extent. Molecules tend to rotate, translate and vibrate. The energy of IR radiation is sufficient to change the vibrational energy states of molecules. There will be an interaction of IR radiation with the molecule if the dipole moment changes due to vibration. Hence, such mode of vibration is said to be IR active. We can observe increase in amplitude of vibration when energy is transferred to the molecule if the frequency of radiation matches with the frequency of a particular vibration. The frequency of vibration can be obtained from Hooke's law

$$\nu = \frac{1}{2\pi c}\sqrt{\frac{K}{\mu}} \tag{2.6}$$

where ν is the vibrational frequency, K is the force constant and μ is reduced mass. So, from the characteristic bands of certain vibrational frequencies in the IR spectra, one can get structural information about the molecules. In the present work, the IR studies were carried out on the oxide samples using a Perkin Elmer Spectrum-One FTIR Spectrometer in the frequency range 400 to 4000 cm^{-1} by properly mixing the sample with spectroscopic grade KBr.

2.2.4 X-Ray Photoelectron Spectroscopy (XPS)

In solid materials surface properties are crucial in determining many properties. There will be an interaction with the surroundings through the surface, the physical and chemical composition of these surfaces determines the nature of interaction. XPS is a surface sensitive technique since it has a relatively low penetration depth (0.5–2 nm) of the elastically scattered electron. XPS is based on the principle of photoelectric effect, emission of an electron when X-rays incident on a solid surface, discovered by Hertz in 1887. This technique has been widely used to characterize materials to get information about the elemental status [37, 38]. Through the electron spectrometer, energy of the emitted photoelectrons can be measured. From the binding energies (BEs), which depend on the element, one can characterize the solid materials. Following equation 2.7 gives the relationship between the parameters involved in the XPS measurement:

$$E_B = h\nu - E_K - W \tag{2.7}$$

where hν is the photon energy, E_K, is the kinetic energy of the electron and W is the spectrometer work function. Binding energy can be calculated from equation 2.7 and hence information about elements can be obtained from the characteristic binding energies. In addition to this, chemical information can be obtained from the shift in binding energies which depend on the chemical bonding of the elements under investigation.

XPS studies in this work have been made on the model VG Microtech Multilab ESCA 3000 spectrometer using a non-monochromatized MgKα source, hν = 1253.6 eV with a base pressure in the analysis chamber as 4 x 10^{-10} torr. The instrument's overall energy resolution was better than 0.7 eV, as determined from the full width at half maximum of the $4f_{7/2}$ core level of gold surface. Further, all the binding energies were corrected if there is any error using C_{1S} peak of carbon with the binding energy value of 285.00 eV as the reference.

2.2.5 Surface Area Measurement

Solids surface may be of porous or non-porous in nature. If there is porosity, depending on the size of the pores, the solids are classified into macroporous (diameter above 50 nm) mesoporous (diameter 2–50 nm) and microporous (diameter less than 2 nm). To

get information about the surface area of a solid, it is important to know the number of molecules that cover the surface with a single layer of the adsorbate, which is nothing but monolayer capacity. From the area of cross section of the adsorbate molecule, the surface area can be calculated. Brunauer-Emmett-Teller (BET) equation for calculating the monolayer capacity of a solid is given by

$$\frac{P}{v(P_0 - P)} = \frac{1}{Cv_m} + \frac{(C-1)P}{Cv_m P_0} \tag{2.8}$$

where P is adsorption equilibrium pressure, P_0 is saturation vapour pressure of the adsorbate at the experimental temperature, v is volume of N_2 adsorbed at a pressure P, v_m is the volume of adsorbate required for monolayer coverage, C is a constant that is related to the heat of adsorption and liquefaction. From the valid BET equation we can get a straight line if we plot $\frac{P}{v(P_0-P)}$ against P/P_0 with the slope s=$\frac{C-1}{v_m C}$ and intercept i = $\frac{1}{v_m C}$. Here, the monolayer capacity is $v_m = \frac{1}{s+i}$. Since v_m is the volume in ml at standard temperature and pressure, the number of molecules is $\frac{v_m N}{22414}$, where N is Avagadro's number. From these relations total surface area of the solid is given by

$$surface\ area = \frac{v_m N}{22414} A_m \times 10^{-20} m^2 \tag{2.9}$$

where A_m is the area of cross section of the adsorbate molecule. The specific surface area of the solid material will be obtained by dividing total surface by mass of the solid [39].

The surface area measurements of the samples were carried out using the model Micromeritics NOVA 1200 (Quanta Chrome) instrument using N_2 as adsorbent.

2.2.6 Thermogravimetric Analysis (TGA)

TGA is a type of thermal analysis in which physical properties of a material are measured as a function of temperature [40]. Information about any weight changes associated with thermally induced transformations can be obtained from TGA. The loss of weight as a function of temperature is the characteristic features of a material since there will be physical and chemical changes over a wide temperature range.

In this work, TGA was performed on a Perkin-Elmer TGA7 analyzer under normal atmospheric conditions.

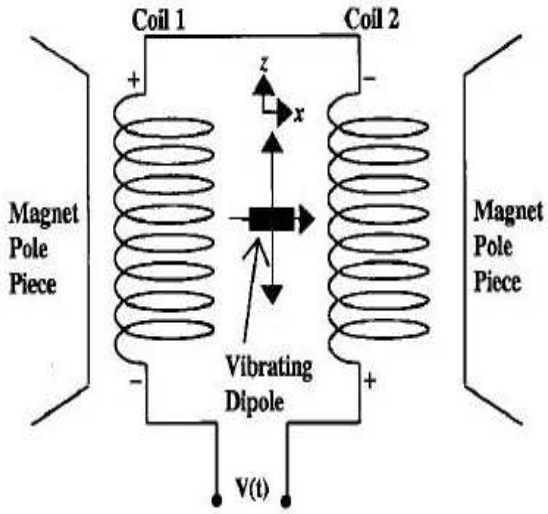

Figure 2.3: Working principle of VSM.

.

2.2.7 Vibrating Sample Magnetometer (VSM)

VSM is an effective tool to get in-depth information about the magnetic properties of a material, both as a function of the applied magnetic field at different temperatures and as a function of temperature at different fields. The working principle of a VSM is based on the Faraday's law, an electromotive force (emf) is induced in a conductor by a time varying magnetic flux [41, 42]. In a VSM, the sample under investigation is subjected to vibrate sinusoidally at a small fixed amplitude with respect to stationary pick-up coils, in the presence of a uniform magnetic field, as shown in Figure 2.3. The magnitude of the induced alternating emf generated in the pick up coils is proportional to the magnetic moment of the sample.

In the present study, a EG&G PAR 4500 vibrating sample magnetometer and a VSM attachment in a physical property measurement system (ppms) of Quantum Design are used for magnetic measurements. For the field variation measurement at a constant temperature, a maximum field of 5 T has been used. By using a closed cycle helium cryostat, the variable temperature magnetic measurement at constant field was carried out from 5 K to room temperature using the PPMS. Magnetic measurements above room temperature were performed on the model EG&G PAR 4500 with the help of an electrically

heated oven attached to it. For room temperature magnetic measurements, sample was subjected to the field at room temperature. For zero field cooled (ZFC) measurement, sample was cooled to the lowest possible temperature in zero magnetic field and then magnetization was recorded while warming it back to room temperature under a constant field. In the case of field cooled (FC) measurement, a constant field was applied during cooling down to the lowest possible temperature and the magnetization was measured under the field while heating back to room temperature.

2.2.8 Catalytic Oxidation

Catalytic oxidation reaction was performed in an autoclave (Parr Instruments) having a total capacity of 300 ml. In a typical oxidation reaction, 0.5 gm (0.3 mmol) of veratryl alcohol was added to 70 ml of methanol. This reaction mixture was charged in the Parr autoclave having provisions of heating arrangement, overhead stirrer, internal cooling loop, pressure gauge as well as a transducer, gas inlet, gas outlet, sampling valve, safety rupture disc, cooling coil, etc. 0.1 gm the catalyst was added to the reaction mixture and was heated up to 130 °C. When the desired temperature was attained, the reactor was pressurized with oxygen up to 100 psig and then the reaction was started by putting on an agitation at the rate of 900 rpm. Total oxygen pressure was kept constant at 100 psi by adding oxygen from time to time. The reaction was continued for 2 h. Liquid samples were analyzed by HPLC using a Hewlett-Packard model 1050 liquid chromatograph equipped with a UV detector for analysis. The analysis was performed on a 25 cm RP-18 column supplied by Hewlett-Packard. The product and reactant were detected using a UV detector at $\lambda_{max} = 223$ nm using 35 % methanol as mobile phase at a column temperature of 35 °C and the flow rate of 1 ml/min. For the analysis, samples of 20 μl were injected into the column using an auto sampler HP1100.

2.2.9 Gas Sensor measurements

Gas sensing measurements were performed in the set up as shown in Figure 2.4. The description of the set up is as follows: It consist of glass chamber (2 liters capacity and ∼11 cm diameter), a nicrome wire heater (resistance ∼55 Ω at room temperature) with a power of 750W. A dimmerstat was used to control the heating. The ceramic

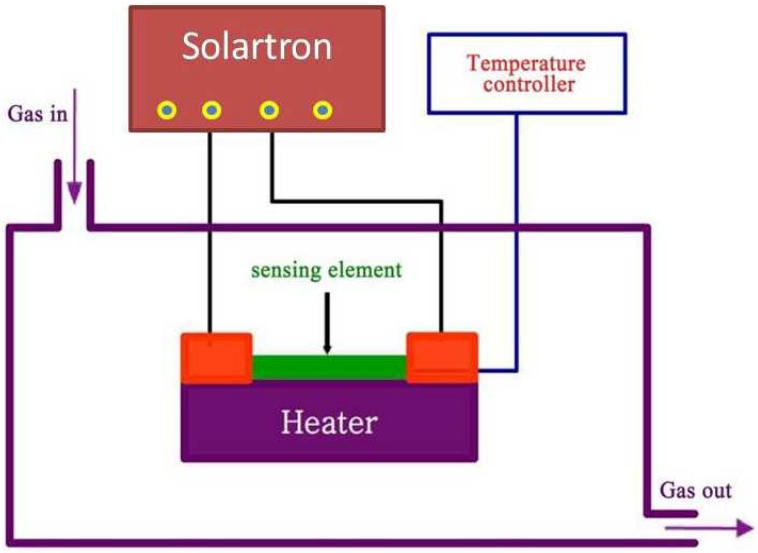

Figure 2.4: Schematic diagram of a gas sensing setup.

.

powder was pressed into a pellet of diameter ∼1 cm and thickness ∼0.1 cm for the sensing measurements. The sensing element was kept directly on the heater in the gas chamber and the temperature was varied from room temperature to the required temperature according to the system. The distance between the sample and gas inlet tube was about 5 cm inside the chamber. A chromel-alumel thermocouple placed in contact with the sensor was used to monitor the temperature. A known volume of the testing gas was introduced into the gas chamber pre-filled with air and it was maintained at atmospheric pressure. The dc current signal was measured as a function of time at a constant applied voltage of 1 V using an electrochemical measurement System (Solartron, 1287) controlled by CorrWare software from Scribner Associates Inc. supplied by Solartron. The relative response factor (S) is defined as,

$$S = \frac{R_g - R_a}{R_a} \times 100\% = \left(\frac{I_a - I_g}{I_a}\right)_v \times 100\% \tag{2.10}$$

where R_a and R_g are values of the resistance in air and in the presence of the testing gas, respectively. In terms of Ohm's law, S can also be represented by the current in air (I_a) and in presence of gas (I_g) at constant measuring voltage.

2.2.10 Electrochemical measurements

Cyclic voltammetry (CV) is an effective tool to study the different electrochemical processes (faradaic and non-faradaic) associated with an electrode material [43, 44]. It can be used to study the electrochemical behavior of species diffusing to an electrode surface, interfacial phenomena at an electrode surface, and bulk properties of materials in or on electrodes. In CV, normally three electrode systems are in common practice although two electrode systems can also be used. In three electrode systems the potential is applied between working electrode and reference electrode while the current is measured in between the working electrode and the counter electrode. To tackle with large currents, normally counter electrode will be with very high surface area.

In the present study all the electrochemical work related to CV and impedance measurements were carried out on both Autolab 30 PGSTAT and Solartron instruments. Charge-discharge experiments were carried out on a home made galvanostatic set up with a Keithley 6514 electrometer and 2010 multimeter connected in series with a variable resistance box.

References

[1] C.N.R. Rao, *Chemical Approaches to the Synthesis of Inorganic Materials,* Wiley Eastern Ltd., New Delhi., 1994.

[2] A.S. Edelstein, R.C. Cammarata, *Nanomaterials: Synthesis, Properties, and Applications, Taylor & Francis,* 1998.

[3] G.A. Ozin, A.C. Arsenault, *Nanochemistry: A Chemical Approach to Nanomaterials,* Royal Society of Chemistry, 2005.

[4] G. Cao, *Nanostructures & Nanomaterials: Synthesis, Properties & Applications,* Imperial College Press, 2004.

[5] D. Segal, *Chemical Synthesis of Advanced Ceramic Materials,* Cambridge Univ Press, 1991.

[6] J.P. Jolivet, *Metal Oxide Chemistry and Synthesis: From Solution to Solid State,* Wiley, New York, 2000.

[7] K.C. Patil, *Chemistry of Nanocrystalline Oxide Materials: Combustion Synthesis, Properties and Applications,* World Scientific Pub Co Inc, 2008.

[8] D. Segal, *J. Mater. Chem.* 7 (1997) 1297.

[9] B.L. Cushing, V.L. Kolesnichenko, C.J. O'Connor, *Chem. Rev.* 104 (2004) 3893.

[10] O. Masala, R. Seshadri, *Annu. Rev. Mater. Res.* 34 (2004) 41.

[11] T.A. Ring, *Fundamentals of Ceramic Powder Processing and Synthesis,* Academic Press, 1996.

[12] A.E. Nielsen, *Kinetics of Precipitation,* Pergamon, 1964.

[13] H. Furedi-Milhofer, *Pure Appl. Chem.* 53 (1981) 2041.

[14] J.A. Dirksen, T.A. Ring, *Chem. Eng. Sci.* 46 (1991) 2389.

[15] I.M. Lifshitz, V.V. Slyozov, *J. Phys. Chem. Solids.* 19 (1961) 35.

[16] R.M. Tromp, J.B. Hannon, *Surf. Rev. Lett.* 9 (2002) 1565.

[17] J.J. Moore, H.J. Feng, *Prog. Mater. Sci.* 39 (1995) 243.

[18] J.J. Moore, H.J. Feng, *Prog. Mater. Sci.* 39 (1995) 275.

[19] K.C. Patil, S.T. Aruna, S. Ekambaram, *Current Opinion Solid State Mater. Sci.* 2 (1997) 158.

[20] K.C. Patil, S.T. Aruna, T. Mimani, *Current Opinion Solid State Mater. Sci.* 6 (2002) 507.

[21] R.D. Purohit, B.P. Sharma, K.T. Pillai, A.K. Tyagi, *Mater. Res. Bull.* 36 (2001) 2711.

[22] Y. Xijuan, X. Pingbo, S. Qingde, *Phys. Chem. Chem. Phys.* 3 (2001) 5266.

[23] C.C. Hwang, J.S. Tsai, T.H. Huang, *Mater. Chem. Phys.* 93 (2005) 330.

[24] G. Avgouropoulos, T. Ioannides, *Appl. Catal. A* 244 (2003) 155.

[25] J.J. Kingsley, K.C. Patil, *Mater. Lett.* 6 (1988) 427.

[26] Y. Han, S. Li, X. Wang, X. Chen, *Mater. Res. Bull.* 39 (2004) 25.

[27] Z. Yue, L. Li, J. Zhou, H. Zhang, Z. Gui, *Mater. Sci. Eng. B* 64 (1999) 68.

[28] J. Zhang, L. Gao, *Mater. Res. Bull.* 39 (2004) 2249.

[29] L.A. Chick, L.R. Pederson, G.D. Maupin, J.L. Bates, L.E. Thomas, G.J. Exarhos, *Mater. Lett.* 10 (1990) 6.

[30] B.D. Cullity, S.R. Stock, *Elements of X-Ray Diffraction,* Addison-Wesley Reading, MA, 1978.

[31] H.P. Klug, L.E. Alexander, *X-Ray Diffraction Procedures,* Wiley New York, 1954.

[32] The software is freely available from http://www.ccp14.ac.uk.

[33] D.B. Williams, C.B. Carter, *The Transmission Electron Microscopy: A Text Book for Materials Science,* Springer 2 nd edition , 2009.

[34] M. De Graef, *Introduction to Conventional Transmission Electron Microscopy,* Cambridge Univ Press, 2003.

[35] B.H. Stuart, *Infrared spectroscopy: Fundamentals and Applications,* Wiley, 2004.

[36] D.L. Pavia, G.M. Lampman, G.S. Kriz, *Introduction to Spectroscopy,* Brooks/Cole Pub Co, 2009.

[37] J.F. Watts, J. Wolstenholme, *An Introduction to Surface Analysis by XPS and AES,* John Wolstenholme, 2003.

[38] G.A. Somorjai, A.S. Mujumdar, *Introduction to Surface Chemistry and Catalysis,* Wiley New York, 1994.

[39] S. Lowell, *Characterization of Porous Solids and Powders: Surface Area, Pore Size, and Density,* Springer, 2004.

[40] H.H. Willard, L.L. Merrit, J.A. Dean, F.A. Settle, *Instrumental Methods of Analysis*, CBS Publishers & Distributers, New Delhi, 1986.

[41] B.D. Cullity, C.D. Graham, *Introduction to Magnetic Materials,* Wiley-IEEE Press, 2008.

[42] S. Foner, *Rev. Sci. Inst.* 30 (1959) 548.

[43] A.J. Bard, L.R. Faulkner, *Electrochemical Methods,* Wiley New York, 2001.

[44] J.F. Rusling, S.L. Suib, *Adv. Mater.* 6 (2004) 922.

Chapter 3

Synthesis, Characterization, and Applications of Nanostructured Co_3O_4 and $ZnCo_2O_4$

3.1 Nanostructured Co_3O_4

Among the transition metal oxides, cobalt oxide (Co_3O_4), an important magnetic *p*-type semiconductor, has received considerable attention in the past few years due to its application potential in many technological areas such as heterogeneous catalysis, anode material in lithium rechargeable batteries, sensors, electrochromic devices, solar energy absorber, etc. [1–5]. However, morphology-controlled synthesis of Co_3O_4 is a great challenge in materials science and its physical and chemical properties are greatly dependent of its size and shape. Therefore, a lot of research is being carried out to develop facile, environmental friendly, rational synthetic approaches to achieve better control over composition and nanostructures having directed pore size distribution. Also, synthesis of Co_3O_4 nanostructures, without the use of templates or surfactants, is again an urgent need since it can eliminate the cost and contamination due to the surfactants, avoiding complicated processes of operation and impurities in the final product, apart from the environmental impact.

Both *p*-type and *n*-type semiconductors are well known for their gas sensing properties. Carbon monoxide (CO) is one of the most harmful pollutants, which poses significant health risks [6–8]. Studies have shown that it interacts with the haemoglobin and damages the human body by producing a reduction in cellular respiration [9]. This aspect has stimulated considerable interest and scientific research, in recent years, to develop a simple and cost-effective chemical sensor for the detection of CO. Many efforts, in this field, are

today devoted to the synthesis of novel sensing materials with enhanced performance [6, 9–12]. Metal oxide semiconductors have been widely investigated in the past decades as gas sensing materials because of their low cost and power consumption, simplicity of fabrication and use, versatility in detecting a wide range of toxic/flammable gases, and stability in harsh environments [13,14]. The metal oxide semiconductors such as SnO_2 [9], In_2O_3 [10] and ZnO [15] have been investigated as CO sensing materials.

Recent studies revealed that nanostructured metal oxides with reduced dimensionality (i.e. in the form of nanoparticles, nanorods, nanotubes, nanowires and nanoribbons) have ultrahigh sensitivity to different gases due to their small grain size and large surface-to-volume ratio [16–21]. Various nanostructured metal oxides like CdO nanoparticles [16], α-Fe_2O_3 nanorods [17], SnO_2 nanotubes [18], In_2O_3 nanowires [19], CuO nanoribbons [20] and ZnO nanorods [21] have been evaluated as gas sensing materials during the past few years. There are only few studies reported on the gas sensing properties of nanostructured Co_3O_4 [3, 22]. A two-step polyol process to synthesize nanostructured Co_3O_4 with different morphologies such as nanoplates, well-organized cabbage like structures and microspherical composites was reported recently by Cao *et al* [22]. The authors investigated the CO and alcohol sensing properties of the synthesized nanostructured Co_3O_4. The synthesized nanostructured Co_3O_4 exhibited good sensitivity (>8-50 ppm), response and recovery times (<10 s), remarkable selectivity and high stability to alcohol at an operating temperature of 300 °C. However, it was found to be insensitive to 50 ppm CO at 300 °C and the resistance change was still at a much lower level for 1000 ppm of CO. Li *et al* [3] prepared Co_3O_4 nanotubes by thermal decomposition of $Co(NO_3)_2.6H_2O$ within an ordered porous alumina template and investigated the gas sensing characteristics of these nanotubes exposed to H_2 and alcohol. The prepared Co_3O_4 nanotubes exhibited excellent sensitivity to hydrogen and alcohol at room temperature.

Similarly, Co_3O_4 is very well known for its use as a catalyst in various reactions such as CO and hydrocarbon oxidation [2,23–25], Fischer-Tropsch synthesis [26], NO decomposition [27], H_2O_2 decomposition [28], etc. Oxidation is one of the most important process step for producing fine chemicals from petroleum and vegetable feedstocks [29]. Selective oxidation of hydroxyl group of alcohols to aldehyde is the most common step in oxidation reactions, and varieties of techniques for carrying out this reaction are known [30].

Oxidation products of alcohols such as aldehydes and carboxylic acids are versatile intermediates in a variety of synthetic transformation in organic synthesis. For the oxidation reactions, in general, the stoichiometric oxidants such as permanganate and dichromate are being used. But their usage has to be avoided since they are expensive, toxic and produce large amounts of waste [23, 31]. Therefore, use of molecular oxygen is preferred as an environmentally acceptable, selective and strong oxidant for liquid-phase oxidation reactions. In the case of oxidation reactions, heterogeneous catalytic oxidation is more acceptable because of inherent advantages of ease of separation, recovery, recycling, and amenability for continuous processing as compared to the homogeneous counterparts [32].

This section describes the synthesis and characterization of a molecular precursor cobalt hydroxy carbonate having controlled rod shaped morphological features. The corresponding oxide, Co_3O_4, was formed with same morphological features as that of the precursor after calcination in air. The techniques such as microanalysis (MA), thermogravimetric analysis (TGA), X-Ray diffraction (XRD), high resolution transmission electron microscopy (HRTEM), Brunauer-Emmet-Teller (BET) surface area, X-Ray photoelectron spectroscopy (XPS), infrared (IR) and magnetic measurements have been employed for the characterization of the material. The as-prepared cobalt oxide in the form of nanorods was tested for the gas sensing properties as well as in catalytic oxidation reactions.

3.1.1 Molecular Precursor Cobalt Hydroxy Carbonate

Remarkable progress for synthesizing Co_3O_4 nanostructures with various morphologies have been reported in the literature [33–35]. There are several chemical methods available for the synthesis of Co_3O_4 nanostructures, including microemulsion [36], spray pyrolysis [37], hydrothermal [38], reduction/oxidation route [39], homogeneous or heterogeneous precipitation of precursor particles [40–44] followed by calcination in air, etc. Among all the reported methods, synthesis of novel nanostructures from coprecipitated molecular precursors is a very convenient method, which can help to control the morphology of nanostructures of Co_3O_4 by precipitating a suitable precursor with desired morphologies. For the synthesis of Co_3O_4, cobalt hydroxy carbonate is a desirable precursor, as no toxic byproducts are liberated during its pyrolysis in air [45, 46]. In most of the reported precipitation routes to obtain cobalt hydroxy carbonate precursor, cobalt nitrate/chloride

solution is added to a solution containing excess precipitants like sodium carbonate, ammonium carbonate, sodium bicarbonate, a mixture of sodium carbonate and sodium hydroxide, etc, or vice versa to get the pH in the range of 7-9 [40–44]. Therefore, initial drastic pH variation during precipitation can not be avoided.

The existence of heterogeneous equilibria in the $Co(NO_3)_2$-Na_2CO_3-H_2O system [47,48] governs the characteristics of the precipitated cobalt hydroxy carbonate. The main problems/difficulties associated with the precipitation reaction are [43–46]: i) the samples synthesized at room temperature have poor crystallinity, ii) the spherical monodispersed nanosized particles produced during precipitation tend to aggregate randomly, iii) if cobalt nitrate and ammonium carbonate are used as starting chemicals then soluble complexes of the type $[Co(NH)_3]^{2+}$ are formed if pH > 8, iv) if $Co(NO_3)_2$ and Na_2CO_3 solutions are mixed together to precipitate cobalt hydroxy carbonate, then, depending on the conditions of coprecipitation, the precursors with different OH^-/CO_3^{2-} ratios are obtained, and v) there is possibility of precipitation of $Co(OH)_xCl_{2-x}.nH_2O$ or chloride containing carbonates of the type $Co(OH)_xCl_y(CO_3)_{0.5(2-x-y)}.nH_2O$ along with cobalt hydroxy carbonate if proper pH is not maintained during precipitation and when cobalt chloride is used as the starting chemical during precipitation. Therefore, it is very important to perform a precipitation reaction with a suitable starting material and in a controlled manner to avoid the problems described above and to optimize the synthesis conditions to get precursors with reproducible properties. By this way, one can avoid the drastic change in the pH during the precipitation reaction [49]. Another important aspect to be taken into consideration is the formation of nanomaterials with high porosity and with specific morphology for many technological applications like sensors [50, 51], Li-ion batteries [52, 53], catalysis [54, 55], solar cells [56], etc. For the synthesis of the precursor, cost effective and pollutant free methods are preferred. Template free method which involves the oriental attachment of particles, in a desired manner, is a right alternative [57, 58]. Oriental attachment of nanocrystalline particles can be obtained by controlled aggregation [59]. Therefore, optimization of synthesis condition is a crucial step to get the desired precursor with controlled morphology.

Coprecipitation/digestion method has been reported for the synthesis of nanocrytalline oxides [49, 60, 61]. It helps to enhance the solubility product of the cations during pre-

cipitation, to a limited extent. As a result of the better solubility products of the cation, improvement in the crystallinity can be attained for the material at a much lower temperature with controlled physical and chemical characteristics by the controlled aggregation process. Otherwise, the product formed is reported to be amorphous [60, 61].

From the solubility diagram reported by Lewis *et al* [48], in the case of cobalt-water-carbonate system, water-free cobalt carbonate is precipitated above 160 °C. However, cobalt hydroxy carbonate is preferentially precipitated at room temperature in the pH range 7.5-9.0. It has been reported that the cobalt hydroxy carbonate precursor particles are not well crystallized at room temperature [43]. Considering these reported observations, co-precipitation/digestion has been carried out at 70 °C in the pH range of 7–8. The pH range has been selected in such a way that supersaturation leads to homogeneous fast nucleation with controlled growth of particles. Synthesis of the metal-hydroxide-carbonates usually involves precipitation reaction at a constant pH in the range of 7–9 [41, 42, 44].

3.1.2 Synthesis

Nanocrystalline Co_3O_4 powder was synthesized by the coprecipitation/digestion method as described in *section 2.1.1*. Analytical grade $Co(NO_3)_2.6H_2O$ and K_2CO_3 were used as the starting materials. Initially, 200 ml of distilled water was taken in a three-necked round bottom flask (RBF) and purged with argon gas for 1 hour to remove the excess oxygen present. The distilled water was then slowly heated to 70 °C on a heating mantle. Burettes having equal volume of water solutions of $Co(NO_3)_2$ (0.0339 M) and K_2CO_3 (0.0627 M) were connected on the two necks of the RBF, while a water condenser was connected to the third neck. The two solutions were added simultaneously to the water heated in the RBF. Concentrations of the acidic and basic solutions were calibrated through trial experiments for maintaining the pH in the range 7–8. The precipitate obtained after completion of addition was digested in the mother liquor, at the same temperature, for 8 hours. The precipitate formed was thoroughly washed with distilled water, several times, to avoid K^+ ion contamination and further dried in an oven at 70 °C and labeled as CC-A.

The as-prepared precursor CC-A was calcined at different temperatures at 300 °C (CC-300), 500 °C (CC-500), 600 °C (CC-600) and 750 °C (CC-750) for 5 hours each

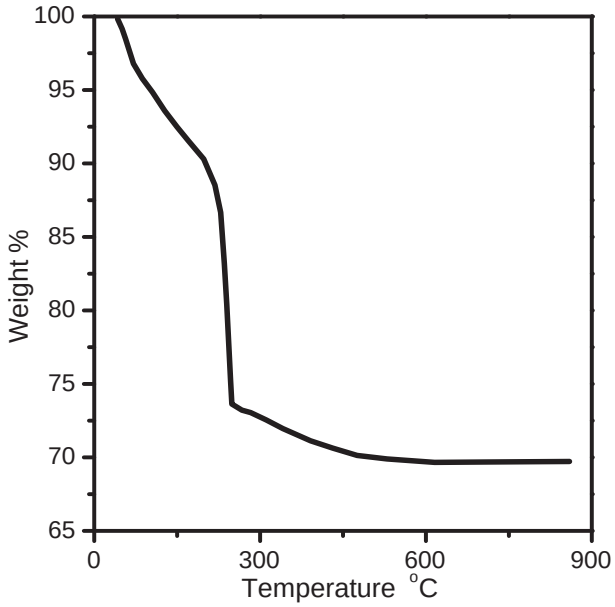

Figure 3.1: TGA curve of the precursor

in air, to obtain the oxide. Two commercial, analytical grade (Aldrich, Fluka) Co_3O_4 samples of purity >99% are also used at different stages for comparison of the results on the present samples.

3.1.3 Characterization

3.1.3.1 Thermogravimetry and Microanalysis

When potassium carbonate and cobalt nitrate solutions are dropped to distilled water kept at 70 °C, the following chemical reaction occurred to precipitate cobalt hydroxy carbonate precursor at pH ∼7–8.

$$Co^{2+} + xOH^- + yCo_3^{2-} + zH_2O \rightarrow Co(OH)_x(CO_3)_y.zH_2O \downarrow \quad (3.1)$$

To confirm that the precipitate formed is cobalt hydroxy carbonate and to determine its composition, microanalysis and thermogravimetric analysis (TGA) are carried out. Figure 3.1 depicts the TGA curve, which shows a total weight loss of 30.01% in three steps. Based on the weight loss obtained from the TGA as well as %C and %H from

Table 3.1: Microanalysis data on cobalt hydroxy carbonate

Element	Experimental Value (%)	Theoretical Value (%)
C	5.5	5.21
H	1.1	1.09

microanalysis, the molecular formula is estimated as $Co(OH)_{1.0}(CO_3)_{0.5}.0.11H_2O$. The experimentally observed total weight loss of 30.01% of the as-dried precursor is in good agreement with that of theoretically calculated weight loss ∼30.19 % for a compound having formula $Co(OH)_{1.0}(CO_3)_{0.5}.0.11H_2O$. Also, the %C and %H calculated from the estimated formula is in good agreement with the %C and %H (CH) obtained by micro-analysis. The CH analysis data is given in Table 3.1. The decomposition of the precursor occurs in air by reaction shown in equation 3.2.

$$3Co(OH)_{1.0}(CO_3)_{0.5}0.11H_2O + \frac{1}{2}O_2 \rightarrow Co_3O_4 + 1.83H_2O + 1.5CO_2 \uparrow \quad (3.2)$$

There is a three step weight loss as shown in the Figure 3.1. The first weight loss can be attributed to the removal of the hydrated water molecules in the material. The major loss in the second step, which is sharp, is due to the simultaneous removal of the structural water and carbondioxide by dehdroxylation and decomposition of carbonate anions and the final loss taking place at the third step could be due to the removal of surface hydroxyl groups [62] or it can be due to the better crystallinity of the precursor, which shows the dehydroxylation and decomposition of carbonate ions in a wider temperature range [43].

3.1.3.2 X-Ray Diffraction

Figure 3.2 shows the XRD pattern of the precursor. The as-dried sample shows good crystallinity as evidenced by the well defined peaks in the XRD pattern. The relatively broader peaks indicate nanocrystalline nature of the sample. All characteristic reflections reported by Xu *et al* [43] for the orthorhombic cobalt hydroxy carbonate phase are seen in the XRD pattern of the as-dried precursor. The orthorhombic lattice parameters are obtained as a =8.83 Å, b =10.16 Å, and c = 4.42 Å, (JCPDS # 48–0083) from refinement of the XRD pattern based on the space group $P22_12$ [43], using the computer program

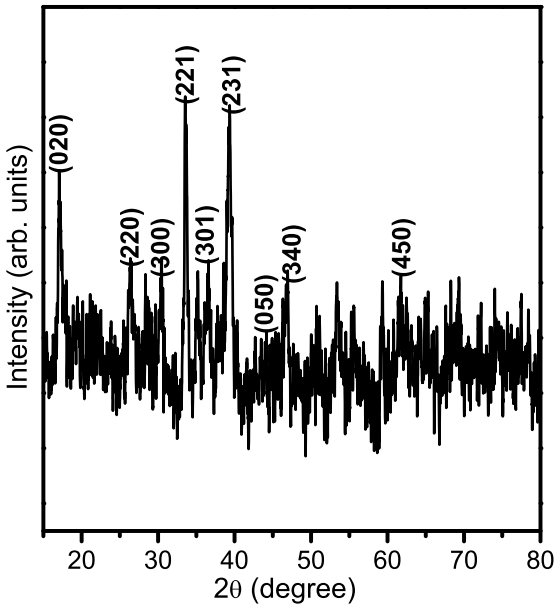

Figure 3.2: Powder XRD pattern of the precursor CC-A

CELREF [63]. Thus, the XRD result confirms that the molecular precursor formed is cobalt hydroxy carbonate $Co(OH)_{1.0}(CO_3)_{0.5}.0.11H_2O$ (CC-A).

The material calcined at different temperatures were subjected to XRD analysis for the phase analysis and the results are shown in Figure 3.3. For comparison, the commercial chemical grade Co_3O_4 from Aldrich and Fluka are also studied. The experimental patterns are compared with the simulated pattern of Co_3O_4. The powder pattern is simulated using the space group Fd3m and the corresponding cubic lattice parameter a = 8.0830 Å (JCPDS # 09-0418). It is clearly evident from the XRD data that the peaks are broad for CC-300 and the peak broadening decreases with increase in the calcination temperature. It is reflected in the decrease in the crystallite size calculated from the value obtained from the full width at half maximum of the most intense peak, using the Scherrer formula. The lattice parameter and crystallite size of the Co_3O_4 samples calcined at different temperatures and the bulk are given in Table 3.2. The calculated values are in good agreement with the reported value for Co_3O_4 (a = 8.083 Å; JCPDS # 09–0418).

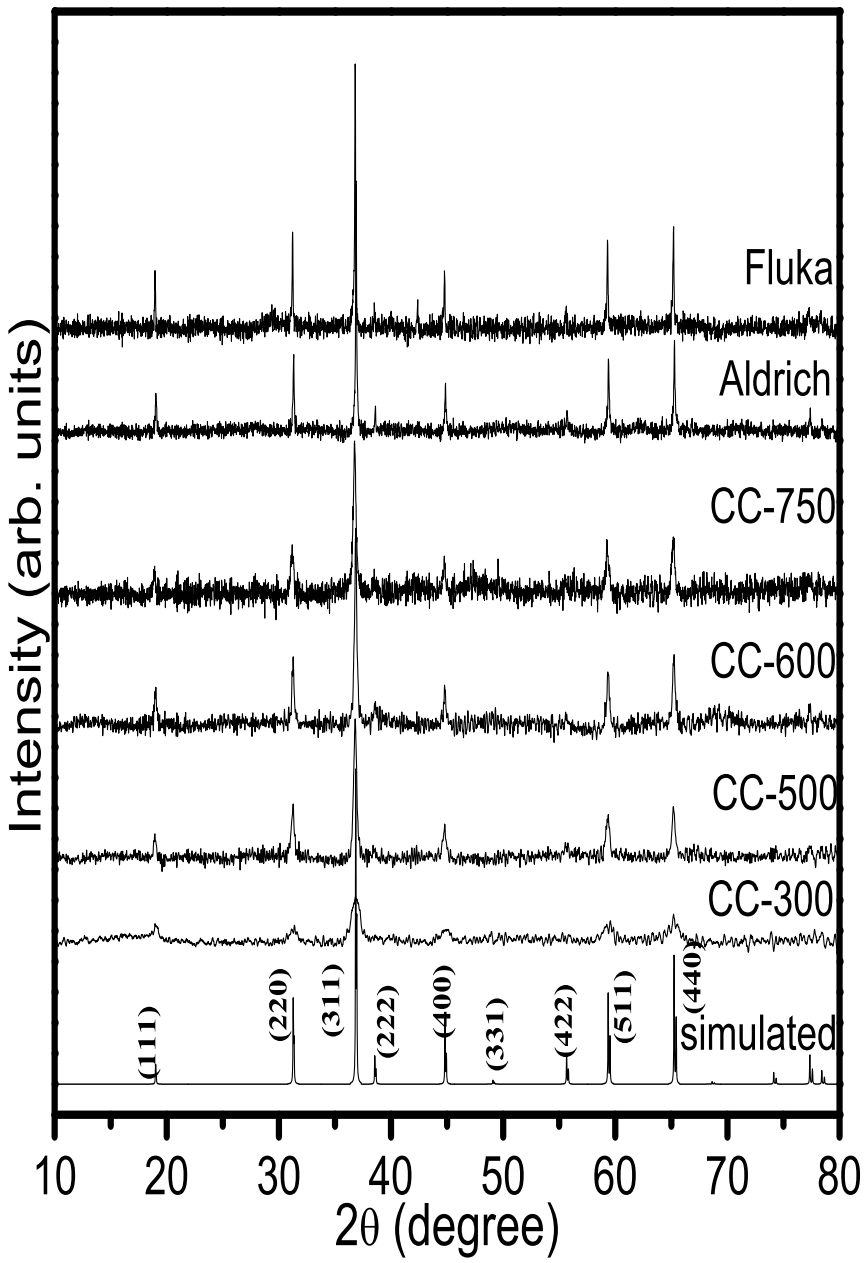

Figure 3.3: Comparison of the powder XRD patterns of the different Co_3O_4 and the commercial samples with the simulated pattern of Co_3O_4.

Table 3.2: Crystallite size and lattice parameter of Co_3O_4 calcined at different temperatures and commercial Co_3O_4.

Sample code	Crystallite size (±1 nm)	Lattice parameter (Å)
CC-300	11	8.0833
CC-500	29	8.0864
CC-600	33	8.0869
CC-750	44	8.0853
Aldrich	25	8.0825
Fluka	< 100	8.0826

3.1.3.3 HRTEM Studies

Figure 3.4 shows the HRTEM images of the precursor CC-A. It is very clear from the image that there is a formation of rod-like particles with 10-15 nm diameter and length of around 20-30 nm. For better understanding the images has been taken at different areas. From the circled areas in Figure 3.4 (a), it is very clear that there are some spherical primary particles of size 2-4 nm. Probably the nanorods are formed by the oriental attachment of the primary particles. Owing to the nanoscale nature of the as-dried sample, only weak diffraction rings are observed in the selected area electron diffraction (SAED) pattern of the aggregated nanorods, indicating polycrystalline nature of the sample. The microstructural information suggests controlled oriental aggregation of nanoparticles of cobalt hydroxy carbonate precursor to form nanorods. The main driving force for the oriental attachment of precursor particles can be attributed to the tendency of particles for reducing high surface energy through the attachment among the primary sparingly soluble precursor particles to give oriental aggregation at grain surfaces. Here, possibly the carbonate ions acts as a structure directing agent, as reported [40, 64, 65]. Carbonate ion can act as an inhibitor that selectively decreases the rates of crystal growth along both [001] and [110] directions, resulting in the [010] elongated nanorods [43, 66].

The HRTEM images of Co_3O_4 particles (CC-300 and CC-600) shown in Figure 3.5 indicate that rod type aggregates (diameter $\approx$ 6-8nm, length $\approx$ 20-30 nm) are probably constructed from 2-3 nm primary particles. In addition to this, some well-bound rods of length $\sim$30 nm are also seen in the images of the sample CC-300, confirming the presences of well defined nanorods also. It is clearly seen from the image that the aggregated Co_3O_4

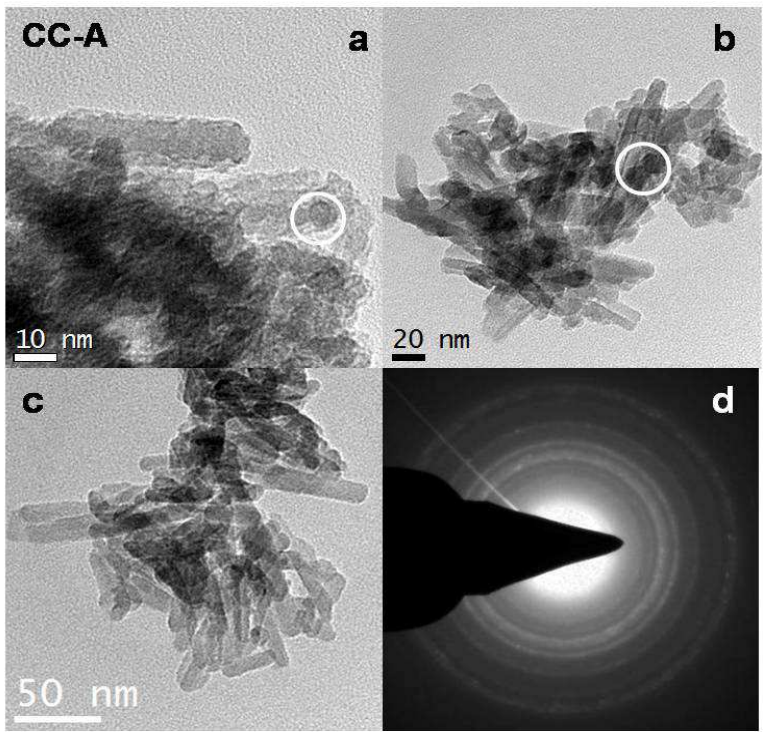

Figure 3.4: HRTEM images of the precursor CC-A along with the SAED pattern

rod like particles are composed of many small Co_3O_4 nanoparticles, which indicates that the Co_3O_4 nanoparticles are assembled in to Co_3O_4 nanorods in the same fashion as in the case of the cobalt hydroxy carbonate precursor. This particular observation indicates that the same aggregated rod type morphological features of cobalt hydroxy carbonate precursor particles are preserved in the corresponding spinel type Co_3O_4 aggregated particles. Also, it is evident from Figure 3.5, that with increase in the calcination temperature of the sample from 300 °C (CC-300) to 600 °C (CC-600) the rod length is also increased. The possible reason could be the fusing of smaller spherical particles together with the increase in the thermal energy. In both the cases, the ring-type SAED patterns reflect the polycrystalline nature of the material. To prove that the obtained morphological features of the sample CC-300 is based on the precursor, the HRTEM images of the commercial sample (Aldrich) are shown in Figure 3.6. Hexagonal-shaped plate-like particles are seen in the micrographs. Single crystalline nature of the sample is proved by the SAED pattern which shows a spot-like pattern.

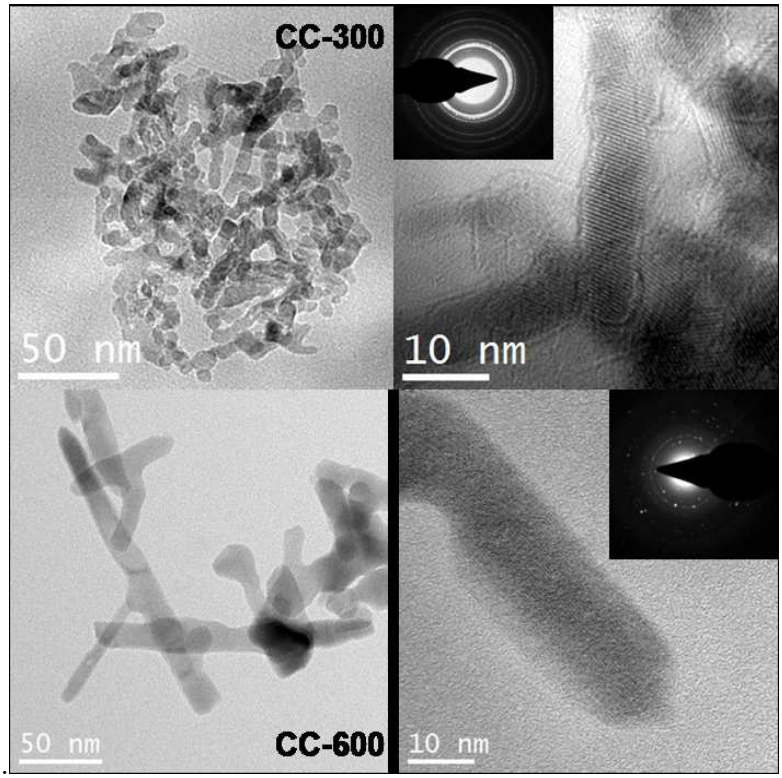

Figure 3.5: HTREM images of CC-300 and CC-600 with the corresponding lattice fringes and SAED patterns on the right side.

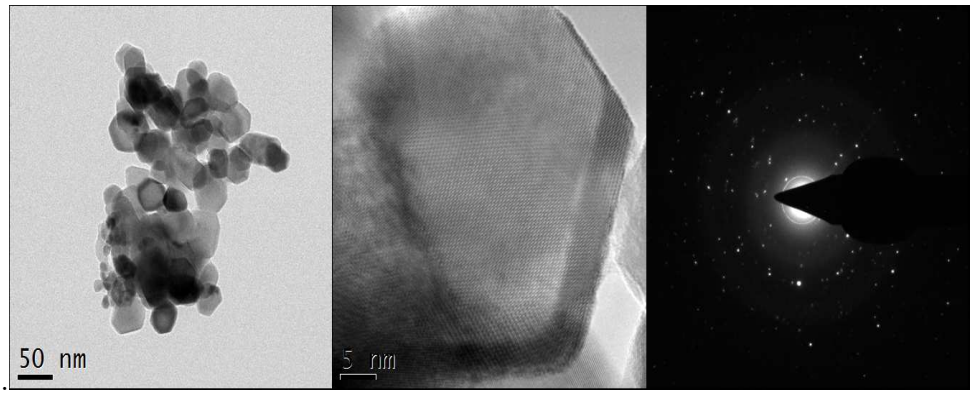

Figure 3.6: HTREM images and SAED pattern of the Aldrich Co_3O_4.

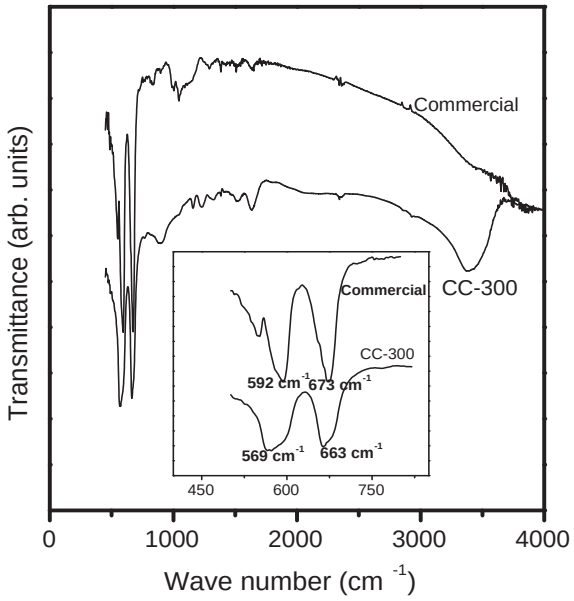

Figure 3.7: FTIR spectra of CC-300 and the commercial Fluka sample . Inset: Enlarged spectra showing the details of the Co-O vibrations.

3.1.3.4 Infrared Spectroscopy

To further confirm and support the structural information obtained from XRD studies, FTIR spectra were recorded on some of the samples. Figure 3.7 shows the FTIR spectra of the present nanostructured Co_3O_4 and a commercial Co_3O_4 sample (Fluka). Co_3O_4 is a normal spinel with the Co^{2+} ions occupying the tetrahedral sites and low-spin Co^{III} ions in the octahedral sites. The appearance of two distinctive bands around 680 cm^{-1} and 600 cm^{-1}, originating from the stretching vibration of the metal-oxygen bond, is a confirmation for the spinel oxide Co_3O_4 [67,68]. These two bands are due to the ν_1 and ν_2 vibrations of the low spin Co^{III} in the octahedral sites. For the commercial sample, the IR spectra shows two bands at 674 cm^{-1} and 593 cm^{-1}, due to the Co^{III}-O vibrations. However, for the sample CC-300, both these bands show some splitting. The ν_1 band is split in to two, with a major band at 663 cm^{-1} and a shoulder at 675 cm^{-1}. Similarly, the ν_2 band gives rise to a major band at 570 cm^{-1} and a shoulder at 593 cm^{-1}. That is, apart from the bands due to the Co^{III}-O vibrations which are observed as shoulders, major bands are observed at lower wave numbers, indicating some changes taking place

Table 3.3: Surface areas of CC-300, 600, 750, compared with that of the Aldrich sample.

S.No	Sample code	Surface area (m^2/g)
1	CC-300	95.20
2	CC-500	72.60
3	CC-600	59.36
4	CC-750	34.03
5	Aldrich	10.00

in the Co environment. This can be due to large number of defects at the surface or changes in the spin state of Co such as presence of intermediate spin or high spin Co^{3+} ions. These defect sites or new spin states of Co are likely to give rise to highly active surfaces in the nanostructured material [69].

3.1.3.5 Surface Area and Porosity

Polycrystalline oxide materials with very high surface area and sharp pore size distribution are potential candidates for many technological applications. To get information about the surface area and nature of the pores, the Co_3O_4 powders calcined at different temperatures such as 300 °C, 600 °C and 750 °C were subjected to the Brunauer-Emmett-Teller (BET) surface area measurements. The N_2 adsorption-desorption isotherms and pore size distribution curves of the three samples are shown in Figure 3.8. The surface area values corresponding to the Co_3O_4 nanorods calcined at different temperatures are given in Table 3.3.

From the surface area values given in Table 3.3, it is clear that the surface area is decreased as the calcination temperature is increased. The decrease in the surface area for the samples calcined at higher temperatures is due to the sintering of the particles. The adsorption isotherms with hysteresis is of type IV [70], indicating porous structure of the material. The sharp pore size distribution obtained for CC-300 from Barret-Joyner-Halenda (BJH) desorption studies indicates a number of pores of size less than 15 nm. The average pore diameter of CC-300 is obtained as 15.4 nm with a total pore volume of 0.367 cm^3/g. The surface area of the rod shaped Co_3O_4 CC-300 is found to be 95.2 m^2/g against 10 m^2/g for commercial Co_3O_4. The large surface area for CC-300 is probably due to the pores of nanorods and the inter-nanorod spaces since they are aggregated in

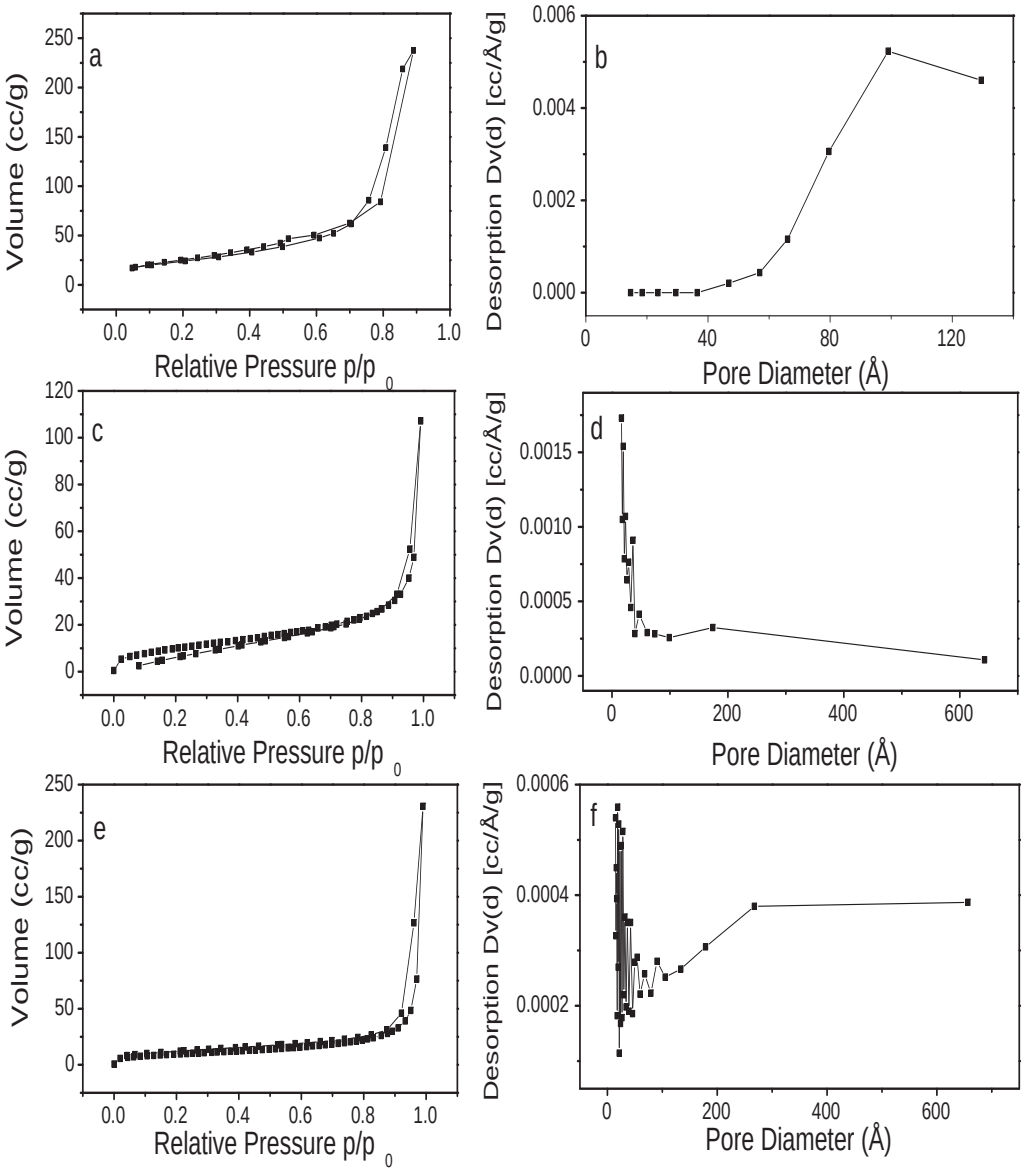

.

Figure 3.8: BET isotherms and pore size distributions of CC-300 (a,b), CC-600 (c,d), and CC-750 (e,f).

to large clusters.

The surface area of CC-300 is much larger than the reported values of 54 m^2/g for 8-13 nm particles [69] and 87.1 m^2/g for 10-20 nm particles [71] for Co_3O_4 nanoparticles obtained after calcination (calcined at 300 °C) of the hydroxy carbonate synthesized by the precipitation of cobalt nitrate and ammonium carbonate at room temperature and at 70 °C, respectively. Thus, the high BET surface area and large pore volume support the fact that the Co_3O_4 aggregated particles have a highly porous structure. The absence of any peak at low angles in the XRD pattern of Co_3O_4 suggested absence of ordered pore structure within the material. Therefore, these aggregated particles have a non-ordered porous structure.

3.1.3.6 X-ray Photoelectron Spectroscopy

The information about the oxidation state of a material can reveal the details about the environment of cations in the structure. For example, in case of Co_3O_4 spinel, the presence of both 2^+ and 3^+ ions can be confirmed by X-ray photoelectron spectroscopy (XPS) studies. In general, upon changes in the oxidation state, changes in the XPS binding energy (BE) can be expected from the chemical effects. In some case like vanadium [72] and tungsten oxides [73], a linear dependence of BE value has been observed on the change in the oxidation states of the metal ions. However, in the case of cobalt, the BE value of inner-shell electrons of Co^{3+} ions is smaller than that of Co^{2+} ions. It can be due to the smaller effective charge due the higher degree of covalency of the bonds. For the spinel type cobalt oxide, the energy separation between Co $2p_{\frac{3}{2}}$ and Co $2p_{\frac{1}{2}}$ is approximately 15.1 eV [74].

Figure 3.9 shows the XPS spectra of CC-300 and commercial samples from Aldrich and Fluka. The binding energy separation of all the three samples shown in Figure 3.9 are in agreement with the literature values. The XPS spectrum of CC-300 shows two major peaks with binding energy values of 780.3 eV and 795.4 eV, corresponding to Co $2p_{\frac{3}{2}}$ and $2p_{\frac{1}{2}}$ core levels, respectively, of the Co_3O_4 phase [75,76]. The formation of Co_3O_4 is further confirmed by the presence of a weak satellite peak between the main peaks Co $2p_{\frac{3}{2}}$ and Co $2p_{\frac{1}{2}}$ [77,78]. The typical satellite peak is observed at a binding energy value of 789.6 eV, about 9.03 eV higher than the BE of Co $2p_{\frac{3}{2}}$. Lack of prominent shake-up

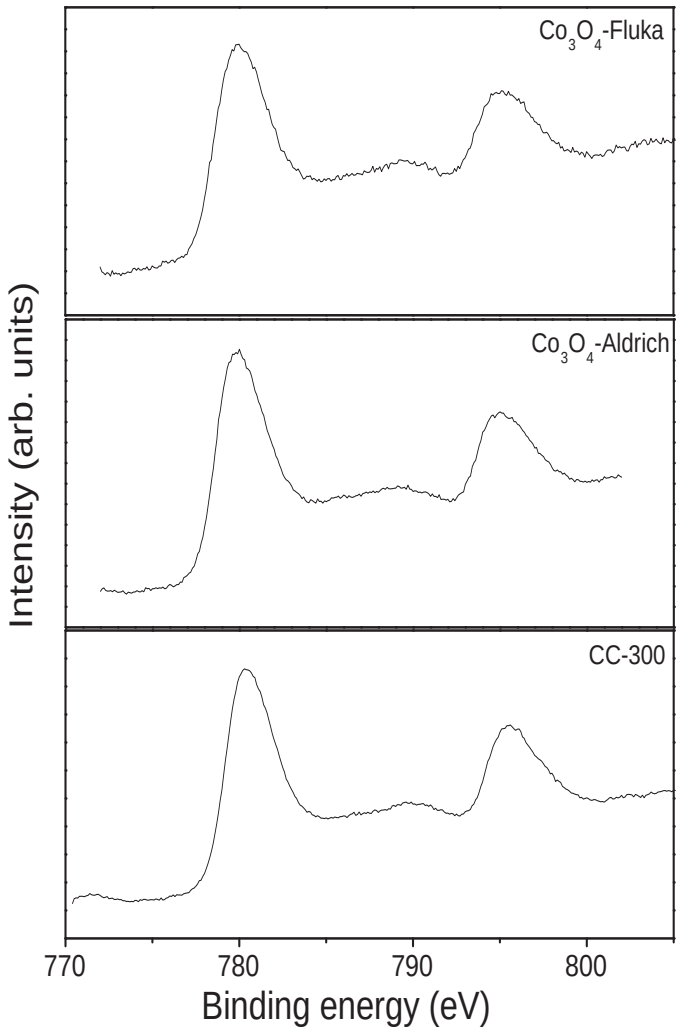

.

Figure 3.9: XPS of CC-300 along with the commercial samples from Aldrich and Fluka.

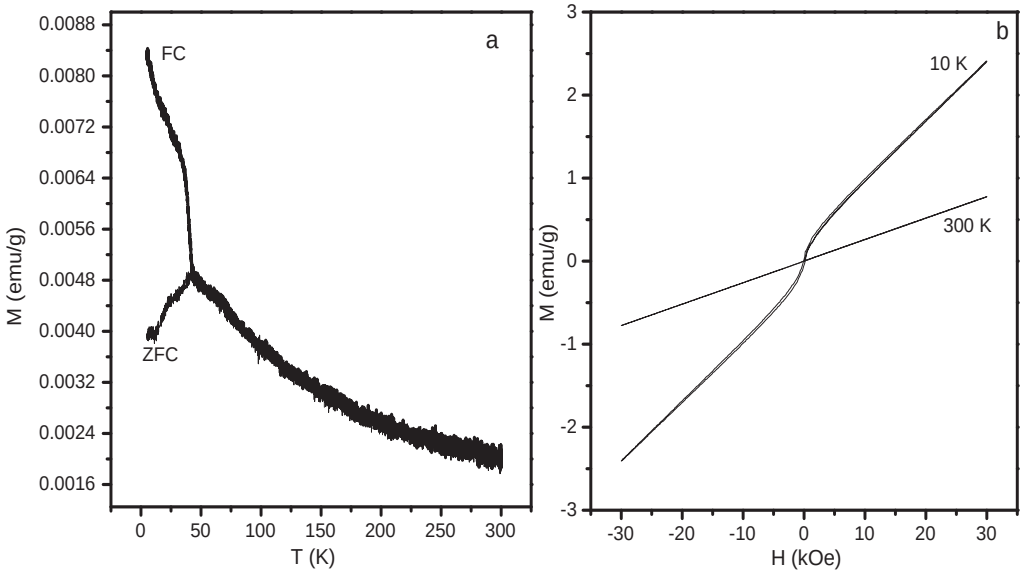

.

Figure 3.10: (a) ZFC and FC curves of CC-300 (H = 100 Oe), (b) M vs H curves at 10 K and 300 K.

satellite peaks in the Co 2p spectra further suggests the presence of mainly Co_3O_4 phase. The Cobalt compounds of valence 2+ are paramagnetic and have a strong satellite peak around 6 eV above the Co $2p_{\frac{3}{2}}$ line, where as Co^{III} does not show any satellites. The mixed valence Co_3O_4 has a weak satellite that characterizes the minor component Co^{2+}. Thus the XPS measurement confirms the formation of Co_3O_4.

3.1.3.7 Magnetic Measurements

The temperature dependence of magnetization was measured to investigate the magnetic behavior of the porous Co_3O_4 nanorods. Bulk Co_3O_4 is a normal spinel with the Co^{2+} ions in the tetrahedral site and the low-spin Co^{III} ions distributed in the octahedral site of the spinel lattice. Therefore, bulk Co_3O_4 is antiferromagnetic with a Neel temperature (T_N) of 40 K. Figure 3.10 shows the zero field cooled (ZFC) and field cooled (FC) magnetization behavior of CC-300. The FC and ZFC magnetization curves, measured in a field of 100 Oe, deviate below 41 K, with a sharp magnetic transition below this temperature, exhibiting typical characteristics expected for ferro- or ferrimagnetic materials [79]. The magnetic

transition is at the Neel temperature reported in the literature for Co_3O_4 [80–82]. Similar characteristics are reported for other antiferromagnetic materials when the particle sizes are reduced to nanometer sizes [83]. The deviation of FC and ZFC magnetizations below T_N suggests ferromagnetic interactions in the nanoparticles [84, 85]. The field dependent magnetization measurements shown in Figure 3.10 suggest that CC-300 is paramagnetic at room temperature. A small magnetic hysteresis loop is observed at 5 K, supporting this conclusion that weak ferromagnetic interactions are present in the nanoparticles. The weak ferromagnetism is possibly due to the presence of some intermediate or high-spin Co^{3+} ions in the octahedral sites and/or possible redistribution of the Co^{2+} and Co^{3+} ions in the tetrahedral and octahedral sites. Similar features are observed for other spinels such as nanosized $ZnFe_2O_4$, where the normal spinel structure changes to mixed spinel structure, giving rise to enhanced magnetic characteristics [86, 87]. Presence of high-spin Co^{3+} ions in the octahedral sites of Co_3O_4 is reported from electronic spectroscopic studies [88].

3.1.4 Application of Co_3O_4 Nanorods in CO Gas Sensing

The CO gas sensing experiments were performed at different temperatures in order to find out the optimum operating temperature for CO gas detection. Before exposing to the CO gas, the sensing element was allowed to equilibrate inside the gas chamber at an operating temperature for 1 h. A number of experiments have been carried out to measure the gas response as a function of the operating temperature. All the time, the gas response of the sensor element had approximately constant values, indicating the repeatability of the sensor. The effect of operating temperature on the gas response of CC-300 to 50 ppm CO gas is shown in Figure 3.11. The relationship between the gas response and the operating temperature exhibits a trend of "increase-maximum decay" behavior to 50 ppm CO gas. At low temperatures, the gas response is relatively low (e.g. 1.66 at 100 °C), but it increases rapidly with an increase in the operating temperature. At 250 °C , the gas response is peaked to its maximum value of 6.55. Above 250 °C, the gas response decreased as the operating temperature increased further. Thus, the optimum operating temperature for the CC-300 to detect CO gas is at 250 °C, which is better than the reported value of 300 °C [22]. Hence, to investigate the CO gas sensing properties

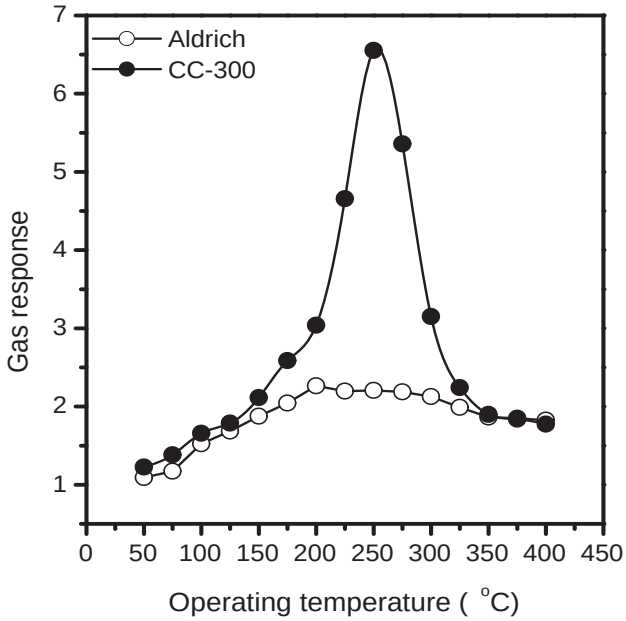

Figure 3.11: Effect of operating temperature on the gas response of CC-300 and commercial Co_3O_4 powder (Aldrich) to 50 ppm CO gas.

such as response and recovery characteristics, reproducibility and selectivity, 250 °C was chosen as the operating temperature.

When the commercially available Co_3O_4 powder is used, the gas response to 50 ppm of CO gas as shown in Figure 3.11 exhibits a broader maximum between the operating temperatures 200-300 °C with a maximum response of ∼2.20. It can also be seen that the gas response of CC-300 is about three times larger than that of the commercial Co_3O_4 powder, indicating the improved sensitivity of the CC-300 sample. These observations reveal that the CO sensing ability of Co_3O_4 is significantly enhanced when it is in the form of nanorods. The enhanced CO gas sensing performance of CC-300 over that of the commercial Co_3O_4 powder may be attributed to the smaller size and higher specific surface area. Generally, gas sensor response of metal oxide semiconductors increases with decrease in their size due to higher surface area and defect density [89]. The defect nature of CC-300 has already been confirmed from the shift in the bands towards lower wave number as shown in the FTIR spectra (inset of Figure 3.7).

The response and recovery characteristics are important for evaluating the performance

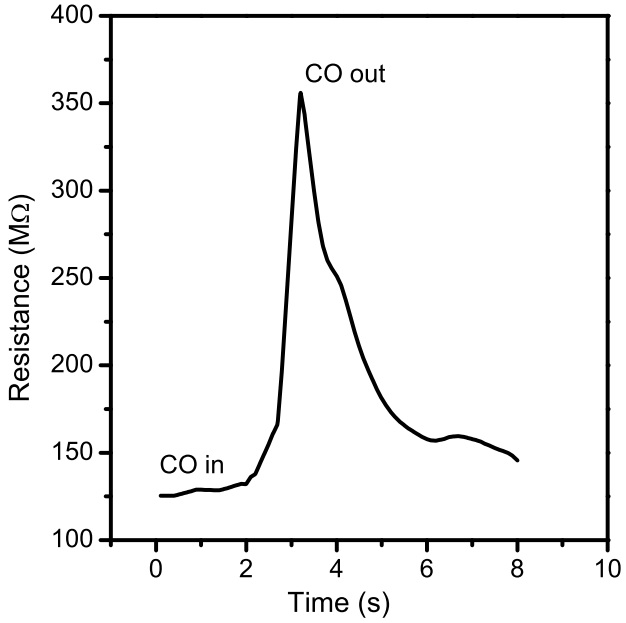

Figure 3.12: Response of CC-300 to 50 ppm CO gas at 250 °C.

of gas sensors. The response and recovery times are defined as the time required for the sensor's electrical resistance to change by 90% of the final resistance. The response and recovery characteristics of CC-300 sample to 50 ppm CO gas at the operating temperature 250 °C is shown in Figure 3.12. To check the reproducibility of the sensing characteristics, five samples were tested from each batch. Also, each sample was tested thrice. It was observed that the resistance of the sensing element increases when exposed to the CO gas. As can be seen from Figure 3.12, the sensor responds very rapidly after introduction of CO gas and recovers immediately when it is exposed to air. The CC-300 have response time of ∼3-4 s and the recovery time of ∼5-6 s. This behavior can be attributed to the higher surface-to-volume ratio of the nanorods.

The reproducibility and stability are important parameters to be considered when evaluating the performance of a gas sensor. It is useful to have both a stable base line resistance and a reproducible signal change to a given analyte concentration. The reproducibility and stability of CC-300 are measured by repeating the test four times. The gas response of the sample upon periodic exposure to 50 ppm CO gas at the operating tem-

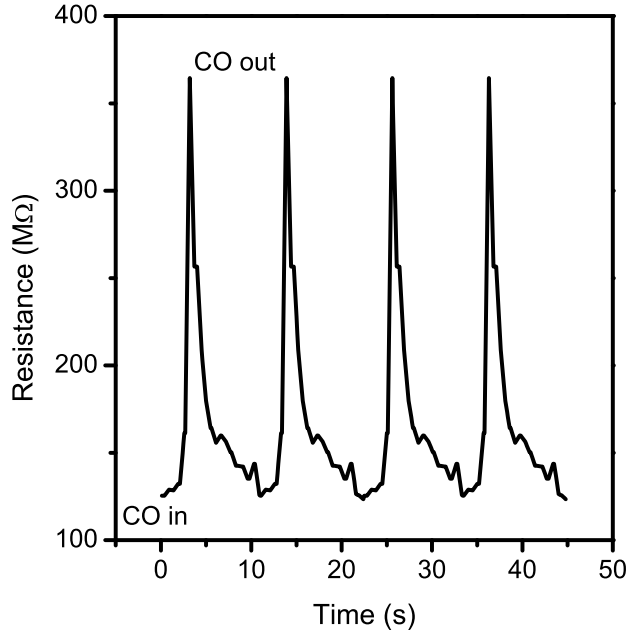

Figure 3.13: Repetitive response of CC-300 to 50 ppm CO gas at the operating temperature of 250 °C.

perature of 250 °C is shown in Figure 3.13. It shows good reproducibility and reversibility upon repeated exposure and removal of CO under the same conditions. Thus, the sample CC-300 exhibit good stability as well as an excellent repeatability of the response. This suggests that CC-300 can be used as a reusable sensing material for the detection of CO.

The dependence of the gas response of CC-300 nanorods on the CO gas concentration at the operating temperature of 250 °C is shown in Figure 3.14. It is observed that the gas response increases linearly up to 50 ppm of CO gas and thereafter the response saturates. It is found that the response of the sample can be empirically represented as $y = 2.91 + 0.0718x$, $R^2 = 0.9990$, where x, y and R^2 represents the CO concentration, gas response and correlation coefficient, respectively. The solid line in Figure 3.14 shows the linear fit to the experimental data, illustrating clearly good quality of the fit. The linear relationship between the gas response and the CO gas concentration at low concentrations (5-50 ppm) may be attributed to the availability of sufficient number of sensing sites to act upon the CO gas. The low gas concentration implies a lower surface coverage of gas molecules, resulting into lower surface interaction between the surface of the nanorods and

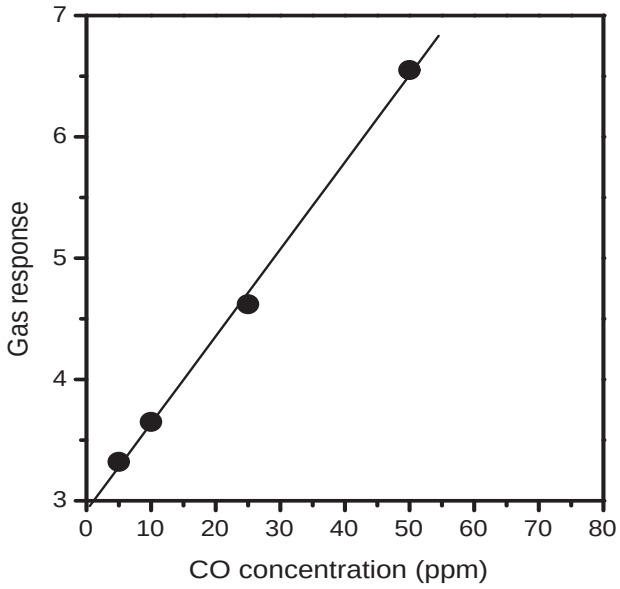

Figure 3.14: Relationship between gas response of CC-300 and CO gas concentration. The circles are experimental data and the solid line is the fit to the data, as discussed in the text.

the gas molecules. The increase in the gas concentration increases the surface reaction due to a large surface coverage. Further increase in the surface interaction will be gradual when saturation of the surface coverage of gas molecules is reached. Thus, the maximum gas response is obtained at the operating temperature of 250 °C for the exposure of 50 ppm of CO gas. The linearity of the gas response in the low CO gas concentration range (5-50 ppm) suggests that the sample can be reliably used to monitor the concentration of CO gas over this range.

Selectivity is an important parameter of gas sensors and it is the ability of a sensor to respond to a certain gas in the presence of other gases. Theoretically, sensors should have high response to some gases and little or no response to other gases in the same surroundings. To study the selective behavior of CC-300 to CO, at the operating temperature of 250 °C, the gas response towards H_2, liquid petroleum gas (LPG), CO_2 and ethanol with concentration 50 ppm each were also measured. The corresponding results are shown in Figure 3.15. The sample exhibit higher response to CO (6.55), whereas it shows a considerably lower response (< 3.51) to H_2, LPG, CO_2 and ethanol. The selectivity coefficient

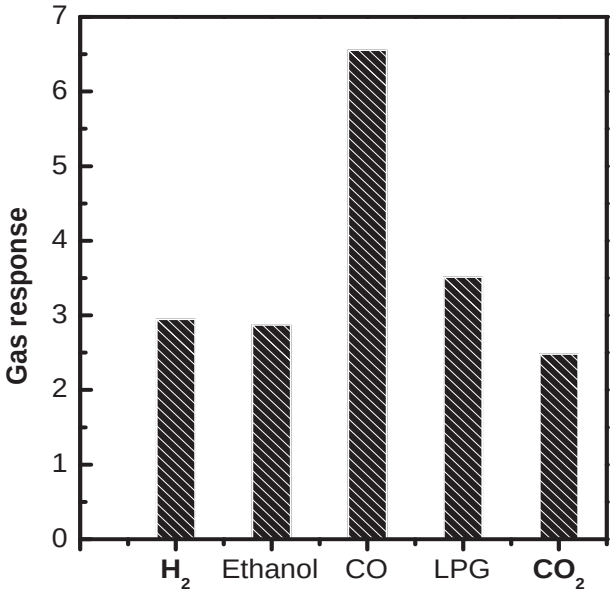

.

Figure 3.15: Bar chart showing the gas response of CC-300 for different gases. The gas concentration and operating temperature in all cases are 50 ppm and 250 °C, respectively.

(K) of CO to another gas is defined as [90]:

$$K = \frac{S_{CO}}{S_B} \tag{3.3}$$

where S_{CO} and S_B are the responses of sensors in CO and gas B, respectively.

The selectivity coefficients for CC-300 are 2.22 for H_2, 2.64 for CO_2, 1.86 for LPG and 2.28 for ethanol. Based on the observed results, it can be concluded that the CC-300 nanorods have good CO sensing properties such as higher gas response, good selectivity, short response time, fast recovery, excellent repeatability and lower operating temperature.

A possible mechanism to explain qualitatively the observed CO sensing properties of the sample is as follows. The sensing performance of semiconductor oxides is usually attributed to the adsorption and desorption of oxygen on the surface of the oxides. It is important to note that the trend in the changing resistance of the p-type semiconductor sensor with the concentration of the reducing gas is completely opposite to that of an n-type of sensor [13,14,91]. Co_3O_4 is a p-type oxide semiconductor and thus, its majority

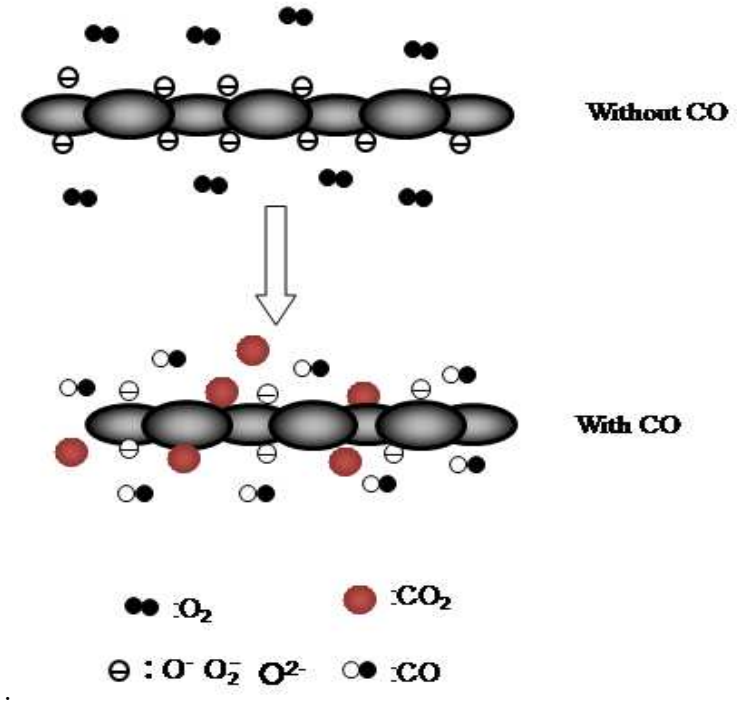

Figure 3.16: Schematic diagram of CO sensing process of the CC-300 nanorods.

carriers are holes. The CO sensing process is based on the changes in the resistance of Co_3O_4 which is controlled by the CO species and the amount of the chemisorbed oxygen on the surface [92, 93].

By considering only a single CC-300 nanorod, the sensing process of CO gas is schematically depicted in Figure 3.16. It is known that a certain amount of oxygen from air will be adsorbed on the surface of Co_3O_4. The adsorbed oxygen molecules capture free electrons from the nanorods and become oxygen anion species such as O^{2-} or O^-. The reaction kinematics may be explained by the following reactions [94, 95]:

$$O_2(gas) + e^- \rightarrow O^{2-}(ads)$$

$$O^{2-}(ads) + e^- \rightarrow O^-(ads)$$

$$2O^-(ads) + e^- \rightarrow O^{2-}(ads) \tag{3.4}$$

In these processes, there exists a transition temperature, $\sim$180 $^\circ C$, below which oxygen adsorbed on the surface is mainly in the form of O_2^-, where as above which chemisorbed oxygen dominates in the form of O^- and O^{2-} [96]. For Co_3O_4, the oxygen adsorption

produces an increase in the hole density in the valence band, which increases the conductivity. The electron transfer from the conduction band to the chemisorbed oxygen results into an increase in the hole density. As a consequence, an increase in the conductivity of Co_3O_4 is observed.

When the Co_3O_4 is exposed to reducing gases like CO, the reaction between CO and adsorbed oxygen (O^- or O_2^-) proceeds by Langmuir-Hinshelwood mechanism [97]:

$$CO_{gas} \rightarrow CO_{ads} \tag{3.5}$$

$$CO_{ads} + O^- \rightarrow CO_2 + e^- \tag{3.6}$$

This reaction decreases the hole density in the surface charge layer and increases the resistance of the CC-300 nanorods.

3.1.5 Application of Co_3O_4 nanorods in catalysis

The substrate chosen for oxidation reaction in this present study is veratryl alcohol. Veratryl alcohol is a model substructure of lignin. It is often used in studies of lignin degradation by enzymes. Oxidation of veratryl alcohol is well studied using the catalyst Co-Salen complex, using water as the solvent and molecular oxygen as oxidant [98, 99]. The proper activation of dioxygen under moderate reaction conditions requires a suitable catalyst and in many industrial processes, simple transition metal complexes are used as catalytic species [98]. With these catalysts, it is often difficult to combine high activity together with high selectivity [99].

Selective oxidation of veratryl alcohol to aldehyde with simple oxidants, such as cheap, abundant, and non-toxic dioxygen, would be an attractive alternative for producing products which have a great demand in chemical industry. Considering the above mentioned aspects, it was decided to study the nanostructured spinel type Co_3O_4 as a catalyst, as it consists of a redox couple and sufficient reactivity which can be tailored by controlling preparation conditions, compositon and structure. The schematic representation of veratryl alcohol oxidation is shown in Figure 3.17. Where the substrate veratryl alcohol (A in Figure 3.17) upon oxidation will get converted into veratryl aldehyde (B in Figure 3.17). Further oxidation of veratryl alcohol will end up with veratric acid (C in Figure 3.17)

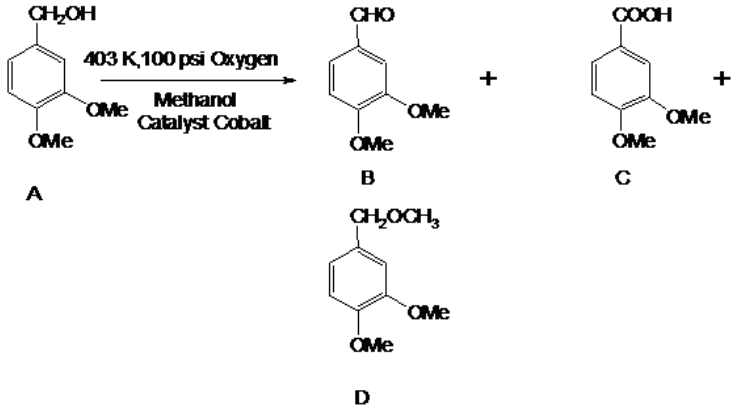

A-veratryl alcohol (3,4 dimethoxy benzyl alcohol)
B-Veratryl aldehyde(3,4 dimethoxy benzanldehyde)
C-Veratric acid (3,4 dimethoxy benzoic acid)
D-Veratric ether(3,4 dimethoxy benzoic methoxy ether)

Figure 3.17: Oxidation of veratryl alcohol to veratryl aldehyde by Co_3O_4 nanorod samples CC-300 and CC-500 and with commercial Co_3O_4 (Aldrich).

and ether (D in Figure 3.17). The product of interest, veratryl aldehyde, can be obtained by optimizing the synthesis conditions. The mixed valency along with presence of more active sites at the surface in the nanostructured Co_3O_4 can give rise to interesting oxidation properties. Hence the as-prepared porous CC-300 and CC-500 are studied for the oxidation of veratryl alcohol to veratryl aldehyde. For comparison, the commercial sample (Aldrich) was also tested under identical conditions.

In the present study, for a typical oxidation reaction, 0.5 gm of veratryl alcohol was taken in the solvent methanol. To this, 100 mg of the cobalt oxide catalyst (CC-300)was added and charged in an autoclave with a total capacity of 300 ml, as described in *section 2.2.8*. During the reaction the temperature was maintained at 130 °C, with the pressure 100 psi. Samples before and after reaction were collected and analyzed by HPLC. The results obtained during the oxidation reactions are given in Table 3.4

From the Table 3.4 it may be seen that maximum selectivity to veratryl aldehyde of 91% with 69% conversion is obtained for CC-300. Also, it is evident that selectivity towards the compound of interest, veratryl aldehyde, decreases with decreasing surface area as in case of CC-500 and the commercial sample. Hence, it may be concluded that porous Co_3O_4 nanorods (CC-300), with very high surface area, is a suitable catalyst

Table 3.4: Result of the activity of veratryl alcohol oxidation to veratryl aldehyde by using Co_3O_4 nanorods.

Catalyst	Surface Area m^2/g	Conv %	% selectivity			
			Veratryl Aldehyde	Veratric Acid	Veratric ether	Others
CC-300	95.2	69.0	91.0	1.12	6.16	1.12
CC-500	72.6	81.0	85.0	4.71	10.02	0.00
Bulk	10.0	13	58.47	0	0	41.53

showing good selectivity with a reasonable conversion for the oxidation of veratryl alcohol to veratryl aldehyde.

3.1.6 Conclusions

A simple and facile coprecipitation/digestion method is utilized to prepare porous Co_3O_4 nanorods through a molecular precursor approach. The obtained molecular precursor has a controlled growth with well-defined morphological features. The same morphological features are maintained in the corresponding Co_3O_4 formed after calcination of the precursor. The as-prepared porous Co_3O_4 was tested for its applicability in CO gas sensing as well as for the oxidation of veratryl alcohol to veratryl aldehyde. The nanorods exhibit better performance as a CO sensor at a moderate operating temperature of 250 °C, with fast recovery and response time. In the case of oxidation of veratryl alcohol to veratryl aldehyde, the nanorods show a reasonable conversion and selectivity with out using any base in the reaction.

3.2 Nanostructured $ZnCo_2O_4$

$ZnCo_2O_4$ is a cobalt based spinel oxide, where the divalent Zn ions occupy the tetrahedral sites in the cubic spinel structure and the trivalent Co ions occupy the octahedral sites. It offers a strong catalytic activity to some reactions such as the oxidation of the alkyl compounds and as effective low temperature absorbent of hydrogen sulphide [71,100,101]. Furthermore, nanostructured $ZnCo_2O_4$ is stable and active in alkaline solutions and it

is cheaper than noble metals [102]. Different methods such as typical coprecipitation [103], combustion method [104], sol-gel route [105], etc, have been proposed recently and developed to make zinc based spinel oxides in the form of nanoparticles.

There are few reports dealing with the study of the gas sensing properties of nanostructured $ZnCo_2O_4$. Chen *et al* [106] prepared MCo_2O_4 (M = Ni, Cu, Zn) nanotubes by using a template assisted method and investigated their gas sensing properties to Cl_2, NO_2, C_2H_5OH, SO_2 and CO. Du *et al* [107] synthesized ZnM_2O_4 (M = Fe, Co, Cr) by microemulsion method and studied the gas sensing properties to Cl_2, NO_2, C_2H_5OH, H_2S, and acetone.

It was found that porous Co_3O_4 nanorods synthesized from the single molecular precursor cobalt hydroxy carbonate showed outstanding CO sensing performance with high gas response, extremely rapid response time, fast recovery, excellent repeatability and good selectivity. Apart from good sensitivity for CO gas, LPG showed a better response value for 50 ppm gas at 250 °C. LPG is widely used as a fuel for domestic and industrial heating to provide a clean source of energy for burning. It is a combustible gas which mainly consists of butane (70–80%), propane (5–10%) and propylene, butylene, ethylene and methane (1–5%) [108]. It is potentially hazardous due to the high possibility of explosion and accidents caused by leakage or by human error. Hence, it is crucial to detect it in the early stages to give alarm and perform effective suppression [109]. This has stimulated considerable interest to develop reliable, efficient, simple and cost-effective chemical sensors to monitor LPG, having good sensitivity and selectivity. To study the effect of replacing Co^{2+} in Co_3O_4 by other divalent ions with fixed valency, zinc substituted cobalt spinel has been synthesized through the same synthesis method and its gas sensing performance was tested.

3.2.1 Synthesis

In a typical synthesis, 0.05 M zinc nitrate solution and 0.1 M cobaltous nitrate solution were mixed together. The mixed solution was added drop wise through a burette to distilled water kept at 70 °C in a three necked round bottom flask (RBF) fitted with a water condenser. Through another burette 0.22 M potassium carbonate solution was added simultaneously to precipitate the mixed nitrate solution. After precipitation, the mother

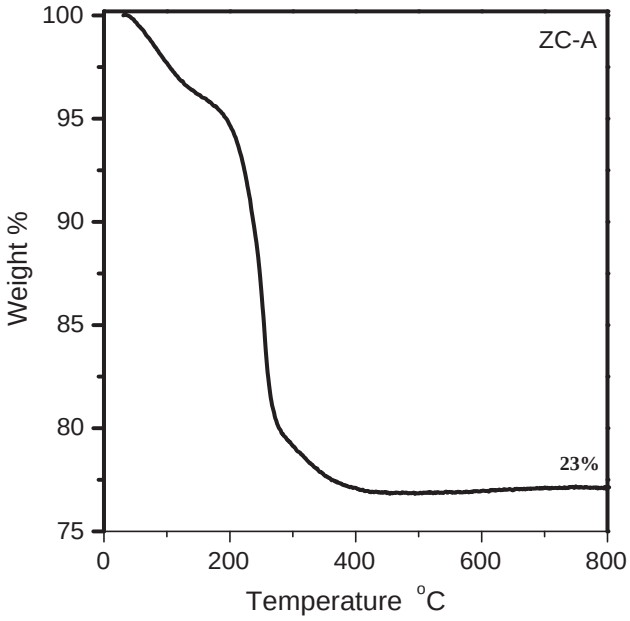

Figure 3.18: TGA curve of the precursor ZC-A.

liquor was allowed to digest for 8 hours. Then the precipitate was washed thoroughly with sufficient amount of distilled water to remove any K^+ ion contamination. The impurity free precipitate was kept in an oven at 70 °C overnight and labeled as ZC-A.

The as-prepared dried precipitate was calcined at different temperatures of 300 °C (ZC-300) 400 °C (ZC-400), 600 °C (ZC-600), and 800 °C (ZC-800), to study the effect of calcination temperature on the formation of $ZnCo_2O_4$. Preliminary studies on the gas sensing property of the calcined powders indicated better performance for the sample calcined at 600 °C (ZC-600). Hence, some of the characterization studies are made only on the sample calcined at 600 °C, to get detailed informations.

3.2.2 Characterization

3.2.2.1 Thermogravimetry and Microanalysis

A single molecular precursor cobalt hydroxy carbonate was obtained during the precipitation of cobaltous nitrate with potassium carbonate. It is reported that hydrated zinc hydroxy carbonate with a composition of $Zn_4(OH)_6(CO_3).2H_2O$ is precipitated at pH

Table 3.5: Microanalysis data on mixed precursor ZC-A

Element	Experimental value (%)	Theoretical value (%)
C	4.22	4.56
H	1.21	1.32

∼7.5-8.0 when zinc nitrate is precipitated with carbonate ions [110]. Hence, it is expected that when potassium carbonate, cobaltous nitrate and zinc nitrate solutions are separately dropped to stirred distilled water kept at 70 °C, the following chemical reaction may occur to precipitate a mixed precursor consisting of cobalt hydroxy carbonate and zinc hydroxy carbonate at pH ∼7.5-8.0.

$$Co^{2+} + OH^- + CO_3^{2-} + H_2O + Zn^{2+} \rightarrow Co(OH)_{1.0}(CO_3)_{0.5}0.11H_2O + Zn_4(OH)_6(CO_3) \tag{3.7}$$

Thermogravimetry (TGA) and microanalysis (MA) were carried out on the mixed precursor to get information on the decomposition behavior and its composition. The TGA curve of the mixed precursor is shown in Figure 3.18. The TGA curve of the as-prepared mixed precursor exhibits two major weight losses in the temperature range 30–200 °C and a minor weight loss in the 200-400 °C temperature region. The continuous loss in the first step can be assigned to the removal of adsorbed and hydrated water molecules. The second step, which is a major one, can be attributed to the decomposition of carbonate ions. The CH and TGA data are presented in Table 3.5 by considering the decomposition scheme shown by the equation 3.8.

$$2Co(OH)_{1.0}(CO_3)_{0.5}0.11H_2O + \frac{1}{4}[Zn_4(OH)_6(CO_3)] \rightarrow ZnCo_2O_4 + 1.25CO_2 \uparrow + 2.22H_2O \tag{3.8}$$

The CH analysis and total weight loss in TGA are consistent with the theoretically calculated CH and weight loss data assuming the composition of the mixed precursors.

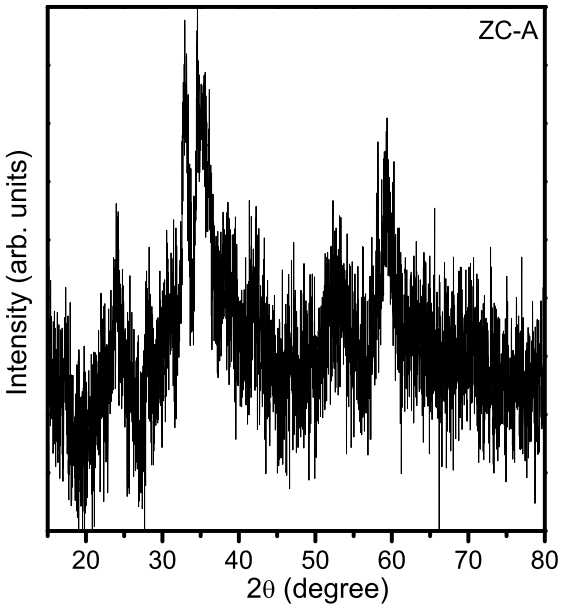

.

Figure 3.19: XRD pattern of the precursor ZC-A.

3.2.2.2 X-Ray Diffraction

Based on the thermal and micro analysis, the precursor has been identified as a mixture of cobalt and zinc hydroxy carbonates. Figure 3.19 shows the XRD pattern of the as-dried precursor. The pattern shows broad peaks. Major peaks of cobalt hydroxy carbonate (see Figure 3.2) is observed in the 2θ region where the broad peaks are observed for ZC-A. Moreover, the powder XRD pattern of $Zn_4(OH)_6CO_3.H_2O$ is shown [110] (JCPDS # 11-0287) to be similar to that observed for the ZC-A, suggesting that the precursor is likely to be a mixture of cobalt and zinc hydroxy carbonates.

XRD patterns of the calcined samples are shown in Figure 3.20. The simulated pattern of $ZnCo_2O_4$ generated based on the space group Fd3m and lattice $a = 8.0946$ Å (JCPDS # 23-1390) is also shown in the figure for comparison. The XRD patterns of the samples calcined up to 600 °C match well with the simulated pattern implying the phase purity of the material. Thus, from the XRD patterns, formation of spinel type $ZnCo_2O_4$ can be confirmed. For the sample ZC-800, some additional peaks are observed corresponding to ZnO as an impurity phase. All the single phase samples show broad peaks in the XRD

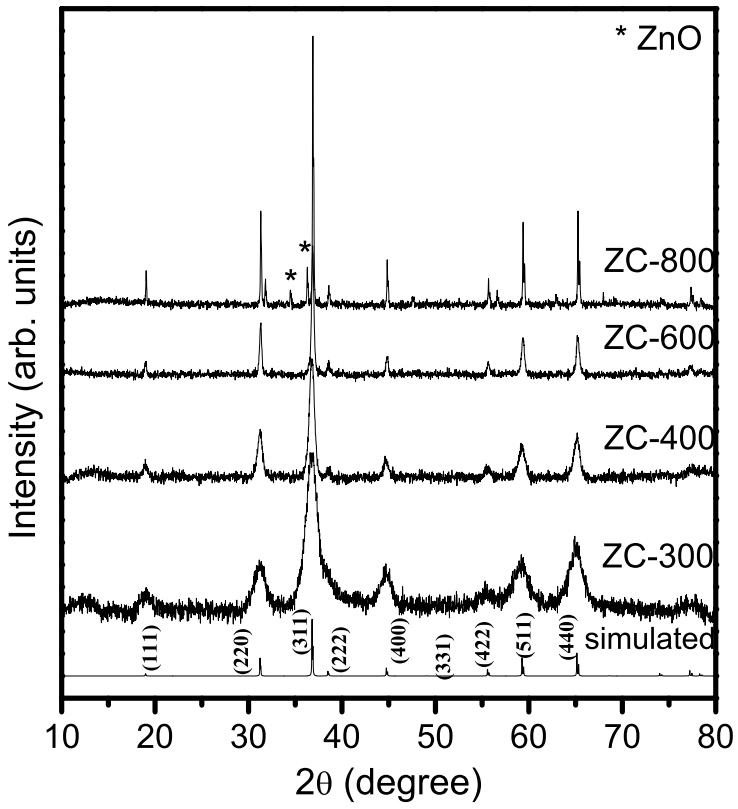

.

Figure 3.20: XRD patterns of the samples calcined at different temperatures.

patterns indicating the nanocrystalline nature of the samples. The widths of the peaks decrease with increasing calcination temperature, indicating increasing particle size. The crystallite sizes calculated using the Scherrer formula for the samples ZC-300, ZC-400 and ZC-600. The calculated crystallite size and lattice parameter values are given in the Table 3.6

3.2.2.3 HRTEM

The morphological features of the samples ZC-A, ZC-400 and ZC-600 are studied using HRTEM. The corresponding images are shown in Figure 3.21 and Figure 3.22. The images of ZC-A clearly shows elongated rods fused together to form clusters. The high resolution image clearly shows the formation of nanorods. After calcination, the images of ZC-400

Table 3.6: Crystallite size and lattice parameter of $ZnCo_2O_4$ calcined at different temperatures.

Sample code	Crystallite size (±1 nm)	Lattice parameter Å
ZC-300	10	8.112
ZC-400	16	8.100
ZC-600	25	8.093

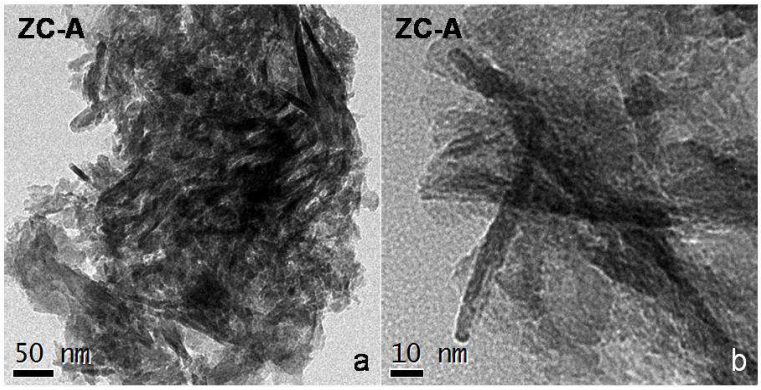

Figure 3.21: HRTEM images of the precursor ZC-A.

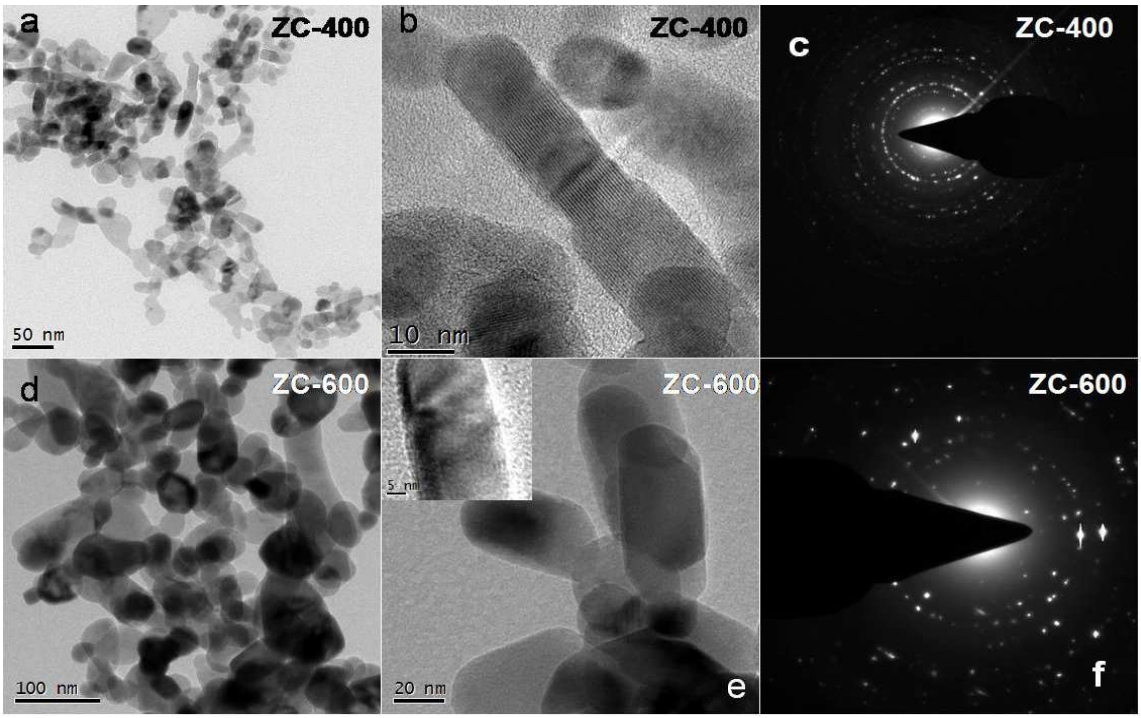

Figure 3.22: HRTEM images and the SAED patterns of the samples ZC-400 (a,b,c) and ZC-600 (d,e,f).

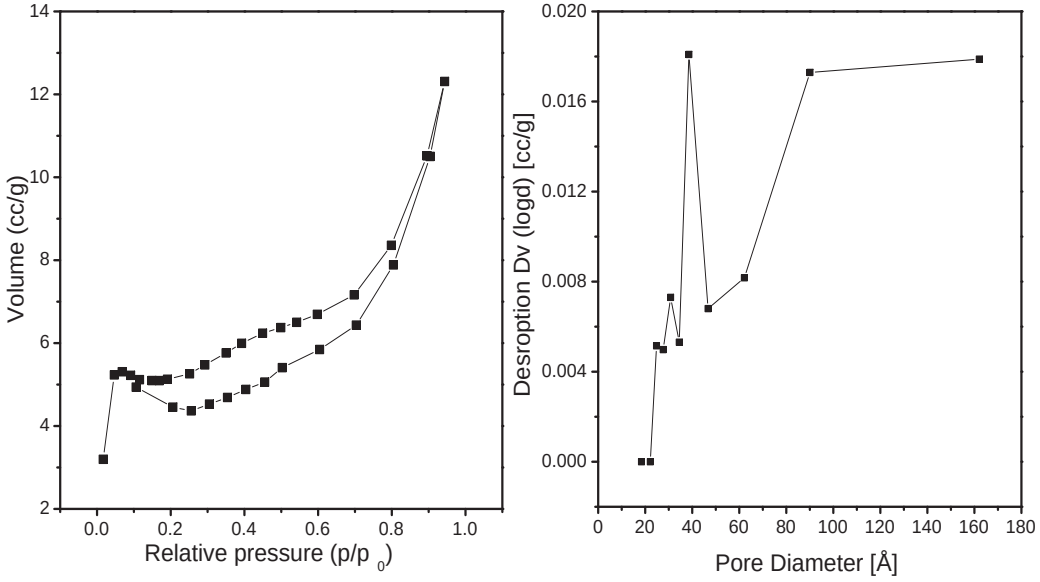

Figure 3.23: BET isotherm (left) and pore size distribution (right) of ZC-600.

shows the formation of spherical particles as well as small rods as shown in Figure 3.22. Both the rods and spherical particles are clearly visible in the image(b). Similarly, in the sample calcined at 600 °C (ZC-600), fused particles are seen (image d). The fusing results in the formation of small but well bound rods (image e). The diameter of the rods are some what bigger as shown in the inset of the image (e). In the case of the calcined powders, there is formation of both spherical as well as fused rods. The calcination helps in fusion of the particles together. In both the cases (ZC-400 and ZC-600) the SAED patterns reflect the polycrystalline nature of the samples.

3.2.2.4 Surface area and porosity

The BET isotherm and pore size distribution of ZC-600 are shown in Figure 3.23. The sample shows type IV isotherm [70] which is the characteristic behavior of mesoporous materials. The surface area of the sample is obtained as 16 m^2/g. The material shows a pore volume of 0.019 cm^3/g and sharp pore size distribution value of 2–10 nm.

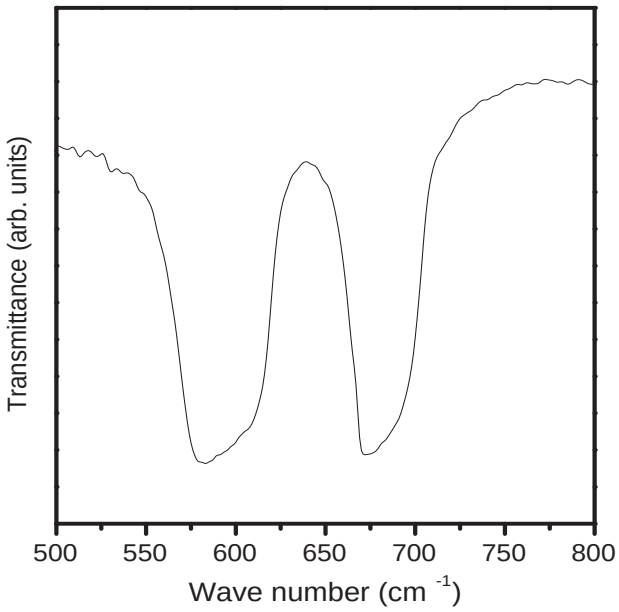

.

Figure 3.24: FTIR spectrum of ZC-600.

3.2.2.5 Infrared Spectroscopy

Figure 3.24 shows the FTIR spectrum of the sample ZC-600. The characteristic features of the spinel phase are observed in the spectra. Two characteristic bands are observed at 582 (ν_1) and 671 cm^{-1} (ν_2) which are related to the vibrations of the lattice of octahedral groups [111]. The IR spectral features are comparable to that observed for Co_3O_4 nanorods, discussed in the previous section (see Figure 3.7). Thus, apart from the bands due to the low-spin Co^{III}-O vibrations, which are observed as shoulders, major bands are observed at lower wave numbers. This indicates some changes in the Co environment in the nanostructured $ZnCo_2O_4$. This can be due to large number of defects at the surface or changes in the spin state of Co such as Co^{2+} or intermediate/high spin Co^{3+} ions. The defect sites and/or new spin states of Co are likely to give rise to high activity for the material.

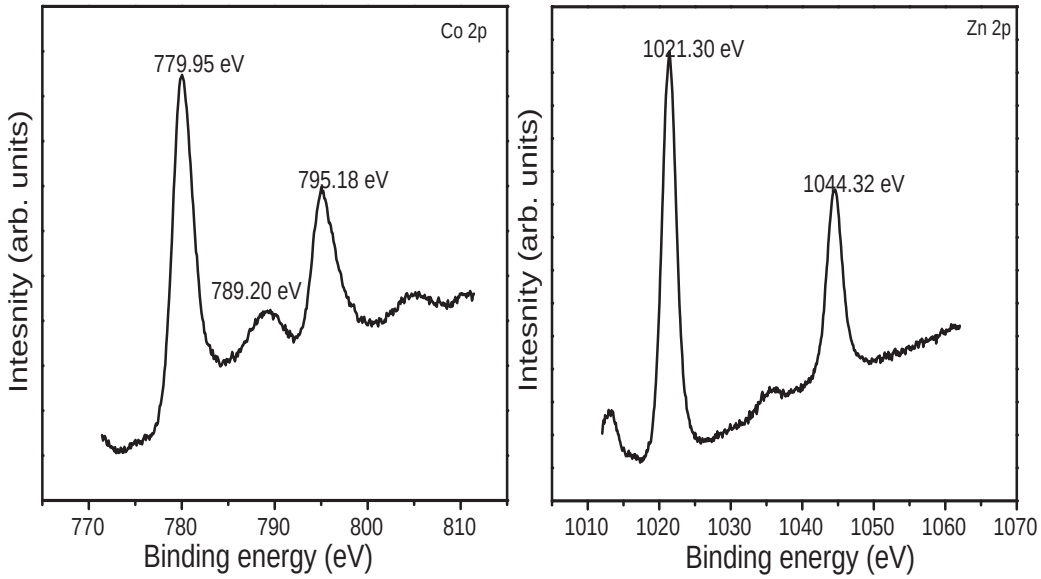

.

Figure 3.25: Co 2p and Zn 2p XPS spectra of ZC-600.

3.2.2.6 X-ray Photoelectron Spectroscopy

In order to further ascertain the formation of $ZnCo_2O_4$ spinel structure, the sample ZC-600 was analyzed by XPS. Figure 3.25 shows the Co 2p and Zn 2p spectra of the sample ZC-600. The Co 2p spectra shows two major peaks with binding energy values of 779.95 and 795.18 eV, corresponding to Co $2p_{\frac{3}{2}}$ and Co $2p_{\frac{1}{2}}$ core level peaks, respectively [75,76]. The Co $2p_{\frac{3}{2}}$ - Co $2p_{\frac{1}{2}}$ peak separation is obtained as 15.23 eV, comparable to that observed for Co_3O_4 nanorods (see Figure 3.9). A weak satellite peak is observed at a binding energy of 789.2 eV, which is characteristic feature of the presence of cobalt in the +3 oxidation state. The Zn 2p spectra of the sample shows two peaks with binding energies of 1021.30 and 1044.32 eV, which are assigned to Zn $2p_{\frac{3}{2}}$ and Zn $2p_{\frac{1}{2}}$ levels with splitting value of 23.0 eV, confirming the presence of Zn in +2 oxidation state [112]. Thus, XPS results in conjunction with XRD data confirmed the formation of nanostructured $ZnCo_2O_4$.

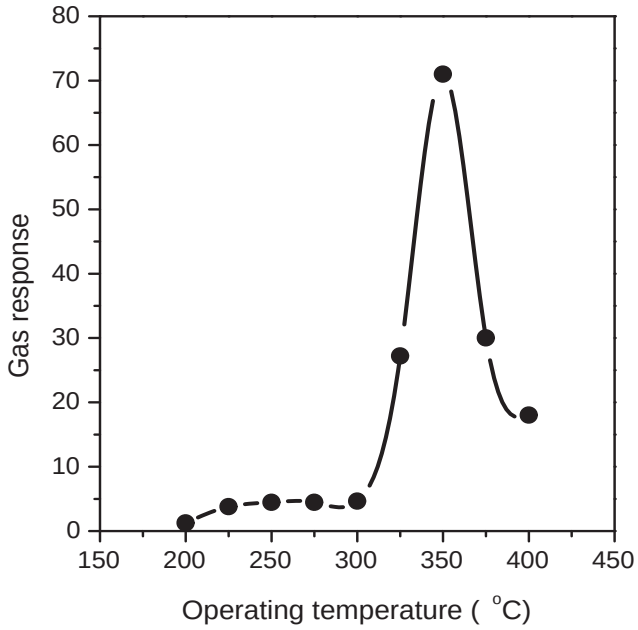

Figure 3.26: Effect of operating temperature on the gas response of ZC-600 to 50 ppm of LPG. The solid line is a guide to the eyes.

3.2.3 LPG Gas Sensing Properties

The nanostructured sample ZC-600 was tested for its LPG sensing properties. The LPG sensing experiments were performed at different temperatures in order to find out the optimum operating temperature for LPG detection. Before exposing to LPG, the sensing element was allowed to equilibrate inside the gas chamber at the operating temperature for 1 h. A number of experiments have been carried out to measure the gas response as a function of the operating temperature. All the time, the gas response of the sensor element had approximately constant values, indicating the repeatability of the sensor.

The gas response of ZC-600 to 50 ppm LPG, as a function of operating temperature, is shown in Figure 3.26. At low temperatures, the gas response is relatively low (e.g. S = 1.25 at 200 °C), but it increases slowly up to 300 °C and then drastically with increase in the operating temperature. The gas response attains a maximum at ∼350 °C (S ≈ 71) and thereafter it decreases with a further increase of the operating temperature. Thus, the optimum operating temperature for the sample ZC-600 to detect LPG is at 350 °C,

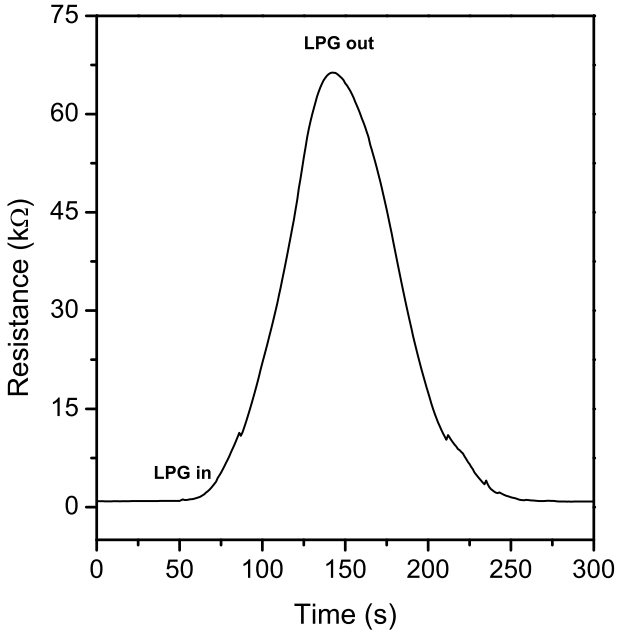

Figure 3.27: Response of ZC-600 to 50 ppm LPG at optimum operating temperature of 350 °C.

which is the modest from the viewpoint of semiconducting oxide gas sensors. Hence, the optimum operating temperature of 350 °C was chosen in order to investigate further LPG sensing properties such as response and recovery times, reproducibility and selectivity.

Besides the gas response, the response and recovery times are also important parameters for evaluating the performance of gas sensors. The response and recovery times are defined as the time required for the sensor-resistance to change by 90% of the final resistance. The response and recovery characteristics of ZC-600 to 50 ppm LPG at the optimum operating temperature of 350 °C is shown in Figure 3.27. Five samples were tested from each batch. It is observed that the resistance of the sensing element increases when exposed to LPG (reducing gas), which suggests that the sample ZC-600 behaves as a p-type semiconductor. As it can be seen from Figure 3.27, the sensor responds within a minute after introduction of LPG and recovers at the same rate when it is exposed to air. The ZC-600 has response time of ∼85-90 s and the recovery time of ∼75-80 s.

The reproducibility and stability of the nanostructured sample ZC-600 were investigated by repeating the test for four times. The gas response curve of ZC-600 sample upon

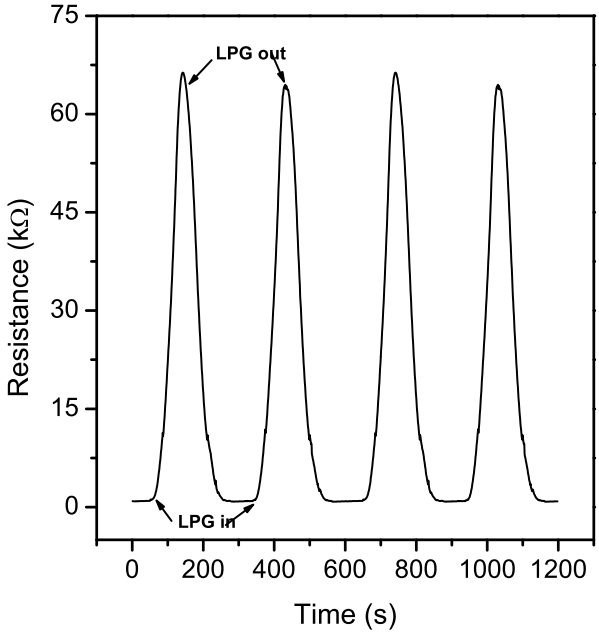

Figure 3.28: Repetitive response of ZC-600 to 50 ppm LPG at the optimum operating temperature of 350 °C

periodic exposure to 50 ppm LPG at the optimum operating temperature of 350 °C is shown in Figure 3.28. The sample shows good reproducibility and reversibility upon repeated exposure and removal of LPG under same conditions. Furthermore, the repeated tests revealed that the gas response values are maintained and the recovery abilities are not reduced after several sensing cycles. Thus, the sample ZC-600 exhibits a stable and repeatable characteristic, which suggests that it can be used as a reusable sensing material for the detection of LPG.

Figure 3.29 shows the gas response of ZC-600 at the optimum operating temperature of 350 °C to LPG with concentrations varying from 20 to 60 ppm. It is observed that the gas response increased with increase in the LPG concentration. Furthermore, the base line remains almost stable and no significant variation in the gas response is observed. The dependence of the gas response of the sample on the LPG concentration at the optimum operating temperature of 350 °C is shown in Figure 3.30. The gas response changed from 1.38 to 190.47 in the investigated range of 20-60 ppm. The ZC-600 sample is able to detect a minimum of 20 ppm LPG with good response (S ∼1.38) at the optimum

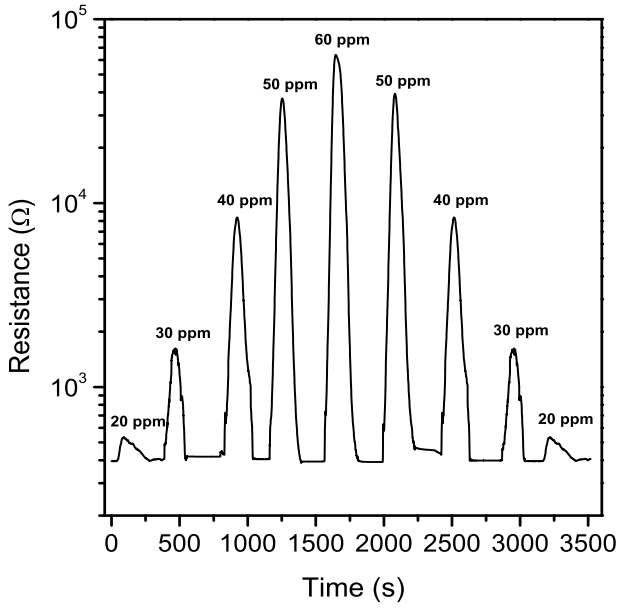

Figure 3.29: Response of ZC-600 upon sequential exposure to LPG with concentrations varying from 20 to 60 ppm at optimum operating temperature of 350 °C

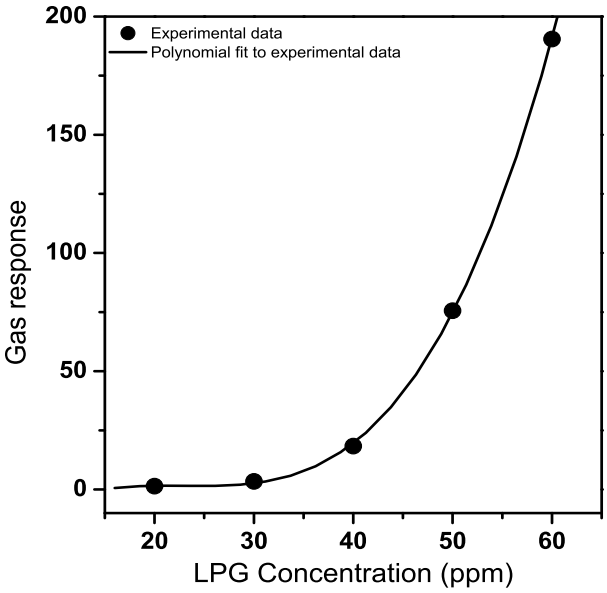

Figure 3.30: Relationship between gas response of ZC-600 and LPG concentration. The circles are experimental data and the solid line is the fit to the data, as discussed in the text.

operating temperature of 350 °C. It is found that the response of ZC-600 can be empirically represented as $y = -42.26 + 5.82x - 0.26x^2 + 0.0037x^3$, $R^2 = 0.9998$, where x, y and R^2 represents the LPG concentration, gas response and correlation coefficient, respectively. The solid line in the figure shows the polynomial fit to the experimental data, illustrating clearly good quality of the fit. Thus, the sample ZC-600 can be reliably used to monitor the concentration of LPG in the range 20-60 ppm.

Selectivity is an important parameter of gas sensors and the gas response toward a specific gas needs to be markedly higher than those for other gases for selective gas detection. To study the selective behavior of the nanostructured ZC-600 to LPG at the optimum operating temperature of 350 °C, the gas responses towards H_2, CO, CO_2 and ethanol, with concentration 50 ppm each, are also measured. The corresponding results are shown in Figure 3.31. The sample exhibits higher response to LPG with the gas response value of 72, whereas it shows considerably lower response ≤ 2 to H_2, CO, CO_2 and ethanol. In order to quantify the selectivity to LPG, the selectivity coefficient (K) is calculated according to [113]

$$K = \frac{S_{LPG}}{S_B}$$

where S_{LPG} and S_B are the responses of sensors in LPG and gas B, respectively. The selectivity coefficients for the nanostructured sample ZC-600 are obtained as 36.00 to H_2, 63.16 to CO_2, 68.57 to CO and 66.66 to ethanol. Higher K value imply the more selective detection of LPG in the presence of other gases. For example, K = 68.57 for CO indicates that the gas response to LPG is 68.57 times higher than that for CO. Thus, the experimental results indicate that ZC-600 has a good selectivity to LPG.

Taking into account the results of gas sensing experiments, it is concluded that ZC-600 has good LPG sensing properties such as higher gas response (∼72 for 50 ppm LPG gas at 350 °C), good selectivity, fast response (∼85-90 s) and rapid recovery (∼75-80 s), excellent repeatability and relatively lower operating temperature.

The sensing performance of semiconductor oxides is usually attributed to the adsorption and desorption of oxygen on the surface of the oxides. The $ZnCo_2O_4$ spinel is a p-type oxide semiconductor and therefore, its majority carriers are holes. The LPG sensing process is based on the changes in the resistance of the $ZnCo_2O_4$ which is controlled by the LPG species and the amount of the chemisorbed oxygen on the surface. The adsorption

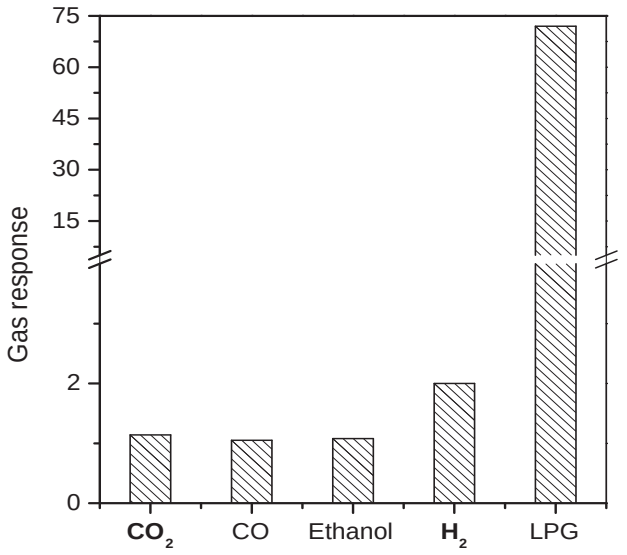

.

Figure 3.31: Bar chart showing the gas response of nanostructured ZC-600 for different gases. The gas concentration and operating temperature in all cases are 50 ppm and 350 °C, respectively

of oxygen on the surface of $ZnCo_2O_4$ can be explained by equation 3.4, as in the case of Co_3O_4, explained in *section 3.1.4*. The electron transfer from the conduction band to the chemisorbed oxygen results in an increase in the hole density. As a consequence, the decrease in the resistance of the $ZnCo_2O_4$ is observed and the equilibration of the chemisorption process results in stabilization of the surface resistance. Any process that disturbs this equilibrium gives rise to changes in the resistance of the $ZnCo_2O_4$.

It is well known that LPG mainly consists of CH_4, C_3H_8 and C_4H_{10}. In these molecules, the reducing hydrogen species are bound to carbon, and therefore, LPG dissociates less easily into the reactive reducing components on the $ZnCo_2O_4$ surface. When exposed to reducing gases like LPG, the gas molecules are chemisorbed at the active sites on the surface of the $ZnCo_2O_4$ surface. The free electrons released via the interaction between the LPG molecules and the pre-adsorbed O^- or O^{2-} neutralize the holes or the majority carriers in p-type $ZnCo_2O_4$ spinel. This compensation results in a decrease in the hole carriers in $ZnCo_2O_4$ and consequently, an increase in the resistance of nanostructured $ZnCo_2O_4$ [20, 114].

The LPG sensing characteristics of the nanostructured ZC-600 sample is better than or comparable to those of the sensors with other oxide semiconductors. Jiao *et al* [115] reported an LPG sensor based on $ZnGa_2O_4$ nanocrystals (10-20 nm) having a maximum sensitivity of ∼7 at 410 °C and having response time of a few seconds, with a recovery time of ∼60 s for 500 ppm of LPG. Waghulade *et al* [16] reported the synthesis of CdO nanoparticles by using chemical coprecipitation method and investigated the LPG sensing performance. The CdO nanoparticles showed a maximum sensitivity of 3.41 at 450 °C with the response and recovery times of 3-5 and 8-10 s for 25 ppm of LPG, respectively. Salunke *et al* [116] reported a chemical bath deposition of unsensitized and Pd-sensitized CdO nanorods and investigated their LPG sensing performance. The unsensitized CdO nanorods exhibited a maximum response of ∼0.14 at 425 °C for 0.1 vol% of LPG, which improved up to 0.35 at an optimum temperature of 375 °C after Pd-sensitization, with response and recovery times of 30 s and 90 s, respectively. Phani *et al* [108] investigated the LPG sensing property of Pd doped SnO_2. The Pd (1.5 wt%) doped SnO_2 showed a maximum sensitivity of 0.97 at 350 °C for 1000 ppm. Sahay *et al* [117] reported chemical spray deposited Al doped ZnO thin films for LPG sensors. The 0.5 at.% Al doped ZnO thin films showed a maximum sensitivity of 0.89 at 325 °C for 1 vol% of LPG. Chaudhari *et al* [118] studied the LPG sensor based on nanosized $BaTiO_3$ (∼65 nm) thick films, which showed a maximum sensitivity of 0.45 at 300 °C for 5000 ppm of LPG and an improvement in the sensitivity and selectivity was observed by doping $BaTiO_3$ with CuO and CdO. However, the present LPG sensor based on nanostructured $ZnCo_2O_4$ without any activators show a high gas response of 72 for 50 ppm of LPG at a relatively lower operating temperature of 350 °C, as shown in Figure 3.26. Furthermore, the material has a high gas response of 1.38-190.47 for 20-60 ppm of LPG, excellent repeatability and good selectivity when operating at 350 °C.

3.2.4 Conclusions

Nanostructured $ZnCo_2O_4$ spinel (26-30 nm) is successfully synthesized by calcining a mixed precursor consisting of cobalt hydroxy carbonate and zinc hydroxy carbonate at at different temperatures. The sample calcined at 600 °C in air for 5 h is found to be a good sensor for LPG gas. The gas response to 50 ppm of LPG is found to be max-

imum at an optimum operating temperature of 350 °C. The maximum gas response is obtained as ∼72, much larger than that reported in the literature using different nanostructured oxide materials, with a response time of nearly 85-90 s and recovery time of 75-80 s. The minimum detection limit of the nanostructured $ZnCo_2O_4$ is 20 ppm of LPG with reasonable response (∼1.38) at 350 °C. Further, the LPG sensor based on $ZnCo_2O_4$ has a high gas response of 1.38-190.47 to 20-60 ppm LPG, excellent repeatability and good selectivity when operating at 350 °C. The overall LPG sensing performance of the nanostructured $ZnCo_2O_4$ is better than those of most of the oxide semiconductor sensors already developed.

References

[1] H.S. Roh, H.S. Potdar, K.W. Jun, J.W. Kim, Y.S. Oh, *Appl. Catal. A: Gen.* 276 (2004) 231.

[2] X. Xie, Y. Li, Z.Q. Liu, M. Haruta, W. Shen, *Nature* 458 (2009) 746.

[3] W.Y. Li, L.N. Xu, J. Chen, *Adv. Func. Mater.* 15 (2005) 851.

[4] L. Fu, Z. Liu, Y. Liu, B. Han, P. Hu, L. Cao, D. Zhu, *Adv. Mater.* 17 (2005) 217.

[5] M. G. Hutchins, P. J. Wright and P. D. Grebenik, *Sol. Energ. Mater.* 16, (1987) 113.

[6] N. Wu, M. Zhao, J.G. Zheng, C. Jiang, B. Myers, S. Li, M. Chyu, S.X. Mao, *Nanotechnology* 16 (2005) 2878-2881.

[7] A. Srivastava, R. K. Jain, *Mater. Chem. Phys.* 105 (2007) 385.

[8] W.J. Moon, J.H. Yu, G.M. Choi, *Sensor. Actuat. B* 87 (2002) 464.

[9] T. Zhang, L. Liu, Q. Qi, S. Li, G. Lu, *Sensor. Actuat. B.* 139 (2009) 287.

[10] K.I. Choi, H.R. Kim, J.H. Lee, *Sensor. Actuat. B* 138 (2009) 497.

[11] B. Bahrami, A. Khodadadi, M. Kazemeini, Y. Mortazavi, *Sensor. Actuat. B* 133 (2008) 352.

[12] L. Zhang, J. Hu, P. Song, H. Qin, K. An, X. Wang, M. Jiang, *Sensor. Actuat. B* 119 (2006) 315.

[13] C.C. Wang, S.A. Akbar, M.J. Madou, *J. Electroceram.* 2 (1998) 273

[14] N. Barsan, U. Weimar, *J. Electroceram.* 7 (2001) 143

[15] J.X. Wang, X.W. Sun, H. Huang, Y.C. Lee, O.K. Tan, M.B. Yu, G.Q. Lo, D.L. Kwong, *Appl. Phys. A* 88 (2007) 611.

[16] R.B. Waghulade, P.P. Patil, R. Pasricha, *Talanta* 72 (2007) 594.

[17] C. Wu, P. Yin, X. Zhu, C. OuYang, Y. Xie, *J. Phys. Chem. B* 110 (2006) 17806.

[18] Y. Jia, L.F. He, Z. Guo, X. Chen, F.L. Meng, T. Luo, M.Q. Li, J.H. Liu,*J. Phys. Chem. C* 113 (2009) 9581.

[19] C. Li, D. Zhang, B. Lei, S. Han, X. Liu, C. Zhou, *J. Phys. Chem. B* 107 (2003) 12451

[20] X. Gou, G. Wang, J. Yang, J. Park, D. Wexler, *J. Mater Chem.* 18 (2008) 965

[21] C.C. Li, Z.F. Du, L.M. Li, H.C. Yu, Q. Wan, T.H. Wang, *Appl. Phys. Lett.* 91 (2007) 032101.

[22] A.M. Cao, J.S. Hu, H.P. Liang, W.G. Song, L.J. Wan, X.L. He, X.G. Gao, S.H. Xia, *J. Phys. Chem. B* 110 (2006) 15858.

[23] Y.Z. Wang, Y.X. Zhao, C.G. Gao, D.S. Liu, *Catal. Lett.* 116 (2007) 136

[24] Y.F.Y. Yao, *J. Catal.* 33 (1974) 108

[25] R.S. Drago, K. Jurczyk, D.J. Singh, V. Young, *App. Catal. B* 6 (1995) 155.

[26] E.V. Steen , H. Schulz, *Appl. Catal. A* 186 (1999) 309

[27] Z.L. Zhang, H.R. Geng, L.S. Zheng, B. Du, *J. Alloy. Compd.* 392 (2005) 317.

[28] M. Casas-Cabanas, G. Binotto, D. Larcher, A. Lecup, V. Giordani, J.M. Tarascon, *Chem. Mater.* 21 (2009) 1939.

[29] M. Guisnet, J. Barrauit, C. Bouchoule, D. Duperz, G. Perot, R. Maure land, C. Montassier, *Heterogeneous Catalysis and Fine Chemicals II.*

[30] T. Mallat, A. Baiker, *Chem. Rev.* 104 (2004) 3037.

[31] Y. Su, L.C. Wang, Y.M. Liu, Y. Cao, H.Y. He, K.N. Fan, *Cataly. Commun.* 8 (2007) 2181.

[32] T. Punniyamurthy, S. Velusamy, J. Iqbal, *Chem. Rev.* 105 (2005) 2329.

[33] Z. Dong, Y. Fu, Q. Han, Y. Xu, H. Zhang, *J. Phys. Chem. C* 111 (2007) 18475.

[34] B.B. Lakshmi, C.J. Patrissi, C.R. Martin, *Chem. Mater.* 9 (1997) 2544.

[35] K.T. Nam, D.W. Kim, P.J. Yoo, C.Y. Chiang, N. Meethong, P.T. Hammond, Y.M. Chiang, A.M. Belcher, *Science* 312 (2006) 885.

[36] R.M. Wang, C.M. Liu, H.Z. Zhang, C.P. Chen, L. Guo, H.B. Xu, S.H. Yang, *App. Phys. Lett.* 85 (2004) 2080.

[37] R.N. Singh, J.F. Koenig, G. Poillerat, P. Chartier, *J. Electrochem. Soc.* 137 (1990) 1408.

[38] B. Li, Y. Xie, C. Wu, Z. Li, J. Zhang, *Mater. Chem. Phys.* 99 (2006) 479.

[39] Y.H. Ni, X.W. Ge, Z.C. Zhang, H.R. Liu, Z.L. Zhu, Q. Ye, *Mater. Res. Bull.* 36 (2001) 2383.

[40] Z. Wang, X. Chen, M. Zhang, Y. Qian, *Solid State Sci.* 7 (2005) 13.

[41] T. Baird, K.C. Campbell, P.J. Holliman, R.W. Hoyle, D. Stirling, B.P. Williams, M. Morris, *J. Mater. Chem.* 7 (1997) 319.

[42] P. Porta, R. Dragone, G. Fierro, M. Inversi, M. Lojacono, G. Moretti, *J. Chem. Soc. Faraday Trans.* 88 (1992) 311.

[43] R. Xu, H.C. Zeng, *J. Phys. Chem. B* 107 (2003) 12643.

[44] D.G. Klissurski, E.L. Uzunova, *Chem. Mater.* 3 (1991) 1060.

[45] A.G. Belous, O.Z. Yanchevskii, A.V. Kramarenko, *Russ. J. Appl. Chem.* 79 (2006) 345.

[46] D.G. Klissurski, E.L. Uzunova, *J. Mater. Sci. Lett.* 9 (1990) 1255.

[47] M.G. Mostafa, A. Matsumoto, K. Wase, Y. Kishi, *Hydrometallurgy* 57 (2000) 97.

[48] S. Lacor, R.P. Van Hille, K. Peterson, A.E. Lewis, *AIChE J.* 51 (2005) 2358.

[49] H.S. Potdar, K.W. Jun, J.W. Bae, S.M. Kim, Y.J. Lee, *App. Catal. A* 321 (2007) 109.

[50] Z. Jin, H.J. Zhou, Z.L. Jin, *Sensor. Actuat. B* 52 (1998) 188.

[51] S.H. Wang, T.C. Chou, C.C. Liu, *Sensor. Actuat. B* 94 (2003) 343.

[52] J. Liu, H. Xia, L. Lu, D. Xue, *J. Mater.Chem.* 20 (2010) 1506.

[53] Y. Wang, H.C. Zeng, J.Y. Lee, *Adv. Mater.* 18 (2006) 645.

[54] S. Park, R.J. Gorte, J.M. Vohs, *Appl. Catal. A:* 200 (2000) 55.

[55] J.C. Ganley, K.L. Riechmann, E.G. Seebauer, R.I. Masel, *J. Catal.* 227 (2004) 26.

[56] M. Sato, H. Hara, H. Kuritani, T. Nishide, *Sol. Ener. Mat. Sol. C* 45 (1997) 43.

[57] E.S. Toberer, M. Grossman, T. Schladt, F.F. Lange, R. Seshadri, *Chem. Mater.* 19 (2007) 4833.

[58] S.A. Corr, D.P. Shoemaker, E.S. Toberer, R. Seshadri, *J. Mater. Chem.* 20 (2010) 1413.

[59] R.L. Penn, J.F. Banfield, *Geochim. Cosmochim. Acta* 63 (1999) 1549.

[60] S.R. Dhage, S.P. Gaikwad, P. Muthukumar, V. Ravi, *Ceram. Int.* 31 (2005) 211.

[61] M. Anilkumar, V. Ravi, *Mater. Res. Bull.* 40 (2005) 605.

[62] T. He, D. Chen, X. Jiao, *Chem. Mater.* 16 (2004) 737.

[63] The software is freely available from http://www.ccp14.ac.uk.

[64] G. Wang, X. Shen, J. Horvat, B. Wang, H. Liu, D. Wexler, J. Yao, *J. Phys. Chem. C* 113 (2009) 4357.

[65] E. Hosono, S. Fujihara, I. Honma, H. Zhou, *J. Mater. Chem.* 15 (2005) 1938.

[66] X. Xie, P. Shang, Z. Liu, Y. Lv, Y. Li, W. Shen, *J. Phys. Chem. C* 114 (2010) 2116.

[67] B. Lefez, P. Nkeng, J. Lopitaux, G. Poillerat, *Mater. Res. Bull.* 31 (1996) 1263.

[68] P. Nkeng, G. Poillerat, J.F. Koenig, P. Chartier, B. Lefez, J. Lopitaux, M. Lenglet, *J. Electrochem. Soc.* 142 (1995) 1777.

[69] C.B. Wang, C.W. Tang, S.J. Gau, S.H. Chien, *Catal. Lett.* 101 (2005) 59.

[70] K.S.W. Sing, D.H. Everett, R.A.W. Haul, L. Moscou, R.A. Pierotti, J. Rouquerol, T. Siemieniewska, *Pure Appl. Chem.* 57 (1985) 603

[71] T. Baird, K.C. Campbell, P.J. Holliman, R.W. Hoyle, M. Huxam, D. Stirling, B.P. Williams, M. Morris, *J. Mater. Chem.* 9 (1999) 599.

[72] C. Blaauw, F. Leenhouts, F. Woude, G.A. Sawatzky, *J. Phys. C: Solid State* 8 (1975) 459.

[73] J. Haber, J. Stoch, L. Ungler, *J. Solid State Chem.* 19 (1976) 113.

[74] B.J. Tan, K.J. Klabunde, P.M.A. Sherwood, *J. Am. Chem. Soc.* 113 (1991) 855.

[75] C.V. Chenck, J.G. Dillard, J.W. Murray, *J. Colloid Interf. Sci.* 95 (1983) 398.

[76] M. Oku, Y. Sato, *Appl. Surf. Sci.* 55 (1992) 37.

[77] T.J. Chuang, C.R. Brundle, D.W. Rice, *Surf. Sci.* 59 (1976) 413.

[78] M.A. Langell, M.D. Anderson, G.A. Carson, L. Peng, S. Smith, *Phys. Rev. B* 59 (1999) 4791.

[79] P.A. Joy, S.K. Date, *J. Magn. Magn. Mater.* 222 (2000) 33.

[80] S. Gangopadhyay, G.C. Hadjipanayis, C.M. Sorensen, K.J. Klabunde, *J. Appl. Phys.* 73 (1993) 6964.

[81] W.L. Roth, *J. Phys. Chem. Solids* 25 (1964) 1.

[82] C.D. Spencer, D. Schroeer, *Phys. Rev. B* 9 (1974) 3658.

[83] S. Vijayanand, M.B. Mahajan, H.S. Potdar, P.A. Joy, *Phys. Rev. B* 80 (2009) 64423.

[84] D. Parker, F. Ladieu, E. Vincent, G. Mriguet, E. Dubois, V. Dupuis, R. Perzynski, *J. Appl. Phys.* 97 (2005) 10A502.

[85] M. Sasaki, P.E. Jnsson, H. Takayama, H. Mamiya, *Phys. Rev. B* 71 (2005) 104405.

[86] S. Deka, P.A. Joy, *J. Nanosci. Nanotech.* 8 (2008) 3955.

[87] M.R. Anantharaman, S. Jagatheesan, K.A. Malini, S. Sindhu, A. Narayanasamy, C.N. Chinnasamy, J.P. Jacobs, S. Reijne, K. Seshan, R.H.H. Smits, *J. Magn. Magn. Mater.* 189 (1998) 83.

[88] C.N.R. Rao, M.M. Seikh, C. Narayana, *Top. Curr. Chem.* 284 (2004) 1.

[89] X.J. Huang, Y.K. Choi, *Sensor. Actuat. B* 122 (2007) 659.

[90] M. Siemons, U. Simon, *Sensor. Actuat. B* 120 (2006) 110.

[91] Z. Liu, T. Yamazaki, Y. Shen, T. Kikuta, N. Nakatani, T. Kawabata, *Appl. Phys. Lett.* 90 (2007) 173119.

[92] H. Huang, O.K. Tan, Y.C. Lee, T.D. Tran, M.S. Tse, X. Yao, *Appl. Phys. Lett.* 87 (2005) 163123.

[93] A. Ponzoni, E. Comini, G. Sberveglieri, J. Zhou, S.Z. Deng, N.S. Xu, Y. Ding, Z.L. Wang, *Appl. Phys. Lett.* 88 (2006) 203101.

[94] H. Mbarek, M. Saadoun, B. Bessa s, *Mater. Sci. Eng. C* 26 (2006) 500.

[95] K. Arshak, I. Gaidan, *Sensor. Actuat. B* 111 (2005) 58

[96] D. Kohl, *Sensor. Actuator.* 18 (1989) 71.

[97] D. Koziej, K. Thomas, N. Barsan, F. Thibault-Starzyk, U. Weimar, *Catal. Today* 126 (2007) 211.

[98] K. Kervinen, P. Lahtinen, T. Repo, M. Svahn, M. Leskel, *Catal. Today* 75 (2002) 183.

[99] K. Kervinen, H. Korpi, M. Leskel, T. Repo, *J. Mole. Cat. A* 203 (2003) 9.

[100] D. Klissurski, E. Uzunova, K. Yankova, *Appl. Catal. A* 95 (1993) 103.

[101] K. Papadatos, K.A. Shelstad, *J. Catal.* 28 (1973) 116.

[102] S. Trasatti, *The Electrochemistry of Novel Materials*, VCH, Weinheim, 1994, 207.

[103] K. Omata, T. Takada, S. Kasahara, M. Yamada, *Appl. Catal. A* 146 (1996) 255.

[104] Y. Sharma, N. Sharma, G.V.S. Rao, B.V.R. Chowdari, *Adv. Funct. Mater.* 17 (2007) 2855.

[105] X. Wei, D. Chen, W. Tang, *Mater. Chem. Phys.* 103 (2007) 54.

[106] G.Y. Zhang, B. Guo, J. Chen, *Sensor. Actuat. B* 114 (2006) 402.

[107] X. Niu, W. Du, W. Du, *Sensor. Actuat. B* 99 (2004) 405.

[108] A.R. Phani, *Appl. Phys. Lett.* 71 (1997) 2358.

[109] L.D. Feng, X.J. Huang, Y.K. Choi, *Microchim. Acta* 156 (2006) 245.

[110] N. Kanari, D. Mishra, I. Gaballah, B. Dupre, *Thermochim. Acta* 410 (2004) 93

[111] J. Preudhomme, P. Tarte, *Spectrochim. Acta A* 27 (1971) 1817.

[112] I. Grohmann, B. Peplinski, W. Unger, *Surf. Interface Anal.* 19 (1992) 591.

[113] M. Siemons, U. Simon, *Sensor. Actuat. B* 126 (2007) 595

[114] D. Patil, P. Patil, V. Subramanian, P.A. Joy, H.S. Potdar, *Talanta* 81 (2010) 37.

[115] Z. Jiao, G. Ye, F. Chen, M. Li, J. Liu, *Sensors* 2 (2002) 71.

[116] R.R. Salunkhe, D.S. Dhawale, U.M. Patil, C.D. Lokhande, *Sensor. Actuat. B.* 136 (2009) 39.

[117] P.P. Sahay, R.K. Nath, *Sensor. Actuat. B* 133 (2008) 222.

[118] G.N. Chaudhari, D.R. Bambole, A.B. Bodade, *Vacuum* 81 (2006) 251.

Chapter 4

Nanocrystalline Co_3O_4 in Li-ion Batteries and Supercapacitors

4.1 Introduction

The ever growing need for better energy storage materials demands compelling improvements in the primary energy technology sector such as batteries, fuel cells, solar cells and supercapacitors. Among them Li-ion batteries (LIB) represent one of the dominant candidates for mobile phones and portable applications, due to their high energy density, modularity and long cycle life [1–5]. The present generation of LIB, however, uses expensive components that will restrict the growth of LIB in the next decade, urging researchers to develop better materials that are cheaper and more efficient. Transition metal oxides are known to have, in principle, higher capacity but suffer major set backs in the perspective of cycle life [6–8]. On the other hand, the commercial batteries use carbonaceous materials as the negative electrode that have shown reasonable cycle life despite posing severe restrictions on the maximum attainable energy density (<372 mAhg^{-1}) along with staging and fading of capacity that is commonly observed in these electrodes [9]. This prompted the need for immense research on alternate electrode materials, from a wide variety of compounds ranging from metal oxides and intercalation compounds of transition metals to nanostructured materials such as Si/Sn based nanowires and hybrid materials like $LiFePO_4$ [10–15]. In the case of nanostructured materials, different morphologies, such as nanowires, nanotubes and nanorods, tend to give varying energy density due to their preferred orientational features [16–20].

The tremendous growth in the consumption of energy resulted in an urgent need for efficient energy conversion and storage. While fuel cells and batteries offer higher energy

density, they cannot offer very high power density. On the other hand, electrochemical supercapacitors provide higher power density when compared to the Li-ion batteries. The simplified Ragone plots (see Figure 1.13 in chapter 1) clearly reveal that to match the performance of internal combustion engines, a hybrid between supercapacitors with fuel cell and/or batteries is necessary [21]. Further, supercapacitors are suitable for many applications such as hybrid electric vehicles, uninterrupted power supplies and backup power sources for computer memory due to their higher power density and longer cycle life. Supercapacitors are generally of two types, electric double layer capacitors (EDLCs), where non-faradaic processes are the key for energy storage while in pseudo-capacitors, the redox process of the active material contributes for the capacitance. The application of $RuO_2.xH_2O$ as an electrode material marked a new breakthrough in pseudo-capacitors that brought the attention towards various transition metal oxides such as NiO, MnO_2, and $Ni(OH)_2$ for electrode applications [22–24].

Among transition metal oxides, Co_3O_4 with selective shapes has recently been shown to be a promising anode material for LIB technology [25–28]. The inherent advantages of the needle like structures obtained through a virus enabled synthesis route is utilized for increased capacity [26]. Similarly, the influence of shape over the capacity has been demonstrated [29]. After proving its utility as an anode material in Li-ion batteries, Co_3O_4 has also prompted the research on its supercapacitive behavior due to the presence of redox couple to show pseudocapacitive behavior [30,31]. An important criterion to improve the energy density of any transition metal oxide based electrode is to improve the electrode-electrolyte interface by means of reducing the particle size and increasing the porosity [31].

Hence, the Co_3O_4 porous nanorods prepared by a template free simple and facile coprecipitation/digestion method, as described in the previous chapter (the sample CC-300) has been tested as an anode material in the LIB application and also evaluated for its performance in a supercapacitor .

4.2 Application as anode in LIB

For the evaluation of Co_3O_4 as the anode material for rechargeable LIB, a mixture of Co_3O_4 obtained by calcining the precursor at 300 °C (CC-300), Vulcan XC-72 carbon and Nafion taken in the ratio of 75:20:5, was brushed on a stainless steel 316 (SS) mesh

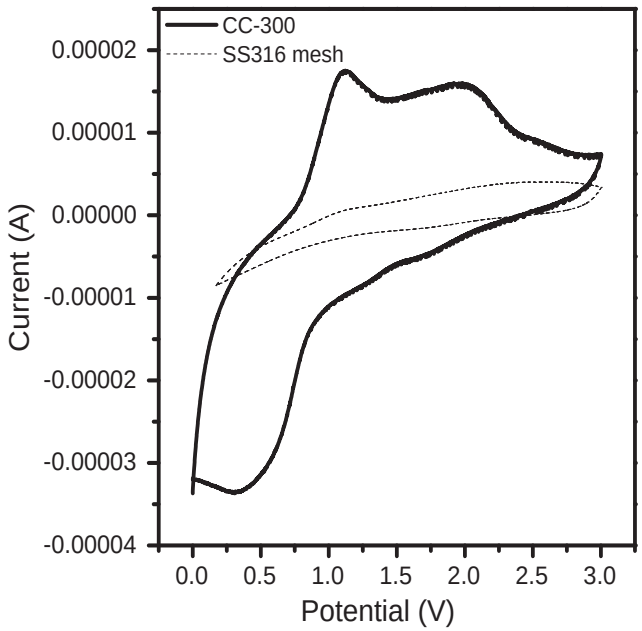

.

Figure 4.1: CV plots measured at a scan rate of 1 mV/s for the CC-300 and bare stainless steel mesh electrodes using $LiClO_4$ dissolved in propylene carbonate as the electrolyte.

and it was used as the working electrode. Li metal served as the counter and reference electrodes with 0.1 M $LiClO_4$ in propylene carbonate (PC) as the electrolyte.

To get detailed information on the characteristics and properties of the CC-300 electrode, various characterization techniques such as XRD, HRTEM, solid state NMR and magnetic measurements have been carried out. The cyclic voltammogram (CV) and impedance measurements were carried out on Autolab 30 PGSTAT and Solartron instruments, respectively. Charge-discharge experiments were carried out on a home made galvanostatic set up using a Keithley 6514 electrometer and 2010 multimeter connected in series with a variable resistance box. All the experiments were carried out in argon atmosphere. Magnetic measurements were carried out on a vibrating sample magnetometer.

Figure 4.1 shows the cyclic voltammogram (CV) of single cell assembly utilizing the porous Co_3O_4 nanorods (CC-300). The CVs are measured at a scan rate of 1 mV/s over the potential window of 0-3 Volt. Two anodic peaks and one cathodic peak are observed

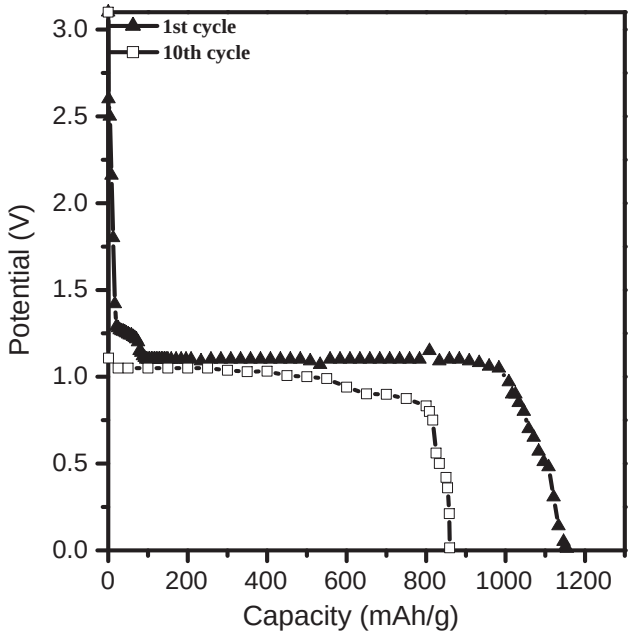

.

Figure 4.2: Galvanostatic discharge curves of the sample CC-300 measured at a discharge rate of 50 $mAhg^{-1}$ using $LiClO_4$ dissolved in propylene carbonate as electrolyte.

and this may be attributed to the Li ion insertion and desertion in the Co_3O_4 matrix. More specifically, the anodic peaks can be ascribed to the oxidation of Co concomitant to the intercalation of Li^+ on to the Co_3O_4 matrix where as the cathodic peak observed at 0.7 V could be attributed to the reduction of Co_3O_4. This is in accordance with literature reports of Co_3O_4 reduction [26, 27]. For example, Nam *et al* have proved that the reduction of Co from higher to lower oxidation state occurs at ∼0.7 V and Au support is shown to be positively influencing the cathodic peak of Co_3O_4 prepared through a virus enabled root [26]. The control experiments carried out with stainless steel 316 mesh did not show any peak in the CV, and this further confirms that the peaks originate from the Co_3O_4 nanorods only.

The open circuit potential (OCP) measured for the porous sample CC-300 coupled with a Li metal foil is 3.6 V which is in very good agreement with the reported values. Figure 4.2 shows constant current discharge curves using lithiated CC-300 as the anode. After an initial drop from the OCP, the potential follows a two step discharge to reveal

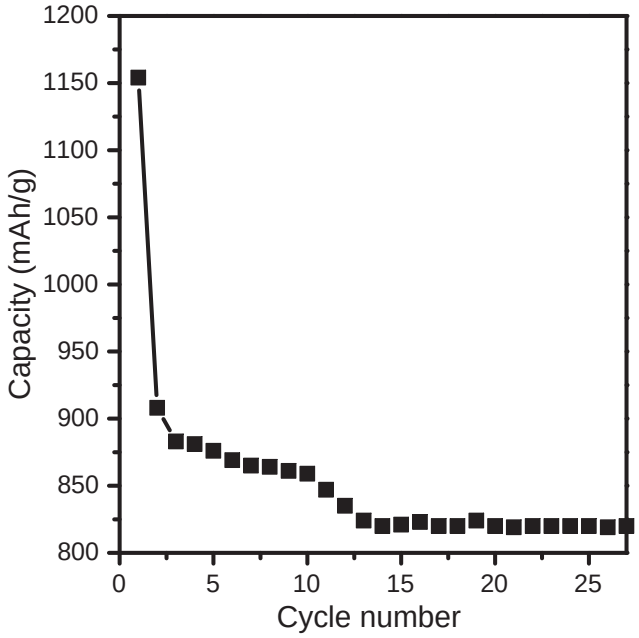

.

Figure 4.3: Cycle life performance of CC-300 measured at a discharge rate of 50 $mAhg^{-1}$ using $LiClO_4$ dissolved in propylene carbonate.

a complete capacity of 1155 $mAhg^{-1}$ which is significantly higher than that of the carbonaceous electrodes used in commercial batteries (providing ca. 372 $mAhg^{-1}$) and other Co_3O_4 based Li ion electrodes (∼850-700 $mAhg^{-1}$) [28, 32].

For the effective application of any material used as an anode in the rechargeable Li-ion batteries, the number of cycles the electrode is able to withstand at the constant discharge rate is important for its usage in practical applications. Hence, the sample CC-300 had been subjected to the cycle life measurements at the constant discharge rate of 50 $mAhg^{-1}$. Interestingly, the cycle life measurements shown in Figure 4.3 reveal that after dropping from a capacity of 1155 to 908 $mAhg^{-1}$, the capacity of the Co_3O_4 becomes steady at 820 $mAhg^{-1}$ for more than 25 cycles, which is still much higher than that of commercial carbon based electrodes. This abides well with the fact that structures with smaller transport pathways will give better Li insertion due to decreased volume change which is expected to give improved capacity and cycle life [20, 28].

Figure 4.4 shows the XRD patterns of the CC-300 electrode material before and after

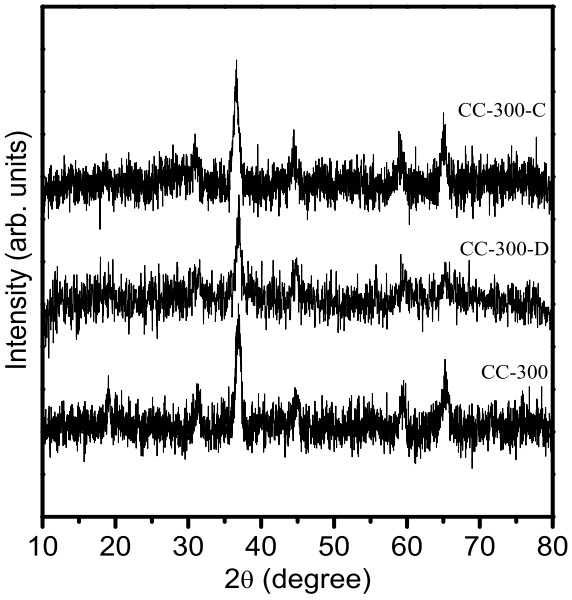

Figure 4.4: Comparison of the XRD patterns of CC-300 with that of the material after discharging (CC-300-D) and charging (CC-300-C).

the charge-discharge cycles. It is observed that the XRD patterns of the charged and discharged samples do not show any noticeable changes when compared to that of the pristine material, demonstrating the stability of the nanorod matrix.

In general, the possible operating mechanism for a metal oxide reacting with Li is the formation of nanodomains of metal and Li_2O in the metal oxide matrix during discharge and reversion of the oxide while charging back [33]. In the case of Co_3O_4 also, it is reported that there is formation of Co nanodomains with Li_2O during discharge and formation of β-CoO instead of Co_3O_4 while charging back. For example, Li *et al* confirmed the formation of Co through the observation of dark grains in the HRTEM image with the lattice fringe value corresponding to the structure of Co. Their XRD pattern showed broad and weak reflections due to Li_2O and fcc Co [34]. However, peak due to Li_2O is not observed in the XRD patterns shown in Figure 4.4, indicating that probably very fine (amorphous) nanosized Li_2O is formed.

Since there are no peaks in the XRD pattern corresponding to Li_2O are observed, changes in the Li environment during discharge was probed through ^{7}Li solid state NMR.

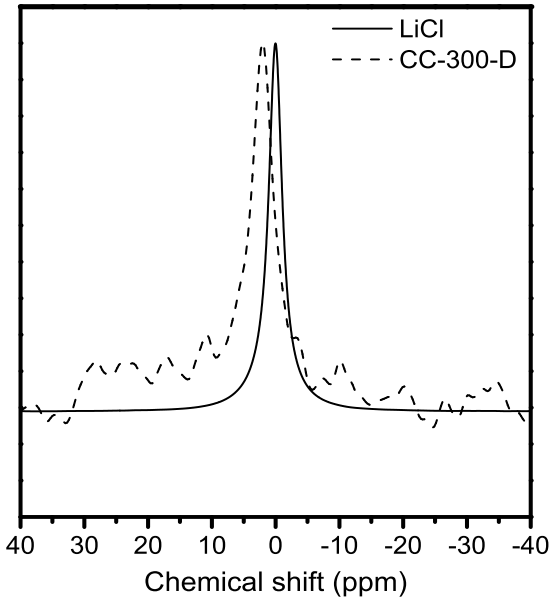

Figure 4.5: ^{7}Li solid state NMR of CC-300 after discharge, compared with lithium chloride as reference.

Figure 4.5 depicts the ^{7}Li NMR spectra of the discharged sample CC-300-D. It clearly shows a chemical shift of ∼2 ppm against LiCl. This result confirms the formation of Li^+ during the discharge (insertion), as the chemical shift resembles more towards the Li^+ than towards the metallic Li (Li^0 state) [16].

HRTEM images of the charged (CC-300-C) and discharged (CC-300-D) samples are shown in Figure 4.6. The images are not clear probably due to the formation of a polymeric film from the electrolyte and also due to the solvent adsorption and intercalation in the pores. As per the reported mechanism [34], formation of Co nanodomains in Li_2O matrix is expected.

Since the presence of Co is not observed in the XRD pattern, the inherent advantage of magnetic measurement is used, which is an effective and sensitive tool to confirm even trace amounts of Co since it is ferromagnetic. From Figure 4.7 it is very clear that the discharged sample CC-300-D shows a ferromagnetic response to the applied field which is a confirmation for the formation of Co nanodomains which are ferromagnetic in nature. The inset in Figure 4.7 shows the response of the samples CC-300-C and CC-300 to the

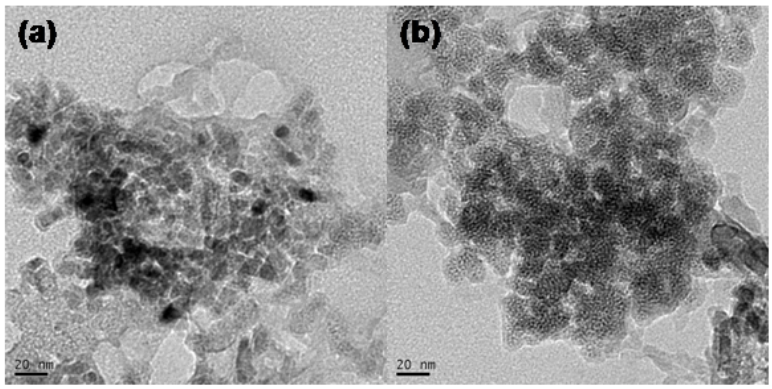

Figure 4.6: HRTEM images of the (a) discharged (CC-300-D and (b) charged (CC-300-C) samples.

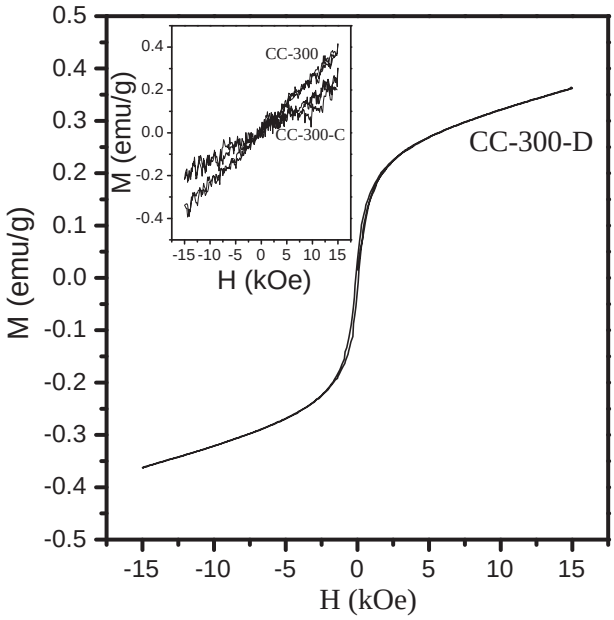

Figure 4.7: M vs H measurement of CC-300-D. Inset: M vs H curves of CC-300-C and CC-300.

applied field. The bare sample and the charged one do not show any ferromagnetic signal since Co_3O_4 is paramagnetic at room temperature. Also, the magnetic measurements reveal that the amount of Co is very less in the discharged sample from its magnetization value of 0.36 emu/gm. For Co nanoparticles of size in the range of ∼10 nm, magnetization value of 20 emu/g is reported against the bulk value of 160 emu/g. This corresponds to less than 1% of Co nanoparticles in CC-300-D, which proves the stability of the material.

A two-step structural modification is anticipated in the Co_3O_4 matrix with initial insertion of Li, which on further Li desertion regains the original structure. Even after 10 charge-discharge cycles, the material is not completely converted into metallic Co, as inferred from the XRD and magnetic measurements. This can be attributed to the stability of the material and the shorter pathways offered by the highly porous structure. Further, it could also be due to the formation of more and more active sites that would be regenerated by the redox process which is favored here due to the structural aspects of the material.

Hence, it can be concluded that the as-prepared porous nanorods of Co_3O_4 is highly stable with more active sites. The material shows a considerably good specific capacity of 1155 $mAhg^{-1}$ and further stabilizes with a value of 820 $mAhg^{-1}$ for more than 25 cycles.

4.3 Application as a supercapacitor material

To study the supercapacitive behavior of the porous CC-300 nanorod sample, cyclic voltammogram (CV) in alkaline medium was measured using 6M KOH solution as the electrolyte. The sample was coated on a carbon paper which serves as the working electrode while Pt wire and foil were used as the reference and counter electrodes, respectively. Figure 4.8 clearly reveals a highly pseudo-capacitive behavior of the CC-300 electrode. The observed reversible electrochemical behavior, in addition to the almost rectangular CV shape, is ideal for a pseudo-supercapacitor due to contributions from both faradaic and non-faradaic processes [35]. The redox peak observed for the $Co^{2+/3+}$ couple is playing a crucial role in improving the capacitance of the electrode. The capacitance value calculated from the CV is 510 Fg^{-1} which is much higher than the reported value of 450 Fg^{-1} [30] and 95 Fg^{-1} [36] for Co_3O_4 nanorods and micro porous nanostructures. The higher value obtained here could be attributed to the enhanced surface area and higher

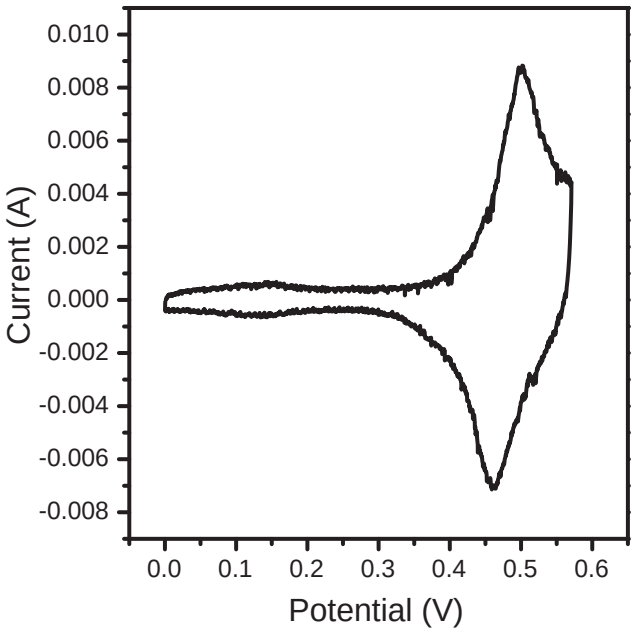

.

Figure 4.8: Cyclic voltammogram of porous CC-300 measured at a scan rate of 5 mV/s using 6 M KOH as the electrolyte.

porosity of the nanorods which improve the electrode-electrolyte interface.

Figure 4.9 shows the scan rate dependant CV of the CC-300 electrode in KOH medium. The figure clearly reveals the quasi-reversible behavior of the CC-300 nanorods which is well known for the Co_3O_4 based systems. A plot of specific capacitance vs scan rate is shown in Figure 4.10. The specific capacitance measured at different scan rates show significant reduction in the capacitance value at higher scan rates. This mainly originates from the quasi-reversible nature of the material and the 3D nature of the pores since at high scan rates the deep insides of the pores can not be accessed.

To get the in depth information about the capacitive nature of the Co_3O_4 nanorod based electrodes, charge-discharge (CDC) experiments are carried out. The charge-discharge (CDC) experiment is carried out in 6 M KOH electrolyte with the charging-discharging rate equivalent to a current density equivalent of 1 A/g. Figure 4.11 shows the calculated capacitance value with CDC cycle number. The region of the curve from 0.1 to 0.6 V on the y-axis represents the electrochemical redox reaction. The capaci-

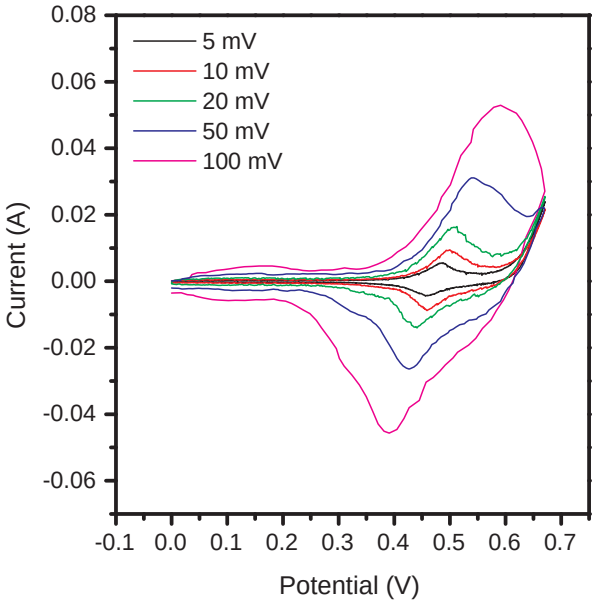

.

Figure 4.9: Comparison of the cyclic voltammetry curves of porous CC-300 measured at different scan rates.

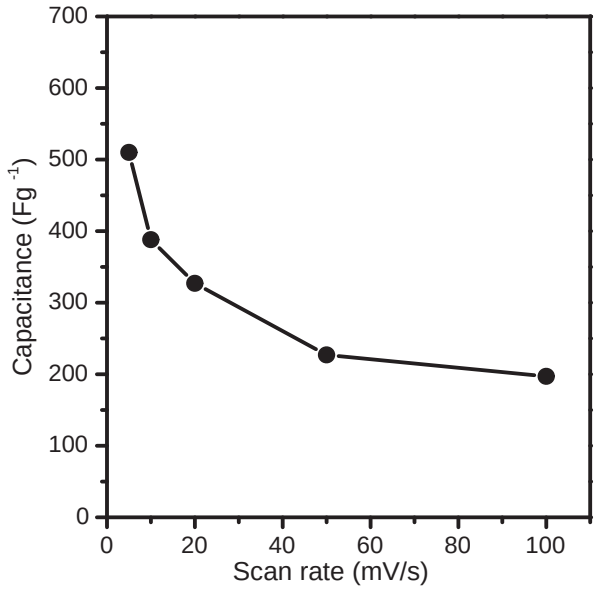

.

Figure 4.10: Scan rate dependent capacitance of CC-300 nanorods.

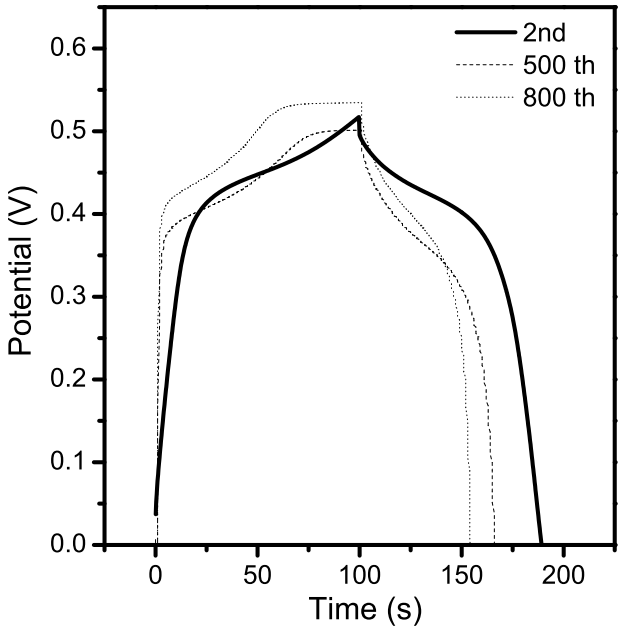

Figure 4.11: Galvanostatic charge-discharge curve obtained for porous CC-300 nanorods at various cycles - 2^{nd}, 500 th and 800 th cycle confirming the cycle stability of the electrode.

tance is measured from the slope of the curve given by $I \times \Delta t/\Delta V \times m$, where I is the galvanostatic discharging current, Δt is the discharging time, ΔV is the potential drop during discharge, and m represents the mass of the electroactive material. The obtained capacitance value is found to be quite high with the value of 600 Fg^{-1} that is in close agreement with the capacitance calculated from the CV measurements. Further, these values are also close to the capacitance value of state of art material RuO_2 (720 Fg^{-1}).

Another important issue is the cycle life. Co_3O_4 based materials are normally known for their poor durability [37]. The CDC curves for the 2^{nd}, 500^{th} and 800^{th} cycles shown in Figure 4.11 confirm that there is no significant variation in the capacitance even after 800 cycles of CDC operation. One interesting observation is that, with cycle number, the contribution of electric double layer charging also increases significantly suggesting the increased pore openings and higher accessibility. This is in accordance with the very high surface area and highly porous nature of the CC-300 nanorods which allows very short paths for the ions to reach the interior and thus keeps the integrity of the material intact.

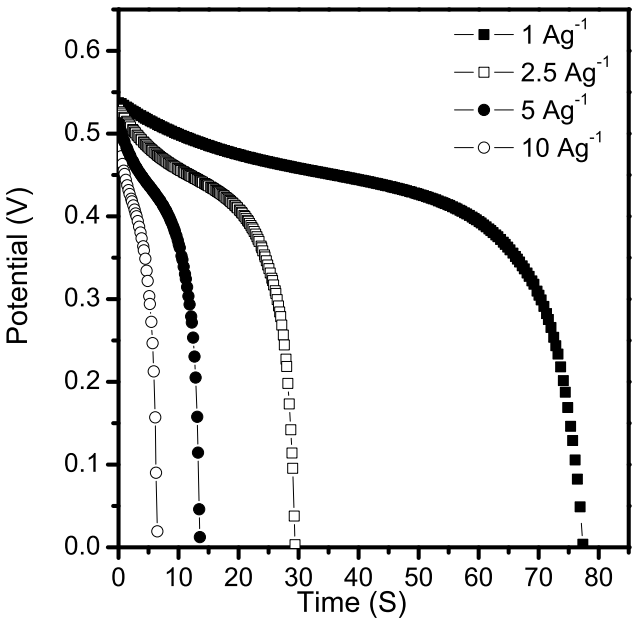

Figure 4.12: Response of CC-300 discharged at different current densities.

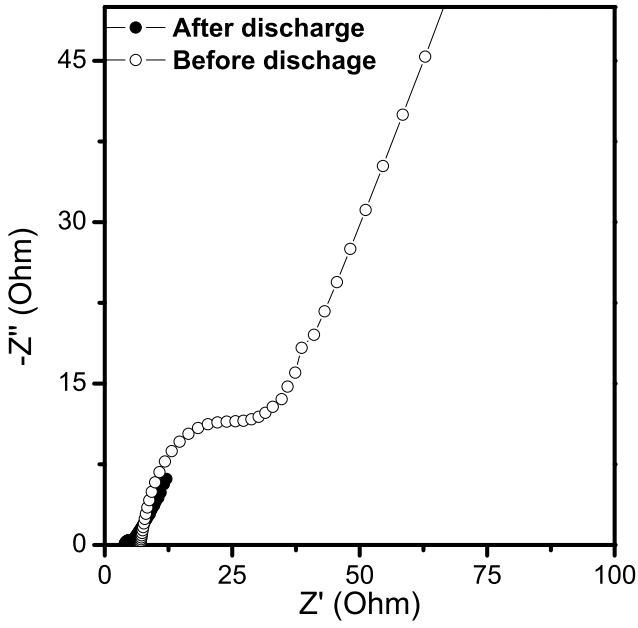

Figure 4.13: Impedance spectroscopy analysis of porous CC-300 nanorods.

The material CC-300 has also been tested at different discharge current densities as shown in Figure 4.12. The figure clearly shows the trend of decrease in the response time as there is an increase in the discharge current densities. The results are well in agreement with the CV data, as at higher CDC rates the capacitance is observed to be low and able to deliver the charge in few seconds. The electrochemical impedance spectroscopy analysis was carried out in the frequency range of 0.01 to 1 MHz with ac voltage amplitude of 5 mV to further substantiate the capacitive performance of CC-300 material at the open-circuit potential. The typical Nyquist plot of CC-300 electrode before and after CDC is shown in Figure 4.13. From the high frequency intercept at the x-axis, one can calculate the electrode-electrolyte total system resistance. An initial resistance value of 28.7 Ω is reduced to 1.7 Ω after CDC experiments, revealing the increased exposure of the pores due to the prolonged operation. This fact further emphasizes that initially not all the pores in the electrode are used for charge storage and also at very high scan rates. However, at low scan rates, majority of the pores could be accessed that result in higher capacitance values.

4.4 Conclusions

The porous Co_3O_4 nanorods are demonstrated to have a capacity of 1155 $mAhg^{-1}$ in Li-ion battery, during initial cycles, followed by excellent durability of providing the capacitance value of 820 $mAhg^{-1}$ for 25 cycles and beyond with out any obvious signs of capacity loss or performance degradation. The reason behind this enhanced capacity is probably due to the porous nature of the nanostructured material, which results in reduced volume change upon insertion/deinsertion, which also results in better cycle life. Solid state NMR study confirms the change in Li environment during the discharge process. The XRD measurements after charge and discharge prove the stability of the material and at the same time the formation of Co nanodomains has been confirmed by magnetic measurements. Also the material exhibited a considerably quite high value of capacitance (600 Ag^{-1}) during the galvanostatic discharge measurement, indicating the applicability of porous nanorods of Co_3O_4 as a suitable material for supercapacitor applications.

References

[1] G. Nazri, G. Pistoia, *Lithium Batteries: Science and Technology,* Springer Netherlands, 2004.

[2] W.A. van Schalkwijk, B. Scrosati, *Advances in Lithium-Ion Batteries,* Plenum Pub Corp, 2002.

[3] M. Wakihara, O. Yamamoto, *Lithium Ion Batteries: Fundamentals and Performance,* Wiley-Vch, 1998.

[4] G. Pistoia, *Battery Operated Devices and Systems: From Portable Electronics to Industrial Products,* Elsevier Science Ltd, 2008.

[5] S. Dhameja, *Electric Vehicle Battery Systems,* Newnes, 2002.

[6] Y.M. Kang, M.S. Song, J.H. Kim, H.S. Kim, M.S. Park, J.Y. Lee, H.K. Liu, S.X. Dou, *Electrochim. Acta.* 50 (2005) 3667.

[7] W. Li, F. Cheng, Z. Tao, J. Chen, *J. Phys. Chem. B* 110 (2006) 119.

[8] M.S. Park, G.X. Wang, Y.M. Kang, D. Wexler, S.X. Dou, H.K. Liu, *Ang. Chem. Int. Ed.* 46 (2007) 750.

[9] S.H. Yoon, C.W. Park, H.J. Yang, Y. Korai, I. Mochida, R.T.K. Baker, N.M. Rodriguez, *Carbon* 42 (2004) 21.

[10] M.V. Reddy, S.S. Manoharan, J. John, B. Singh, G.V.S. Rao, B.V.R. Chowdari, *J. Electrochem. Soc.* 156 (2009) A652.

[11] C.K. Chan, H.L. Peng, G. Liu, K. McIlwrath, X.F. Zhang, R.A. Huggins, Y. Cui, *Nat. Nanotechnol.* 3 (2008) 31.

[12] X.P. Gao, J.L. Bao, G.L. Pan, H.Y. Zhu, P.X. Huang, F. Wu, D.Y. Song, *J. Phys. Chem. B* 108 (2004) 5547.

[13] Y. Wang, H.C. Zeng, J.Y. Lee, *Adv. Mater.* 18 (2006) 645.

[14] D.W. Kim, I.S. Hwang, S.J. Kwon, H.Y. Kang, K.S. Park, Y.J. Choi, K.J. Choi, J.G. Park, *Nano Lett.* 7 (2007) 3041.

[15] M.S. Whittingham, *Chem. Rev.* 104 (2004) 4271.

[16] Y. Idota, T. Kubota, A. Matsufuji, Y. Maekawa, T. Miyasaka, *Science* 276 (1997) 1395.

[17] J. Chen, L. Xu, W. Li, X. Gou, *Adv. Mater.* 17 (2005) 582.

[18] P.L. Taberna, S. Mitra, P. Poizot, P. Simon, J.M. Tarascon, *Nat. Mater.* 5 (2006) 567.

[19] T. Cassagneau, J.H. Fendler, *Adv. Mater.* 10 (1998) 877

[20] J.B. Goodenough, Y. Kim, *Chem. Mater.* 22 (2010) 587.

[21] M. Winter, R.J. Brodd, *Chem. Rev.* 104 (2004) 4245.

[22] P. Justin, S.K. Meher, G.R. Rao, *J Phys Chem C.* 114 5203.

[23] V. Subramanian, H. Zhu, B. Wei, *J. Power Sources* 159 (2006) 361.

[24] J. Cheng, G.P. Cao, Y.S. Yang, *J. Power Sources* 159 (2006) 734.

[25] Y. Li, B. Tan, Y. Wu, *Nano Lett.* 8 (2008) 265.

[26] K.T. Nam, D.W. Kim, P.J. Yoo, C.Y. Chiang, N. Meethong, P.T. Hammond, Y.M. Chiang, A.M. Belcher, *Science* 312 (2006) 885.

[27] F. Zhan, B. Geng, Y. Guo, *Chem. Eur. J.* 15 (2009) 6169.

[28] W.Y. Li, L.N. Xu, J. Chen, *Adv. Funct. Mater.* 15 (2005) 851.

[29] B. Guo, C. Li, Z.Y. Yuan, *J. Phys. Chem. C* 114 (2010) 12805

[30] L. Cui, J. Li, X.G. Zhang, *J. App. Electrochem.* 39 (2009) 1871.

[31] S.L. Xiong, C.Z. Yuan, M.F. Zhang, B.J. Xi, Y.T. Qian, *Chem. Eur. J.* 15 (2009) 5320.

[32] X.W. Lou, D. Deng, J.Y. Lee, J. Feng, L.A. Archer, *Adv. Mater.* 20 (2008) 258.

[33] P. Poizot, S. Laruelle, S. Grugeon, L. Dupont, J.M. Tarascon, *Nature* 407 (2000) 496.

[34] Y. Li, B. Tan, Y. Wu, *Nano lett.* 8 (2008) 265.

[35] Y. Liu, W. Zhao, X. Zhang, *Electrochim. Acta* 53 (2008) 3296.

[36] S.L. Xiong, C.Z. Yuan, M.F. Zhang, B.J. Xi, Y.T. Qian, *Chem. Eur. J.* 15 (2009) 5320.

[37] L. Wang, X. Liu, X. Wang, X. Yang, L. Lu, *Curr. Appl. Phys.* 10 (2010) 1422.

Chapter 5

Synthesis and Magnetic Properties of Nanocrystalline Spinel Ferrites

5.1 Introduction

Spinel type ferrites crystalize with the general formula MFe_2O_4, where M is a divalent ion such as Mg, Fe, Mn, Ni, Zn, Co, Cu etc [1]. Most of the commercially used ferrites are solid solutions of more than one ferrite, represented by the general formula $M_{1-x}M'_xFe_2O_4$, where M and M' are divalent metal ions [2]. Ferrites are well known for their ability to combine extremely high electrical resistivity with magnetic properties, which helps in the operation without any eddy-current loss at high frequencies.

Spinel type ferrites in the nanocrystalline form have attracted the attention of the researchers because of the interesting properties that they exhibit [3–7]. The properties such as superparamagnetic blocking temperature, saturation and remnant magnetizations, coercivity, etc, depend on the particle size [8, 9]. The distribution of cations in the tetrahedral and octahedral sites of the spinel structure is an important factor deciding the properties they exhibit. The degree of inversion of the cations between tetrahedral and octahedral sites are found to be different in nanosized ferrite particles [10]. Higher Curie temperatures are reported for nanoparticles due to the difference in the cation distribution [11, 12]. Room temperature ferrimagnetism is observed in nanosized zinc ferrite particles where as the bulk material is paramagnetic [13, 14]. Hence, due to the nanosized nature, different magnetic properties are exhibited by ferrite particles when compared to their bulk counter parts. Monodispersed ferrite particles such as that of magnetite or maghemite exhibiting superparamagnetic property are widely studied for their use in biomedical applications such as in drug delivery, MRI contrasting agent, etc [15–17].

A simple and facile coprecipitation/digestion method was found to be effective for the synthesis of the spinel type cobalt oxide (Co_3O_4) nanorods using a molecular precursor approach. The same synthetic protocol is employed for the synthesis of nanocrystalline spinel type ferrites Fe_3O_4, $ZnFe_2O_4$ and $CoFe_2O_4$, and their magnetic properties have been evaluated.

5.2 Nanocrystalline Fe_3O_4

Magnetite (Fe_3O_4) is a naturally available mineral, the first magnetic material known to the mankind. It is an important compound of interest from both scientific and technological point of view. It has a cubic inverse spinel structure with the tetrahedral sites occupied by Fe^{3+} ions and the octahedral sites occupied by Fe^{3+} and Fe^{2+} ions. Fe_3O_4 is ferrimagnetic at room temperature with a Curie temperature as high as 873 K [18]. The very high saturation magnetization of bulk Fe_3O_4 at room temperature (92 emu/g) makes this material applicable in giant magnetoresistance (GMR) devices, as an oxide layer as well as a magnetic layer [19]. A large magnetoresistance effect up to 500% at room temperature has been reported for nanocrystalline Fe_3O_4 powders. Hence, it is a potential candidate to use as a tunneling junction in stacked monolayers [20]. Also, due to its biocompatability, it is highly useful in biomedical applications [16, 21].

There are several methods available for the synthesis of nanocrystalline Fe_3O_4 such as coprecipitation [22], γ-ray radiation [23], microwave [24], hydrothermal method [25] etc. Nanocrystalline Fe_3O_4 is sensitive to air and moisture, hence its surface can get oxidized in air. So it can be slowly converted into maghemite (γ-Fe_2O_3). Maghemite is a mineral belongs to the family of ferrites with a structure similar to that of Fe_3O_4. It can be considered as an Fe(II)-deficient magnetite (Fe_3O_4) with the general formula $(Fe_8^{III})_A[Fe_{40/3}^{III}\square_{8/3}]_BO_{32}$, where A and B represents the tetrahedral A and octahedral B sites, respectively in the spinel AB_2O_4 lattice [26]. It has a cubic unit cell with the a value of 8.34 Å. Eight cations occupy the tetrahedral sites and the remaining cations are randomly distributed over the octahedral sites [27]. The vacancies are confined to the octahedral sites. One of the potential application of maghemite is its usage in magnetic recording [28]. There are several methods available for the synthesis of maghemite [29–35].

It is well known that magnetite can be readily oxidized to maghemite. It can be ob-

served by the colour change of the magnetite from its black colour to the brown colour of maghemite, even at room temperature [36]. At higher temperatures > 300 °C, further transformation may take place to give rise to hematite (α-Fe_2O_3). The following section describes the synthesis of Fe_3O_4 in the form of nanoparticles by the coprecipitaion/digestion method. The effect of digestion time on the structure and magnetic properties is investigated.

5.2.1 Synthesis

Nanocrystalline Fe_3O_4 samples were prepared by the coprecipitation/digestion method as described in *section 2.1.1*. In a typical synthesis, the ratio between Fe^{2+} and Fe^{3+} is maintained as 1:2. Initially a four necked round bottom flask (RBF) containing distilled water was heated at 70 °C. A condenser circulating water was fixed to one of the necks of the RBF to avoid any evaporation of the solvent. Through a gas purger, constant flow of argon gas was maintained. Under this condition a mixed water solution of 0.05 M ferrous chloride and 0.1 M ferric chloride were added drop wise through a burette. A calibrated amount of ammonium carbonate solution (0.5 M) was taken in a separate burette and added simultaneously to the RBF. After the complete addition of the two solutions, the precipitate formed was allowed to digest for different durations. Then the precipitate was filtered and washed thoroughly with sufficient amount of distilled water to remove the chloride impurity. The precipitate was dried and stored in a vacuum desiccator. The corresponding codes of the samples synthesized under different digestion times are given in Table 5.1.

5.2.2 Characterization and Magnetic Properties

Figure 5.1 shows the powder XRD patterns of the Fe_3O_4 samples prepared by varying the digestion time from 0–8 hours. All the patterns can be indexed to the cubic spinel type Fe_3O_4 (a = 8.396 Å, JCPDS # 19-0629). A close observation of the XRD patterns, as shown in Figure 5.2, reveals that there is a shift in the position of the peaks to higher diffraction angles with increase in the digestion time. This indicates a decrease in the lattice parameter with digestion time. Since γ-Fe_2O_3 (JCPDS # 39-1346) has a similar structure to that of Fe_3O_4, with a lower lattice parameter of 8.336 Å, it is possible that

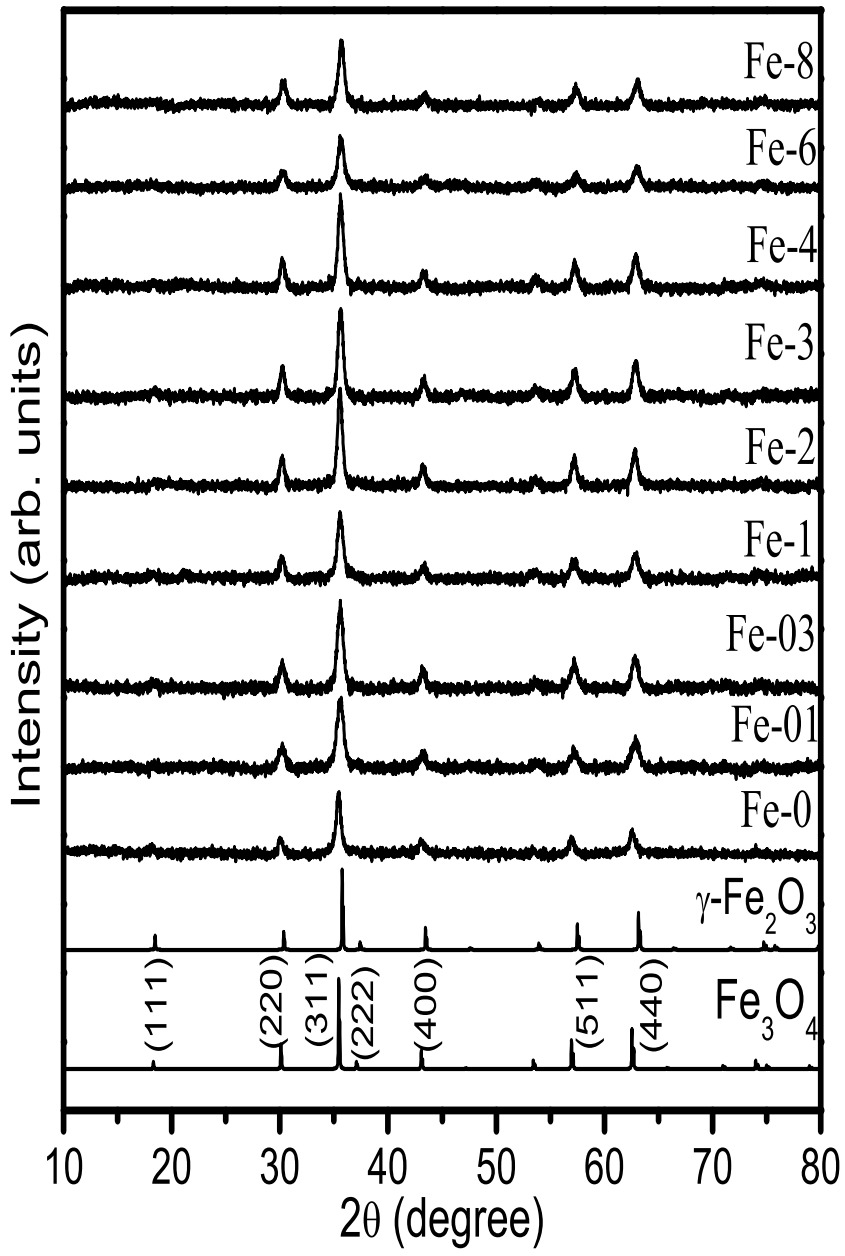

Figure 5.1: Powder XRD patterns of the different samples, Fe-0 to Fe-8. The simulated patterns of Fe_3O_4 and γ-Fe_2O_3 are shown for comparison.

.

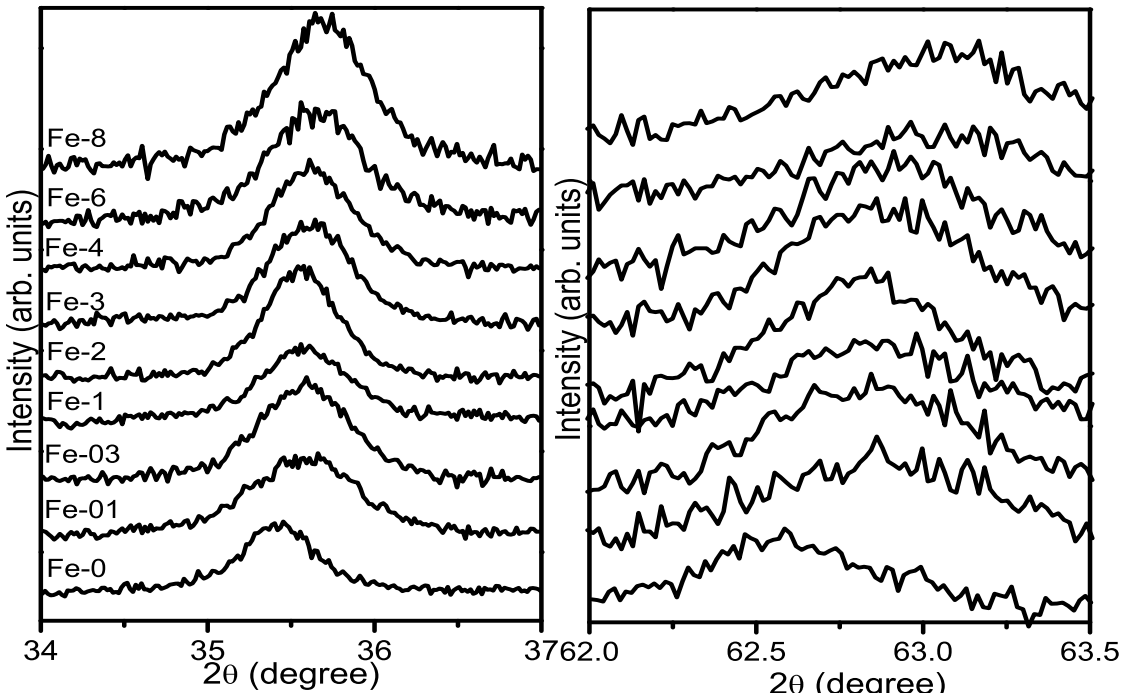

Figure 5.2: Shift in the (311) and (440) reflections of the samples synthesized at different digestion times.

.

the surface of the particles get oxidized and there is a possibility for the formation of γ-Fe_2O_3 on the surface of the particles. Because of the similar structure and comparable lattice parameters, XRD studies could not be used to distinguish the two materials [37].

The cubic lattice parameter is calculated by least-squares fitting of the patterns and the values are given in Table 5.1. The lattice parameter of Fe-0 is less than that of Fe_3O_4 reported in the literature (8.396 Å) and the lattice parameter decreases with increasing digestion time. Lattice parameter is known to decrease with increasing cation deficiency. A variation in the lattice parameter from 8.38 Å to 8.33 Å is reported for the variation of the Fe:O ratio from 0.72 (defect Fe_3O_4) to 0.67 (γ-Fe_2O_3) [38]. Thus the results suggest that Fe-0 is slightly cation deficient and the cation deficiency increases and the composition moves towards that of γ-Fe_2O_3 with increasing digestion time. The calculated lattice parameter shows that Fe-8 is more closer to $\gamma - Fe_2O_3$.

Broad peaks are observed in all the XRD patterns and the peak broadening indicates

Table 5.1: Sample code, digestion time, crystallite size and lattice parameter of the Fe_3O_4 samples digested for different durations.

Sample code	Digestion time (h)	Crystallite size (±1 nm)	Lattice parameter (Å)
Fe-0	0	9	8.373
Fe-01	0.15	12	8.375
Fe-03	0.30	12	8.366
Fe-1	1.00	14	8.367
Fe-2	2.00	18	8.366
Fe-3	3.00	16	8.367
Fe-4	4.00	17	8.367
Fe-6	6.00	18	8.364
Fe-8	8.00	18	8.345

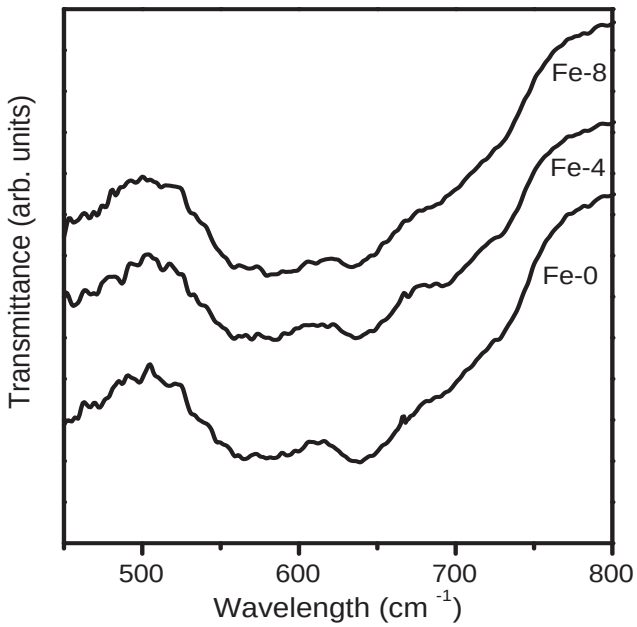

.

Figure 5.3: FTIR spectra of Fe-0, Fe-4 and Fe-8

..

the nanocrystalline nature of the samples. The average crystallite sizes are calculated using the Scherrer formula and the calculated values are shown in Table 5.1. There is a continuous increase in the crystallite size with increasing digestion time, due to the growth of the particles during the digestion.

The different samples are further characterized by infrared spectroscopy to get information on the structural changes taking place with variation in the digestion time. Figure 5.3 shows the FTIR spectra of the samples Fe-0, Fe-4 and Fe-8. Two broad bands are observed at ∼570 cm^{-1} and ∼635 cm^{-1}. For spinel type ferrites, four bands are expected in the infrared spectra [39]. Fe_3O_4 exhibits two strong bands at 570 cm^{-1} and 390 cm^{-1}, due to ν_1 and ν_2 modes of vibrations. The ν_1 vibration is assigned to Fe-O stretching mode of Fe in the octahedral and tetrahedral sites and ν_2 due to Fe-O stretching mode in the octahedral site [40]. For defect-free Fe_3O_4, with lattice parameter of 8.396 Å, a strong band at 570 cm^{-1} is expected. Splitting of the ν_1 and ν_2 bands is expected with increasing cation deficiency [41]. The ν_1 band gives rise to another band at 630 cm^{-1} due to the splitting. As Fe-0 shows two bands at ∼570 cm^{-1} and ∼635 cm^{-1}, these bands can be assigned to the Fe-O stretching mode of the tetrahedral and octahedral sites and it can be assumed that the sample is cation deficient Fe_3O_4. Also, the lower lattice parameter of this sample (8.373 Å) compared to that of stoichiometric magnetite (8.396 Å) supports this conclusion, as the lattice parameter decreases with increasing cation deficiency [38]. The IR spectral data along with the structural data indicate that the deficiency increases with increasing digestion time and that the sample obtained after 8 hour digestion is a defective spinel close to that of γ-Fe_2O_3.

Figure 5.4 reveals the morphological features of the samples Fe-0 and Fe-8. The particle sizes of both the samples are in the range 10-20 nm. In both the cases, the particles are almost spherical in nature. It is clear from the images that the particles are aggregated together. From the ring type pattern observed in SAED, the polycrystalline nature of the samples can be confirmed.

The effect of the digestion time on the magnetic properties of the samples are analyzed from the magnetic measurements. The room temperature magnetization curves of the samples digested for different time durations are shown in Figure 5.5 and the corresponding enlarged curves are shown in inset of Figure 5.5. The initial magnetization

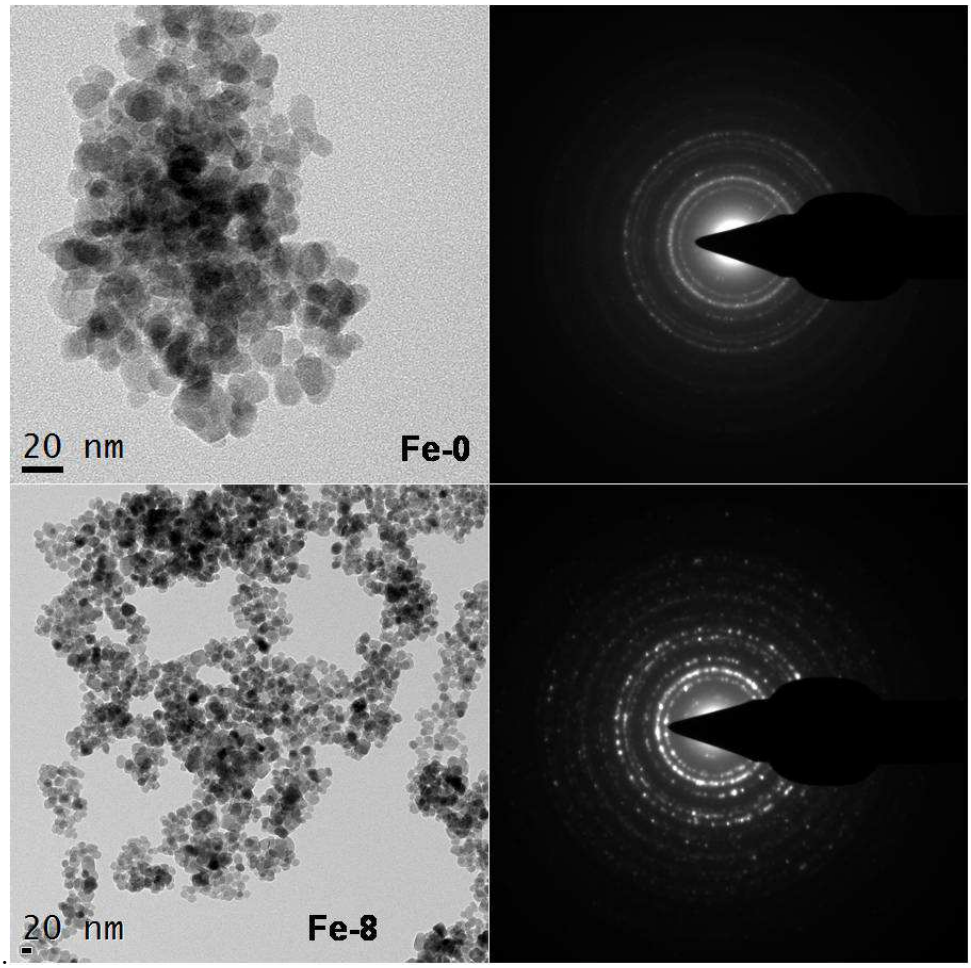

Figure 5.4: HRTEM images of Fe-0 and Fe-8 and the corresponding SAED patterns (right).

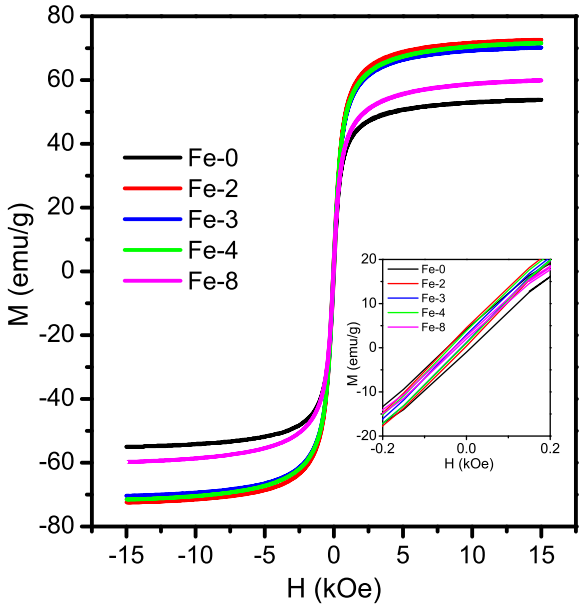

Figure 5.5: M vs H curves of Fe-0, Fe-2, Fe-3, Fe-4 and Fe-8 at room temperature.

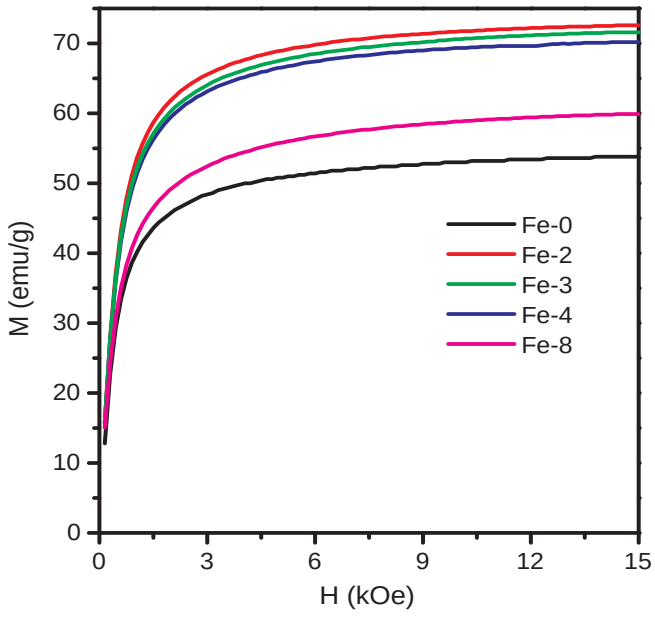

Figure 5.6: Initial magnetization curves of Fe-0, Fe-2, Fe-3, Fe-4 and Fe-8.

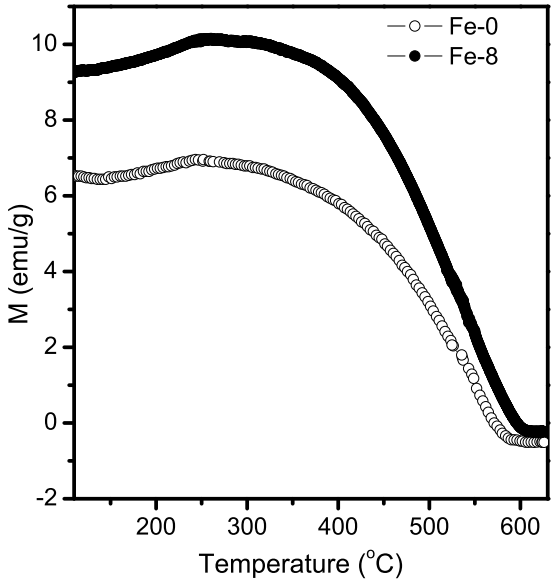

Figure 5.7: M vs T measurement above room temperature of Fe-0 and 8 at 50 Oe.

curves of the samples are shown in Figure 5.6. Magnetization is almost saturated at 15 kOe. Coercivity values in the range 10-30 Oe is observed for the different samples. Observation of a coercive field at room temperature indicates that the superparamagnetic blocking temperature is above room temperature. The saturation magnetization is obtained as 53.8 emu/g for Fe-0 and the magnetization initially increased and then decreased with increasing digestion time and a maximum value of 72.6 emu/g is obtained for Fe-2. The value remains almost constant in the range 70–72 emu/g for digestion times of 2–4 hr. For Fe_3O_4, saturation magnetization is ∼92 emu/g and the corresponding value for γ-Fe_2O_3 is ∼75 emu/g [42, 43]. Hence, a decrease in the saturation magnetization is expected with increasing cation deficiency. However, the magnetization will increase with increasing particle size. Therefore, both factors are responsible in the present case for the initial increase and further decreasing value of magnetization for the cation deficient samples. The variation in the M_s can be due to the various factors, such as particle size and distribution, surface properties, cation deficiency, and cation distribution. For example, Fe_3O_4 nanoparticles with size 40 nm showed M_s value of ∼85.8 emu/g [44] slightly

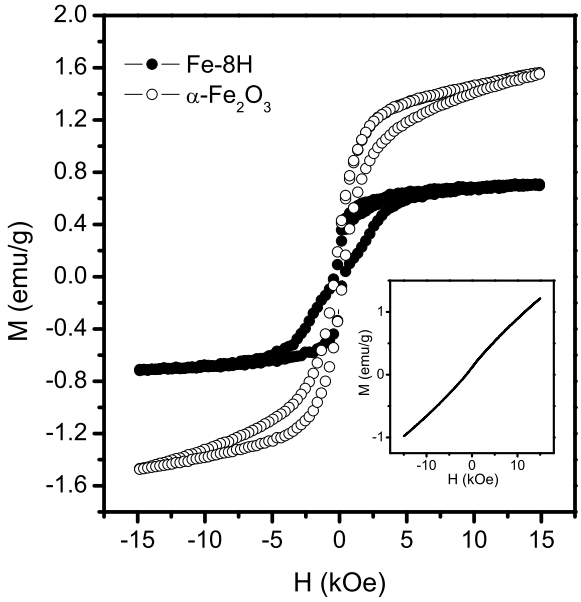

Figure 5.8: M vs H measurement of Fe-8H, commercial α-Fe_2O_3 (Aldrich), and A-Fe-8 at room temperature.

below that of the bulk Fe_3O_4 (92 emu/g) [42, 43], where as with a size of 25 nm the obtained saturation magnetization is 12.3 emu/g [44]. Similarly, a value of 67.8 emu/g [45] is obtained for the particle size of 12.4 nm, when compared to the value of 12.3 emu/g for the particle size of 25 nm [44]. Hence, depending on the value of M_s alone one can not distinguish between Fe_3O_4 and γ-Fe_2O_3, especially in the case of nanocrystalline samples and defect structures.

Although it is very difficult to distinguish between Fe_3O_4 and γ-Fe_2O_3 through XRD and room temperature magnetization measurements, it is well known that γ-Fe_2O_3 is thermally unstable. It will be converted to the more stable hexagonal α-Fe_2O_3 at 673 K when heated in air. This phase transformation can be observed as a magnetic transition, when the magnetization is recorded as a function of temperature. On the other hand Fe_3O_4 is highly stable and it will retain its magnetization value until its transition temperature (T_C) of $\sim$873 K is reached [46]. Hence, to know the nature of the samples, both Fe-0 and Fe-8 were subjected to magnetic measurement as a function of temperature above room temperature and the results are shown in Figure 5.7. Both the samples did not show

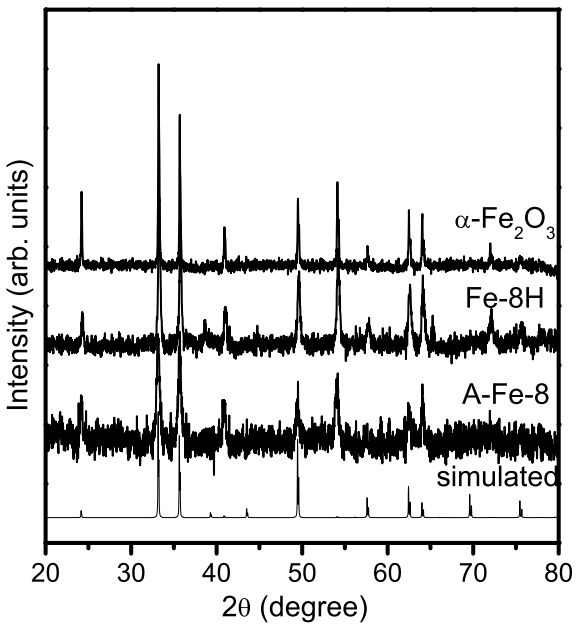

Figure 5.9: XRD patterns of A-Fe-8, α-$Fe_2O_3$and Fe-8H. T he simulated pattern of α-Fe_2O_3 is shown for comparison.

any magnetic transition at 673 K where the conversion of γ-Fe_2O_3 to stable α-Fe_2O_3 is expected. The observed magnetic transition is around 873 K, closer to the T_C of Fe_3O_4. This indicates that sample Fe-8 is not γ-Fe_2O_3, even though the lattice parameter is closer to that of this compound.

Further, to confirm the nature of the sample after high temperature (HT) magnetic measurements, the magnetization of Fe-8 is measured at room temperature, after cooling. This sample is labeled as Fe-8H. Figure 5.8 shows the room temperature magnetic data of the sample Fe-8H. During the high temperature measurement the sample was heated above 600 °C, hence it is expected that there will be a conversion of Fe_3O_4 to α-Fe_2O_3, due to the defect structure. It is well known that α-Fe_2O_3 exhibits a weak ferromagnetism [47]. Hence, for comparison, magnetization of commercial α-Fe_2O_3 is also measured. Figure 5.8 compares the magnetic characteristics of the sample Fe-8H with the commercially available α-Fe_2O_3. Compared to the value for commercial sample, the magnetization of Fe-8H is slightly smaller. The possible reason may be the particle size of Fe-8H (35 nm) which is

smaller than the particle size of the commercial sample (70 nm). To confirm the particle size effect, α-Fe_2O_3 was freshly prepared (A-Fe-8) through the same synthesis method using only ferric nitrate. Particle size of A-Fe-8 is obtained as 15 nm, comparable to that of Fe-8 and the magnetization curve of this sample is shown in the inset of Figure 5.8. It exhibits a superparamagnetic behavior. The XRD patterns of the samples Fe-8H, commercial α-Fe_2O_3 (Aldrich) and A-Fe-8 are compared in Figure 5.9. XRD analysis has confirmed that the recovered sample Fe-8H is α-Fe_2O_3.

5.2.3 Conclusions

A simple coprecipitation/digestion method is employed for the synthesis of nanosized Fe_3O_4. The effect of digestion time on the structure and properties has been analyzed. A decrease in the cubic lattice parameter, shifting towards the value for γ-Fe_2O_3, is observed with increase in the digestion time. This coupled with IR analysis indicated presence of cation deficiency in the samples, where the Fe:O ratio decreasing with increasing digestion time. Room temperature saturation magnetization initially increased and further decreased with increasing digestion time and this could be explained in terms of the competition between increasing particle size and increasing cation deficiency. Magnetic measurements above room temperature showed that the compositions of the samples are closer to that of Fe_3O_4.

5.3 Nanocrystalline $ZnFe_2O_4$

$ZnFe_2O_4$ belongs to the normal spinel type structure with the Zn^{2+} ions occupying the tetrahedral sites and the Fe^{3+} ions occupying the octahedral sites [2]. The material is paramagnetic at room temperature and becomes antiferromagnetic below the Néel temperature of about 10.5 K. However, Néel suggested that small antiferromagnetic particles can exhibit superparamagnetism and weak ferromagnetism due to uncompensated spins in the two sublattices [48].

It is well known that by changing the cation distribution in ferrites, one can tune the magnetic and electrical properties [13,14,49–52]. There are several reports demonstrating that when normal spinel ferrites becomes nanosized there is a change in the cation distribution, which enhances the magnetic properties [13,53–60]. When $ZnFe_2O_4$ is prepared in

Table 5.2: Sample codes and synthesis conditions of $ZnFe_2O_4$ (ZFO) synthesized by the coprecipitation/digestion method at 70 °C

Sample code	Digestion time (h)
ZF-0	0
ZF-4	4
ZF-8	8

nanocrystalline form, Zn ions can enter into the octahedral sites, resulting in a flexibility in the composition [13, 61]. When a fraction of Zn^{2+} ions prefers to occupy the B sites, there will be a simultaneous occupancy of the A sites by Fe^{3+} ions making the system partially inverted [56, 62]. Studies showed that there is 80% inversion in the case of 4 nm $ZnFe_2O_4$ particles, 40% inversion for 6 nm particles, and negligible inversion for particles of size 7 nm and above [63]. A saturation magnetization (M_s) value of 54.6 emu/gm [64] has also been reported at room temperature. Whereas, in some cases superparamagnetic behavior has been observed for particles of comparable size [56, 65]. Very high Curie temperature is reported for nanoparticles of zinc ferrite [66]. It has been shown that surface effects are more prominent in determining the magnetic properties [51].

Several methods such as coprecipitation [53], hydrothermal [64, 67], mechanochemical reaction [68], electric discharge method [69] and wet milling method [70] have been employed for the synthesis of nanosized $ZnFe_2O_4$. Some synthesis methods also result in the formation of minor amounts of impurity phases like ZnO and α-Fe_2O_3 also during the synthesis. Since the particle size and synthesis methods have influence over the magnetic properties, it is very crucial to synthesize phase pure nanosized $ZnFe_2O_4$ particles.

An attempt has been made to synthesize single phase nanosized $ZnFe_2O_4$ by the modified coprecipitation/digestion method and through a self ignited auto-combustion method using glycine as the fuel. The effect of digestion time in the coprecipitation/digestion method on the magnetic properties has been studied and compared with the sample synthesized through the auto-combustion method.

5.3.1 Synthesis

Nanocrystalline $ZnFe_2O_4$ (ZFO) was synthesized by the coprecipitation/digestion and also by the glycine-nitrate auto-combustion method. The detailed description of the coprecipitaion method is given in *section 2.1.1.* In brief, a mixed water solution of 0.05 M zinc nitrate and 0.1 M ferric nitrate was added drop wise to distilled water kept at 70 °C in a three necked RBF connected with a condenser. To this 0.40 M potassium carbonate solution was added simultaneously to precipitate the nitrate solution. The precipitate formed was then digested in the mother liquor for different time intervals as mentioned in the Table 5.2. After digestion, the precipitate was washed thoroughly to remove the K^+ ion contamination. The precipitate was filtered and dried in an oven at 70 °C overnight.

For the sample synthesized by the auto-combustion method, glycine is used as the fuel. The details of the method is explained in *section 2.1.2.* In a typical synthesis 1 mole of zinc nitrate and 2 moles of ferric nitrate were dissolved in minimum amount of distilled water. To this 1 mole of glycine dissolved in distilled water was added and mixed together. The homogeneous solution was kept on a hot plate at ∼200 °C until it is burned completely. The corresponding fluffy mass obtained is labeled as ZFG1.

5.3.2 Characterization and Magnetic Properties

Figure 5.10 shows the powder XRD patterns of the samples synthesized by the coprecipitation/digestion and auto-combustion methods. The simulated pattern of $ZnFe_2O_4$ is also shown in the figure for comparison. All the peaks in the XRD patterns correspond to that of zinc ferrite. There are no extra reflections other than the ones corresponding to spinel zinc ferrite (JCPDS # 22-1012) with a=8.441 Å, confirming that the material is phase pure. The crystallinity of the samples ZF-0 to ZF-8 increases with increasing digestion time, as evidenced from the increasing intensity and decreasing width of the diffraction peaks. This indicates that the digestion at 70 °C for longer duration helps in improving the crystallinity. The XRD pattern of ZFG1 exhibits much broader peaks due to the nanosized particles. The crystallite size of the samples is calculated using the Scherrer formula. The calculated crystallite size and the corresponding lattice parameter are given in Table 5.3. The lattice parameters of all the samples are comparable to that of $ZnFe_2O_4$.

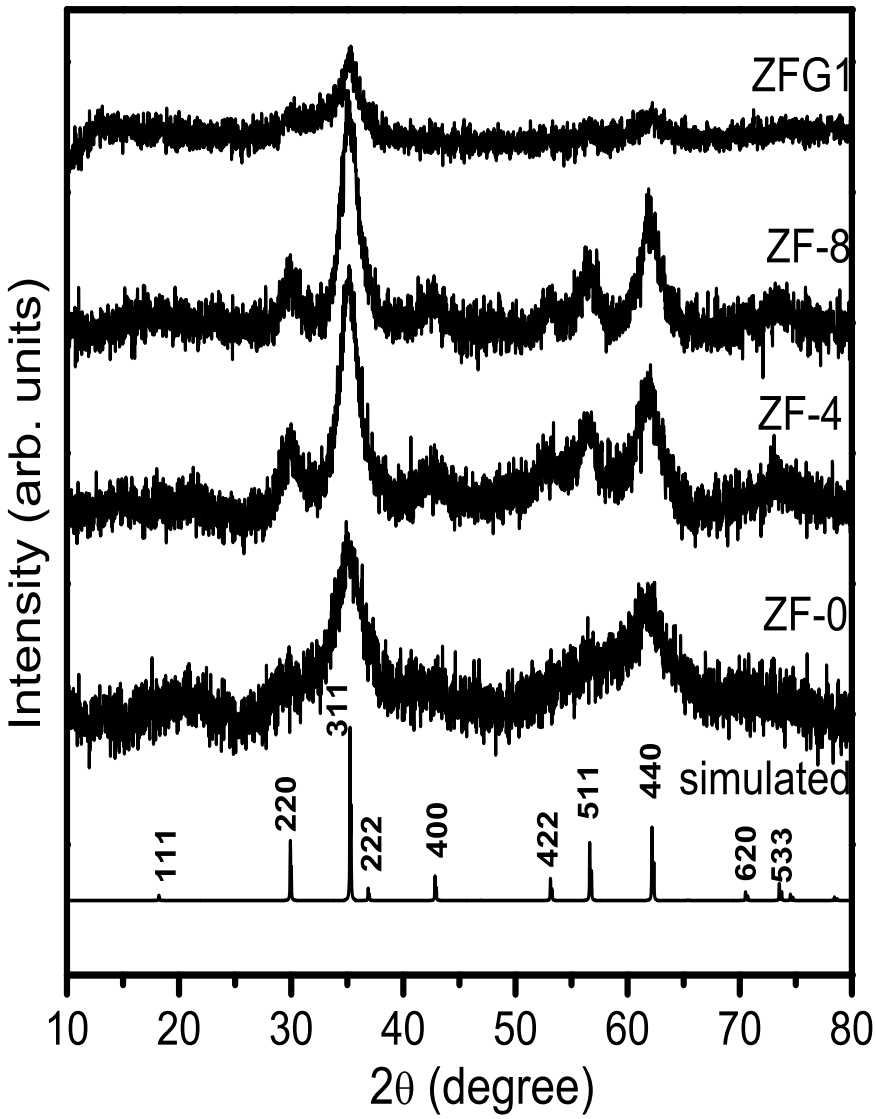

.

Figure 5.10: XRD pattern of ZF-0, ZF-4, ZF-8 and ZFG1, compared with the simulated pattern of $ZnFe_2O_4$

..

Table 5.3: Crystallite size and lattice parameters of different $ZnFe_2O_4$ samples.

Sample code	Crystallite size (± 1 nm)	Lattice parameter (Å)
ZF-0	3	8.450
ZF-4	5	8.457
ZF-8	6	8.458
ZFG1	8	8.434

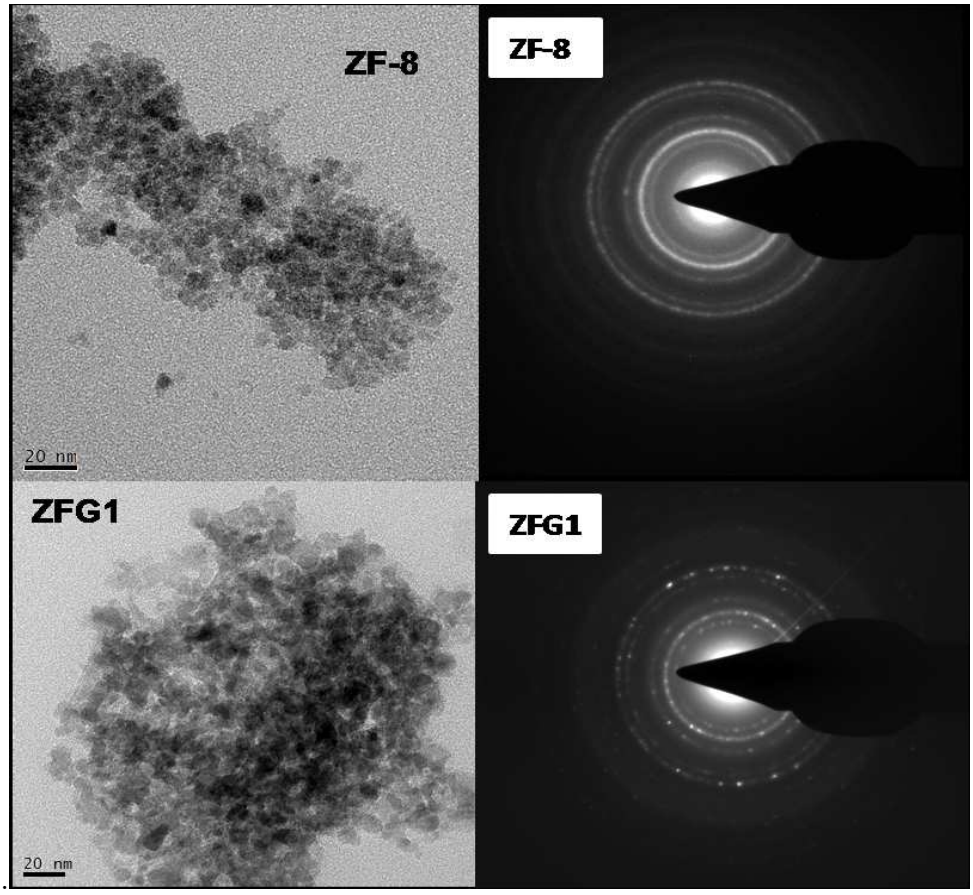

Figure 5.11: HRTEM images and the corresponding SAED patterns of ZF-8 and ZFG1

..

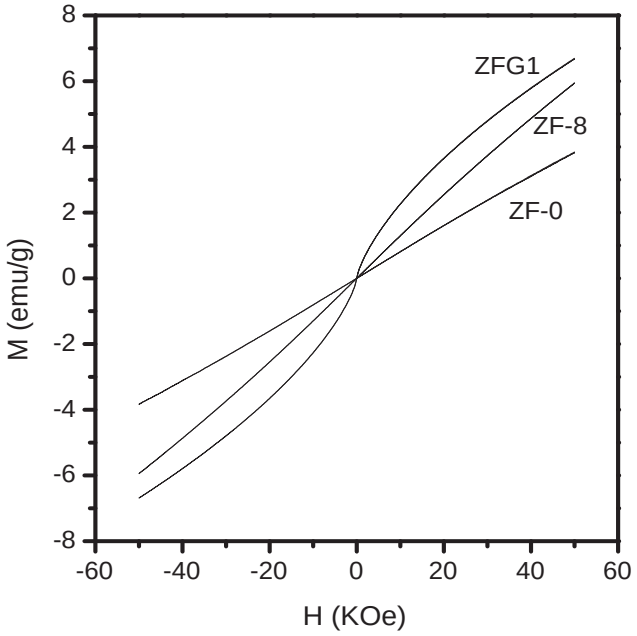

.

Figure 5.12: M vs H curves of ZF-0, ZF-8 and ZFG1 at 300 K

..

Morphological features the samples ZF-8 and ZFG1 are obtained from HRTEM as shown in Figure 5.11. The micrographs show that the particle size distribution is narrow in both the cases. In both the cases the particles formed are spherical in nature and aggregated together. The average particle size obtained from HRTEM is 6–8 nm for ZF-8 and 8–10 nm for ZFG1. In both the cases, ring type patterns are observed in SAED which reflects the polycrystalline nature of the samples.

To get information on the effect of digestion time and the method of synthesis on the magnetic properties, magnetic measurements were carried out on all samples. The magnetization as a function of field (M-H) recorded at room temperature for the samples ZF-0, ZF-8 and ZFG1 are shown in Figure 5.12. The samples ZF-0 and ZF-8 are paramagnetic in nature, where as the sample ZFG1 synthesized through the auto-combustion method shows superparamagnetic behavior. The M_s value of ZFG1 is calculated as 10.2 emu/g by extrapolating the M vs 1/H curve to 1/H = 0. The M-H curves measured at 5K are shown in Figure 5.13. All the three samples show magnetic hysteresis loops and the coer-

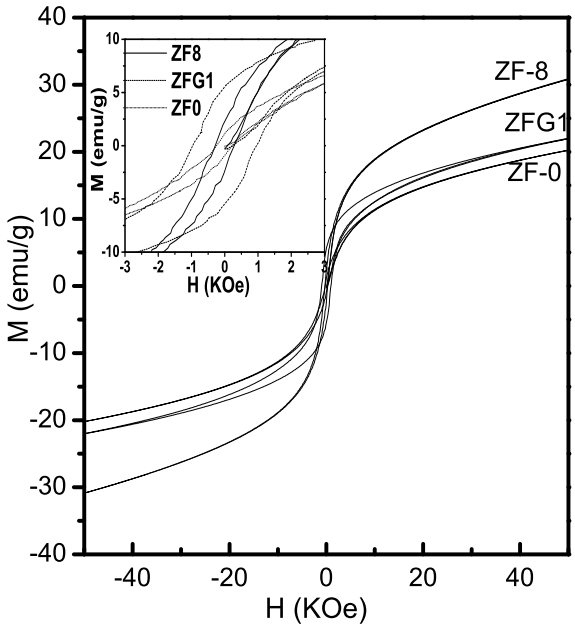

Figure 5.13: M vs H curves of ZF-0, ZF-8 and ZFG1 at 5 K

civity values for ZF-0, ZF-8, and ZFG1 are 235 Oe, 284 Oe and 962 Oe, respectively. The coercivity increases with increasing particle size, as expected for nanocrystalline materials.

In the literature, it has been reported that inversions up to 80% and 40% for the particles of size of 4 nm and 6 nm and almost negligible inversion for particles of size 7 nm and above [63]. If it is assumed that the particle size is the main factor for the inversion of cations to take place, superparamagnetic behavior would have been observed at room temperature for ZF-0 and ZF-8 having particle sizes of ∼4 nm and ∼6 nm. But both samples exhibit paramagnetic nature at room temperature. Hence it may be concluded that the degree of inversion not only depends on the particle size but also on the preparation and processing conditions. M_s value of 54.4 emu/g is reported for 300 nm particles of $ZnFe_2O_4$ synthesized by hydrothermal method [64]. Similarly, different M_s values have been obtained for particles with size >10 nm, synthesized by various methods [57, 65].

Figure 5.14 shows variation of magnetization with temperature for ZF-0, ZF-8 and

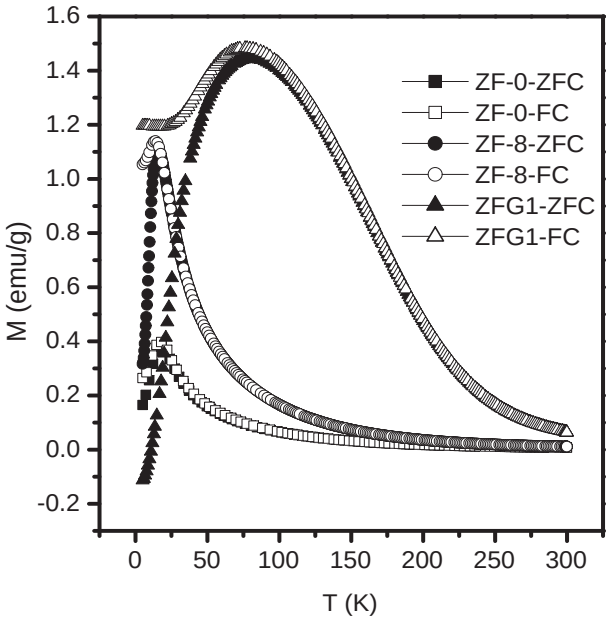

.

Figure 5.14: M vs T measurement of ZF-0, ZF-8 and ZFG1 from 300 K to 5 k at 100 Oe

..

ZFG1. Both zero field cooled (ZFC) and field cooled (FC) measurements were measured under a field of 100 Oe from 5 K to 300 K. In general, for antiferromagnetic materials, there will be a strong cusp at the Néel temperature (T_N). But in the case of ZF-0 and ZF-8 there are sharp peaks in both FC and ZFC curves at 15 K and 17 K, slightly above the T_N of the bulk (10 K). In both cases the behavior of the curves are similar except for the higher magnetization value observed in the case of ZF-8 compared to ZF-0. Also, the divergence between FC and ZFC magnetizations takes place below the peak temperatures. These characteristics are that of superparamagnetic particles. The decreasing FC magnetization below the blocking temperature indicates strong interacting nature of the particles [71,72]. The sample ZFG1 shows a very broad maximum in both the FC and ZFC curves at 77 K. The broad peak in the ZFC magnetization curve can be due to wider particle size distribution [73], compared to the narrow distribution (narrow peak) for ZF-8. The higher blocking temperature of this sample is indicating larger particle size and/or different degree of inversion when compared to that of ZF-8. For ZFG1 also, the characteristics of the FC curve is indicating strong inter-particle interactions.

5.3.3 Conclusions

Nanocrystalline $ZnFe_2O_4$ has been synthesized at a mild condition of 70 °C by a coprecipitation/digestion method. During the synthesis, digestion time is varied and this gives particles of different sizes. Particles of size 3 and 6 nm shows paramagnetic behavior at room temperature and superparamagnetic blocking temperatures of 15 K and 17 K, respectively. Nature of the magnetization curves indicate narrow particle size distribution. For a sample synthesized by an auto-combustion method, with comparable average particle size, superparamagnetic behavior is observed at room temperature. This sample shows a larger blocking temperature of 77 K and a broad peak in the ZFC magnetization indicating wider particle size distribution. Particles of comparable sizes show widely differing magnetic behavior. This indicates that the degree of inversion of the cations depends not only the size but also on the method of synthesis.

5.4 Nanocrystalline $CoFe_2O_4$

$CoFe_2O_4$ is a technologically important ferrimagnetic oxide with high coercivity, moderate saturation magnetization and with remarkable chemical stability. The material has been extensively studied for its various properties [74–78] and applications such as anode material for Li-ion batteries [6], as a gas sensor [79], and in high density magnetic recording. Cobalt ferrite has been studied for its magnetostrictive properties [80, 81]. In the field of medicine, it may find application as heating agents in magnetically activated drug delivery system [82].

$CoFe_2O_4$ crystalizes in the inverse cubic spinel structure. It can be represented with the general formula $(Co_xFe_{1-x})[Co_{1-x}Fe_{1+x}]O_4$. The cation distribution factor x describes the fraction of tetrahedral sites occupied by Co^{2+} cations [83]. The degree of inversion of the cations is determined by the preparation and processing conditions [84, 85]. The migration of ions between the two sites has been experimentally studied by using Mössbauer spectroscopy [86], Raman spectroscopy [76]. Depending on the particle size [9, 87] and cation distribution [76, 88], the magnetic properties are known to vary for the $CoFe_2O_4$ system. Very recently, inverse magnetocaloric effect is reported for nanoparticles of cobalt ferrite [89].

Table 5.4: Sample codes and calcination temperature of $CoFe_2O_4$ (CFC) synthesized by the corecipitation/digestion method.

Sample code	Calcination temperature (°C)
CFC-300	300
CFC-500	500
CFC-650	650
CFC-750	750
CFC-900	900
CFC-1000	1000

There are several methods employed for the synthesis of nanosized $CoFe_2O_4$ powders such as sol-gel [6,90], hydrothermal [91], using a bolck copolymer route [92], electrochemical [93], microwave assisted combustion synthesis [94], microemulsion [95], coprecipitation [87], auto-combustion [96], sonoreduction [97] etc. The following section describes the synthesis of cobalt ferrite nanoparticles by the coprecipitation/digestion method as well as the glycine-nitrate auto-combustion method and studies on the magnetic properties of the nanoparticles of different sizes.

5.4.1 Synthesis

The nanosized $CoFe_2O_4$ (CFC) particles were synthesized by the coprecipitation/digestion and the glycine-nitrate auto-combustion methods. The mixed water solution of cobaltous nitrate (0.05 M) and ferric nitrate (0.1 M) was added drop wise to distilled water taken in an RBF kept at 70 °C. The precipitant used was 0.27 M potassium carbonate, which was added simultaneously to the RBF. Further, the precipitate formed was digested for 3 hours in the mother liquor. Then the precipitate was filtered and washed thoroughly with sufficient amount of distilled water to remove any contamination such as K^+. After washing the precipitate was dried in an oven at 70 °C overnight. Unlike in the case of Fe_3O_4 and $ZnFe_2O_4$, the ferrite is not directly formed on precipitation. The precipitate was found to be a mixture of cobalt hydroxy carbonate and amorphous ferric hydroxide. The corresponding spinel type $CoFe_2O_4$ has been formed after calcination of the precipitate at 300 °C in air. Further, the calcination temperature has been varied as 500 °C, 650 °C, 750 °C, 900 °C, and 1000 °C, to see the effect of particle size on the magnetic properties.

Table 5.5: Crystallite size and cubic lattice parameter of samples synthesized by the coprecipitation/digestion method

Sample code	Crystallite size (± 1 nm)	Lattice parameter (Å)
CFC-300	6	8.394
CFC-500	10	8.373
CFC-650	22	8.389
CFC-750	33	8.383
CFC-900	55	8.385
CFC-1000	64	8.381

For the sample synthesized through auto-combustion method, glycine is used as a fuel. In a typical synthesis 1 mole of cobaltous nitrate and 2 moles of ferric nitrate were dissolved in minimum amount of water. To this, a water solution of glycine was added and mixed together. The homogeneous solution was kept on a hot plate at ∼200 °C until it burns. The amount of glycine was varied from 0.25 to 2 moles to vary the particle size.

Table 5.4 gives the sample codes for the samples synthesized by the coprecipitation/digestion method and calcined at different temperatures.

5.4.2 Characterization and Magnetic Properties

The phase purity of the samples calcined at different temperatures has been analyzed by XRD measurements. The XRD patterns of the different samples are given in Figure 5.15. All the patterns match well with simulated pattern of $CoFe_2O_4$ (JCPDS #77 -0426), using the lattice parameter $a = 8.40$ Å. There are no additional peaks observed in the XRD patterns other than the peaks corresponding to the spinel phase, revealing the single phase nature of the materials. It can be seen that the peaks in the XRD patterns become narrower as the calcination temperature is increased indicating the increase in the crystallite size. Cubic lattice parameter is calculated from least-squares fitting of the diffraction patterns. Crystallite size is calculated using the Scherrer formula. The calculated crystallite size and the lattice parameter are given in Table 5.5. The average crystallite size is considered as the average particle size in the subsequent sections.

Figure 5.16 shows the room temperature magnetic measurements of the samples synthesized by the coprecipitation/digestion method and calcined at different temperatures.

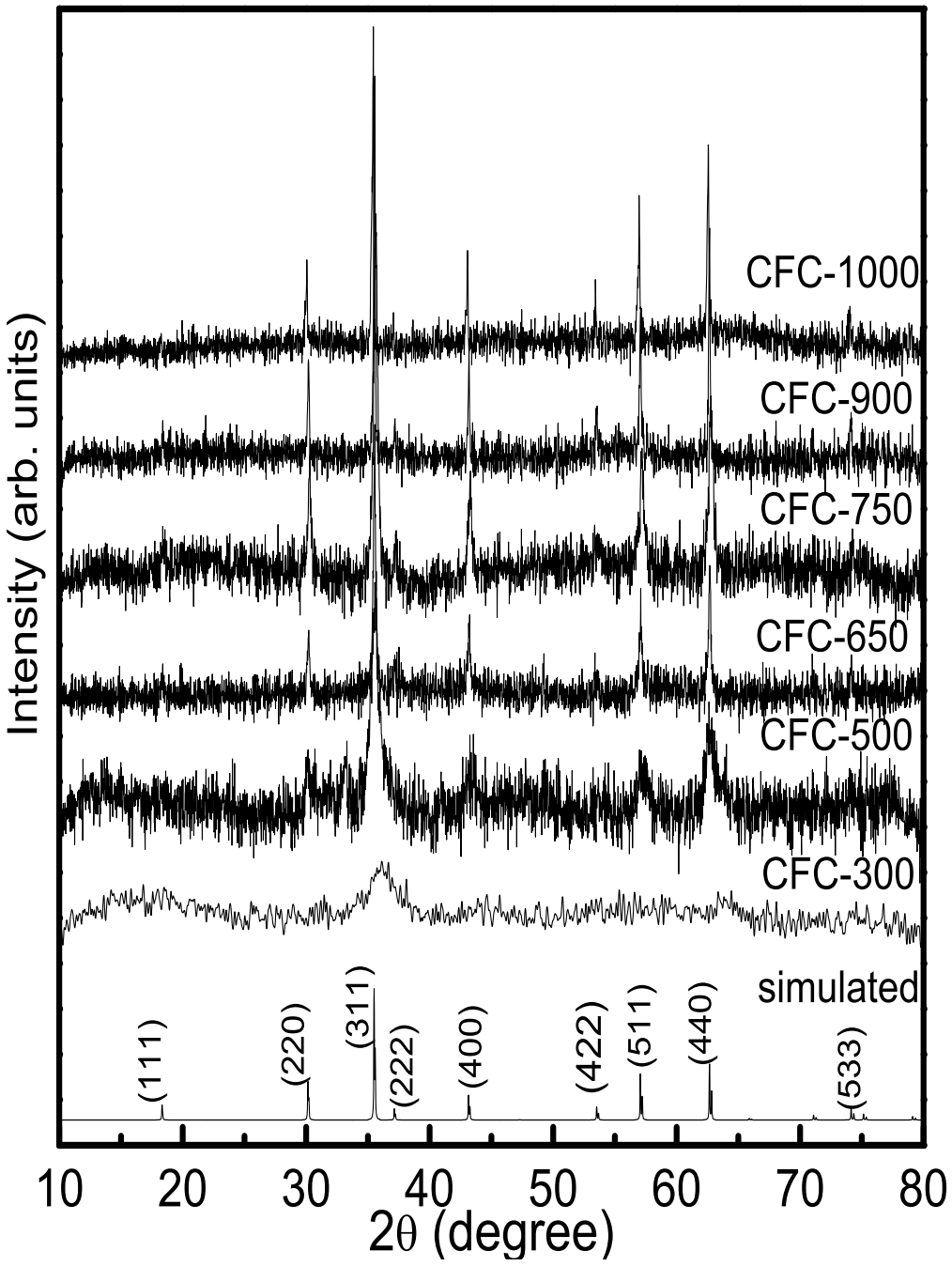

Figure 5.15: Powder XRD patterns of the samples calcined at different temperatures compared with the simulated pattern of $CoFe_2O_4$.

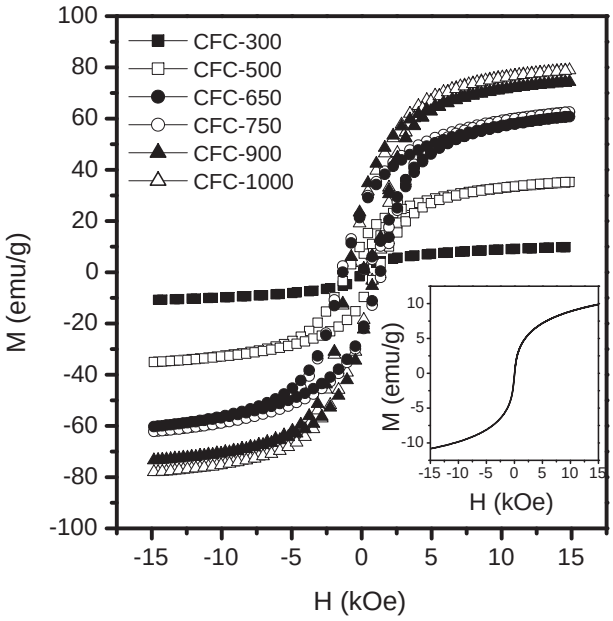

.

Figure 5.16: M vs H curves of $CoFe_2O_4$ samples calcined at different temperatures.

.

The sample CFC-300, having particle size 6 nm shows superparamagnetic behavior as shown in the inset of the figure. All the other samples with particle size varying from 10 to 64 nm show magnetic hysteresis loops with increasing saturation magnetization with increasing particle size. The magnetization at 15 kOe is almost saturated. Saturation magnetization is obtained by extrapolating the M vs 1/H cure to 1/H = 0. Variation of the saturation magnetization as a function of particle size is shown in Figure 5.17. The trend of increase in the saturation magnetization with increase in the particle size is as reported in the literature [87, 98].

It is known that the saturation magnetization decreases with decreasing particle size following the relationship [99],

$$M_s(d) = M_s(bulk)(1 - c/d) \tag{5.1}$$

where M_s(d) is the saturation magnetization of the particles of diameter d, M_s(bulk) is the saturation magnetization of the bulk ferrite and c is a constant. Least-squares fit to the data shown in Figure 5.17 using the above equation gives the value of M_s(bulk) = 87.5

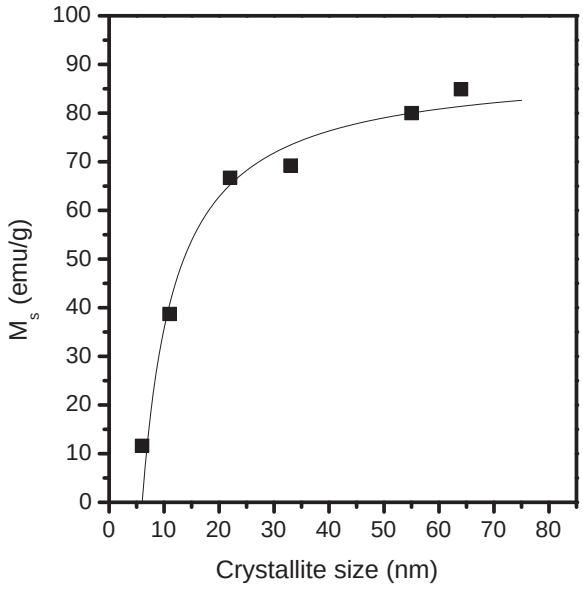

Figure 5.17: Variation of saturation magnetization with particle sizes (symbols). The solid line is the fitted curve as described in the text.

emu/g, which is comparable to the reported value of 88 emu/g for the bulk material [100]. The value of c is obtained as 5.4 nm. For the nanosized materials, a decrease in the saturation magnetization is expected due to the increasing surface area to volume ratio. It is assumed that a magnetically dead layer is formed on the surface of the particles due to the uncompensated exchange interactions in a surface layer of thickness, t. The thickness of this dead layer is related to c as c = 6t. From this relation, the value of t is obtained as 0.9 nm. This value is comparable to the unit cell parameter of cobalt ferrite (0.84 nm). The thickness of the magnetically dead layer obtained is comparable to the values reported in the literature for different ferrites [11, 99, 101]. This indicates that at least one unit cell on the surface layer of the nanoparticles is magnetically inactive. However, it is also possible that the lower magnetization of the nanoparticles is due to a different distribution of the cations in the ferrite lattice and the distribution is likely to change with increasing particle size due to calcination at higher temperatures.

Increase in the particle size during calcination will result in a change in magnetic domain size. This fact will be reflected in the coercivity of the sample. It is expected to

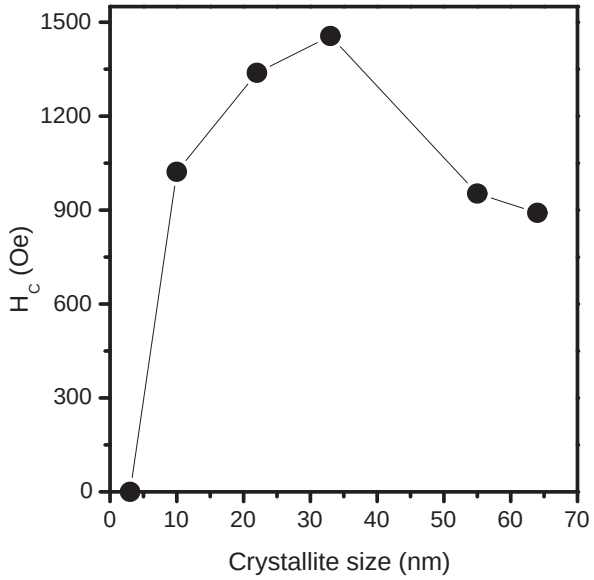

Figure 5.18: Coercivity of $CoFe_2O_4$ as a function of particle size. The solid line is a guide to the eye.

get a maximum in the coercivity at a critical size for stable single domain particles. In general, the coercivity is expected to increase as the particle size is decreased from bulk and after reaching a maximum for stable single domain particle, the coercivity further decreases [87]. Figure 5.18 depicts the effect of particle size on the coercivity. The variation is as expected. A maximum coercivity of 1470 Oe is observed for the particles of size 33 nm. For spinel type ferrite particles, maximum value of the coercivity is reported for particles of size in the range 30–40 nm [87].

To see the effect of the synthesis conditions on the magnetic properties, and for comparison, a series of samples have been synthesized by the auto-combustion method. The ratio of glycine-to-metal ion was varied from 0.25 to 2.00 moles to get particles of different sizes. The corresponding sample codes are given in Table 5.6

The phase purity of the samples is analyzed by XRD measurements. The results are shown in Figure 5.19 and Figure 5.20. Figure 5.19 shows the patterns of the samples corresponding to the glycine-to-metal ratio of 0.25 to 1.00 moles. All the samples are found to be phase pure, as there are no impurity peaks found other than that of the

Table 5.6: Sample codes and glycine-to-metal ratio used for the synthesis of $CoFe_2O_4$ by the auto-combustion method.

Sample code	Moles of glycine/metal ion
CFG25	0.25
CFG40	0.40
CFG50	0.50
CFG70	0.70
CFG100	1.00
CFG125	1.25
CFG150	1.50
CFG175	1.75
CFG200	2.00

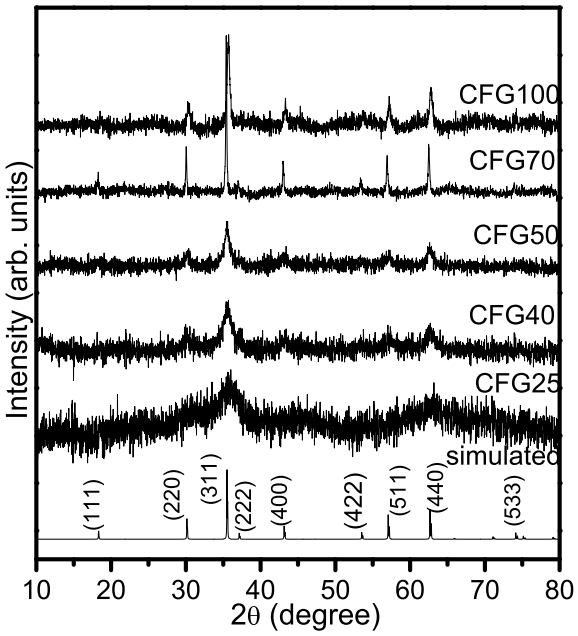

Figure 5.19: Powder XRD patterns of CFG25, CFG40, CFG50, CFG70, CFG100. The simulated pattern of $CoFe_2O_4$ is shown for comparison.

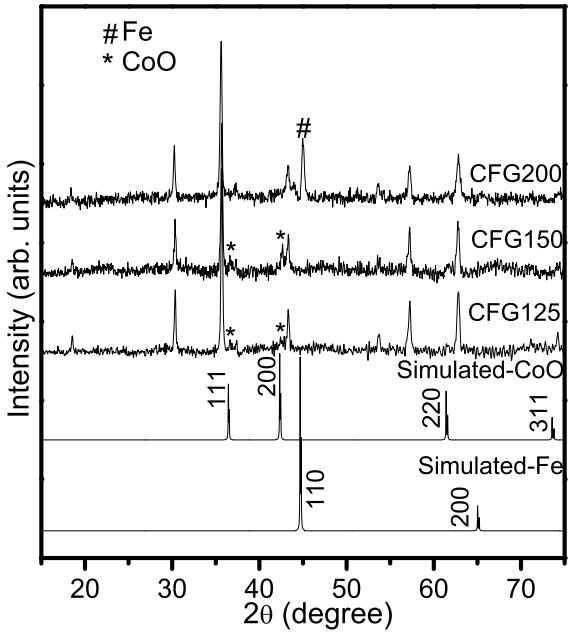

Figure 5.20: Powder XRD patterns of CFG125, CFG150, CFG200. The simulated patterns of CoO and Fe are shown for comparison.

spinel phase. On the other hand, the XRD patterns of the samples CFG125 and CFG150 (Figure 5.20) shows the formation of CoO as an impurity phase. Compared to the sample CFG125, there is an increase in the intensity of the peaks due to CoO in CFG150. Further increase in the ratio to 2.00 mole/metal ion (CFG200) shows the presence of Fe as an impurity phase. For comparison, the simulated patterns of both CoO and Fe are shown in the figure. Similar result on the formation of metal oxides and metals when larger amount of glycine is used for the synthesis has been reported earlier [102].

Further detailed studies are made on the single phase materials obtained using the glycine-to-metal ratio of 0.25–1.00. The average crystallite is calculated using the Scherrer formula and the cubic lattice parameter is calculated by least-squares fitting of the patterns. The corresponding values of the crystallite sizes and lattice parameters are given in Table 5.7. From the Table 5.7, it can be observed that there is an increase in the crystallite size as the number of moles of glycine is increased. In all the cases the obtained

Table 5.7: Crystallite size and lattice parameter of samples synthesized using various moles of glycine

Sample code	Crystallite size (±1 nm)	Lattice parameter (Å)
CFG25	5	8.393
CFG40	6	8.382
CFG50	10	8.387
CFG70	24	8.396
CFG100	48	8.395

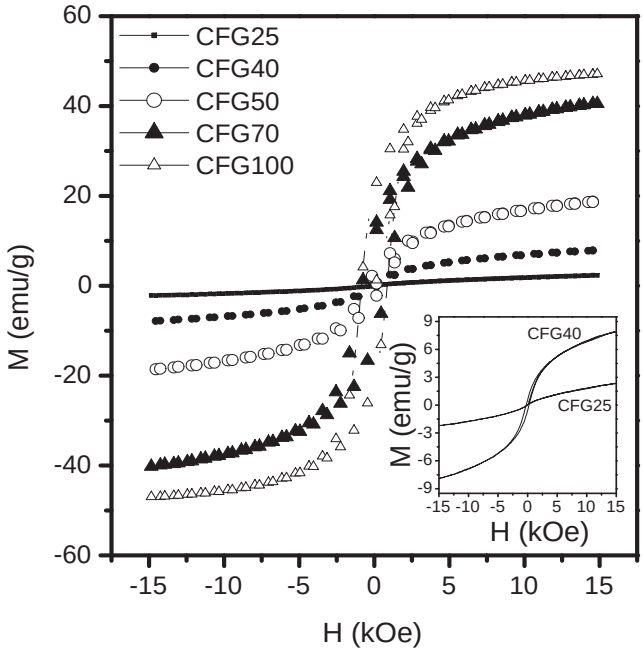

.

Figure 5.21: M vs H curves of $CoFe_2O_4$ samples synthesized with various glycine to metal ratios from 0.25–1.00. Inset: M vs H of CFG25 and CFG40

..

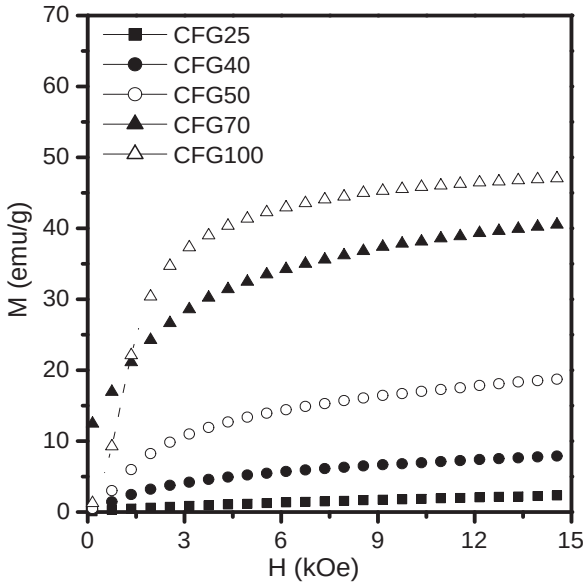

Figure 5.22: Initial magnetization of $CoFe_2O_4$ samples synthesized with various glycine ratios from 0.25–1.00

lattice parameter is in agreement with the standard value of 8.40 Å (JCPDS # 77-0426).

Figure 5.21 shows the room temperature magnetization data of the phase pure samples CFG25–CFG100. It is evident from the figure that the magnetization increases as a function of the number of moles of glycine used. The sample corresponding to 0.25 moles exhibits superparamagnetism without any magnetic hysteresis as shown in the inset of the figure, where as all other samples show clear hysteresis loops. The increase in the magnetization value can be clearly seen from initial magnetization curves shown in Figure 5.22. The magnetization curves of the samples with impurity phase CoO (CFG125 and CFG150) and Fe (CFG200) are shown in Figure 5.23. It can be seen that the magnetization values are lower for CFG125 and CFG150 compared to that of CFG100, due to the formation of non-magnetic CoO as impurity. For the sample CFG200 higher magnetization is obtained due to the formation of Fe as impurity phase.

Figure 5.24 shows the saturation magnetization value (M_s) as a function of crystallite size. The saturation magnetization was obtained by extrapolating M_s vs 1/H curves to 1/H = 0. As expected, it shows a trend of increasing M_s with increase in the particle

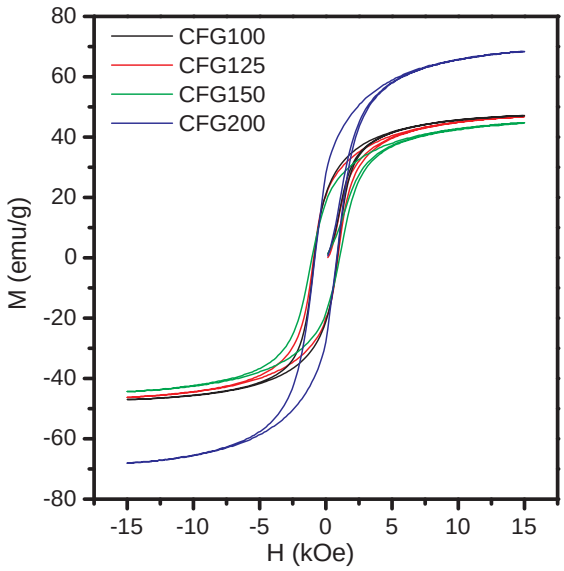

Figure 5.23: M vs H of $CoFe_2O_4$ samples synthesized with glycine ratios 1.25, 1.50 and 2.00

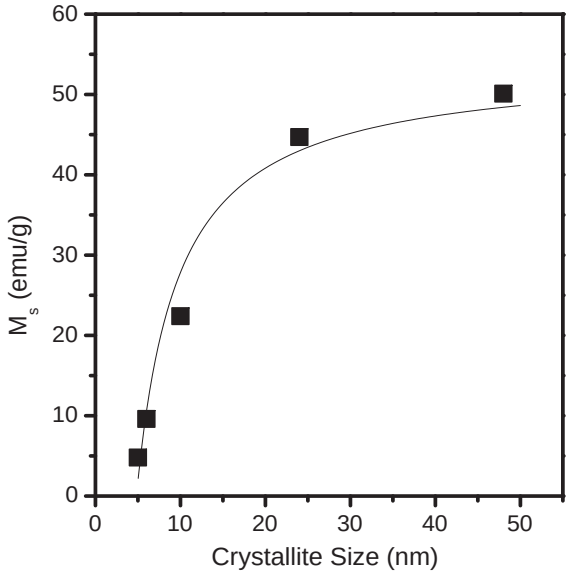

Figure 5.24: Saturation magnetization vs crystallite size for $CoFe_2O_4$ samples synthesized with various glycine ratios. The solid line is a fit to the data as discussed in the text.

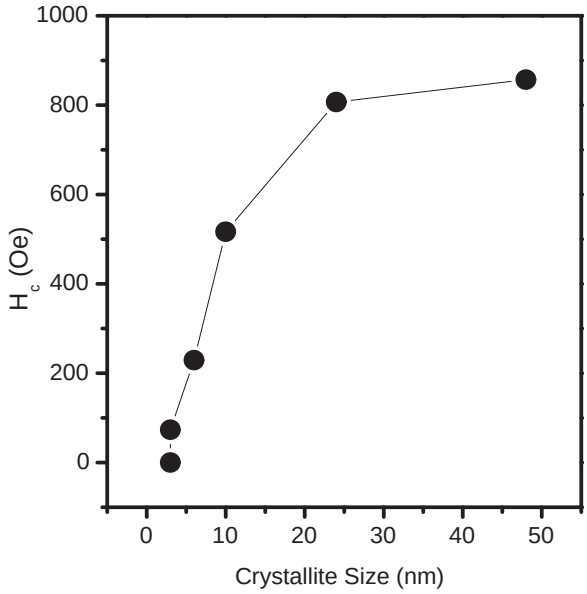

Figure 5.25: Coercivity as a function of crystallite size for $CoFe_2O_4$ samples synthesized with various glycine ratios. The solid line is a guide to the eye.

size. The data could be fitted to the model assuming a magnetically dead layer on the surface of the particles, using equation 5.1. Even though the fit is very good, a lower value of 53.8 emu/g is obtained for M_s(bulk) and the thickness of the dead layer is obtained as 0.8 nm. This indicates that probably there are other factors controlling the magnetic characteristics of the samples synthesized by the auto-combustion method. Similar difference in the behavior is also observed in the case of coercivity. The coercivity increases with the increase in the crystallite size as shown in the Figure 5.25. The H_c value is almost saturated when the crystallite size reaches 24 nm, corresponding to CFG70. The maximum value of 856 Oe is obtained for the sample CFG100 having the crystallite size of 48 nm.

The nanosized $CoFe_2O_4$ samples prepared through the coprecipitation/digestion and auto-combustion methods show a similar trend in the magnetic measurements. Hence, to compare the effect of the method of synthesis on the magnetic properties, the room temperature magnetization data of CFG25 and CFC-300 are compared in Figure 5.26. The HRTEM images of CFG25 and CFC-300 are compared in Figure 5.27. Both samples show

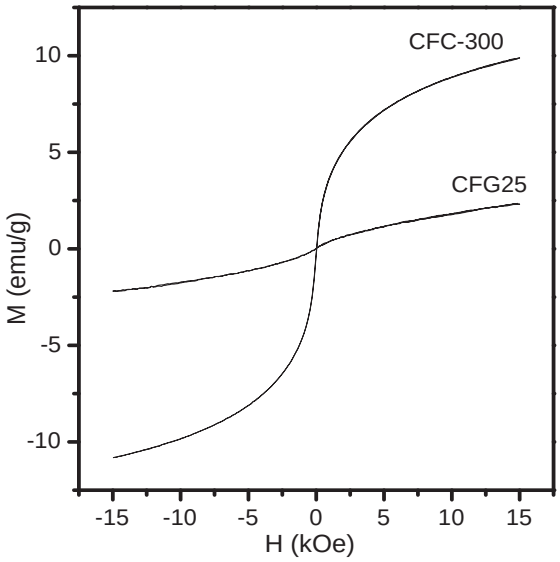

Figure 5.26: Comparison of M vs H at room temperature for CFG25 synthesized by the auto-combustion method and CFC-300 obtained by the coprecipitation method, having comparable particle sizes.

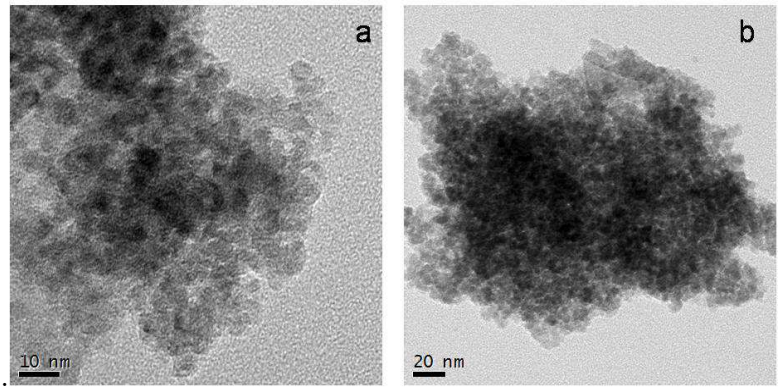

Figure 5.27: Comparison of the HRTEM images of (a) CFG25 and (b) CFC-300

comparable particle sizes of ∼5-7 nm. Though both the samples are of comparable size, CFC-300 shows higher magnetization value with the saturation magnetization (extrapolated) of 11.7 emu/g compared to the value of 3.08 emu/g for CFG25. Similarly, compared to the saturation magnetization obtained for the samples synthesized by the coprecipitation method, the magnetization is less for the samples synthesized by the auto-combustion method and having comparable particle sizes. Similarly, maximum in the coercivity is obtained for particles of size 48 nm. These differences in the magnetic characteristics of the samples synthesized by the two different methods could be due to the difference in the cation distribution and/or the presence of un-decomposed organic matter present in the auto-combustion samples. In the case of the auto-combustion reaction, the rate of reaction is very fast and drastic, where as in the case of the coprecipitation/digestion, the material can attain well homogeneity during the reaction. After precipitation, the sample has been subjected to thermal annealing during calcination at 300 °C for 5 hours. Therefore, the possibility for the migration of the cations may be different in the latter case, as it is reported that the cation migration depends on the preparation conditions [84] and thermal history [85].

As both CFG25 and CFC-300 do not show any magnetic hysteresis at room temperature, ZFC magnetization measurements below room temperature are carried out on both the samples to get information about the blocking temperature. The results are shown in Figure 5.28 and Figure 5.29. Both samples show almost similar behavior. A broader maximum and lower T_B is obtained for CFG25 compared to the slightly higher T_B of CFC-300. On the other hand, the FC curve is flat at lower temperatures for CFC-300 whereas FC magnetization increases with decreasing temperature for CFG25. The increasing FC magnetization below T_B for CFG25 is an indication for reduced interparticle interactions, probably due to the un-decomposed glycine coated on the surface of the particles. The broad maximum in the ZFC magnetization curve is an indication of wider particle size distribution in both the cases.

To confirm the phase purity both the samples CFG25 and CFC-300 have been subjected to high temperature magnetic measurements to measure the magnetic transition temperatures. Figure 5.30 shows the magnetization measured above room temperature,in a field of 100 Oe. Both the samples show a clear magnetic transition at 526 °C which

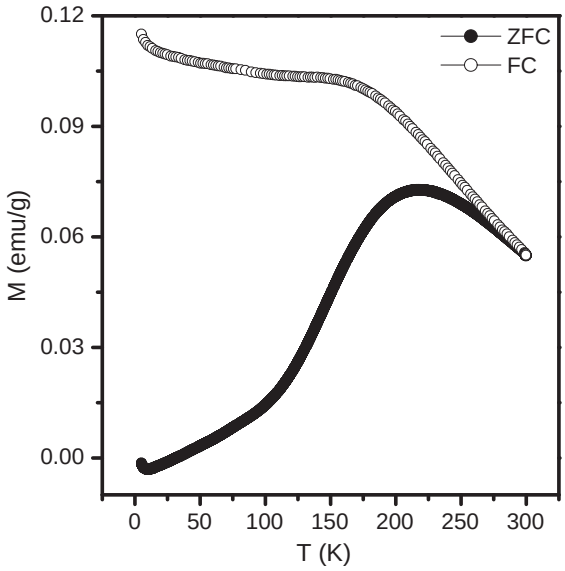

.

Figure 5.28: FC and ZFC magnetization measurements below room temperature for the sample CFG25.

.

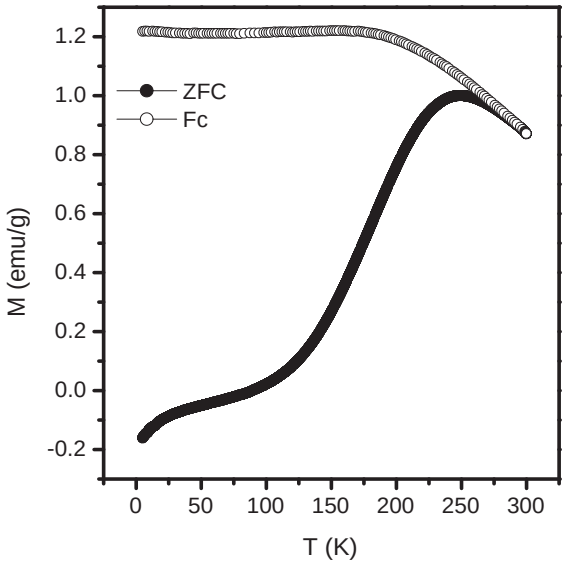

.

Figure 5.29: FC and ZFC magnetization measurement below room temperature for the sample CFC-300.

..

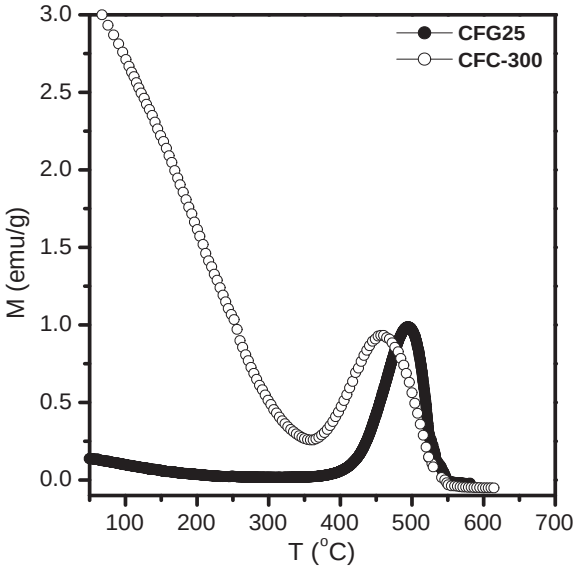

.

Figure 5.30: Magnetic measurement above room temperature for CFG25 and CFC-300.

..

matches well with the Curie temperature reported for bulk $CoFe_2O_4$ [103, 104]. The increase in the magnetization above 350 °C and the peak-like behavior are due to the increase in the particle size during the measurement [99] as well as due to the magnetocrystalline anisotropy contribution of cobalt ferrite [105].

5.4.3 Conclusions

Nanoparticles of $CoFe_2O_4$ are synthesized by a coprecipitaion/digestion and glycine-nitrate auto-combustion methods. The particle size is varied by calcining the samples at different temperatures in the former case and by changing the glycine-to-metal ratio in the latter. The effect of the method of synthesis as well as the particle size on the magnetic properties has been studied and compared. There is clear effect of the synthesis method on the magnetic properties, as evidenced from the comparison of the results of the sample having very small size from the two different batches. High temperature magnetic measurement confirm that the samples correspond to $CoFe_2O_4$. Identical Curie temperatures are obtained, for both samples, indicating the single phase nature of the samples synthesized by the two different methods.

References

[1] O. Muller, R. Roy, *Major Ternary Structural Families,* Springer-Verlag, 1974.

[2] A. Goldman, *Modern Ferrite Technology,* Van Nostrand Reinhold, New York, 1990.

[3] C.T. Yavuz, J.T. Mayo, W.W. Yu, A. Prakash, J.C. Falkner, S. Yean, L. Cong, H.J. Shipley, A. Kan, M. Tomson, *Science* 314 (2006) 964.

[4] D.N. Srivastava, N. Perkas, A. Gedanken, I. Felner, *J. Phys. Chem. B* 106 (2002) 1878.

[5] J. Li, Z. Huang, D. Wu, G. Yin, X. Liao, J. Gu, D. Han, The *J. Phys. Chem. C* 114 (2010) 1586.

[6] P. Lavela, J.L. Tirado, *J. Power Sources* 172 (2007) 379.

[7] J. Chen, L. Xu, W. Li, X. Gou, *Adv. Mater.* 17 (2005) 582.

[8] Q. Song, Z.J. Zhang, *J. Am. Chem. Soc.* 126 (2004) 6164.

[9] K.V.P.M. Shafi, A. Gedanken, R. Prozorov, J. Balogh, *Chem. Mater.* 10 (1998) 3445.

[10] F. Bernard, J. Lorimier, V. Nivoix, N. Millot, P. Perriat, B. Gillot, J.F. Berar, J.C. Niepce, *J. Solid State Chem.* 141 (1998) 105.

[11] J.P. Chen, C.M. Sorensen, K.J. Klabunde, G.C. Hadjipanayis, E. Devlin, A. Kostikas, *Phys. Rev. B* 54 (1996) 9288.

[12] N. Ponpandian, A. Narayanasamy, C.N. Chinnasamy,N. Sivakumar, J.M. Greneche, K. Chattopadhyay, K. Shinoda, B. Jeyadevan, K. Tohji, *Appl. Phys. Lett.* 86 (2005) 192510.

[13] J.F. Hochepied, P. Bonville, M.P. Pileni, *J. Phys. Chem. B* 104 (2000) 905.

[14] T. Kamiyama, K. Haneda, T. Sato, S. Ikeda, H. Asano, *Solid State Commun.* 81 (1992) 563.

[15] P.C. Wu, W.S. Wang, Y.T. Huang, H.S. Sheu, Y.W. Lo, T.L. Tsai, D.B. Shieh, C.S. Yeh, *Chem. Eur. J.* 13 (2007) 3878.

[16] C. Sun, C. Fang, Z. Stephen, O. Veiseh, S. Hansen, D. Lee, R.G. Ellenbogen, J. Olson, M. Zhang, *Nanomedicine* 3 (2008) 495.

[17] J.F. Schultz, J.D. Bell, R.M. Goldstein, J.A. Kuhn, T.M. McCarty, *Ann. Surg. Oncol.* 6 (1999) 691.

[18] R.C. O'Handley, *Modern Magnetic Materials: Principles and Applications,* Wiley New York, 2000.

[19] J.J. Versluijs, M.A. Bari, J.M.D. Coey, *Phys. Rev. Lett.* 87 (2001) 26601.

[20] P. Poddar, T. Fried, G. Markovich, *Phys. Rev. B* 65 (2002) 172405.

[21] A.K. Gupta, M. Gupta, *Biomaterials* 26 (2005) 3995.

[22] L. Shen, P.E. Laibinis, T.A. Hatton, *Langmuir* 15 (1999) 447.

[23] S. Wang, H. Xin, Y. Qian, *Mater. Lett.* 33 (1997) 113.

[24] W.W. Wang, Y.J. Zhu, M.L. Ruan, *J. Nanopart. Res.* 9 (2007) 419.

[25] D. Chen, R. Xu, *Mater. Res. Bullet.* 33 (1998) 1015.

[26] R.M. Cornell, U. Schwertmann, *The Iron Oxides: Structure, Properties, Reaction, Occurance and Uses.* Wiley-VCH Weinheim, 2003.

[27] G.A. Waychunas, *Rev. Mineral. Geochem.* 25 (1991) 11.

[28] M.P. Sharrock, R.E. Bodnar, *J. Appl. Phys.* 57 (1985) 3919.

[29] E.M. Moreno, M. Zayat, M.P. Morales, C.J. Serna, A. Roig, D. Levy, *Langmuir* 18 (2002) 4972.

[30] T. Hyeon, S.S. Lee, J. Park, Y. Chung, H.B. Na, *J. Am. Chem. Soc.* 123 (2001) 12798.

[31] F. Del Monte, M.P. Morales, D. Levy, A. Fernandez, M. Ocana, A. Roig, E. Molins, K. O'Grady, C.J. Serna, *Langmuir* 13 (1997) 3627.

[32] X. Dong, H. Chen, W. Zhao, X. Li, J. Shi, *Chem. Mater.* 19 (2007) 3484.

[33] K.E. Gonsalves, H. Li, P. Santiago, *J. Mater. Sci.* 36 (2001) 2461.

[34] L. Suber, P. Imperatori, G. Ausanio, F. Fabbri, H. Hofmeister, *J. Phys. Chem. B* 109 (2005) 7103.

[35] S. Basak, K.S. Rane, P. Biswas, *Chem. Mater.* 20 (2008) 4906.

[36] E. Murad, U. Schwertmann, *Clay. Clay Miner.* 41 (1993) 111.

[37] N. Pinna, S. Grancharov, P. Beato, P. Bonville, M. Antonietti, M. Niederbergers, *Chem. Mater.* 17 (2005) 3044.

[38] E.J. Fasika, *Corros. Sci.* 7 (1967) 833.

[39] R.D. Waldron, *Phys. Rev.* 99 (1955) 1727.

[40] M. Ishii, M. Nakahira, *Solid State Commun.* 11 (1972) 209.

[41] S. Nasrazadani, A. Raman, *Corros. Sci.* 34 (1993) 1355.

[42] J.M.D. Coey, *Magnetic Properties of Iron in Soil; Iron Oxides and Clay Minerals* In: Stucki, J. W.Goodman, B. A. Schwertmann, U. (eds) Iron in soils and clay minerals, D Reidel Pub Co, (1988) 397-466.

[43] D.H. Han, J.P. Wang, H.L. Luo, *J. Magn. Magn. Mater.* 136 (1994) 176.

[44] J. Wang, J. Sun, Q. Sun, Q. Chen, *Mater. Res. Bullet.* 38 (2003) 1113.

[45] R.N. Panda, N.S. Gajbhiye, G. Balaji, *J. Alloy. Compd.* 326 (2001) 50.

[46] J. Smit, H.P.J. Wijn, *Ferrites,* Philips Technical Library, Eindhoven, 1959.

[47] T. Moriya, *Magnetic Ions in Insulators Their Interactions, Resonances and Optical Properties,* Volume 1, Magnetism, Edited by G. T. Rado and H. Suhl, Acaemic Press, Newyork and London, 1963, p86.

[48] L. Neel, *Compt. Rend.* 252 (1961) 4075.

[49] J.G. Na, T.D. Lee, S.J. Park, *IEEE T. Magn.* 28 (1992) 2433.

[50] Z.J. Zhang, Z.L. Wang, B.C. Chakoumakos, J.S. Yin, *J. Am. Chem. Soc.* 120 (1998) 1800.

[51] S.D. Shenoy , P.A. Joy, M.R. Anantharaman, *J. Magn. Magn. Mater.* 269 (2004) 217

[52] R. Arulmurugan, B. Jeyadevan, G. Vaidyanathan, S. Sendhilnathan, *J. Magn. Magn. Mater.* 288 (2005) 470.

[53] T. Sato, K. Haneda, M. Seki, T. Iijima, *Appl. Phys. A* 50 (1990) 13.

[54] F.S. Li, L. Wang, J.B. Wang, Q.G. Zhou, X.Z. Zhou, H.P. Kunkel, G. Williams, *J. Magn. Magn. Mater.* 268 (2004) 332.

[55] F. Grasset, N. Labhsetwar, D. Li, D.C. Park, N. Saito, H. Haneda, O. Cador, T. Roisnel, S. Mornet, E. Duguet, *Langmuir* 18 (2002) 8209.

[56] H.H. Hamdeh, J.C. Ho, S.A. Oliver, R.J. Willey, G. Oliveri, *J. Appl. Phys.* 81 (1997) 1851.

[57] C.N. Chinnasamy, A. Narayanasamy, N. Ponpandian, K. Chattopadhyay, H. Guerault, J.M. Greneche, *J. Phys. Cond. Matter* 12 (2000) 7795.

[58] M. Hofmann, S.J. Campbell, H. Ehrhardt, R. Feyerherm, *J. Mater. Sci.* 39 (2004) 5057.

[59] M.K. Roy, B. Haldar, H.C. Verma, *Nanotechnology* 17 (2006) 232.

[60] J.H. Shim, S. Lee, J.H. Park, S.J. Han, Y.H. Jeong, Y.W. Cho, *Phys. Rev. B* 73 (2006) 64404.

[61] D. Makovec, M. Drofenik, *J. Nanopart. Res.* 10 (2008) 131.

[62] B. Jeyadevan, K. Tohji, K. Nakatsuka, *J. Appl. Phys.* 76 (1994) 6325.

[63] C. Upadhyay, H.C. Verma, V. Sathe, A.V. Pimpale, *J. Magn. Magn. Mater.* 312 (2007) 271.

[64] S.H. Yu, T. Fujino, M. Yoshimura, *J. Magn. Magn. Mater.* 256 (2003) 420.

[65] F. Li, H. Wang, L. Wang, J. Wang, *J. Magn. Magn. Mater.* 309 (2007) 295.

[66] S. Deka, P.A. Joy, *J. Nanosci. Nanotech.* 8 (2008) 3955.

[67] X.J. Xu, L.H. Zhou, Q.G. Zhai, C.Z. Lu, *J. Am. Ceram. Soc.* 90 (2007) 1959.

[68] H. Yang, X. Zhang, C. Huang, W. Yang, G. Qiu, *J. Phys. Chem. Solids* 65 (2004) 1329.

[69] P.Y. Lee, H. Suematsu, T. Nakayama, W. Jiang, K. Niihara, *J. Magn. Magn. Mater.* 312 (2007) 27.

[70] S. Ozcan, B. Kaynar, M.M. Can, T. Firat, *Mater. Sci. Eng. B* 121 (2005) 278.

[71] D. Parker, F. Ladieu, E. Vincent, G. Mriguet, E. Dubois, V. Dupuis, R. Perzynski, *J. Appl. Phys.* 97 (2005) 10A502.

[72] M. Sasaki, P.E. Jnsson, H. Takayama, H. Mamiya, *Phys. Rev. B* 71 (2005) 104405.

[73] S. Mørup, F. Bdker, P.V. Hendriksen, S. Linderoth, *Phys. Rev. B* 52 (1995) 287.

[74] A.J. Rondinone, A.C.S. Samia, Z.J. Zhang, *Appl. Phys. Lett.* 76 (2000) 3624.

[75] J. Ding, Y.J. Chen, Y. Shi, S. Wang, *Appl. Phys. Lett.* 77 (2000) 3621.

[76] T. Yu, Z.X. Shen, Y. Shi, J. Ding, *J. Phys. Cond. Matter* 14 (2002) L613.

[77] A.C. Nunes, C.F. Majkrzak, A.E. Berkowitz, *J. Magn. Magn. Mater.* 39 (1983) 59.

[78] A. Mumtaz, K. Maaz, B. Janjua, S.K. Hasanain, M.F. Bertino, *J. Magn. Magn. Mater.* 313 (2007) 266.

[79] C. Xiangfeng, J. Dongli, G. Yu, Z. Chenmou, *Sensor. Actuat. B: Chem.* 120 (2006) 177.

[80] J.A. Paulsen, A.P. Ring, C.C.H. Lo, J.E. Snyder, D.C. Jiles, *J. Appl. Phys.* 97 (2005) 044502.

[81] S.D. Bhame, P.A. Joy, *J. Am. Ceram. Soc.* 91 (2008) 1976.

[82] D.H. Kim, D.E. Nikles, D.T. Johnson, C.S. Brazel, *J. Magn. Magn. Mater.* 320 (2008) 2390.

[83] M.R. DeGuire, R.C. OHandley, K. Gretchen, *J. Appl. Phys.* 65 (1989) 3167.

[84] P.N. Vasambekar, C.B. Kolekar, A.S. Vaingankar, *Mater. Chem. Phys.* 60 (1999) 282.

[85] K. Haneda, A.H. Morrish, *J. Appl. Phys.* 63 (1988) 4258.

[86] C.S. Kim, S.W. Lee, P.S. L., J.Y. Park, Y.J. Oh, *J. Appl. Phys.* 79 (1996) 5428.

[87] Y. Qu, H. Yang, N. Yang, Y. Fan, H. Zhu, G. Zou, *Mater. Lett.* 60 (2006) 3548.

[88] S. Li, V.T. John, C. OConnor, V. Harris, E. Carpenter, *J. Appl. Phys.* 87 (2000) 6223.

[89] E.V. Gopalan, I.A. Al-Omari, D.S. Kumar, Y. Yoshida, P.A. Joy, M.R. Anantharaman, *Appl. Phys. A* 99 (2010) 497.

[90] J.G. Lee, *J. Magn. Magn. Mater.* 177 (1998) 900.

[91] L.J. Cote, A.S. Teja, A.P. Wilkinson, Z.J. Zhang, *Fluid Phase Equilibr.* 210 (2003) 307.

[92] S.R. Ahmed, P. Kofinas, *Macromolecules* 35 (2002) 3338.

[93] S.D. Sartale, C.D. Lokhande, *Ceram. Int.* 28 (2002) 467.

[94] N. Kasapoglu, A. Baykal, Y. Kseoglu, M.S. Toprak, *Scripta Mater.* 57 (2007) 441.

[95] V. Pillai, D.O. Shah, *J. Magn. Magn. Mater.* 163 (1996) 243

[96] S.D. Bhame, P.A. Joy, *Sensor. Actuat. A Phys.* 137 (2007) 256.

[97] M. Mohan, V. Chandra, S.S. Manoharan, *Curr Sci. India* 93 (2008) 473.

[98] M. Rajendran, R.C. Pullar, A.K. Bhattacharya, D. Das, S.N. Chintalapudi, C.K. Majumdar, *J. Magn. Magn. Mater.* 232 (2001) 71.

[99] S. Verma, P.A. Joy, *J. Appl. Phys.* 98 (2005) 124312.

[100] R. Mller, W. Schppel, *J. Magn. Magn. Mater.* 155 (1996) 110.

[101] V. Sreeja, S. Vijayanand, S. Deka, P.A. Joy, *Hyperfine Int.* 183 (2008) 99.

[102] N. Kikukawa, M. Takemori, Y. Nagano, M. Sugasawa, S. Kobayashi, *J. Magn. Magn. Mater.* 284 (2004) 206.

[103] J. Teillet, F. Bouree, R. Krishnan, *J. Magn. Magn. Mater.* 123 (1993) 93.

[104] S.D. Bhame, P.A. Joy, *J. Appl. Phys.* 100 (2006) 113911.

[105] P.A. Joy, S.K. Date, *J. Magn. Magn. Mater.* 222 (2000) 33.

Chapter 6

Magnetic Properties of Nanocrystalline Multiferroic $BiFeO_3$

This chapter describes the results from the studies on the magnetic properties of nanocrystalline multiferroic $BiFeO_3$ system. The compound has been synthesized by a coprecipitation/digestion method as well as a self ignition auto-combustion method. The detailed magnetic properties studied on the basis of the effect of synthetic methodology have been discussed.

6.1 Magnetoelectric multiferroics

Ferromagnetism and ferroelectricity are well known properties of solids and have been studied extensively and individually in materials, especially in perovskite type compounds of the general formula ABO_3. The magnetic perovskites have been extensively studied and tabulated by Goodenough and Longo [1]. Mitsui *et al* have compiled a list of hundreds of ferroelectric perovskites [2]. If one considers a perovskite type structure, ferroelectricity requires a B-site ion with d^0 configuration, whereas for magnetism, a d^j electronic configuration, with j different from zero, is required for the B-site ion [3]. It is well known that in the oxide perovskites such as $BaTiO_3$, the Ti ion plays a key role for ferroelectricity. Even though ferromagnetism and ferroelectricity tend to exclude one another, there are some systems in which these properties co-exist and such systems are known as magnetoelectric or multiferroic materials [4,5]. In such materials, the origins of ferroelectricity and ferromagnetism are from different sources. In the case of magnetoelectric materials, there can be a spontaneous magnetization that can be switched by an applied magnetic field, a spontaneous polarization that can be switched by an applied electric field and often

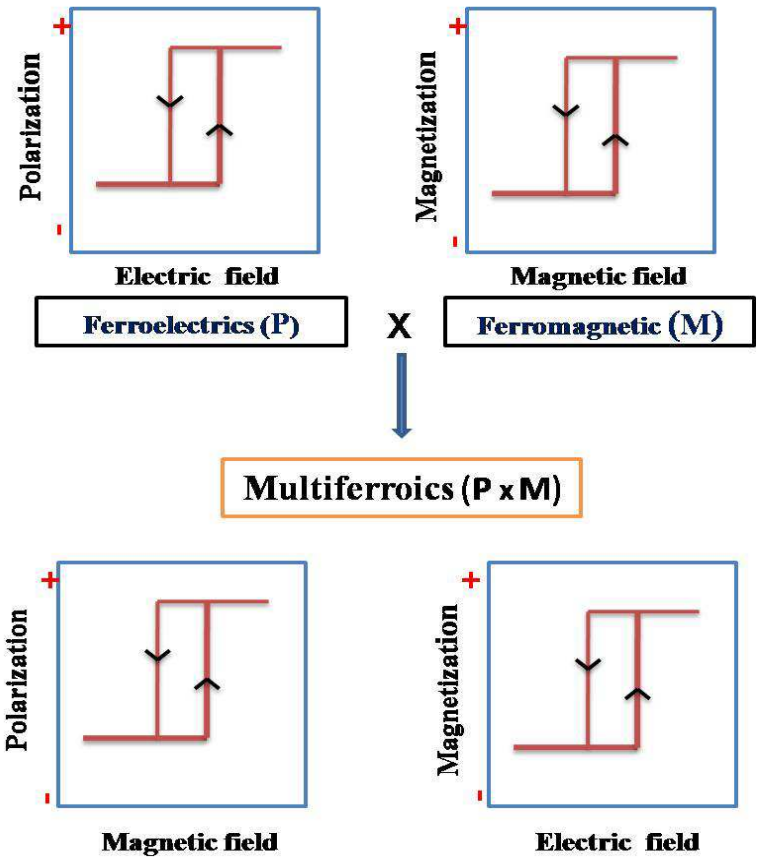

Figure 6.1: Multiferroics and magnetoelectric control.

coupling between the two. There are many reviews devoted to this area, which discuss the magnetoelectric materials and their properties in detail [5–7].

Multiferroics, which are simultaneously ferroelectric and ferro- or antiferromagnetic, have potential applications of both their parent ferroelectric and ferromagnetic materials. In addition, a whole range of new applications can be envisaged. The magnetoeletric coupling enables the control of ferroelectric polarization by a magnetic field and conversely the manipulation of the magnetization by an applied electric field, as depicted in Figure 6.1. Due to their importance in potential applications in information storage, spintronics and sensors, there has been considerable research activities taking place in the area of magnetoelectric multiferroics. There are two different types of multiferroic materials; i) a single material exhibiting both ferro- or ferri- or antiferromagnetic and ferroelectric properties, and ii) a composite containing ferroelectric and ferro- or ferrimagnetic materials.

There are many single phase materials showing the multiferroic properties [8–11]. For

example, $YMnO_3$ is a hexagonal perovskite that is antiferromagnetic with Néel temperature (T_N) of 80 K and ferroelectric with Curie temperature (T_C) of 914 K [8]. Similarly, $BiMnO_3$, a monoclinic perovskite, is both ferromagnetic (T_N ≈100 K) and ferroelectric (T_C ≈450 K) [9, 10]. For practical applications, room temperature multiferroism is an important criteria. Hence, $BiFeO_3$ becomes the potential candidate because it is the only material which shows magnetoelectric coupling at or above room temperature [12]. Bulk $BiFeO_3$ is antiferromagnetic below $T_N \approx 645$ K, and it exhibits ferroelectric behavior below $T_C \approx 1100$ K [13]. It also exhibits weak magnetism at room temperature due to residual magnetic moment from a canted spin structure [14]. The information on the magnetic ordering of the Fe ions in $BiFeO_3$ has been extensively studied by Sosnowska *et al* [15].

The magnetoelectric response exhibited by single phase materials is either too weak or occurs at very low temperatures [16]. The alternate choice is composite materials made out of piezoelectric and magnetostrictive components. The magnetoelectric effect in a composite material is nothing but the product properties of the two separate phases [17]. The magnetoelectric response which they exhibit will be larger than those of the single phase materials [18–20]. Magnetoelectric perovskite-spinel composites have attracted considerable attention in the recent past [21]. For example, a composite of $BaTiO_3$ and $CoFe_2O_4$ [20–22] is known for its enhanced magnetoelectric effect. In this composite, both the materials are well known for their ferroelectric and ferrimagnetic properties, respectively. In the composite made out of $BaTiO_3$ and $CoFe_2O_4$, a polarization value of ∼23 $\mu C/cm^2$, with a piezoelectric hysteresis value of ∼50 pm/V, and saturation magnetization value of ∼350 emu/cm^3 have been reported [20]. Similarly, self assembled nanostructures of the composites $CoFe_2O_4$-$PbTiO_3$ [23], $CoFe_2O_4$-$BiFeO_3$ [24], and $BaTiO_3$-$NiFe_2O_4$ [25] have been studied for their magnetoelectric properties. In the case of $CoFe_2O_4$-$BiFeO_3$, room temperature magnetization reversal induced by an electric field has been demonstrated [24]. The application of a magnetoelectric read-head, using bilayered heterostructures of $BaTiO_3$-$NiFe_2O_4$ and $BaTiO_3$-$CoFe_2O_4$ has been demonstrated [26]. Hence, considerable attention has been focused in the area of multiferroic composites [20, 22, 27–30]. Such composites are useful in several types of devices [31, 32].

Being the single phase multiferroic material with ferroelectric and antiferromagnetic

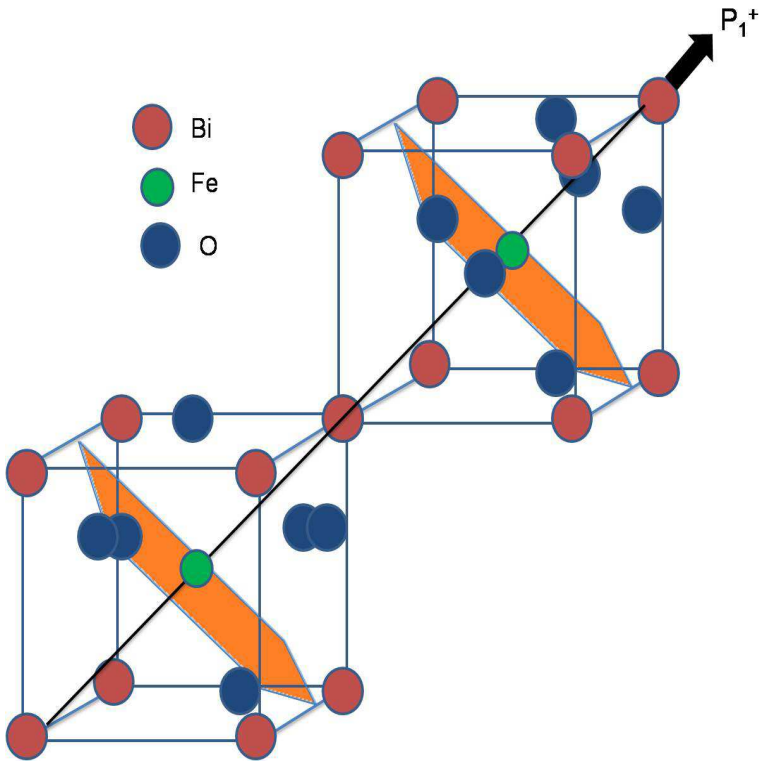

Figure 6.2: Schematics of the crystal structure of $BiFeO_3$ and the direction of ferroelectric polarization (arrow) and antiferromagnetic planes (shaded) [33].

transition temperatures above room temperature, $BiFeO_3$ has attracted considerable interest in the recent past.

6.2 Structure of $BiFeO_3$

Bulk $BiFeO_3$ crystalizes in rhombohedrally distorted perovskite crystal structure with the point group R3c and lattice parameters value of $a = 5.63$ Å and $\alpha = 59.35°$, or equivalently $a = 5.58$ Å and c = 13.87 Å, in the hexagonal representation [34–37]. It has ferroelectric polarization along $[111]_{pseudocubic}$ [37]. Figure 6.2 shows the two distorted perovskite unit cells connected along their body diagonal, to form a rhombohedral unit cell. The ferroelectricity arises mainly because of the large displacement of the Bi ions relative to the FeO_6 octahedra. Hence the ferroelectric displacement of Bi^{3+} and Fe^{3+} is with respect to the [111] direction in the rhombohedral unit cell [38]. Magnetism in $BiFeO_3$ is due to the unpaired electrons in the d^5 high spin ion Fe^{3+}.

The magnetic structure of $BiFeO_3$ is of G-type antiferromagnetic, with a modulated spiral spin structure having a long periodicity of 62 nm [15]. Recent neutron diffraction studies revealed that the character of the modulated cycloidal ordering of the Fe^{3+} magnetic moments remains the same from 4 K up to the Néel temperature, suggesting that the magnetic interactions are relatively stable in this temperature range [39]. Similarly, high resolution synchrotron radiation diffraction measurement did not show any sign of charge ordering nor any crystal symmetry breaking in $BiFeO_3$ in the temperature range 5–1000 K [40]. The cycloidal periodic spin arrangement cancels out the macroscopic magnetic moment and as a result, very weak magnetoelectric effect is observed. There are ways to suppress the spiral magnetic ordering by application of a very high magnetic field, by decreasing the dimensions of the sample below spin periodicity (nanoparticles or thin films) or by chemical substitution of Bi^{3+} or Fe^{3+} by other suitable ions of comparable ionic sizes. Reduction in dimension is shown to enhance the magnetization in thin films and in nanoparticles [41–43].

6.3 Synthesis of $BiFeO_3$

Though $BiFeO_3$ is known to be a potential candidate for multiferroic applications, it is very hard to avoid the formation of impurity phases during the synthesis. $BiFeO_3$ can be stabilized only within a narrow temperature range, as depicted in the phase diagram shown in Figure 6.3. Bi-rich $Bi_{25}FeO_{40}$ and Fe-rich $Bi_2Fe_4O_9$ are the stable compounds on each side of $BiFeO_3$ [44, 45]. $BiFeO_3$ can be made by the conventional solid state method of synthesis by firing a mixture of Bi_2O_3 and Fe_2O_3 with slightly excess amount of Bi_2O_3. But the compound after formation always ends with the impurity phases such as $Bi_2Fe_4O_9$ and $Bi_{25}FeO_{40}$ [46]. Impurity phases formed during this process has to be leached out by washing the product with dilute nitric acid [47]. An attempt has been made successfully to synthesize a phase pure $BiFeO_3$ through a technique called "rapid liquid phase sintering", where an equimolar mixture of the precursor oxides is rapidly heated and fired for a short time. During this process the temperature maintained was slightly above the melting temperature of Bi_2O_3 (T_{fus} = 817 °C) [46, 48, 49]. There are many wet chemical routes reported such as sol-gel method [50–54],coprecipitation method [55], hydrothermal method [56,57], classic Pechini method [58], sonochemical and

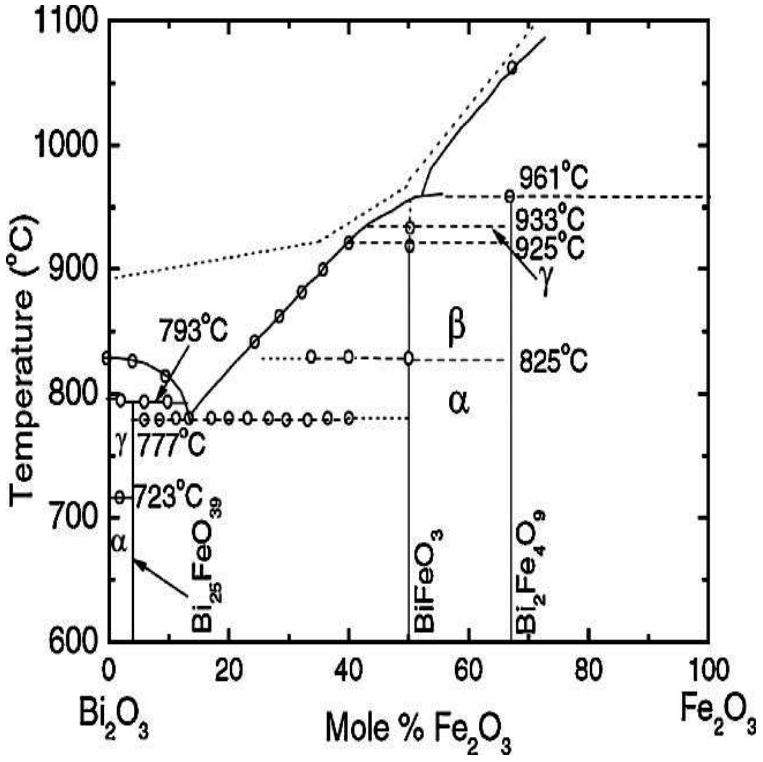

Figure 6.3: Compositional phase diagram of $BiFeO_3$ [61].

microemulsion techniques [59], auto-combustion method [60], etc.

Although there are several soft chemical methods developed for the synthesis of $BiFeO_3$, there is no general conclusion on the optimised conditions for the synthesis of phase pure material. For example, in the case of sol-gel method, depending on the gelation agent, the phase purity is getting affected. In one case, when citric acid and ethylene glycol were used [53] impurity phases were formed, where as in another case when acetic acid, ethanol, and ethylene glycol were used to prepare thin films, a phase pure material was obtained [52]. Ghosh *et al* [51] observed that phase pure material can be obtained when tartaric acid was used whereas when citric acid was used, $BiFeO_3$ was formed with impurities. Like wise, synthesis conditions has been optimized in the case of hydrothermal method by Chen *et al* [56] to get the phase pure material. If temperature and oxygen partial pressure are not controlled accurately during crystallization, the kinetics of phase formation always lead to impurity phases $Bi_2Fe_4O_9$, $Bi_2O_{2.75}$ and $Bi_4Fe_2O_{72}$ [46].

6.4 Properties of $BiFeO_3$

There are also contradictions in the reported properties of $BiFeO_3$ synthesized by various methods. Some authors have reported large polarization values with interesting magnetic properties [41, 62–64]. Although the large polarization is not in agreement with the value for bulk [38], it is in good agreement with the theoretical values [65–67]. Similarly, there are reports on the observation of very high magnetization [53, 60, 68]. Wang *et al* [41] have reported very large polarization value which is 15 times larger than that of the bulk, apart from very large ferromagnetism with a value of *ca.* 1.0 Bohr magneton (μ_B) per unit cell. Further research by other groups could confirm the large polarization as an intrinsic property of $BiFeO_3$ [69–71] whereas the intrinsic magnetization value was thought to be zero [72, 73] i.e with the value of *ca.* 0.02 μ_B/unit cell.

There are many reports on the different magnetic behavior exhibited by $BiFeO_3$. Zero-field-cooled (ZFC) and field-cooled (FC) magnetization studies on single crystals, measured in a field of 10 kOe, showed a decrease below 350 K like a conventional antiferromagnet but the two curves diverge below 250 K, indicating spin glass behavior [74]. However, further studies on thin films reported a spin-glass transition at 50 K [75]. Recent studies indicated few more weak magnetic transitions below and above room temperature. From the studies on the temperature dependence of the Raman integrated intensities of the electromagnon on single crystals of $BiFeO_3$, a maximum around 140 K is observed, indicating a small spin reorientation out of the cycloidal plane [76]. Phase transitions at 90, 140, 200, and 250 K are also discovered from further Raman spectroscopic studies [77, 78]. These transitions are also observed in dielectric constant measurements and thermomechanical studies [79]. These transitions are assigned to different origins such as magnetic but glassy and with magnetoelectric coupling phase transition at 50 K, dominantly magnetic transition at 140 K, magnetoelastic phase transition at 200 K, and magnetic but glassy transition at 230 K.

Recently there has been considerable interest on the studies of nanosized $BiFeO_3$, because of the possibility of inducing ferromagnetism in the material by decreasing the particle size. As the magnetic structure of $BiFeO_3$ if of G-type antiferromagnetic, with a modulated spiral spin structure having a long periodicity of 62 nm, material having particle size comparable or smaller than the 62 nm is expected to exhibit a strong size

dependent magnetization. Hence, many efforts have been made to synthesize nanometer sized $BiFeO_3$ [41, 42, 51, 60, 80, 81]. Especially much attention has been focused on the studies on thin films, because it is difficult to observe the ferroelectric hysteresis loops in the bulk $BiFeO_3$ ceramics. Therefore, considerable interest is paid to prepare $BiFeO_3$ in thin film form, in order to improve ferroelectric properties [41, 82–86]. Especially in the thin film form, extremely large spontaneous polarization has been observed [41, 82, 86].

6.5 Studies on $BiFeO_3$ synthesized by a coprecipitation/digestion method

As the coprecipitation/digestion method is found to be a convenient method for the synthesis of nanoparticles of spinel type oxides, the same procedure is extended for the synthesis of nanoparticles of the multiferroic $BiFeO_3$. Nanoparticles of single phase $BiFeO_3$ has been synthesized by the coprecipitation/digestion method followed by calcination and the magnetic properties are evaluated [87].

6.5.1 Synthesis

The synthesis is based on the coprecipitation/digestion method discussed in *section 2.1.1*. $Bi(NO_3)_3.5H_2O$ and $Fe(NO_3)_3.9H_2O$ were used as the precursors for Bi and Fe, respectively, and K_2CO_3 was used as the precipitant for the synthesis. $Bi(NO_3)_3.5H_2O$ was dissolved in dil. HNO_3 and $Fe(NO_3)_3.9H_2O$ was dissolved in distilled water and in a typical experiment, 0.05M $Bi(NO_3)_3.5H_2O$, 0.05M $Fe(NO_3)_3.9H_2O$ and 0.6M K_2CO_3 were used. The metal nitrate solutions were initially mixed together and stirred well to obtain a homogenous solution. Equal volumes of the mixed metal nitrate solution and K_2CO_3 were taken in separate burettes. Both the solutions were added simultaneously to distilled water taken in a three-necked round bottom flask. After the complete addition of the two solutions at 70 °C, a precipitate formed was allowed to digest for 2 hours. To avoid any contamination like K^+ ions, the precipitate was washed thoroughly and repeatedly with 2 liters of distilled water. The washed precipitate was then kept overnight at 70 °C in an oven for drying. The as-dried precursor was labeled as BFA.

The as-dried precursor (sample code: BFA) was calcined at different temperatures;

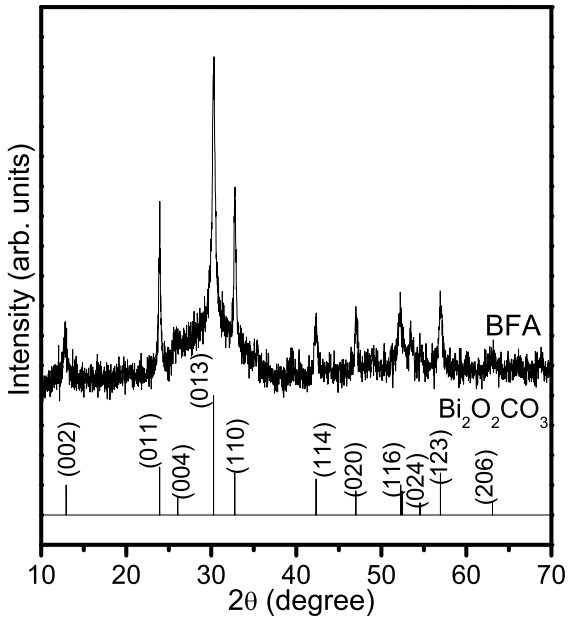

Figure 6.4: Powder XRD pattern of the as-dried precipitate BFA

400 °C (sample code: BFO400), 500 °C (sample code: BFO500), 650 °C (sample code: BFO650) and 750 °C (sample code: BFO750) for 3 hours each.

6.5.2 Characterization

Figure 6.4 shows the powder XRD pattern of the as-dried precursor BFA. Sharp peaks corresponding to bismuth oxide carbonate (JCPDS # 41–1488), with an amorphous background, is observed indicating that the precipitate contains the crystalline bismuth oxide carbonate and probably amorphous iron hydroxide as the constituents.

Thermogravimetric analysis (TGA) is carried out to obtain the calcination temperature of the as-dried precipitate. TGA curve of BFA is shown in Figure 6.5. The curve shows a two-step weight loss, where the continuous weight loss from room temperature to 100 °C is probably due to loss of adsorbed water and water of hydration and the second weight loss above 300 °C probably due to the loss of carbonates and nitrates. There is no considerable weight loss above 400 °C and therefore, the minimum calcination temperature for the formation of the oxide phase is chosen as 400 °C.

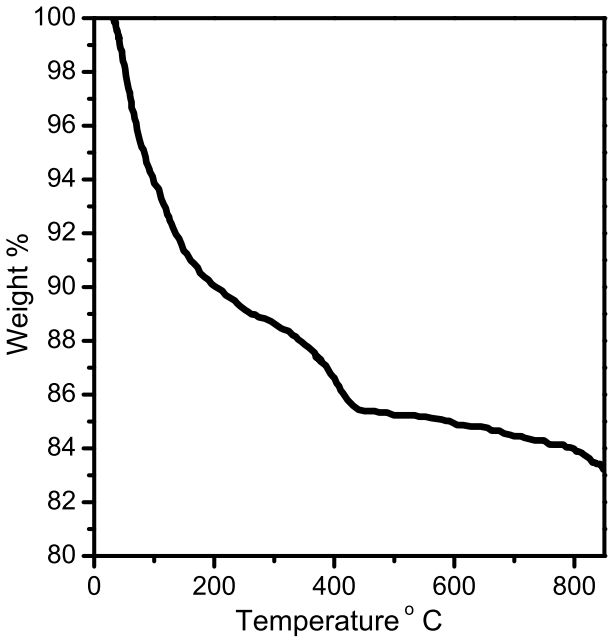

Figure 6.5: Thermogravimetric analysis of BFA

The different calcined samples are characterized by powder XRD for phase analysis. Figure 6.6 shows the XRD patterns of the BFA sample calcined at 400, 500, 650 and 750 °C. The experimental patterns are compared with the simulated pattern of $BiFeO_3$. The powder pattern is simulated using the rhombohedral space group R3c and the corresponding hexagonal lattice parameters $a = 5.5810$ Å, and $c = 13.8685$ Å, as reported in the literature [34, 35]. Almost single phase $BiFeO_3$ is obtained after calcination of BFA at 400 °C, but a weak reflection is observed due to bismuth oxide carbonate. However, single phase $BiFeO_3$ is obtained with out any impurity phase after calcination at 500 °C and the phase is stable even after calcination at 650 °C. Further calcination at 750 °C leads to the formation of small amounts of Bi_2O_3 (JCPDS # 77–2008) as the impurity phase. The lattice parameters of BFO500 and BFO650 calculated by least squares refinement of the diffraction patterns are found to be comparable to the values reported for single crystalline $BiFeO_3$. All the reflections in the XRD pattern of BFO500 are broad due to the nanocrystalline nature of the sample synthesized at low temperatures. The average crystallite size is calculated from X-ray line broadening using the Scherrer for-

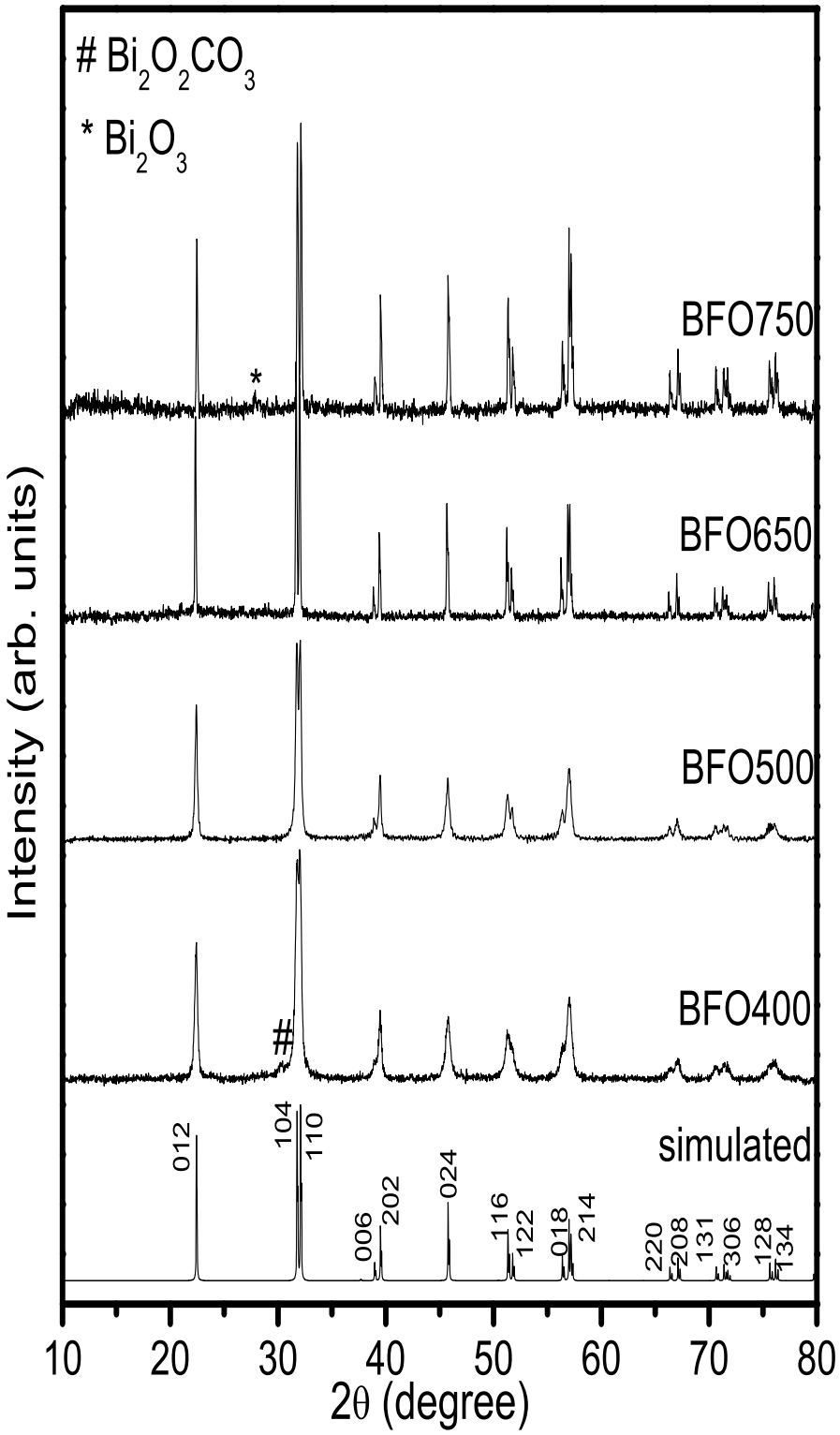

Figure 6.6: Powder XRD patterns of BFO samples calcined at different temperatures. The simulated pattern of $BiFeO_3$ is indexed and shown for comparison.

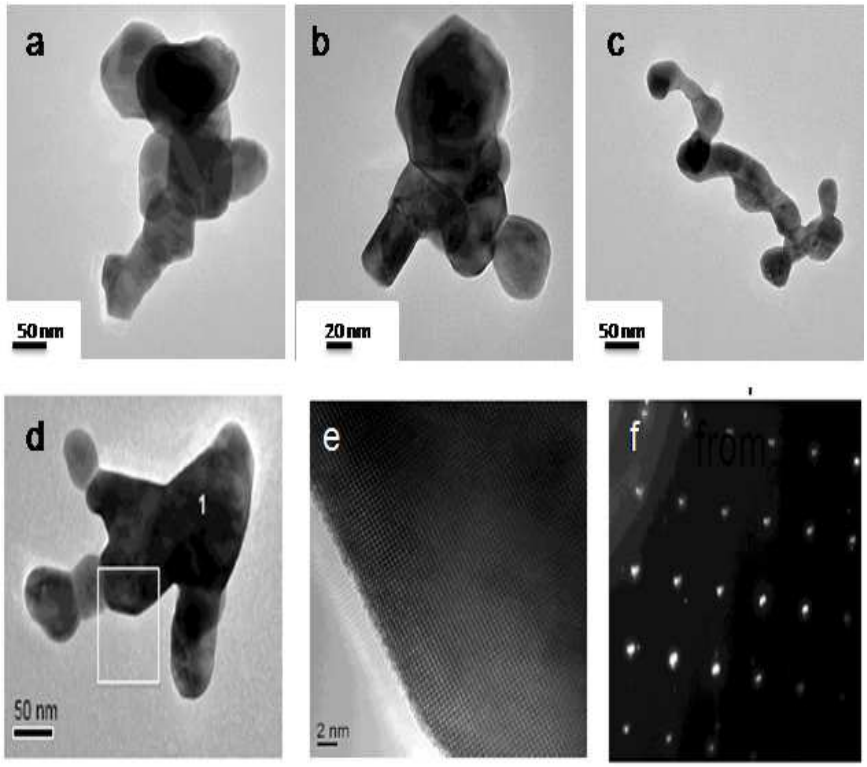

Figure 6.7: HRTEM images and SAED pattern of BFO500

mula, $D = 0.9\lambda/Bcos\theta$, where D is the crystallite size in Å, B is the half maximum line width corrected for instrumental line broadening and λ is the wavelength of X-rays. The crystallite size is obtained as 48 nm for BFO500 and as 97 nm for BFO650.

HRTEM studies have been carried out on the BFO500 sample to confirm the nanocrystalline nature of the sample. Figure 6.7 shows the morphological features of the BFO500 sample. Nearly spherical nanoparticles are connected together to form clusters. The corresponding lattice fringes and the diffraction patterns are given in (e) and (f) of Figure 6.7. The sample is highly crystalline and therefore, well-defined diffraction pattern is observed. The HRTEM analysis shows that the particle size is less than 50 nm. To get the stoichiometric ratio details between Bi and Fe, EDAX mapping has been done. Figure 6.8 clearly shows that Bi and Fe are uniformly distributed in the material, indicating homogeneity and single phase nature of the material.

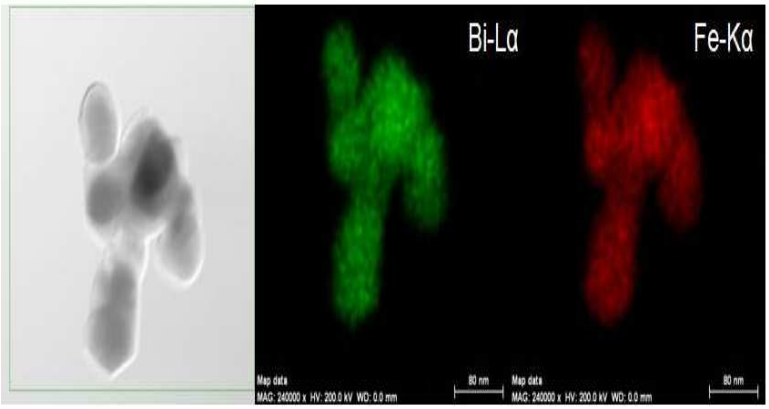

Figure 6.8: EDAX mapping of BFO500

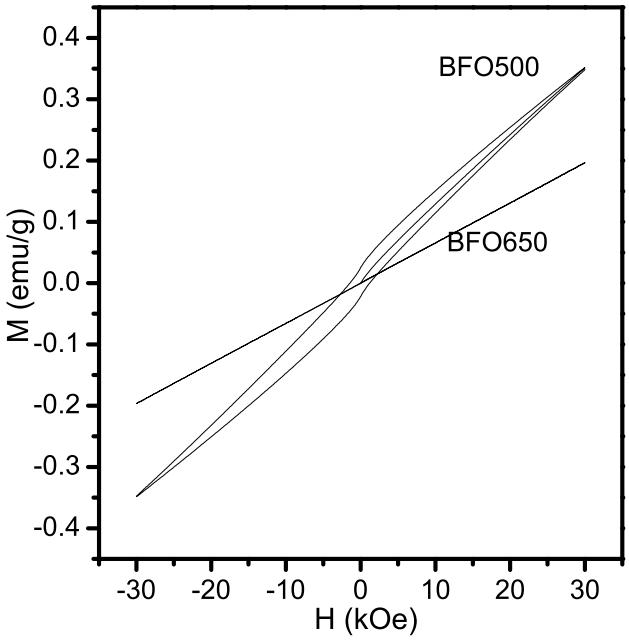

Figure 6.9: Magnetization of BFO500 and BFO650 as a function of magnetic field at room temperature.

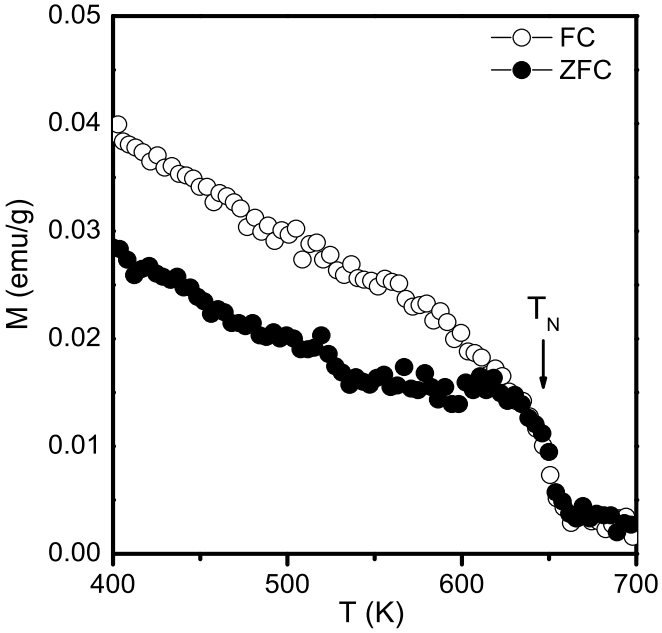

Figure 6.10: FC and ZFC magnetization curves of BFO500 above room temperature.

6.5.3 Magnetic properties

Figure 6.9 shows a comparison of the magnetization of BFO500 and BFO650, measured as a function of field, at room temperature. BFO650 having particle size of ∼100 nm shows the typical behavior expected for an antiferromagnetic material. On the other hand, BFO500 shows a hysteresis loop of coercivity value of 1330 Oe and magnetization at 30 kOe larger than that for the sample BFO650. The observed magnetization behavior of BFO500 may be because the particle size is less than the spiral spin periodicity so that the material becomes ferromagnetic. Also, it is possible that the particles are having an antiferromagnetically ordered core and a shell comprising of weak ferromagnetic moments due to the canting of spins on the surface layer of the particles.

To further confirm the phase purity and the intrinsic magnetic properties of nanosized $BiFeO_3$, magnetic measurements are performed on BFO500 above room temperature. FC and ZFC magnetization curves of BFO500 above 300 K are shown in Figure 6.10. The magnetization curves show a magnetic transition below 650 K, indicating that the sample becomes ferromagnetic at the Neel temperature of $BiFeO_3$ (645 K). The divergence

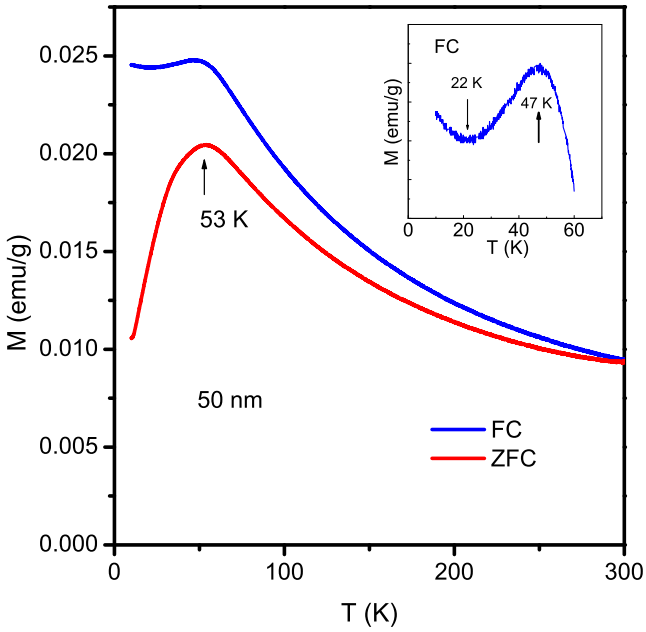

Figure 6.11: FC and ZFC magnetization curves of BFO500 below room temperature. The inset shows the enlarged FC curve below 50 K.

between FC and ZFC magnetization curves below 640 K is similar to that found for other ferro- and ferrimagnetic materials [88]. These results suggest that BFO500 is single-phase $BiFeO_3$ and that it becomes ferromagnetic when the particle size is reduced.

ZFC and FC magnetization curves of BFO500 below 300 K are shown in Figure 6.11. Deviation between the FC and ZFC magnetizations is observed below 300 K. A broad maximum is observed at 53 K in the ZFC magnetization curve. The FC magnetization decreases initially with increasing temperature and after going through a minimum at 22 K, a maximum is reached at 47 K and the magnetization decreases again at higher temperatures. To see the effect of particle size on the magnetic properties at low temperatures, BFO650 with the crystallite size of ∼100 nm, has been subjected to the magnetic measurements below room temperature as shown in Figure 6.12. Both the FC and ZFC magnetization show a deviation below 230 K and show further enlarged deviation with a slope change below 150 K. Both the curves show a large increase in the magnetization below 23 K.

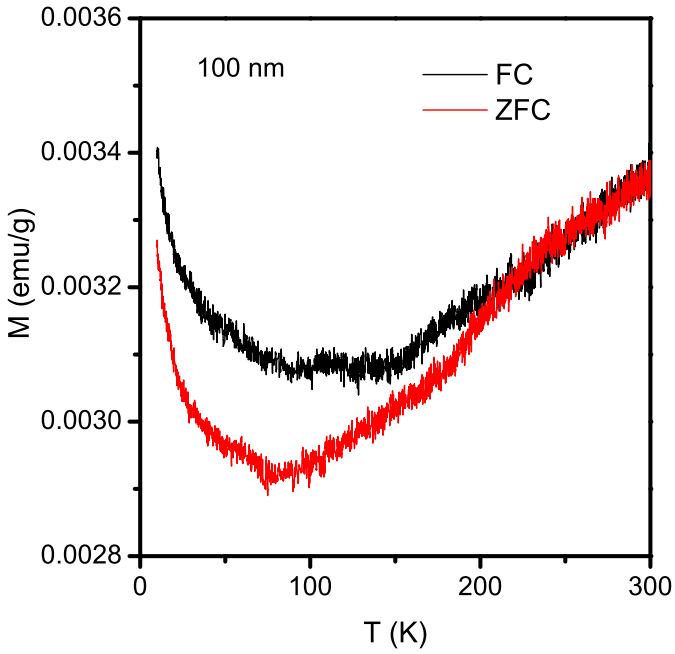

Figure 6.12: FC and ZFC magnetization curves of BFO650 below room temperature.

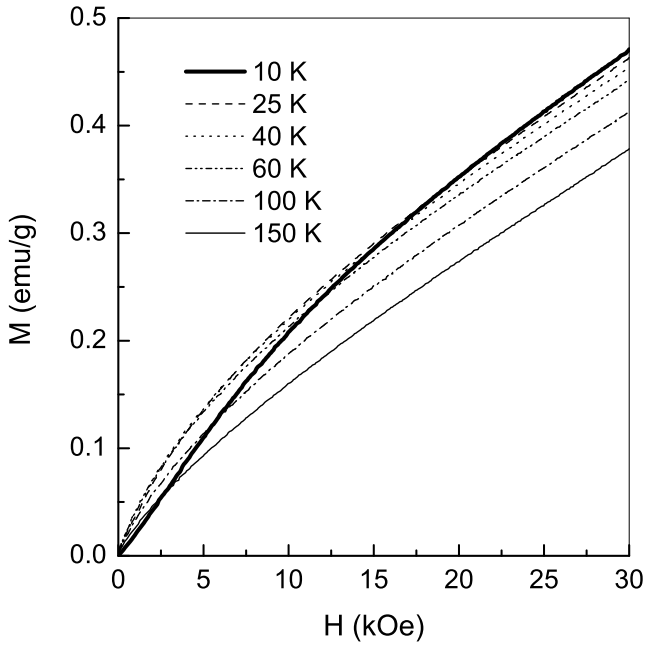

Figure 6.13: Initial magnetization curves of BF500 measured at different temperatures.

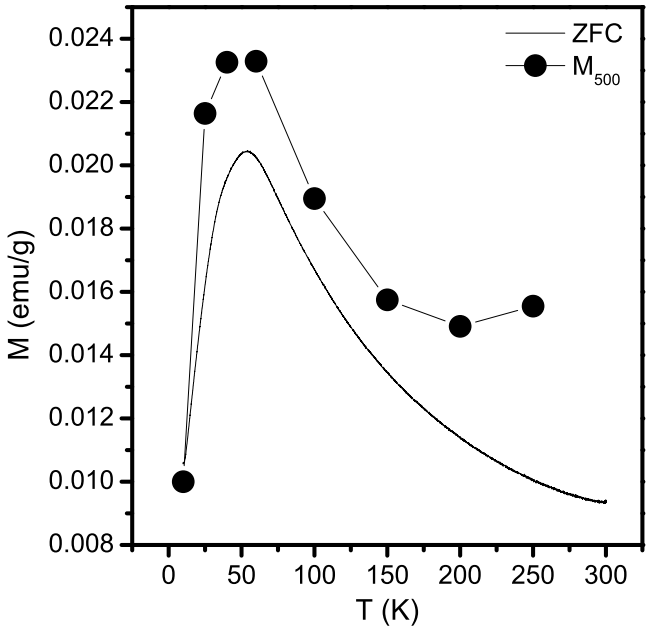

Figure 6.14: Comparison of the initial magnetization of BFO500 at 500 Oe as a function of temperature with the ZFC magnetization measured at 500 Oe.

Initial magnetization curves of BFO500 measured at different temperatures, shown in Figure 6.13, give more information on the changes in the magnetic characteristics of the sample at low temperatures. As the magnetization is not saturated, the saturation magnetization is obtained by extrapolating the M vs $1/H$ curve to $1/H = 0$. At 10 K, the magnetization is very low at low fields where as higher magnetization is observed in the 25–75 K region. It is known that the initial magnetization curve reflects the domain pinning effects of a magnetic system and the same is reflected in the shape of the ZFC magnetization curves [89]. A comparison of the initial magnetization at 500 Oe as a function of temperature is compared with the ZFC magnetization measured at 500 Oe in Figure 6.14. Apart from a maximum at 50 K, a minimum is observed at 200 K in the initial magnetization recorded at 500 Oe. The shapes of both curves are almost similar, except for the larger values of M_{500} extracted from the initial magnetization curves. This is possibly due to the fact that there was a small remanent magnetization after the measurements at the successive low temperatures.

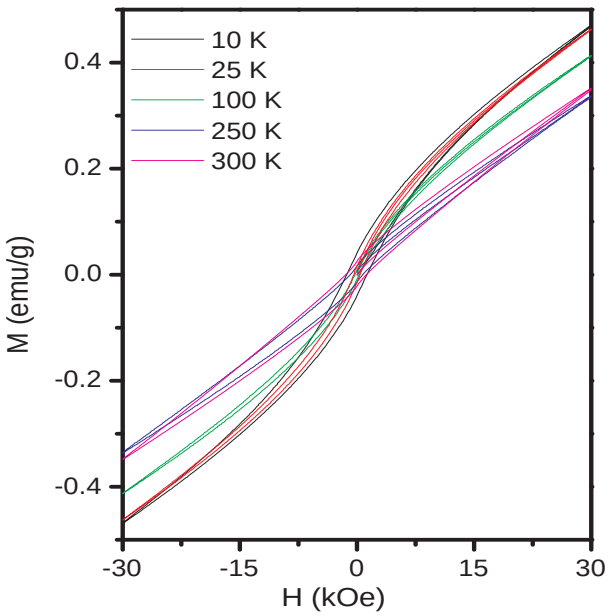

Figure 6.15: M vs H curves of BFO500 recorded at different temperatures.

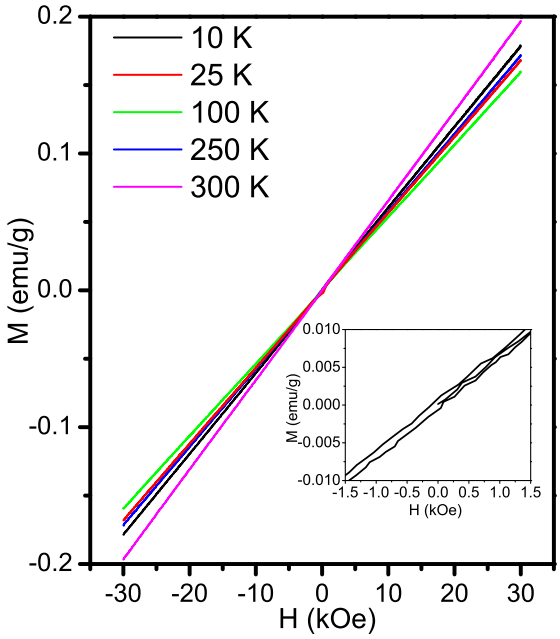

Figure 6.16: M vs H curves of BFO650 recorded at different temperatures. Inset: M-H at 10 K

The particle size effect on the samples can be clearly seen by comparing the magnetic hysteresis curves measured at different temperatures in the range of 10-300 K as shown in Figure 6.15 and Figure 6.16. BFO500 shows magnetic hysteresis at room temperature, with a coercivity of 1330 Oe, indicating that the sample is not antiferromagnetic. Coercivity of the sample is larger than that reported by Park *et al* (425 Oe) [42], for particles of similar size (51 nm) synthesized by a different method. Similarly, the exchange field, $H_{ex} = (H_{c1} - H_{c2})/2$, is also much larger in the present case (125 Oe when compared to 25 Oe). These results suggest that the magnetic characteristics of the nanoparticles of the material are depending on the method of synthesis which determine the surface characteristics. The origin of the higher magnetic moment for $BiFeO_3$ nanoparticles is attributed to surface contribution [42]. For BFO650, the M-H curve recorded at 10 K (inset of Figure 6.16) indicates very weak ferromagnetism with a coercivity of 75 Oe.

Various parameters derived from the magnetic hysteresis curves are shown in Figure 6.17. There are some interesting observations from the temperature dependence coercivity (H_c), remanent magnetization (M_r), and saturation magnetization (M_s). There is a large drop in the coercivity as the temperature is decreased down to 200 K. The coercivity then remains almost constant with a minimum at ∼50 K and increases to a large value below 30 K as the temperature is decreased. Similar characteristics are observed in the case of the remanent magnetization and M_r/M_s ratio also. On the other hand, the magnetization at 30 kOe (3 T, maximum field used for measurement) as well as the saturation magnetization shows a minimum at ∼250 K and increases continuously as the temperature is decreased down to 10 K.

Phase transitions at 90, 140, 200, and 250 K are discovered from Raman spectroscopic studies [78] and spin-glass-like transitions are reported at 30 K [74], 50 K [75], and 250 K [74] from magnetic studies on single crystals and thin films of $BiFeO_3$. The phase transitions observed in the Raman spectroscopic studies are not directly observed in the magnetic measurements, indicating that these are not dominant magnetic transitions as suggested. Similarly, there cannot be many spin-glass-like transitions in the same material, as reported. Hence, the anomalies observed at the specified temperatures are likely to be some changes associated with the domain structure of the material at low temperatures.

Figure 6.18 and Figure 6.19 shows a comparison of the FC and ZFC magnetization

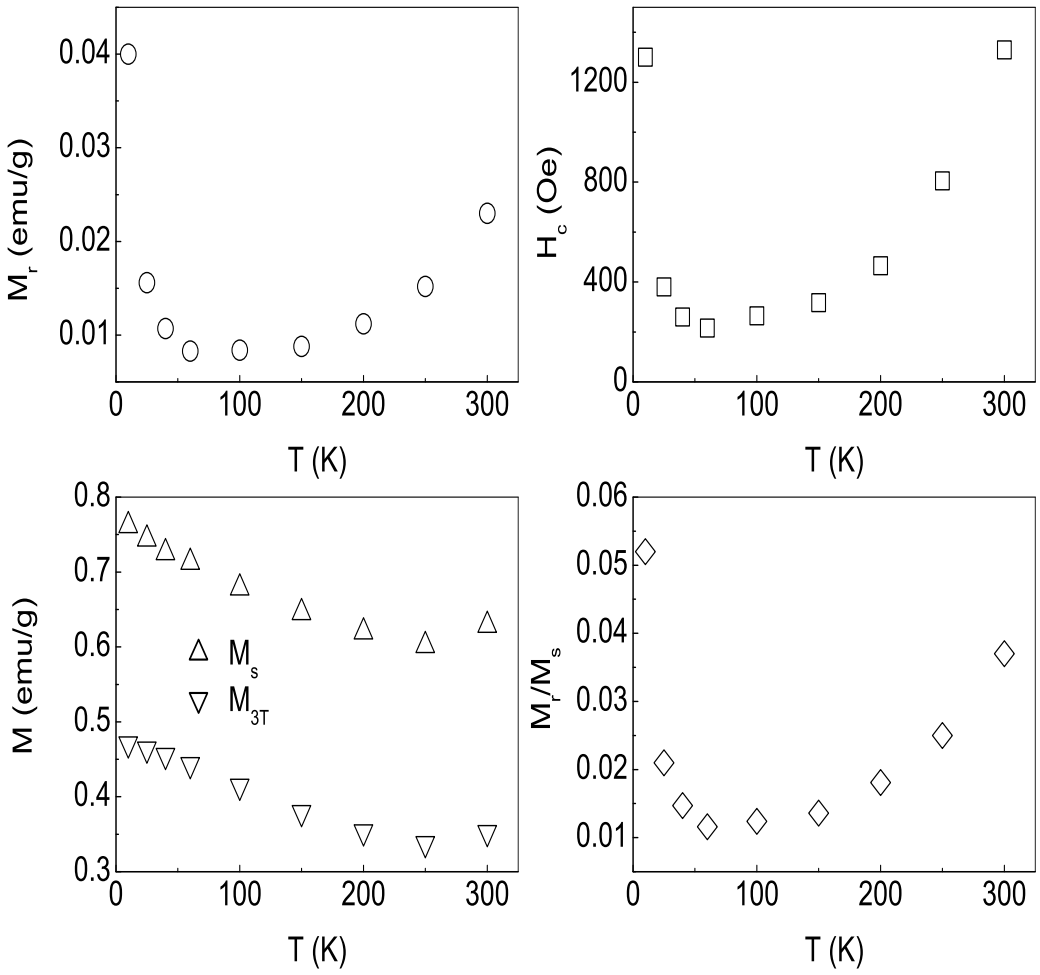

Figure 6.17: Coercivity H_c, remnant magnetization M_r, magnetization at 30 kOe M_{3T}, saturation magnetization M_s, and the ratio M_r/M_s of BFO500 as a function of temperature.

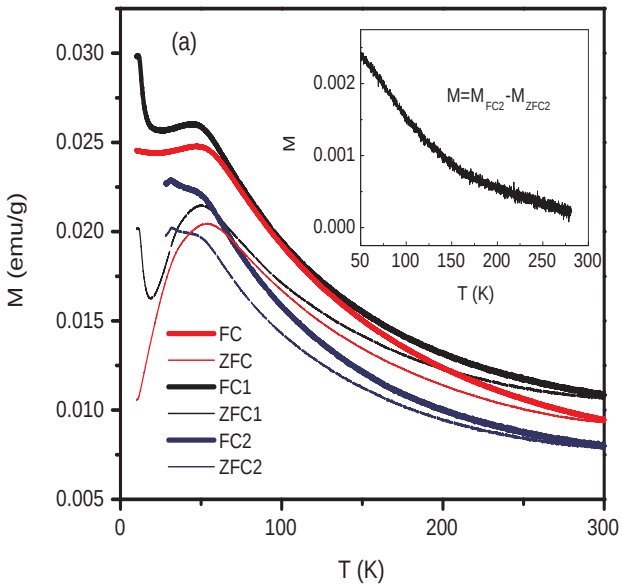

Figure 6.18: Comparison of the FC and ZFC magnetization curves of BFO500 measured under normal and different conditions.

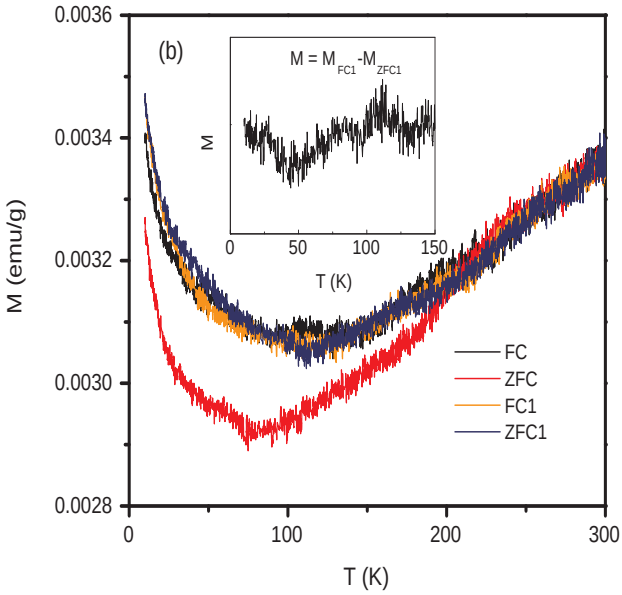

Figure 6.19: Comparison of the FC and ZFC magnetization curves of BFO650, measured under normal and different conditions.

curves of BFO500 and BFO650, measured under normal and different conditions. Apart from the normal FC and ZFC measurements, the field-cooled and zero-field-cooled magnetization measurements were also carried out after applying a large field and then degaussing the sample at the lowest temperature. Such measurements clearly give evidence for the contribution from domain pinning effects [89, 90]. The sample was initially cooled from room temperature to 10 K in zero external magnetic field. At the lowest temperature, a large magnetic field of 10 kOe was applied. The magnetic field was then reduced to zero and the sample was then degaussed at 10 K. After the remanent magnetization was reduced to zero by degaussing at 10 K, the samples magnetization was recorded while warming in a field of 500 Oe as in the case of the usual ZFC magnetization measurement. The same experiment was repeated after cooling the sample in a field of 500 Oe as in the case of normal FC measurements. Similar measurements were repeated after cooling the sample under FC and ZFC conditions to 28 K, a temperature slightly above 22 K where a minimum is observed in the FC magnetization measurements.

For BFO500, after applying a field and degaussing at 10 K, the ZFC magnetization curve as shown in Figure 6.18 (ZFC1) shows a large drop in the magnetization value up to 20 K and the rest of the features are the same as in the normal ZFC curve. However, the magnetization is larger at all temperatures and a larger increasing difference is observed above ∼100 K so that the room-temperature value is much larger than that of the virgin sample. Similar features are observed in the case of the FC magnetization (FC1) shown in Figure 6.18 also. Here, the minimum is shifted to 26 K and the magnetization shows larger difference above ∼140 K. Both the new FC and ZFC curves show a maximum at ∼50 K. On the other hand, when the sample is cooled down to 28 K only, during the FC and ZFC measurements, the natures of both FC and ZFC magnetization curves (FC2 and ZFC2) in Figure 6.18 are almost identical after degaussing. In this case, only a shoulder is observed at 50 K in the magnetization curves. This indicates that the maximum observed at 50 K in the normal FC or ZFC curve is not associated with any spin-glass-like transition or phase transition. Also, the magnetization at 300 K is lower than that of the virgin sample. The difference between M_{FC2} and M_{ZFC2} (inset of Figure 6.18) shows a larger slope change around 140 K, indicating a possible change in the domain structure of the material at this temperature. For BFO650, after degaussing at 10 K, there is not much

difference between the FC and ZFC (FC1 and ZFC1 in Figure 6.19). Both curves show a minimum at 110 K, slight deviation below 100 K, and again overlapping below 25 K. This may be clearly seen from the difference between M_{FC1} and M_{ZFC1} (inset of Figure 6.19) which shows a minimum at 50 K.

Previous studies on $BiFeO_3$ single crystals showed a sharp decrease in the magnetization in both the FC and ZFC curves up to 30 K [74]. AC susceptibility studies indicated a frequency-dependent cusp at 29 K assigned to spin-glass nature and weak ferromagnetism. From the present results, it appears that the large decrease in the FC magnetization up to 25 K as the temperature is increased, for both BFO500 and BFO650, is due to some changes in the magnetic anisotropy or domain pinning behavior of the system which can also show frequency dependence in the ac susceptibility. The effect of pinned domain walls is expected to reflect in the coercivity of the material [90] and this is observed as a large decrease in the coercivity up to 30 K as shown in Figure 6.17.

A sharp cusp in the ZFC curve at 50 K is assigned to a superparamagnetic blocking of the spins [74]. Recent studies on (111) oriented thin film of $BiFeO_3$ showed that the maximum at 50 K is field dependent and varies according to the well known de Almeida-Thouless (AT) line where the freezing temperature $T_f \propto H^{2/3}$ suggesting an acentric long-range spin-glass behavior and mean-field system [75]. The AT line deviates above 140 K and this temperature corresponds to the temperature at which the magnon cross section diverges. However, it has been concluded that the AT behavior is not a proof for the spin-glass behavior as it can be due to superparamagnetism as well as domain pinning effects. Park *et al* showed that a maximum in the magnetization is observed at this temperature for samples of all sizes, bulk, as well as nanoparticles [42]. This suggests that the feature at 50 K is an intrinsic property of $BiFeO_3$. Present results show that the coercivity is minimum at this temperature for BFO500 and the maximum at 50 K in the ZFC and FC curves can be suppressed after degaussing the sample at a lower temperature, indicating that this feature also is due to some domain pinning behavior.

The shape of the ZFC magnetization curve when measured in a low magnetic field is related to the magnitude and temperature variation of the coercivity which is a measure of the anisotropy [91]. Thus, there is a direct correlation between the shape of the ZFC magnetization curve and the domain structure of a material. The inverse of the coercivity

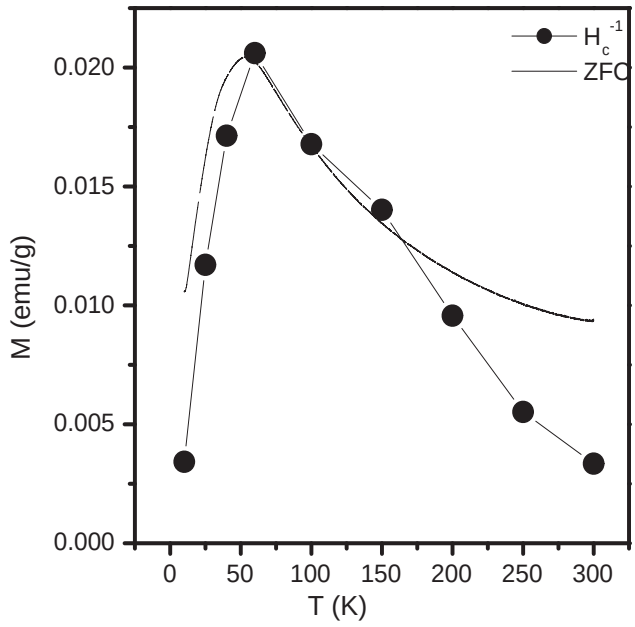

Figure 6.20: The inverse of the coercivity of BFO500, normalized with respect to the maximum in the ZFC magnetization.

of BFO500, normalized with respect to the maximum in the ZFC magnetization, is compared in Figure 6.20. The features of both curves are comparable at low temperatures. Although there is no strong magnetic feature for BFO500 at 100 K corresponding to the minimum observed in the FC and ZFC curves for BFO650, a minimum in the remanence is observed at 100 K for BFO500. Also, a large deviation in the inverse of the coercivity is observed above 150 K and the coercivity shoots up above this temperature. These facts again suggest the correlation between the magnetic characteristics and the domain structure of the material.

A broad minimum is observed around 150 K in the FC and ZFC measurements on single crystals [74]. A ferromagnetic transition is observed at this temperature from studies on oriented thin films [92]. The present results show that this is not a true ferromagnetic transition. No indication for such a magnetic transition is observed from studies on BFO500, except that i) a large deviation in the inverse of the coercivity is observed above 150 K, ii) a slope change in this temperature region is observed in the difference

between FC and ZFC magnetizations after degaussing of BFO500, and iii) the coercivity shoots up above this temperature. These facts again suggest the correlation between the magnetic characteristics and the domain structure of the material. The divergence between FC and ZFC magnetization curves of single crystalline $BiFeO_3$ below 250 K is previously assigned to spin glass behavior [74]. A similar feature is observed for the larger particles of $BiFeO_3$ (BFO650) in the present work. However, this divergence between FC and ZFC is observed immediately below the magnetic transition temperature ($\sim$645 K) for the smaller particles (BFO500), similar to other ferromagnetic systems. A minimum in the saturation magnetization is observed around 250 K for BFO500, indicating that the divergence between FC and ZFC curves for BFO650 below 230 K is not a true spin glass behavior. For larger particles, this can be due to the strong coupling between the antiferromagnetic and ferroelectric domain structures.

6.5.4 Conclusions

$BiFeO_3$ nanoparticles with average size of $\sim$50 nm, smaller than the spin periodicity value, is synthesized by a coprecipitation/digestion method. The material becomes ferromagnetic below the Neel temperature of the bulk material ($\sim$645 K). There is a divergence between FC and ZFC magnetization, immediately below the magnetic transition temperature, similar to that observed in the case of other ferromagnetic systems. On the other hand, for larger particles of size $\sim$100 nm (BFO650) the divergence is observed only below 230 K, as in the case of the bulk material. This temperature is comparable to the minimum in the saturation magnetization observed for BFO500 at 250 K, indicating that the divergence observed in case of BFO650 with larger particle size can be due to the strong coupling between the antiferromagnetic and ferroelectric domain structures. For nanoparticles of $BiFeO_3$ of two different sizes, anomalous magnetic characteristics are observed at temperature regions closer to that of the phase transitions reported in the literature at 90, 140, 200 and 250 K from Raman spectroscopic studies and spin-glass-like transitions reported at 30, 50, 150, and 250 K from magnetic studies on single crystals and thin films. Some changes in the magnetic characteristics are observed at these temperatures when the measurements are done under different experimental conditions, suggesting that the phase transitions or spin-glass-like transitions are directly associated

with changes in the intrinsic magnetic nature of the $BiFeO_3$, strongly coupled with the lattice. The phase transitions observed in the Raman spectroscopic studies are not directly observed in the magnetic measurements, indicating that these are not dominant magnetic transitions as suggested. Similarly, there cannot be many spin-glass-like transitions in the same material, as reported. Hence the anomalies observed at the specified temperatures are likely to be some changes associated with the domain structure of the material at low temperatures.

6.6 Studies on $BiFeO_3$ powders synthesized by an auto-combustion method

It has been reported that room temperature ferromagnetism with high saturation magnetization of $0.4\mu_B$/Fe can be achieved for 4 nm sized particles of $BiFeO_3$ synthesized by a combustion method using glycine as a fuel [60]. On the other hand, for particles of comparable average sizes synthesized by a sol-gel method, much lower magnetic moments are reported [42]. Therefore, it appears that ferromagnetism in nanocrystalline $BiFeO_3$ depends on the method of synthesis. This is probably due to the nature of surface defects, lattice strain, presence of Fe^{2+} in the nanomaterials due to oxygen deficiency, etc. We have synthesized single phase nanocrystalline $BiFeO_3$ by controlling the stoichiometry of the fuel used in the auto-combustion method reported previously [60,93], and studied the magnetic properties of the material above and below room temperature.

In this present work glycine-to-metal molar ratio has been optimized to get the single phase BFO. Further, detailed magnetic measurements have been carried out to get information on the possible cause of the high value of room temperature saturation magnetization of 0.25 (μ_B/Fe) observed in the present work [43].

6.6.1 Synthesis

$BiFeO_3$ was synthesized by the glycine-nitrate auto-combustion method. The starting materials for the synthesis were the metal nitrates $Bi(NO_3)_3.5H_2O$, $Fe(NO_3)_3.9H_2O$ and glycine, $C_6H_5NH_2$, as fuel. Stoichiometric amounts of $Bi(NO_3)_3.5H_2O$ and $Fe(NO_3)_3.9H_2O$ were dissolved in distilled water. The water solutions of the metal nitrates and glycine were

Table 6.1: Sample codes, glycine-to-metal ratios tried in the combustion reaction and the final products obtained. Bi to Fe ratio is kept as 1:1 for the synthesis.

Sample code	Ratio of moles of glycine/metal ion	Phases formed
BFO-A	0.50	Amorphous phase
BFO-B	0.90	Amorphous phase + $BiFeO_3$
BFO-C	1.00	$BiFeO_3$ + Bi_2O_3
BFO-D	1.20	$BiFeO_3$ + Bi_2O_3
BFO-E	1.25	$BiFeO_3$
BFO-F	1.50	$BiFeO_3$ + Bi_2O_3+$Bi_{25}FeO_{40}$ + Fe_3O_4
BFO-G	1.67	$BiFeO_3$ + $Bi_{25}FeO_{40}$ + Fe_3O_4
BFO-H	2.00	$BiFeO_3$ + $Bi_{25}FeO_{40}$ + Fe_3O_4 + Bi

mixed together in a large crystallizing dish and kept over a hot plate for auto-combustion at 200 °C. After complete evaporation of water, a thick gel was formed, which subsequently burnt to give a fluffy mass. This was ground using an agate mortar and pestle to get a fine powder and further characterized by XRD measurements. Different glycine-to-metal ratios have been tried to optimize the condition to get single phase material. Table 6.1 gives the details of the sample code and glycine-to-metal ratio tried to obtain single phase material.

The combustion reaction of the metal nitrates as the oxidizer and glycine as fuel can be written as,

$$3Bi(NO_3)_3.5H_2O+3Fe(NO_3)_3.9H_2O+10C_2H_5O_2N \rightarrow 3BiFeO_3+20CO_2+14N_2+25H_2O \tag{6.1}$$

or

$$Bi(NO_3)_3.5H_2O+Fe(NO_3)_3.9H_2O+\frac{10}{3}C_2H_5O_2N \rightarrow BiFeO_3+\frac{20}{3}CO_2+\frac{14}{3}N_2+\frac{25}{3}H_2O \tag{6.2}$$

As per the above equation 1.67 moles of glycine per mole of metal ion is required as a fuel to form $BiFeO_3$ by the combustion reaction. Therefore, in this present study, by taking 1.67 moles glycine as a reference, the mole ratios of glycine has been varied from 0.5 to 2.

6.6.2 Characterization

Figure 6.21 shows the powder XRD patterns of the as-prepared samples by varying the glycine-to-metal molar ratio. From the figure it is clear that when the glycine-to-metal ratio is very low (0.50) the material formed is highly amorphous (BFO-A). This is because, sufficient fuel is not available for the combustion reaction and the temperature is very low. When the ratio is increased to 0.90 (BFO-B), weak reflections due to $BiFeO_3$ are observed, apart from an amorphous phase. Further increase in the ratio to 1.00 (BFO-C) shows improvement in the crystallinity of the $BiFeO_3$ phase, with the formation of Bi_2O_3 (JCPDS # 74–2008) as an impurity phase. The intensity of the peak due to this impurity phase is decreased with increasing the amount of glycine further to 1.20 (BFO-D) and when the ratio is 1.25, single phase $BiFeO_3$ is formed (BFO-E). As the glycine to metal ratio is increased further, including the stoichiometric ratio of 1.67 for the combustion reaction (obtained from the equation), other impurity phases such as Fe_3O_4 (JCPDS # 19–0629), Bi (JCPDS # 01–0688), $Bi_{25}FeO_{40}$ (JCPDS # 46–0416), etc., are formed apart from $BiFeO_3$.

All the observed peaks of BFO-E correspond to $BiFeO_3$ as evidenced from a comparison of the experimental and simulated patterns. The XRD pattern is indexed on the reported rhombohedral structure of the compound (space group R3c) with lattice parameters value of $a = 5.586$ Å, and $c = 13.863$ Å [34,35]. All the reflections in the experimental patterns are some what broad indicating nanocrystalline nature of the sample. The average crystallite size is calculated as 26 nm from the full width at half maximum of the (024) peak, using the Scherrer formula, $D = 0.9\lambda/\beta cos\theta$.

Figure 6.22 shows the TEM image of BFO-E, indicating the morphological features of the sample. The image shows flaky type particles forming clusters. Similar morphological features have been reported for different types of oxides synthesized by the glycine nitrate combustion process [94,95]. Since the combustion reaction is very rapid, it is very difficult to control the morphology in case of the auto-combustion method. The selected area electron diffraction (SAED) pattern shown in Figure 6.22 indicates that the material is polycrystalline in nature.

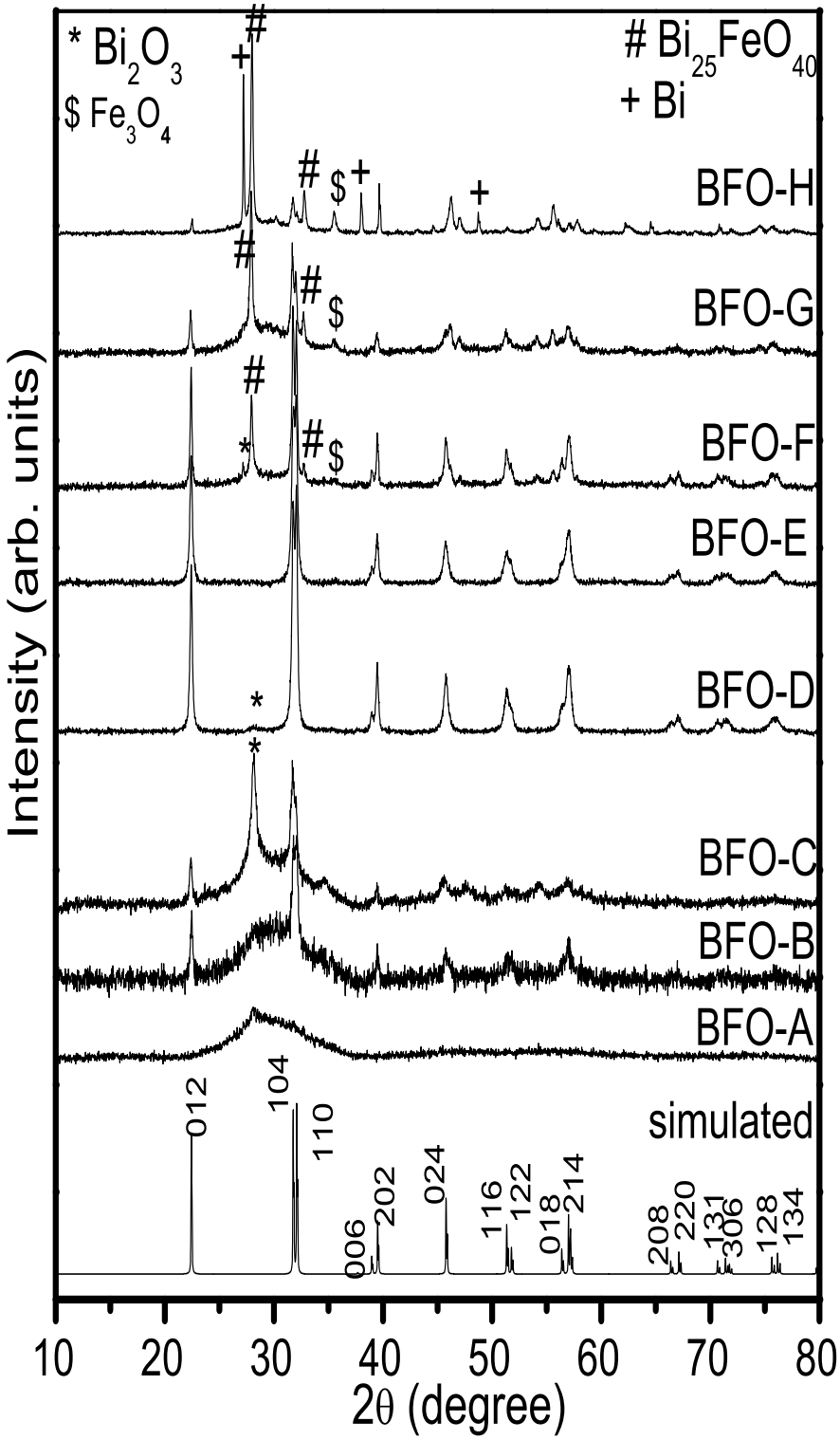

Figure 6.21: Powder XRD patterns of BFO-A to BFO-H. The simulated XRD pattern of $BiFeO_3$ is indexed and shown for comparison.

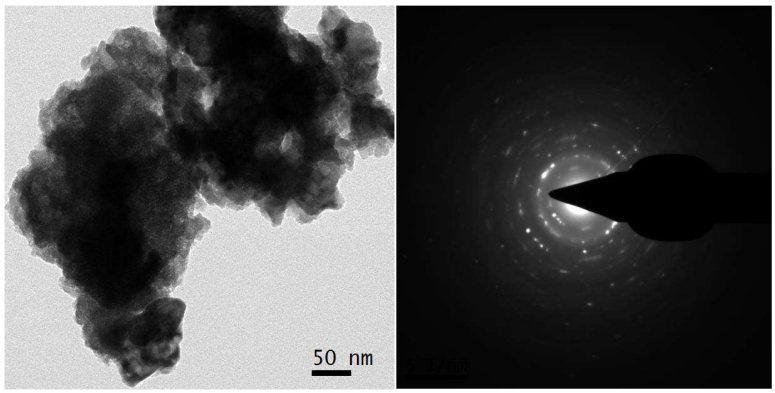

Figure 6.22: HRTEM image and SAED pattern of the sample BFO-E

6.6.3 Magnetic properties

Detailed magnetic studies have been carried out on the single phase sample BFO-E. Magnetic measurements indicate that the sample BFO-E is ferromagnetic at room temperature, as evidenced from Figure 6.23. The magnetization as a function of field at different temperatures has been measured, up to a field of 5 kOe. The magnetization is almost saturated at 5 kOe and the saturation magnetization is almost an order of magnitude larger than that reported for nanoparticles of comparable size, synthesized by sol-gel method [42]. Magnetic hysteresis is observed at room temperature with a coercivity of 147 Oe. Coercivity increases with decreasing temperature. It is observed that the magnetization is larger at the intermediate temperature of 140 K.

To get detailed information on the magnetic nature of the sample, the saturation magnetization (M_s) has been plotted against temperature as shown in Figure 6.24. The magnetization at 5 kOe has been considered as saturation magnetization. There are many noticeable changes taking place at different temperatures, in the temperature variation of magnetization. Magnetization is increased as the temperature is decreased below 300 K and the magnetization remains almost constant in the 100–250 K region, with a maximum around 140 K. There is a large drop in the magnetization below 100 K, with a minimum at 25 K. Similarly, in the case of coercivity, the increase is almost linear at low and high temperatures with a slope change around 150 K, as shown in the inset of Figure 6.24. The variation of the magnetic parameters as a function of temperature is almost similar to that observed for the sample synthesized by the coprecipitation/digestion method, as discussed

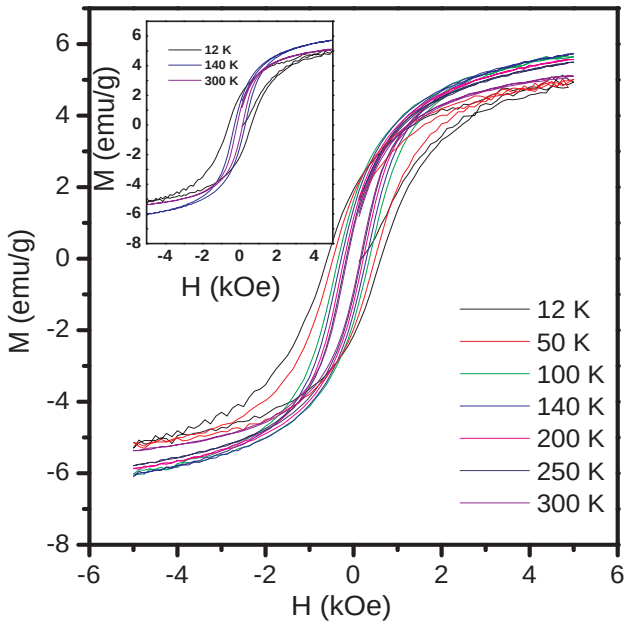

Figure 6.23: M-H curves of BFO-E recorded at different temperatures. Inset:MH loops at 12, 140 and 300K.

in the previous section. Thus, it appears that the higher magnetization of the sample is an intrinsic property of the material. The temperatures at which some of the anomalies are observed are comparable to the temperatures at which anomalies are reported from Raman studies as well as dielectric measurements on single crystals [78, 79].

Field cooled (FC) and zero field cooled (ZFC) magnetization measurements in a small applied magnetic field of 100 Oe have been performed on the sample to get detailed information on the various changes that taking place at low temperatures. During the field cooled measurement, the sample was cooled under a constant field (100 Oe in the present case) to the lowest possible temperature and magnetization was recorded while heating back the sample to room temperature. In the zero field cooled measurement, the sample was taken to the lowest possible temperature in the absence of field and magnetization was measured at 100 Oe while heating back to room temperature. FC and ZFC magnetization measurements below room temperature, shown in Figure 6.25, show some anomalies at certain temperatures. The ZFC magnetization curve shows a slope

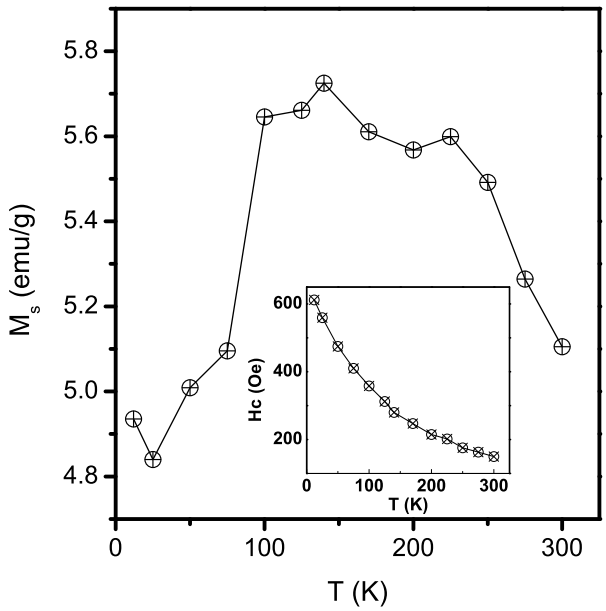

Figure 6.24: Magnetization at 5 kOe as a function of temperature. Inset: Temperature variation of coercivity.

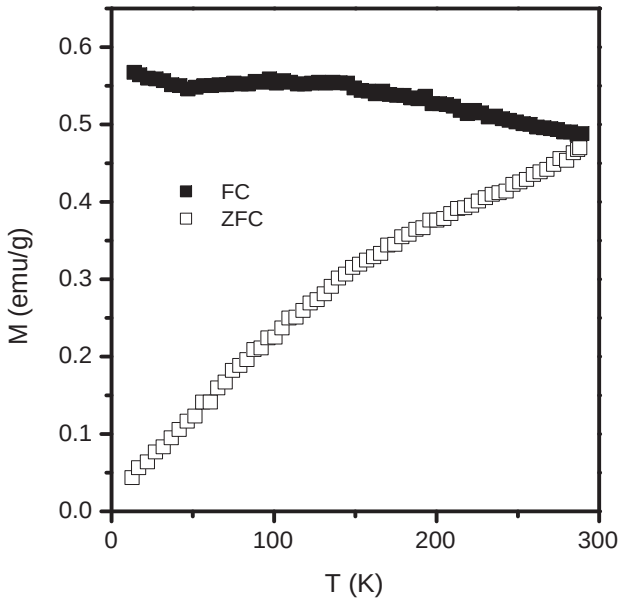

Figure 6.25: Zero field cooled and field cooled magnetization of BFO-E measured below room temperature in a field of 100 Oe.

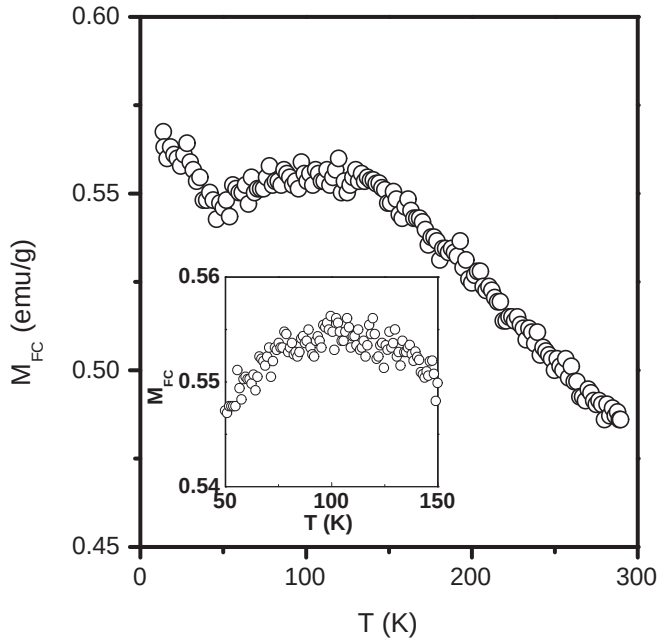

Figure 6.26: Details of the field cooled magnetization of BFO-E showing anomalies at different temperatures.

change around 150 K, as observed in the case of temperature variation of the coercivity below room temperature (inset of Figure 6.24). The shape of the ZFC magnetization curve when measured in a low magnetic field is related to the magnitude and temperature variation of the coercivity which is a measure of the anisotropy [91]. Figure 6.26 shows detailed information of the FC magnetization curve. The FC magnetization curve shows a minimum at 50 K, a broad maximum around 100 K and a linear decrease above 150 K. Studies on single crystals of antiferromagnetic $BiFeO_3$ showed some anomalies at these temperatures in the FC and ZFC magnetization data [74]. Combining this observation with the anomalies observed in the magnetization measured at different temperatures (Figure 6.24), it can be concluded that the observed high ferromagnetic moment of the nanocrystalline material is likely to be intrinsic in nature.

To get information about the magnetic transition which is expected to be at around 645K, magnetic measurement is made as a function of temperature above room temperature. Figure 6.27 clearly shows that the sample becomes ferromagnetic below the Néel

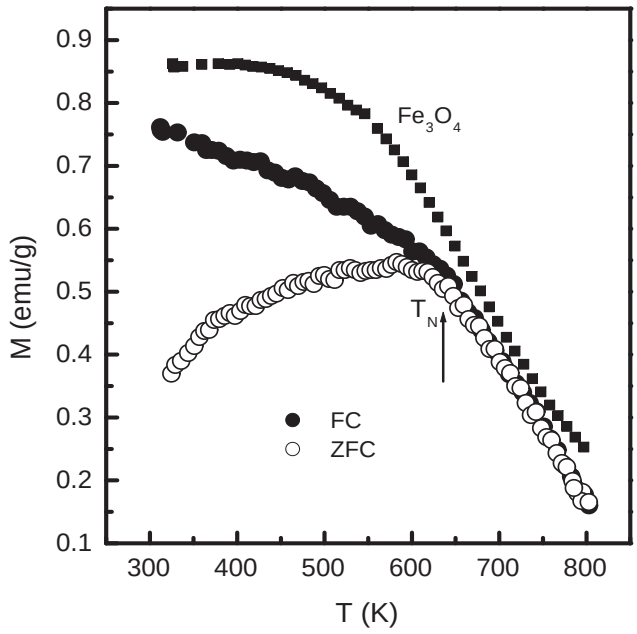

Figure 6.27: Zero field cooled and field cooled magnetization of BFO-E measured above room temperature in a field of 100 Oe.

temperature of $BiFeO_3$ (645 K). The divergence between FC and ZFC magnetization curves below 645 K is similar to that found for other ferro- and ferrimagnetic materials [88], suggesting that $BiFeO_3$ becomes ferromagnetic when the particle size is reduced. However, the magnetic transition is very broad above 645 K, when compared to the sharp transition observed for 47 nm particles discussed in the previous section (see Figure 6.10). It can be argued that the broad transition above T_N could be due to the much smaller particles of the present sample, due to the finite size effect. Such increase in the magnetic transition temperature is reported in the case of some spinel ferrites [96–98]. However, in the case of the spinel ferrite nanoparticles, the higher transition temperatures could be attributed to changes in the cation distribution in the tetrahedral and octahedral sites.

It is possible that the broad magnetic transition below 800 K, which is very close to the Curie temperature of Fe_3O_4, is a contribution from Fe_3O_4 as a magnetic impurity phase formed during the synthesis. The formation of Fe_3O_4 as an impurity phase is observed in the XRD patterns of the samples synthesized with glycine-to-metal ratios

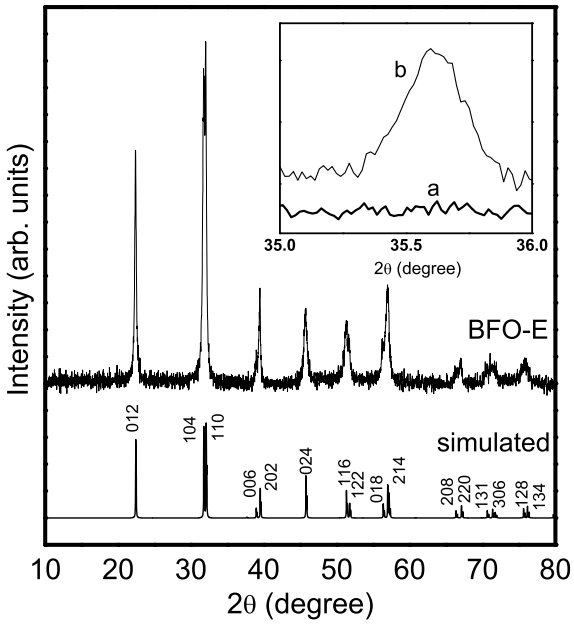

Figure 6.28: Powder XRD pattern of $BiFeO_3$ with simulated pattern. Inset (a) normal and (b) slow scan XRD patterns in the 2θ region where the most intense (311) reflection from Fe_3O_4 is expected.

above 1.25. Thus, it is possible that minor amounts of this impurity phase is formed which could not be detected in the powder XRD pattern of BFO-E. The magnetization curve of nanocrystalline Fe_3O_4, measured in a magnetic field of 100 Oe, above room temperature, is compared in Figure 6.27. The nature of the magnetization behavior of BFO-E, above 650 K, is almost identical to that of nanocrystalline Fe_3O_4, suggesting that presence of Fe_3O_4 impurity phase is the most probable origin of the broad magnetic transition observed for $BiFeO_3$.

Since the presence of Fe_3O_4 is not detected from powder XRD studies, it is possible that the impurity phase is present in very small amounts, below the detection limit of powder XRD. To verify whether the presence of extremely small amounts of the impurity phase can be detected, the XRD pattern is recorded at a very slow scan rate in the 2θ region where the maximum intense peak of Fe_3O_4 is expected. This procedure is known to be highly efficient for detecting very small quantities of impurity phases [99]. The XRD data is recorded at a very slow scan rate in the 2θ range 35° to 36° where the

(311) reflection of Fe_3O_4 is expected. In the Figure 6.28 it can be seen that a very weak reflection is observed at 2θ =35.6° corresponding to the d-spacing of 2.53Å, comparable to d_{311} of Fe_3O_4 (JCPDS # 19–0629). This confirms that Fe_3O_4 is present as an impurity phase, in very small amounts, in the ferromagnetic sample. This undetected impurity phase could be responsible for the higher magnetic moment of the sample synthesized by the auto-combustion method, reported in the literature [60].

6.6.4 Conclusions

Almost single phase nanocrystalline multiferroic $BiFeO_3$ is synthesized by the glycine-nitrate auotcombustion method by optimizing the synthesis conditions. Unexpectedly high magnetic moment is observed at room temperature for the sample synthesized by the auto-combustion method. The possible effect of the synthetic methodology influencing the magnetic properties of the $BiFeO_3$ system has been explained from detailed structural and magnetic characterization. Very large saturation magnetization is obtained at room temperature for nanoparticles of size ∼25 nm. A broad magnetic transition above the Neel temperature (T_N) of $BiFeO_3$, which is extended up to 800 K, suggests the presence of Fe_3O_4 as a possible magnetic impurity phase responsible for the high magnetic moment at room temperature. Normal XRD analysis failed to detect small amounts of any impurity phase. However, detailed XRD studies showed the presence of very small amounts of Fe_3O_4 impurity phase, as evidenced from magnetic measurements. Thus, the present studies, in general, give information on the importance of the detailed material characterization studies required before coming to any final conclusions on the unusual properties observed for functional nanomaterials.

References

[1] J.B. Goodenough, J.M. Longo, *Crystallographic and magnetic properties of perovskite and perovskite-related compounds*, Landbolt-Börnstein, New Series, vol. III.4(a), Springer, Berlin, 1970, p. 126.

[2] T. Mitsui, S. Nomura, A.M. Hellinege, K.H. Hellwege, *Ferroelectrics and related substances*, Landolt-Börnstein, New Series, vol. 16(a),Springer, Berlin, 1981.

[3] A. Filippetti, N.A. Hill, *Phys. Rev. B.* 65 (2002) 195120.

[4] K.F. Wang , J.-M. Liu, Z.F. Ren, *Adv. Phys.* 58 (2009) 321.

[5] M. Fiebig, *J. Phys. D: Appl. Phys.* 38 (2005) R123.

[6] H. Schmid, *Ferroelectrics* 162 (1994) 317.

[7] W. Eerenstein, N.D. Mathur, J.F. Scott, *Nature* 442 (2006) 759.

[8] A. Filippetti, N.A. Hill, *J. Magn. Magn. Mater.* 236 (2001) 176.

[9] R. Seshadri, N.A. Hill, *Chem. Mater.* 13 (2001) 2892.

[10] A.M. dos Santos, S. Parashar, A.R. Raju, Y.S. Zhao, A.K. Cheetham, C.N.R. Rao, *Solid State Commun.* 122 (2002) 49.

[11] S. Sagar, P.A. Joy, M.R. Anantharaman, *Ferroelectrics* 392 (2009) 13.

[12] W. Prellier, M.P. Singh, P. Murugavel, *J. Phys.: Condens. Matter.* 17 (2005) R803.

[13] S.M. Selbach, T. Tybell, M.A. Einarsrud, T. Grande, *Adv. Mater.* 20 (2008) 3692.

[14] G.A. Smolenski, I.E. Chupis, *Sov. Phys. Uspekhi.* 25 (1982) 475.

[15] I. Sosnowska, T.P. Neumaier, E. Steichele, *J. Phys. C: Solid State* 15 (1982) 4835.

[16] N.A. Hill, *J. Phys. Chem. B* 104 (2000) 6694.

[17] J. Van Suchtelen, *Philips Res. Rep.* 27 (1972) 28.

[18] G. Srinivasan, E.T. Rasmussen, B.J. Levin, R. Hayes, *Phys. Rev. B* 65 (2002) 134402.

[19] S. Dong, J. Zhai, J.F. Li, D. Viehland, *Appl. Phys. Lett.* 88 (2006) 082907

[20] H. Zheng, J. Wang, S.E. Lofland, Z. Ma, L. Mohaddes-Ardabili, T. Zhao, L. Salamanca-Riba, S.R. Shinde, S.B. Ogale, F. Bai, *Science* 303 (2004) 661

[21] L. Yan, Y. Yang, Z. Wang, Z. Xing, J. Li,D. Viehland, *J. Mater. Sci.* 44 (2009) 5080.

[22] I. Levin, J. Li, J. Slutsker, A.L. Roytburd, *Adv. Mater.* 18 (2006) 2044.

[23] J. Li, I. Levin, J. Slutsker, V. Provenzano, P.K. Schenck, R. Ramesh, J. Ouyang, A.L. Roytburd, *Appl. Phys. Lett.* 87 (2005) 072909.

[24] F. Zavaliche, H. Zheng, L. Mohaddes-Ardabili, S.Y. Yang, Q. Zhan, P. Shafer, E. Reilly, R. Chopdekar, Y. Jia, P. Wright, *Nano Lett.* 5 (2005) 1793

[25] C. Deng, Y. Zhang, J. Ma, Y. Lin, C.W. Nan, *J. Appl. Phys.* 102 (2007) 074114.

[26] Y. Zhang, Z. Li, C. Deng, J. Ma, Y. Lin, C.W. Nan, *Appl. Phys. Lett.* 92 (2008) 152510

[27] A. Run, D.R. Terrell, J.H. Scholing, *J. Mater. Sci.* 9 (1974) 1710

[28] G. Harshe, J.P. Dougherty, R.E. Newnham, *Int. J. Appl. Electromagn. Mater.* 4 (1993) 145

[29] M.I. Bichurin, I.A. Kornev, V.M. Petrov, I.V. Lisnevskaya, *Ferroelectrics* 204 (1997) 289

[30] M.I. Bichurin, V.M. Petrov, *Ferroelectrics.* 162 (1994) 33

[31] Y.K. Fetisov, G. Srinivasan, *Electron. Lett.* 41 (2005) 1066

[32] S.X. Dong, J.G. Bai, J.Y. Zhai, J.F. Li, G.Q. Lu, D. Viehland, S.J. Zhang, T.R. Shrout, *Appl. Phys. Lett.* 86 (2005) 182506

[33] Y.H. Chu, L.W. Martin, M.B. Holcomb, R. Ramesh, *Mater. Today* 10 (2007) 16.

[34] C. Michel, J.M. Moreau, G.D. Achenbach, R. Gerson, W.J. James, *Solid State Commun.* 7 (1969) 701.

[35] J.D. Bucci, B.K. Robertson, W.J. James, *J. Appl. Crystallogr.* 5 (1972) 187.

[36] P. Fischer, M. Polomska, I. Sosnowska, M. Szymanski, *J. Phys. C: Solid State* 13 (1980) 1931.

[37] F. Kubel, H. Schmid, *Acta Crystallogr. B* 46 (1990) 698.

[38] J. Teague, *Solid State Commun.* 8 (1970) 1073.

[39] R. Przenioslo, A. Palewicz, M. Regulski, I. Sosnowska, R. M. Ibberson, and K. S. Knight, *J. Phys.: Condens. Matter* 18 (2006) 2069.

[40] A. Palewicz, T. Szumiata, R. Przenioslo, I. Sosnowska, I. Margiolaki, *Solid State Commun.* 140 (2006) 359.

[41] J. Wang, J.B. Neaton, H. Zheng, V. Nagarajan, S.B. Ogale, B. Liu, D. Viehland, V. Vaithyanathan, D.G. Schlom, U.V. Waghmare, N.A. Spaldin, K.M. Rabe, M. Wuttig, R. Ramesh, *Science* 299 (2003) 1719.

[42] T.J. Park, G.C. Papaefthymiou, A.J. Viescas, A.R. Moodenbaugh, S.S. Wong, *Nano Lett.* 7 (2007) 766.

[43] S. Vijayanand, H.S. Potdar, P.A. Joy, *Appl. Phys. Lett.* 94 (2009) 182507.

[44] A. Maitre, M. Francois, J. Gachon, *J. Phase Equilib.* 25 (2004) 59.

[45] H. Koizumi, N. Niizeki, T. Ikeda, *Jpn. J. Appl. Phys.* 3 (1964) 495.

[46] M.Mahesh Kumar, V.R. Palkar, K. Srinivas, S.V. Suryanarayana, *Appl. Phys. Lett.* 76 (2000) 2764.

[47] G.D. Achenbach, W.J. James, R. Gerson, *J. Am. Ceram. Soc.* 50 (1967) 437.

[48] Y.P. Wang, L. Zhou, M.F. Zhang, X.Y. Chen, J.M. Liu, Z.G. Liu, *Appl. Phys. Lett.* 84 (2004) 1731.

[49] G.L. Yuan, S.W. Or, Y.P. Wang, Z.G. Liu, J.M. Liu, *Solid State Commun.* 138 (2006) 76.

[50] S.M. Selbach, M.A. Einarsrud, T. Tybell, T. Grande, *J. Am. Ceram. Soc.* 90 (2007) 3430.

[51] S. Ghosh, S. Dasgupta, A. Sen, H.S. Maiti, *J. Am. Ceram. Soc.* 88 (2005) 1349.

[52] S.W. Lee, C.S. Kim, *J. Magn. Magn. Mater.* 304 (2006) e772.

[53] M. Kumar, K.L. Yadav, G.D. Varma, *Mater. Lett.* 62 (2008) 1159.

[54] J.K. Kim, S.S. Kim, W.J. Kim, *Mater. Lett.* 59 (2005) 4006.

[55] S. Shetty, V.R. Palkar, R. Pinto, *Pramana* 58 (2002) 1027.

[56] C. Chen, J. Cheng, S. Yu, L. Che, Z. Meng, *J. Crys. Growth* 291 (2006) 135.

[57] J.T. Han, Y.H. Huang, X.J. Wu, C.L. Wu, W. Wei, B. Peng, W. Huang, J.B. Goodenough, *Adv. Mater.* 18 (2006) 2145.

[58] M.P. Pechini, *US Patent* (1967) US3,330,697.

[59] N. Das, R. Majumdar, A. Sen, H.S. Maiti, *Mater. Lett.* 61 (2007) 2100.

[60] R. Mazumder, P.S. Devi, D. Bhattacharya, P. Choudhury, A. Sen, M. Raja, *Appl. Phys. Lett.* 91 (2007) 062510.

[61] G. Catalan, J.F. Scott, *Adv. Mater.* 21 (2009) 2463.

[62] J. Wang, H. Zheng, Z. Ma, S. Prasertchoung, M. Wuttig, R. Droopad, J. Yu, K. Eisenbeiser, R. Ramesh, *Appl. Phys. Lett.* 85 (2004) 2574.

[63] J. Li, J. Wang, M. Wuttig, R. Ramesh, N. Wang, B. Ruette, A.P. Pyatakov, A.K. Zvezdin, D. Viehland, *Appl. Phys. Lett.* 84 (2004) 5261.

[64] R.R. Das, D.M. Kim, S.H. Baek, C.B. Eom, F. Zavaliche, S.Y. Yang, R. Ramesh, Y.B. Chen, X.Q. Pan, X. Ke, *Appl. Phys. Lett.* 88 (2006) 242904.

[65] C. Ederer, N.A. Spaldin, *Phys. Rev. B 71* (2005) 224103.

[66] J.B. Neaton, C. Ederer, U.V. Waghmare, N.A. Spaldin, K.M. Rabe, *Phys. Rev. B* 71 (2005) 014113.

[67] C. Ederer, N.A. Spaldin, *Phys. Rev. Lett.* 95 (2005) 257601.

[68] P.K. Siwach, H.K. Singh, J. Singh, O.N. Srivastava, *Appl. Phys. Lett.* 91 (2007) 122503.

[69] D. Lebeugle, D. Colson, A. Forget, M. Viret, P. Bonville, J.F. Marucco, S. Fusil, *Phys. Rev. B* 76 (2007) 024116.

[70] R.P.S.M. Lobo, R.L. Moreira, D. Lebeugle, D. Colson, *Phys. Rev. B* 76 (2007) 172105.

[71] M. Cazayous, D. Malka, D. Lebeugle, D. Colson, *Appl. Phys. Lett.* 91 (2007) 071910.

[72] W. Eerenstein, F.D. Morrison, J. Dho, M.G. Blamire, J.F. Scott, N.D. Mathur, *Science* 307 (2005) 1203a.

[73] H. Béa, M. Bibes, A. Barthélémy, K. Bouzehouane, E. Jacquet, A. Khodan, J.P. Contour, S. Fusil, F. Wyczisk, A. Forget, *Appl. Phys. Lett.* 87 (2005) 072508.

[74] M.K. Singh, W. Prellier, M.P. Singh, R.S. Katiyar, J.F. Scott, *Phys. Rev. B* 77 (2008) 144403.

[75] M.K. Singh, R.S. Katiyar, W. Prellier, J.F. Scott, *J. Phys.: Condens. Matter* 21 (2009) 042202.

[76] M. Cazayous, Y. Gallais, A. Sacuto, R. De Sousa, D. Lebeugle, D. Colson, *Phys. Rev. Lett.* 101 (2008) 037601.

[77] M.K. Singh, R.S. Katiyar, J.F. Scott, *J. Phys.: Condens. Matter* 20 (2008) 252203.

[78] J.F. Scott, M.K. Singh, R.S. Katiyar, *J. Phys.: Condens. Matter* 20 (2008) 322203.

[79] S.A.T. Redfern, C. Wang, J.W. Hong, G. Catalan, J.F. Scott, *J. Phys.: Condens. Matter* 20 (2008) 452205.

[80] J. Chen, X. Xing, A. Watson, W. Wang, R. Yu, J. Deng, L. Yan, C. Sun, X. Chen, *Chem. Mater.* 19 (2007) 3598

[81] T.J. Park, Y. Mao, S.S. Wong, *Chem. Commun.* 2004 (2004) 2708

[82] J. Li, J. Wang, M. Wuttig, R. Ramesh, N. Wang, B. Ruette, A.P. Pyatakov, A.K. Zvezdin, D. Viehland, *Appl. Phys. Lett.* 84 (2004) 5261

[83] K.Y. Yun, M. Noda, M. Okuyama, *Appl. Phys. Lett.* 83 (2003) 3981

[84] Y.H. Chu, Q. Zhan, L.W. Martin, M.P. Cruz, P.L. Yang, G.W. Pabst, F. Zavaliche, S.Y. Yang, J.X. Zhang, L.Q. Chen, *Adv. Mater.* 18 (2006) 2307

[85] H.W. Jang, D. Ortiz, S.H. Baek, C.M. Folkman, R.R. Das, P. Shafer, Y. Chen, C.T. Nelson, X. Pan, R. Ramesh, *Adv. Mater.* 21 (2009) 817.

[86] Y. Yun, D. Ricinschi, T. Kanashima, M. Noda, M. Okuyama, *Jpn. J. Appl. Phys.* 43 (2004) L647.

[87] S. Vijayanand, M.B. Mahajan, H.S. Potdar, P.A. Joy, *Phys. Rev. B* 80 (2009) 64423.

[88] P.A. Joy, S.K. Date, *J. Magn. Magn. Mater.* 222 (2000) 33.

[89] P.A. Joy, S.K. Date, *J. Magn. Magn. Mater.* 218, (2000) 229.

[90] C.R. Sankar, P.A. Joy, *Phys. Rev. B*72 (2005) 024405.

[91] P.A. Joy, S.K. Date, *J. Magn. Magn. Mater.* 220 (2000) 106.

[92] R. Palai, H. Huhtinen, R. S. Katiyar, J. F. Scott, http://www.arXiv.org:0707.1657v1.

[93] C. Paraschiv, B. Jurca, A. Ianculescu, O. Carp, *J. Therm. Anal. Cal.* 94 (2008) 411.

[94] W. Morales, M. Cason, O. Aina, N.R. de Tacconi, K. Rajeshwar, *J. Am. Chem. Soc.* 130 (2008) 6318.

[95] S. Deka, P.A. Joy, *J. Nanosci. Nanotech.* 8 (2008) 3955.

[96] V. Sreeja, S. Vijayanand, S. Deka, P.A. Joy, *Hyperfine Interact.* 183 (2008) 99.

[97] J.P. Chen, C.M. Sorensen, K.J. Klabunde, G.C. Hadjipanayis, E. Devlin, A. Kostikas, *Phys. Rev. B* 54 (1996) 9288.

[98] N. Ponpandian, A. Narayanasamy, C.N. Chinnasamy,N. Sivakumar, J.M. Greneche, K. Chattopadhyay, K. Shinoda, B. Jeyadevan, K. Tohji, *Appl. Phys. Lett.* 86 (2005) 192510.

[99] J.A.T. Taylor, *Am. Ceram. Soc. Bull.* 74 (1995) 81.

Chapter 7

Conclusions

Nanostructured metal oxides with various morphologies such as nanoparticles, nanorods, nanotubes, nanoplates, etc, are useful for various applications. It is important to make nanostructures with well-defined and hierarchically arrangedmorphologies for most of the applications such as in catalysis, sensors, Li-ion batteries, fuel cells, etc. In most of the cases employed for the synthesis of nanomaterials with well-defined morphological features, templates are used which limit the growth of the nanomaterials in some dimensions, and the templates need to be removed after formation of the materials of interest. In this respect, it is preferable to get control on the morphology without using any templates. Many different wet chemical methods are available for the synthesis of nanostructured oxide materials. Many of the physical properties of the nanostructured oxide materials are known to be dependent on the method of synthesis and processing conditions. Also, the properties and applications of the nanostructured oxides depend on the size, morphology, surface area, porosity, etc. Therefore, still it is a challenge to optimize the synthesis and processing conditions to get morphologically defined porous nanostructured oxides with high surface area. The main objective of this work was to synthesize some spinel based oxides in nanocrystalline form by the well-known coprecipitation method and to study their properties.

The simple and facile coprecipitation method is modified to get a molecular precursor with well-defined morphology, to synthesize cobalt based spinel Co_3O_4. Porous nanorods of Co_3O_4, with the same morphology as that of the precursor, is obtained after calcination in air. The optimized synthesis conditions improved the crystallinity of the molecular precursor, cobalt hydroxy carbonate. This also helped in the formation of porous nanorods of Co_3O_4. The nanocrystalline porous Co_3O_4 is obtained with high surface area and the

material is found to be a promising material for selective CO gas sensing. The porous nanorods exhibited better performance as a CO sensor, at a moderate operating temperature of 250 °C, with fast recovery and response time. Similarly, the nanomaterial is also found to be a good catalyst for oxidation reactions. In the case of oxidation of veratryl alcohol to veratryl aldehyde, the nanorods showed a reasonable conversion and selectivity.

The porous Co_3O_4 nanorods are found to be a good anode material for Li-ion battery. A capacity of 1155 $mAhg^{-1}$ is obtained during initial cycles, which reduced to 820 $mAhg^{-1}$ after few cycles. This value is found to be higher than that reported for non-porous nanorods of Co_3O_4. Excellent durability is observed for 25 cycles and beyond, with out any obvious signs of further capacity loss or performance degradation. The mechanism of charge-discharge process is studied using solid state NMR, powder XRD and magnetic measurements. These studies, after charge and discharge, proved the stability of the material and formation of Co nanodomains. The porous nanostructured Co_3O_4 is found to exhibit a considerably high value of capacitance indicating the applicability of porous nanorods of Co_3O_4 as a suitable material for supercapacitor applications.

To study the role of Co^{2+} in Co_3O_4, nanostructured $ZnCo_2O_4$ spinel was synthesized under identical conditions. The nanocrystalline material obtained through a mixed molecular precursor is found to be a good sensor for LPG gas. The overall LPG sensing performance of the nanostructured $ZnCo_2O_4$ is better than that reported for most of the oxide semiconductor based sensors already developed. Thus the studies showed that nanocrystalline Co_3O_4 which is a good sensor for CO gas with better selectivity can be modified to selectively detect LPG gas by replacing Co^{2+} with Zn^{2+}.

Thus, the present studies indicated that there is lot of scope in the future for the improvement of the performance of the cobalt based spinel oxides in various applications. The present method of synthesis, without using any templates, is a convenient, cost effective and faster method for developing morphology controlled nanostructures by suitably modifying the synthesis and processing conditions. The method is also found to be highly reproducible and scalable for large scale production. It is expected that much higher surface areas can be achieved by modifying the synthesis conditions. Similarly, the performance in various applications can be possibly improved by controlling the porosity, surface area and morphology. Also, the properties and applications can be modified and

controlled by proper substitution of Co^{2+} and Co^{3+} in Co_3O_4 by other transition metal ions. The present studies suggest further scope for future work to suitably modify the materials for a wide range of energy saving and environmental applications.

The same synthetic protocol as used for the synthesis of cobalt based spinels has been extended to Fe based spinels of the general formula AFe_2O_4, where A = Fe, Zn, and Co. However, when Co^{3+} in ACo_2O_4 is replaced by Fe^{3+}, nanoparticles are obtained instead of nanorods, indicating the role of the constituent ions in determining the morphology of the final product. The oxides Fe_3O_4 and $ZnFe_2O_4$ are obtained directly on precipitation. On the other hand, in the case of cobalt ferrite, a homogeneously mixed active precursor has been formed by optimizing the synthesis conditions which on calcination gave the spinel oxide. Fe_3O_4 with cation deficiency is obtained by the present method of synthesis and the Fe:O ratio or the cation deficiency could be controlled by varying the digestion time. In all the cases, the crystallinity is improved by digesting the precipitate at a mild condition of 70^o C. Further, as the spinel type ferrites are magnetic, the magnetic properties have been studied and used as a tool to get detailed information on the characteristics of the nanostructures. To get insight and information on the dependence of synthesis conditions on the magnetic properties, the mixed ferrites have also been synthesized through an auto-combustion method. The magnetic properties are correlated with the effect of synthesis conditions. The present method of synthesis by coprecipitation followed by digestion at 70 °C suggests that the particle size, morphology and hence the properties of the spinel ferrite nanoparticles can be controlled by varying a single parameter, ie. the digestion time. The method may be suitable for the synthesis of surfactant coated and other core-shell type magnetic oxide nanoparticles for various applications, suggesting scope for further research.

The important single phase multiferroic system, $BiFeO_3$, has attracted attention in the recent times because of its applications. The bulk antiferromagnetic material can be made ferromagnetic by decreasing the particle size. As the coprecipitation/digestion method is found to be a convenient method for the synthesis of nanoparticles of spinel type oxides, the same procedure is extended for the synthesis of nanoparticles of the multiferroic $BiFeO_3$ (bismuth ortho-ferrite). There are many contradictions reported in the literature on the magnetic properties of nanocrystalline $BiFeO_3$ synthesized by vari-

ous methods. Hence, nanoparticles of single phase $BiFeO_3$ has been synthesized by the coprecipitation/digestion method followed by calcination as well as by a self ignition auto-combustion method. The magnetic properties of the nanocrystalline material synthesized by the two different methods are compared to study the effect of synthesis conditions on the magnetic properties.

$BiFeO_3$ nanoparticles with average size of ∼50 nm is synthesized by a coprecipitation/digestion method. It is found that the material becomes ferromagnetic below the Neel temperature of the bulk material (∼645 K). For nanoparticles of $BiFeO_3$, anomalous magnetic characteristics are observed at temperature regions closer to that of the phase transitions reported in the literature, from Raman spectroscopic studies, on bulk materials and single crystals. These results suggest that the phase transitions are directly associated with changes in the intrinsic magnetic nature of the $BiFeO_3$, strongly coupled with the lattice. It has been concluded that the anomalies observed at the specified temperatures are likely to be some changes associated with the domain structure of the material at low temperatures.

Single phase nanocrystalline multiferroic $BiFeO_3$, as evidenced from powder XRD studies, could be synthesized by the glycine-nitrate auto-combustion method by optimizing the synthesis conditions. Unexpectedly high magnetic moment is observed for the nanocrystalline sample synthesized by the auto-combustion method. The possible effect of the synthetic methodology influencing the magnetic properties of the $BiFeO_3$ system has been explained from detailed structural and magnetic characterization. Detailed XRD studies and high temperature magnetic measurements indicated the presence of very small amounts of Fe_3O_4 as a magnetic impurity phase responsible for the higher and unexpected magnetic moment, which could not be detected from normal XRD studies. Thus, the present studies indicated the importance of the detailed material characterization studies required before coming to any final conclusions on the unusual properties observed for functional nanomaterials.

List of Publications

1. "Nanostructured spinel $ZnCo_2O_4$ for the detection of LPG": **S. Vijayanand**, P. A. Joy and H. S. Potdar, D. Patil and P. Patil *Sensors and Actuators B* (Accepted for publications).

2. "A simple chemical co-precipitation/calcination route for the synthesis of simulated synroc-B and synroc-C powders" H.S. Potdar, **S. Vijayanand**, K. Khaja Mohaideen, K.R. Patil, P.A. Joy, R. Raja Madhavan, K.V.G. Kutty, R.D. Ambashta, P.K. Wattal. *Mater. Chem. Phys.* 123 (2010) 695.

3. "Magnetic characteristics of nanocrystalline multiferroic $BiFeO_3$ at low temperatures": **S. Vijayanand**, M. B. Mahajan, H. S. Potdar, and P. A. Joy. *Phys. Rev. B* 80 (2009) 064423.

4. "Highly sensitive and fast responding CO sensor based on Co_3O_4 nanorods : D. Patil, P. Patil, **S. Vijayanand**, P A. Joy and H. S. Potdar. *Talanta* 81 (2010) 37.

5. "Origin of high room temperature ferromagnetic moment of nanocrystalline multiferroic $BiFeO_3$: **S. Vijayanand,** H. S. Potdar, and P. A. Joy. *App. Phys. Lett.* 94 (2009) 182507.

6. "Ferromagnetic to spin glass cross over in $(La,Tb)_{2/3}Ca_{1/3}MnO_3$" : C. Raj Sankar, **S. Vijayanand** and P.A. Joy. *Solid State Sci.* 11 (2009) 714.

7. "Magnetic and Mssbauer spectroscopic studies of NiZn ferrite nanoparticles synthesized by a combustion method": V. Sreeja, **S. Vijayanand,** S. Deka, and P. A. Joy. *Hyperfine Interact.* 183 (2008) 99.

8. "Highly active nanostructured Co_3O_4 catalyst with tunable selectivity for liquid phase air oxidation of p-Cresol": Vikas S. Kshirsagar, **S. Vijayanand,** H. S. Potdar, P. A. Joy, K. R. Patil, and C. V. Rode. *Chem. Lett.* 37 (2008) 310.

9. "Photocatalytic decomposition of methylene nanocrystalline titania prepared by different blue on methods": V. Ramaswamy, N.B. Jagtap, **S. Vijayanand,** D.S. Bhange, P.S. Awati. *Mater. Res. Bull.* 43 (2008) 1145.

10. "Direct comparison of the aging and memory effects of magnetic nanoclusters and nanoparticles": C. Raj Sankar, **S. Vijayanand,**, Seema Verma, P. A. Joy. *Solid State Commun.* 141 (2007) 307.

11. "Investigation of oxygen reduction at platinum loaded poly (o-phenylenediamine) electrode in acid medium": P. Gajendran, **S. Vijayanand,** R. Saraswathi. *J. Electroanal. Chem.* 601 (2007) 132.

Awards:

"**Award of Senior Research Fellowship (SRF)**" for 2007-2010, by Council of Scientific and Industrial Research (CSIR), Govt. of India, New Delhi.